DISSERTATION

ATOM-PHOTON INTERACTIONS IN SLOW-LIGHT WAVEGUIDE QED

ausgeführt zum Zwecke der Erlangung des akademischen Grades eines Doktors der Naturwissenschaften unter der Leitung von

ASSOC. PROF. PETER RABL
141
ATOMINSTITUT

eingereicht an der Technischen Universität Wien
Fakultät für Physik

von

GIUSEPPE CALAJÓ, DOTT. MAG.
Matrikelnummer: 1428978
Bennogasse 30/1
1080 Wien, Austria

Wien, am

Diese Dissertation haben begutachtet:

Prof. Dr. S. Pascazio

Prof. Dr. J. J. García Ripoll

Abstract

Waveguide quantum electrodynamics (QED) refers to a scenario where single or multiple atoms or solid-state emitters are coupled to a one dimensional optical channel. The efficient interaction between individual quantum systems with photons that are confined along a single direction makes this setting particularly interesting for investigating quantum optical phenomena and for future quantum networking applications.

In this thesis, we go beyond the standard scenario and address the new regime of "slow-light waveguide QED", where due to a narrow photonic bandwidth the maximal photonic group velocity inside the waveguide is significantly reduced compared to free space. We first discuss the properties of atom-photon bound states, which emerge as the new elementary excitations of the system when the atom-field coupling strength becomes comparable to the photonic bandwidth. Such bound states are formed by an atom and a localized photonic excitation and represent the continuum analog of the familiar dressed states in single-mode cavity QED. In this thesis we analyze the linear and nonlinear spectral features associated with single- and multi-photon dressed states and we describe how the formation of bound states affects the waveguide-mediated dipole-dipole interactions between separated atoms.

We then consider a narrow-bandwidth waveguide coupled to atoms that are moving with velocities comparable to the reduced speed of light. Under these conditions, we observe a velocity-induced directionality and the emergence of effective divergencies in the photonic density of states. This anomalous interaction between atoms and co-propagating Cherenkov photons gives rise to a range of novel phenomena and non-perturbative effects in the emission of photons and the resulting photon-mediated interactions between moving atoms.

Finally, we consider the coupling of multiple emitters to a slow-light waveguide in the presence of propagating acoustic waves. In this case, the strong index modulations induced by such waves can substantially modify the effective photonic density of states and thereby influence the strength, the directionality, as well as the overall characteristic of photon emission and absorption processes. The generalization of these control techniques to two dimensional photonic lattices creates a new scenario for chiral quantum optics, where non- reciprocal light-matter interactions are established along a single direction and with an extremely slow radial decay. These effect provide a versatile tool for implementing various quantum communication protocol in large-scale photonic networks.

Zusammenfassung

Das Gebiet der Wellenleiterquantenelektrodynamik (QED) befasst sich mit der Kopplung von Atomen oder Emittern in Festkörpern an das Lichtfeld in einem eindimensionalen optischen Leiter. Durch den transversalen Einschluss der emittierten Photonen können diese langreichweitige Wechselwirkungen zwischen den einzelnen Quantensystemen vermitteln, was diese Architektur für die Untersuchung quantenoptischer Phänomene und für die Realisierung zukünftiger Quantennetzwerke besonders interessant macht.

In dieser Doktorarbeit werden verschiedene neue Aspekte der Wechselwirkung zwischen Licht und Atomen in nanophotonischen Wellenleitern theoretisch untersucht. Diese Arbeiten adressieren dabei vor allem ein neues Regime der "Wellenleiter-QED mit langsamen Photonen", in dem die maximale Gruppengeschwindigkeit im Inneren des Wellenleiters, im Vergleich zum freien Raum, erheblich reduziert ist. Solche Bedingungen ergebenen sich, z.B., in der Nähe von Bandkanten in photonischen Kristallen und führen zu einer extremen Verstärkung der Atom-Licht-Kopplung. In dieser Dissertation werden zunächst die Eigenschaften gebundener Zustände zwischen Atomen und Photonen, die die neuen Elementaranregungen dieses Systems darstellen, untersucht. Dabei werden zum ersten Mal auch die Bindung von mehreren Photonen an ein einzelnes Atom analysiert und die sich daraus ergebenden linearen und nichtlinearen spektralen Charakteristika dieser "multiphoton dressed states" beschrieben.

Des Weiteren wird der interessante Fall betrachtet, in dem sich die Atome mit einer Geschwindigkeit bewegen, die mit der reduzierten Lichtgeschwindigkeit der Photonen vergleichbar ist. Unter diesen Vorraussetzungen beobachtet man eine von der Bewegung induzierten Richtungsabhängigkeit der emittierten Photonen und das Auftreten von nicht-perturbativen Effekten in der Atom-Licht-Kopplung. Diese Anomalien ergeben sich aus der lang anhaltenden Wechselwirkung mit den emittierten Cherenkov-Photonen, welche sich mit gleicher Geschwindigkeit wie die Atom entlang des Wellenleiters bewegen. Als Gegenstück dazu werden in einem weiterem Projekt dann die Auswirkungen von starken akustischen Wellen auf die Emissionseigenschaften von statischen Atomen analysiert. Dabei findet man, dass, im Regime des langsamen Lichts, diese akustische Wellen die Photon im Wellenleiter "mitziehen" können und damit sowohl die Richtung als auch die Form der emittierten Lichtpakete beeinflussen. Diese Effekte können direkt für die Übertragung von Quantenzuständen in photonischen Netzwerken ausgenützte werden.

Contents

Introduction

Reaching a detailed understanding of the interaction between atoms and light at the quantum level is of fundamental importance to be able, one day, to implement quantum information processing on a large scale. The nature of this interaction depends strongly on the detailed structure of the electromagnetic environment and can result in drastically different physical phenomena. In this thesis we analyse the coupling of atoms or other emitters to the radiation field confined in low dimensional photonic structures, where the reduced speed of propagation gives rise to new interesting scenarios for light-matter interactions.

From free space to waveguide QED

The necessity of structured photonic environments arises from the intrinsically weak nature of light-matter interactions. Indeed, in free space, the radiative properties of few emitters are characterized by a small atomic dipole moment and by the large extension of the unconfined field. This results, for example, in the case of spontaneous emission, in an irreversible decay to a lower energy state and an emission of photons propagating into random direction [1, 2]. Obviously, such a process constitutes a major limitation, if the final goal is to implement efficient atom-atom interactions mediated by the field.

This natural "deficiency" of light-matter interactions in free space has motivated a lot of efforts to modify the electromagnetic environment by changing the geometry of the considered systems. Indeed, by confining the optical field to a small region in space the light-matter interaction strength can be drastically increased. This has led to the development of the field of cavity-QED (CQED) [3, 4], where in recent years the fabrication of optical cavities with high quality factors has enabled the control of the radiative properties of small matter systems in a way that was unthinkable before. The effect of the field confinement is not only limited to the enhancement or the inhibition of spontaneous emission [91], but can also lead to a coherent emission and reabsorption of photons. This feature, combined with atom-atom interactions makes cavity QED a promising platform for processing quantum information. On the other hand, for the final goal of building a complex quantum network [5], cavity QED systems are not enough. Indeed, due to their limited extension, they cannot provide the distribution of such information on a large scale. This task can instead be successfully accomplished by optical waveguides where, due to the one dimensional

confinement, photons can carry quantum information over a long distance.

For this reason and also due to the experimental developments in nanophotonics and superconducting circuits, there has been a lot of interest over the past years on interfacing two-level emitters with 1D waveguides. This new scenario for light-matter interactions is known as "waveguide QED" [6, 7, 8, 9, 10, 11]. Here the 1D confinement of light does not only allow efficient transport of information, but can also mediate long-range interactions between consecutive atoms along the waveguide. This effect can lead to new types of many-body physics and quantum information applications, such as correlated photon scattering [11, 12, 13, 14], self-organized atomic lattices [15, 16, 17], generation of long-distance entanglement [18, 19, 20, 21, 22, 23, 24, 25, 26, 27, 28, 29] and new realizations of quantum gates [30, 31, 32].

Slow-light waveguide QED

A major limitation to build an emitter-waveguide interface relies on the fact that the system is still embedded into a 3D environment and the atom can also emit into other radiative and non-radiative decay channels. A solution for this problem can be found again by engineering the electromagnetic environment. In particular, in photonic crystal waveguides [33, 34, 35, 36, 37, 38, 39, 40], the periodic modulation of the refractive index generates a photonic band structure, where, due to the presence of divergencies in the photonic density of states, the atomic emission into the guided modes can be significantly enhanced. On the other hand, this increase of the decay rate combined with a reduction of the photon group velocity leads to a new non-perturbative regime for atom-light interactions. In particular, such conditions can lead to the formation of so-called "atom-photon bound states" [34, 41, 42, 43, 44, 45, 46], which appear as additional discrete energy levels inside the photonic gap. The existence of such bound states leads to interesting new effects such as light localization and re-absorption of emitted photons, excitation trapping and coherent dipole-dipole long-range interactions [47, 48, 49] and many new possibilities for quantum simulation of many-body physics [49, 50, 51].

In photonic crystal waveguides usually the width of the photonic band is much larger than the atom-field coupling. This makes, in most of cases, the atom-photon bound states weakly hybridized. In this thesis we focus on new physical phenomena that arise in the opposite regime, namely when the bandwidth of the waveguide is extremely narrow and comparable to typical atomic decay rates. This does not only have an impact on the nature of the atom-photon bound states, but also significantly affects the propagation of photons inside the structure, which leads to a strong reduction of the maximal group velocity of the photons. Therefore, this regime of light-matter interactions is then referred to as "slow-light waveguide QED" [52], which is the central topic of this PhD thesis. As we will see, the small bandwidth of these waveguides leads to many interesting effects that will be discussed in chapters 4 – 6.

A simple way to capture the main features of slow-light waveguides is to consider a tight binding model for an array of coupled cavities [53, 54, 55, 56, 57, 58, 59, 60,

52, 61, 62]. The atom-photon bound states of this model are discussed in detail in chapter 4. Compared to usual photonic crystal waveguides, the narrow width of the band gives rise to states with strongly hybridized atomic and photonic components. This hybridization makes it possible, for a single emitter, to localize more than one excitation, leading to the formation of multi-photon bound states [52, 61]. The dressed nature of these states manifests itself in an intrinsic non-linear energy spectrum that could be used to achieve the regime of quantum non-linear optics in a waveguide. Another effect related to the bound states is the modification of the usual long-range dipole-dipole interactions between multiple emitters obtained in broadband waveguides. Indeed, the bound-state localization leads to modified short-range dipole-dipole interactions where the polaritonic (not just atomic) nature of the states cannot be neglected.

A different feature of slow-light waveguides that we address in chapter 5 is related to the strong reduction of the maximum photonic group velocity, which can become comparable to typical atomic velocities, i.e. $v \sim 10^4$m/s. This slow-light propagation combined with the strong atom-light interactions discussed in the previous chapter, leads to an unconventional Cherenkov physics for atoms moving close to the waveguide and coupled to the confined field. Indeed, the atomic motion does not only induce a directional emission, but also gives rise to the formation of divergencies in the photonic density of states. Due to such divergencies we find a non-perturbative directional emission of the atom that can enhance the excitation transfer between multiple emitters [63].

The reduced group velocity in slow-light waveguides can be comparable not only to atomic velocities, but also to the speed of sound. In chapter 6, we consider a scenario where propagating acoustic waves induce, through the acousto-optic effect, a deformation of the photonic band structure. This effect goes beyond conventional Brillouin scattering and leads to a strong and controllable directional emission. This tunability enables the control of emitter-emitter interactions in an extended quantum network and to generate stationary entangled states. When generalized to two dimensional photonic lattices we find that the acoustic waves induce a strongly focused, directional emission with a slow radial decay. This property can be exploit for realizing an almost chiral interaction between emitters in 2D. Therefore, these findings can have a significant impact on future implementations of extended quantum networks.

Outline of the thesis

This thesis summarizes my scientific contributions achieved during the four years of my PhD and is divided into three main parts. The first three chapters (chapters 1 – 3) provide an introduction to the thesis, starting from the general framework of light-matter interactions in free space and cavity QED (chapter 1), passing to a basic overview of waveguide QED (chapter 2) and concluding with an introduction to slow-light waveguide QED (chapter 3).

The central part of the thesis (chapters 4 – 6) then summarizes the results of my

main research projects. Chapter 4 presents the properties of atom-photon bound states in a slow-light waveguide and the generalization thereof to the multi-photon and multi-atom scenarios. Chapter 5 describes the emission and the interaction of atoms moving close to a slow-light waveguide. In chapter 6 an acousto-optic waveguide is analyzed where a propagating modulation of the structure induced by an acoustic wave can be used to control atom-light interactions.

The last part of the thesis (chapter $7-8$) contains the results of two additional side projects that are not connected to slow-light waveguides. In chapter 7 a setup is considered where a single emitter is coupled to a semi-infinite waveguide. In this configuration some of the eigenstates of the system are so-called bound states in the continuum (BIC) [64, 65, 66, 67, 68, 19, 27]. In this project it is shown how these states can be prepared via multi-photon scattering processes [69]. Chapter 8 presents another side project of my PhD, where a circuit QED [70, 71] setup with multiple superconducting qubits coupled to a microwave resonator is considered. In this system it has been shown that, in the ultra-strong coupling regime [72, 73], the low-energy states have a high degree of multi-qubit entanglement [74]. In this project a protocol has been developed that exploits a time-dependent control of some system parameters to be able to extract and energetically isolate these states [75].

List of publications

Part of the results described in this thesis (chapters 4, 5 and 8) have been published in peer-review journals. The work presented in chapter 7 has been posted on arxiv [69] and has been submitted to a peer-review journal. An other publications regarding the work presented in chapters 6 is currently in preparation.

PHYSICAL REVIEW A 93,033833 (2016) [52]

Atom-field dressed states in slow-light waveguide QED

G. Calajó, F. Ciccarello, D. Chang, P. Rabl

In this article we discuss the properties of atom-photon bound states in waveguide QED systems consisting of single or multiple atoms coupled strongly to a finite-bandwidth photonic channel. Such bound states are formed by an atom and a localized photonic excitation and represent the continuum analog of the familiar dressed states in single-mode cavity QED. Here we present a detailed analysis of the linear and nonlinear spectral features associated with single- and multi-photon dressed states and show how the formation of bound states affects the waveguide-mediated dipole-dipole interactions between separated atoms. Our results provide a both qualitative and quantitative description of the essential strong-coupling processes in waveguide QED systems, which are currently being developed in the optical and the microwave regime. For this work, I performed all the analytical and numerical calculation described in the paper under the supervision of P. Rabl.

PHYSICAL REVIEW A 95,043824 (2017) [63]

Strong coupling between moving atoms and slow-light Cherenkov photons

G. Calajó and P. Rabl

In this article we describe the coupling of moving atoms to a one dimensional photonic waveguide in the regime where the atomic velocities are comparable to the effective speed of light. Such conditions could be achieved, for example, in photonic crystals or coupled resonator arrays, where the maximal photonic group velocity is significantly reduced compared to free space. In this case the interplay between a velocity-induced directionality and the emergence of new divergencies in the photonic density of states gives rise to a range of novel phenomena and non-perturbative effects in the emission of photons and the resulting photon-mediated interactions between moving atoms. We show that apart from potential implementations with optical waveguides, Rydberg atoms flying above a coupled array of superconducting microwave resonators provide a versatile platform for exploring this new regime of atom-light interactions under experimentally accessible conditions. For this work, I performed all the analytical and numerical calculation described in the paper under the supervision of P. Rabl.

PHYSICAL REVIEW LETTERS 119,183602 (2017) [75]

Harvesting Multiqubit Entanglement from Ultrastrong Interactions in Circuit Quantum Electrodynamics

F.Armata, G. Calajó, T. Jaako, M. S. Kim, P. Rabl

In this article we analyze a multiqubit circuit QED system in the regime where the qubit-photon coupling dominates over the system's bare energy scales. Under such conditions a manifold of low-energy states with a high degree of entanglement emerges. Here we describe a time-dependent protocol for extracting these quantum correlations and converting them into well-defined multipartite entangled states of noninteracting qubits. Based on a combination of various ultrastrong-coupling effects, the protocol can be operated in a fast and robust manner, while still being consistent with experimental constraints on switching times and typical energy scales encountered in superconducting circuits. Therefore, our scheme can serve as a probe for otherwise inaccessible correlations in strongly coupled circuit QED systems. It also shows how such correlations can potentially be exploited as a resource for entanglement-based applications. For this work, I contributed as a second author and I supported F. Armata (first author) performing parts of the analytic and numerical calculations regarding the entanglement harvesting protocol. The circuit implementation of the protocol was developed by T. Jaako. The work was done under the supervision of P. Rabl.

Chapter 1

Atom-light interactions in structured environments

In this first chapter we briefly review the main features regarding the interaction of one or multiple two-level atoms (TLA or sometimes we will refer to them as qubits) with localized modes of the electromagnetic field. Throughout this thesis (with the exception of the project discussed in chapter 8) we will focus on the limit where the atom-field coupling strength is much smaller than the bare atomic and photonic frequencies involved in the dynamics. In this limit is possible to apply the rotating wave approximation (RWA) and neglect the fast rotating terms that appear in the atom-light interaction Hamiltonian [3, 4].

In section 1.1 we will briefly introduce the QED Hamiltonian that describes this atom-light system under the RWA and along the rest of chapter we will show how it is drastically affected by the confinement of the light. In the first section 1.2, we consider the field in free space and we focus on the single and collective behaviour of an atomic ensemble coupled to it. In section 1.3 we show how the confinement of the field in an optical cavity can drastically affect the radiation properties of single and multiple emitters. Finally, in section 1.4 we introduce the field confinement in a one dimensional waveguide, a topic that we will then discuss more extensively in chapter 2.

1.1 QED Hamiltonian in RWA

Let us consider a setup where N_a two-level atoms (TLA) are located at positions $\vec{x}_i$ and coupled to the electromagnetic field in a non-specified geometry. The atoms have a ground state $|g\rangle$ and an excited state $|e\rangle$, which are separated in frequency by ω_i. The electromagnetic field in second quantization is described by a collection of quantized modes indexed by the wavevector $\vec{k}$ and described in terms of the annihilation and creation operators $a_{\vec{k}}$ and $a^\dagger_{\vec{k}}$, respectively. The $a^\dagger_{\vec{k}}$ define the field vacuum state: $a_k|0\rangle = 0$, while annihliation operators create excitations from the vacuum: $(a^\dagger_{\vec{k}})^n|0\rangle = \sqrt{n!}|n_{\vec{k}}\rangle$. They both obey the commutation relations $\left[a_{\vec{k}}, a^\dagger_{\vec{k}'}\right] =$

$\delta_{\vec{k},\vec{k}'}$, where $\delta_{\vec{k}',\vec{k}}$ is the Kronecker delta. If we work under the dipole and the RWA the Hamiltonian describing the system reads

$$H = \sum_{i=1}^{N_a} \hbar\omega_i |e\rangle_i\langle e| + \sum_{\vec{k}} \hbar\omega_{\vec{k}} a^\dagger_{\vec{k}} a_{\vec{k}} + \hbar \sum_{i=1}^{N_a} \sum_{\vec{k}} \left[g^*_{\vec{k}}(\vec{x}_i) a^\dagger_{\vec{k}} \sigma^i_- + g_{\vec{k}}(\vec{x}_i) a_{\vec{k}} \sigma^i_+ \right], \tag{1.1}$$

where $g_{\vec{k}}(\vec{x}_i)$ is the atom-field coupling strength and $\sigma^i_- = (\sigma^i_+)^\dagger = |g\rangle_i\langle e|$ is the atomic annihilation operator. Here $\omega_{\vec{k}}$ are the field angular frequencies, which are obtained form the solutions of the Helmholtz equation:

$$\left(\nabla^2 + n^2(\vec{x}) \frac{\omega^2_{\vec{k}}}{c^2} \right) \vec{\Phi}_{\vec{k}}(\vec{\vec{x}}) = 0, \tag{1.2}$$

where c is the speed of light, $n(\vec{x})$ is the refractive index of the medium and $\vec{\Phi}_{\vec{k}}(\vec{\vec{x}})$ are the mode functions of the field. Equation (1.2) is of fundamental importance not only because it provides the eigenfrequencies of the field, but also because it gives the mode functions that determine the atom-field coupling

$$g_{\vec{k}}(\vec{x}_i) = \sqrt{\frac{\omega_{\vec{k}}}{2\hbar\epsilon_0}} \vec{d}^i_{eg} \cdot \vec{\Phi}_{\vec{k}}(\vec{x}_i) \tag{1.3}$$

where ϵ_0 is the vacuum permittivity and $\vec{d}^i_{eg} = \langle e|\vec{d}^i|g\rangle$ is the atomic transition dipole moment of the i-th atom. The mode functions are normalized as:

$$\int d^3\,\vec{x} \vec{\Phi}^*_{\vec{k}'}(\vec{\vec{x}}) \cdot \vec{\Phi}_{\vec{k}}(\vec{\vec{x}}) = \delta_{\vec{k}',\vec{k}}. \tag{1.4}$$

This last condition depends crucially on the boundary conditions for the field and thus on the system geometry. In the next section we will show how considering different geometries leads to completely different types of atom-light interactions.

1.2 Free field in three dimension

In free space ($n(\vec{x}) = 1$) the field is infinitely extended such that the spacing of the wave-vectors approaches zero and the index $\vec{k}$ spans an unbounded continuum of modes. In this case the mode functions of the electromagnetic field are plane waves of the form:

$$\vec{\Phi}_{\vec{k},\lambda}(\vec{\vec{x}}) = \vec{e}_\lambda(\vec{k}) \frac{1}{\sqrt{(2\pi)^3}} e^{i\vec{k}\cdot\vec{x}}, \tag{1.5}$$

where $\vec{e}_\lambda(\vec{k})$ are the polarization unit vectors that satisfy $\vec{k}\cdot\vec{e}_\lambda(\vec{k}) = 0$. This condition follows from the Coulomb gauge and indicates that there are two possible independent perpendicular components for the field, labelled by the index $\lambda = 1, 2$, both in the plane orthogonal to the propagation direction. By plugging the ansatz (1.5) into the Helmholtz equation leads to the usual linear dispersion relation $\omega_k = ck$, where $k = |\vec{k}|$ and the speed of light c coincides with the group velocity.

It is important to observe that in free space the atom-light coupling strength is inherently weak compare to all the other energy scales. This feature, combined with the huge amount of photonic degrees of freedom, allows one to treat atom-light interactions with perturbation theory techniques. This can be done not only at the Hamiltonian level, with the already mentioned RAW approximation, but also in the dynamics, for example, by making a Born-Markov approximation to adiabatically eliminate the field degrees of freedom. In the following we will show how such techniques can still lead to interesting effects for the collective emission of TLA ensembles.

1.2.1 Collective emission of N_a atoms

The full dynamics described by Hamiltonian (1.1) is in general a complex many-body problem. Nevertheless, it is possible to get an effective description by just writing down a master equation for the reduced atomic dynamics. Throughout this thesis we will make use of this technique many times so in this section we will briefly review the main steps of its derivation for the specific case of an ensemble of N_a atoms interacting with the free space electromagnetic field. This problem both in free space and in cavity QED has been studied for decades [76, 77]. To further simplify the calculation we will assume that all the atoms have the same frequency $\omega_i = \omega_a$ and that they are located inside a small volume as shown in Fig. 1.1(a).

Let us define by ρ_{tot} the total density operator for the atoms and the field, which evolves in interaction picture according to the Von Neumann equation:

$$\dot{\rho}_{\text{tot}}(t) = -\frac{i}{\hbar}[H_I(t), \rho_{\text{tot}}(t)]. \tag{1.6}$$

Here we took the continuum limit to rewrite Hamiltonian (1.1) in the interaction picture:

$$H_I(t) = \hbar \sum_{i=1}^{N_a} \sum_{\lambda} \int d^3\vec{k} \left[g^*_{\vec{k},\lambda}(\vec{x}_i) a^\dagger_{\vec{k},\lambda} \sigma^i_- e^{-i\delta^i_{\vec{k}} t} + g_{\vec{k},\lambda}(\vec{x}_i) a_{\vec{k},\lambda} \sigma^i_+ e^{i\delta^i_{\vec{k}} t} \right], \tag{1.7}$$

where we denoted by $\delta_{\vec{k}} = \omega_a - \omega_{\vec{k}}$ the atom-field detuning. We are interested in deriving an effective description for the reduced atomic system operator $\rho(t) = \text{Tr}_f\{\rho_{\text{tot}}(t)\}$, where the index f refers to the field degrees of freedom. By formally integrating the Von Neumann equation (1.6) and after tracing over the bath degrees of freedom we get:

$$\begin{aligned} \rho(t) =& \rho(0) - \frac{i}{\hbar} \int_0^t dt' \, \text{Tr}_f\{[H_I(t'), \rho_{\text{tot}}(0)]\} \\ & - \frac{1}{\hbar^2} \int_0^t dt' \int_0^{t'} dt'' \, \text{Tr}_f\{[H_I(t'), [H_I(t''), \rho_{\text{tot}}(t'')]]\}. \end{aligned} \tag{1.8}$$

This expression, which is still exact, can be simplified by applying two widely used approximations in quantum optics: the Born and the Markov approximation [78, 79, 80]. The first approximation assumes that the atomic system does not affect

the state of the electromagnetic environment. This assumption is always true in free space, where the atom-field strength is weak enough and does not considerably alter the infinite amount of degrees of freedom associated to the field. As we will see below, this approximation can fail in structured environments. When valid, the Born approximation allows to decouple the atomic and field dynamics as $\rho_{\rm tot} \simeq \rho \bigotimes \rho_f$, where $\bigotimes$ indicates the tensor product. The second approximation assumes that the atom-field correlations decay in a time τ_c negligibly small compared to the evolution time of the atomic system. In free space the correlation time is basically given by the inverse of the atomic frequency $\tau_c \sim 1/\omega_a$ and the atomic evolution (in the interaction picture) happens on a time scale much bigger than τ_c. Under this condition we can apply the Markov approximation and for $t \gg \tau_c$ approximate $\rho(t') \simeq \rho(t)$. Note that for $N_a > 1$, it is necessary to add another requirement, namely we must assume that the interaction between the atoms is instantaneous on the timescale of the atomic evolution. Physically, this means that the time needed for the photons to travel from one side to the other of the ensemble, τ_R, i.e the retardation time, should be much smaller than the remaining timescales of the system dynamics.

Under all these approximations and after rearranging (1.8) we end up with the master equation:

$$\dot{\rho}(t) = -\int_0^\infty d\tau \, \mathrm{Tr}_f\{[H_I(t),[H_I(t-\tau),\rho(t)\otimes\rho_f(0)]]\} \tag{1.9}$$

where, consistently with the previous assumptions, we replaced the upper limit of the integration by infinity. If we assume that the electromagnetic field is initially in the vacuum, a situation that will consider throughout this thesis, and we change back into the Schrödinger picture, the master equation (1.9) can be written as:

$$\dot{\rho}(t) = -\frac{i}{\hbar}[H_S,\rho(t)] + \sum_{ij}\frac{\Gamma_{ij}}{2}\left(2\sigma_-^j\rho\sigma_+^i - \sigma_+^i\sigma_-^j\rho - \rho\sigma_+^i\sigma_-^j\right). \tag{1.10}$$

Here

$$H_S = \sum_i \hbar\omega_i|e\rangle_i\langle e| + \frac{\hbar}{2}\sum_{ij}\Delta_{ij}\sigma_+^i\sigma_-^j \tag{1.11}$$

describes the coherent dynamics of the atomic system and we defined the coefficients $\Gamma_{ij}/2 = \mathrm{Re}\{A_{ij}\}$ and $\Delta_{ij} = \mathrm{Im}\{A_{ij}\}$ that depend on the correlation function:

$$A_{ij} = \int_0^\infty d\tau \int d^3\vec{k}\, g^*_{\vec{k},\lambda}(\vec{x}_j)g_{\vec{k},\lambda}(\vec{x}_i)e^{i\delta_{\vec{k}}\tau}\langle a_{\vec{k},\lambda}a^\dagger_{\vec{k},\lambda}\rangle, \tag{1.12}$$

where the expectation value of the bosonic operators in vacuum is $\langle a_{\vec{k},\lambda}a^\dagger_{\vec{k},\lambda}\rangle = 1$. The real part of A_{ij} describes the irreversible radiative decay of the atomic system. The imaginary part of the correlation function (1.12) instead provides the Lamb shift [81, 2, 77] ($i = j$), that can be absorbed in the atomic frequencies, and the strength of the coherent dipole-dipole interactions ($i \neq j$).

The correlation function (1.12) can be evaluated by using spherical coordinates and by performing an angular integration. We thus get the following expression:

$$A_{ij} = \frac{c|\vec{d}_{eg}|^2}{4\pi\hbar\epsilon_0\pi^2}\int_0^\infty d\tau \int dk\, I(k|\vec{x_{ij}}|)k^3 e^{i\delta_{\vec{k}}\tau}, \tag{1.13}$$

where we defined the function:

$$\begin{aligned} I(k|\vec{x_{ij}}|) = &\left[1 - \frac{(\vec{d}_{eg}\cdot\vec{x}_{ij})^2}{|\vec{x}_{ij}|^2}\right]\frac{\sin(k|\vec{x}_{ij}|)}{k|\vec{x}_{ij}|} \\ &+ \left[1 - 3\frac{(\vec{d}_{eg}\cdot\vec{x}_{ij})^2}{|\vec{x}_{ij}|^2}\right]\left[\frac{\cos(k|\vec{x}_{ij}|)}{(k|\vec{x}_{ij}|)^2} - \frac{\sin(k|\vec{x}_{ij}|)}{(k|\vec{x}_{ij}|)^3}\right]. \end{aligned} \tag{1.14}$$

Within the Markov approximation it is easy to perform the time integration in (1.13), which is nothing else than the Fourier transform of the Heaviside function. We thus end up with the following expression for the atomic decay rates:

$$\Gamma_{ij} = \frac{|\vec{d}_{eg}|^2\omega_a^3}{4\pi\hbar\epsilon_0\pi c^3} I\left(\frac{\omega_a}{c}|\vec{x}_{ij}|\right). \tag{1.15}$$

The terms $\Gamma_{i=j}$ correspond to to the well known atomic spontaneous emission rate given by:

$$\Gamma = \frac{|\vec{d}_{eg}|^2\omega_a^3}{3\pi\hbar\epsilon_0 c^3} \tag{1.16}$$

that predicts an exponential decay for an isolated atom in free space. All the other terms $\Gamma_{i\neq j}$ describe instead the collective radiative behaviour of the ensemble. The dependence of these rates on the function $I(\frac{\omega_a}{c}|\vec{x}_{ij}|)$ underlines the crucial role played by the arrangement of the atoms in space. By considering different geometries the radiative behaviour of the ensemble can be dramatically affected. The study of the collective emission of many atoms in different geometries such as one dimensional (1D) linear chains or two (2D) and three (3D) dimensional lattices in free space and in cavities is an active field of research [82, 83, 84, 85]. In the next section, restricting the discussion to the simple case of two atoms in free space, we will briefly present the most important consequence of collective emission: super- and subradiance.

1.2.2 Two atoms in free space: super- and sub-radiant states

Here we want to describes the dynamics of two atoms interacting with the electromagnetic vacuum in free space. The bare basis set given by the tensor product of the two atomic eigenstates $|e_i\rangle|g_i\rangle$ is not the best choice because these states are not eigenvectors of the modified Hamiltonian (1.11). It is more convenient to work with the new basis defined by $|e_1e_2\rangle = |e_1e_2\rangle$, $|g_1g_2\rangle = |g_1g_2\rangle$, $|\pm\rangle = 1/\sqrt{2}(|e_1g_2\rangle \pm |g_1e_2\rangle)$, which are the angular momentum eigenstates of two spins. Working in this basis

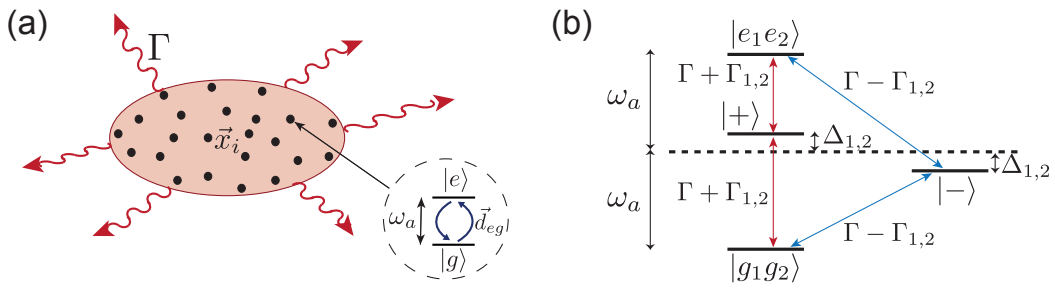

Figure 1.1: (a) Sketch of an ensemble of two level atoms that are located in a infinite region in space and interact with the EM field. (b) Level structure of two atoms interacting with the free space electromagnetic field. The colored arrows indicate the transition between the levels.

we can use (1.10) to get the following coupled equation for the diagonal elements of the reduced density operator:

$$\begin{aligned}
\frac{d\rho_{ee}}{dt} &= -2\Gamma\rho_{ee}, \\
\frac{d\rho_{+}}{dt} &= (\Gamma+\Gamma_{12})\rho_{ee} - (\Gamma+\Gamma_{12})\rho_{+}, \\
\frac{d\rho_{-}}{dt} &= (\Gamma-\Gamma_{12})\rho_{ee} - (\Gamma-\Gamma_{12})\rho_{-}, \\
\frac{d\rho_{gg}}{dt} &= (\Gamma+\Gamma_{12})\rho_{+} + (\Gamma-\Gamma_{12})\rho_{-}.
\end{aligned} \tag{1.17}$$

These equations show how the cross decay rates combine together with the single atomic emission affecting the radiative behaviour. In particular, if $\Gamma \pm \Gamma_{12} > \Gamma$, the collective contribution enhances the emission and leads to a so-called super-radiant decay. On contrary, if $\Gamma \pm \Gamma_{12} < \Gamma$, the correlation effects can decrease the spontaneous emission decay rate leading to a phenomena known as sub-radiance. In the limit of small atomic distances, $k|\vec{x}_{ij}| \ll 0$, $\Gamma_{12} \to \Gamma$ [see (1.13) and (1.15)] and the state $|+\rangle$ decays at a maximum rate of $\sim 2\Gamma$ while the antisymmetric state $|-\rangle$ becomes completely decoupled from the electromagnetic field and cannot radiate at all: it becomes a dark state. In Fig. 1.1(b) we show a sketch of the level structure and the corresponding decay rates. The same physic shown here for two atoms can be generalized to N_a atoms, where the collective decay rate in the single excitation subspace can reach a maximum value of $\sim N_a\Gamma$.

As we discussed in this section, the light-matter interaction in free space is in general weak and allows to use the Born-Markov approximation to describe the reduced system dynamics. One of the main achievement of quantum optics was the ability to increase the atom-light interaction coupling strength by confining the electromagnetic field inside photonic structures such as cavities, waveguides or photonic crystals. In the next section we will make a short overview of some of these systems.

1.3 Cavity QED

Let us consider a Fabry-Perot cavity consisting of two mirrors of area A separated by a distance L along the z axis. The field, confined inside a volume $V = AL$, has to be zero at the mirror positions. Such a boundary condition leads to a discrete set of mode functions, labelled by the index n:

$$\vec{\Phi}_n(z) = \vec{e}\sqrt{\frac{2}{V}}\sin(k_n z), \tag{1.18}$$

where the wavevectors $k_n = n\pi/L$ are now discretized and $\vec{e}$ indicates again the polarization of the field. Eq. (1.18) shows clearly that the field modes are no longer associated with a propagating field, but are now stationary waves localized between the mirrors. The resulting coupling strength between the n-th mode and the i-th atom reads:

$$g_n(z_i) = \vec{d}^i_{eg}\cdot\vec{e}\sqrt{\frac{\hbar\omega_n}{\epsilon_0 V}}\sin(k_n z_i). \tag{1.19}$$

It is important to notice that now the coupling (1.19) scales as $\sim V^{-1/2}$. This shows that, by confining the field in small volumes, it is possible to increase the atom-field interaction strength. This is not the only advantage of considering small confinements for the field. Indeed the eigenfrequencies of the field are now also discretized according to $\omega_n = k_n c$ and the spacing between neighbouring modes depends inversely on the mirror distance $\Delta\omega = \pi c/L$. This means that, in many cases, it is possible to individually address and resolve a single cavity mode and to adopt a single mode approximation. Note that this is not always the case and multi-mode cavity QED is an active theoretical and experimental field of research [86, 87]. For our discussion regarding cavity QED we will consider only the case where the atoms interact with a single mode of the confined electromagnetic field. From now on we will assume that this mode is described by the bosonic operators a with momenta k_0 and frequency $\omega_c = ck_0$.

1.3.1 Single atom

Jaynes-Cumming model

The well known Jaynes-Cumming (JC) model describes the interaction between a single atom $N_a = 1$ and a single quantized cavity mode [3]. If we assume that the atom is at rest and located at position z_a we can set $g := g(z_a)$ and the system Hamiltonian reads:

$$H_{JC} = \hbar\omega_a|e\rangle\langle e| + \hbar\omega_c a^\dagger a + \hbar g(\sigma_+ a + \sigma_- a^\dagger). \tag{1.20}$$

While the first term in the Hamiltonian describes the unperturbed energies of the atom and photonic states, the second term instead describes the coherent exchange of excitations between the atom and the cavity. The operator $\hat{N} = |e\rangle\langle e| + a^\dagger a$, that

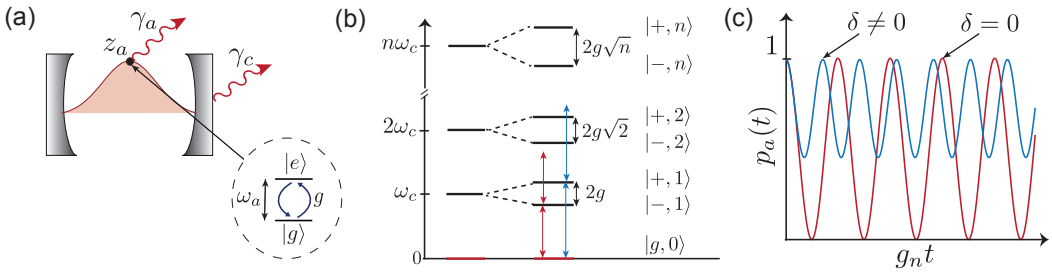

Figure 1.2: (a) Sketch of a two-level atom coupled to a single cavity mode with strength g. Both the atom and the cavity mode can also decay into the external environment with decay rates γ_a and γ_c, respectively. (c) Jaynes-Cumming energy ladder. The blue and red arrow highlight the nonlinearity of the spectrum. (c) Sketch of the Rabi oscillation for the spontaneous emission of an atom inside a cavity in the resonant, $\delta = 0$, and the detuned case, $\delta \neq 0$.

provides the total number of excitations, commutes with the Hamiltonian. This means that there is a conserved quantity and that H_{JC} can be block-diagonalized. Each block, indicated by the number of excitations n, consists of a two dimensional subspace spanned by the bare atom-cavity basis $\{|g,n\rangle, |e,n-1\rangle\}$. The only exception is the unique vacuum state $|g,0\rangle$. The eigenstates of each excitation subspace are known as atom-field dressed state and consist of a superposition of photonic and atomic excitations. They have energies

$$E_{n,\pm} = n\hbar\omega_c + \hbar\frac{\delta}{2} \pm \frac{\hbar}{2}\sqrt{\delta^2 + 4g^2 n}, \tag{1.21}$$

with $\delta = \omega_a - \omega_0$ being the atom-cavity detuning, and they can be written as

$$\begin{aligned} |+,n\rangle &= \cos\frac{\theta}{2}|g,n\rangle + \sin\frac{\theta}{2}|e,n-1\rangle, \\ |-,n\rangle &= -\sin\frac{\theta}{2}|g,n\rangle + \cos\frac{\theta}{2}|e,n-1\rangle, \end{aligned} \tag{1.22}$$

where $\tan\theta = 2g\sqrt{n}/\delta$ is the mixing angle. While for large detuning, $\delta \gg g$ the dressed energies almost coincide with the uncoupled states, for small detuning, $\delta \ll g$, the degeneracy of the bare states is broken by the interaction and the two states are split into two levels separated by $2g\sqrt{n}$, as shown in Fig. 1.2(b). The dependence of the splitting on the number of photons makes the spectrum highly non-linear and this is one of the main features of the Jaynes-Cumming model. The blue and red arrows in Fig. 1.2(b) schematically illustrate this feature. If a photon resonantly excites one of the eigenstates, a second photon, arriving with the same frequency just after the first, will be off-resonant and it will be hardly absorbed by the system. This photon number dependent transmission in cavity QED is know as photon blockade and enables the implementation of effective photon-photon interactions [88] and generation of non-classical states of light [89, 90].

Another important feature of the Jaynes-Cumming model arises when the time evolution of the system is considered. In particular, let us consider the simple case of an atom initially excited in resonance ($\delta = 0$) with a cavity containing n photons. If we work in interaction picture respect to the first term in Hamiltonian (1.20), the initial state of the system $|\phi(0)\rangle = |e, n\rangle$, will evolve in time according to:

$$|\phi(t)\rangle = \frac{1}{\sqrt{2}}\left[e^{-ig_n t}|+, n\rangle + e^{ig_n t}|-n\rangle\right], \tag{1.23}$$

where we defined $g_n = g\sqrt{n+1}$. From this expression it is easy to compute the probability of finding the atom in the excited state that is given by $p_a(t) = |\langle e|\phi(t)\rangle|^2 = \cos^2(g_n t)$. This reversible energy exchange between the atom and the cavity at frequency g_n is known as quantum Rabi oscillations. In Fig. 1.2(c) this probability is shown as function of time for both the resonant and the detuned case, where also in the latter case an oscillating behaviour with smaller amplitude is observed. This time evolution is drastically different from the free space case discussed in Sec. 1.2, where the spontaneous emission is intrinsically irreversible and once a photon is emitted by the atom it never goes back. On the contrary, when the field is confined in a cavity not only the atomic emission is enhanced, but also the emitted photon can be reabsorbed by the atom leading to multiple interactions. Within the open system language this behaviour that keeps track of all the system evolution and correlations is often referred as non-Markovian in contrast to the memoryless Markovian dynamics.

Dissipative cavity

In the previous section we described an ideal situation where the atom and the cavity were perfectly isolated from the outside world. In realistic situation the system is not closed and can loose excitations in the environment trough the lossy cavity mirrors and trough spontaneous emission of the atom into free space. To account for these effects it is necessarily to use some of the open system techniques such as quantum Langevin equations or the master equation formalism. In particular, similarly as done in Sec 1.2.1, we will adopt the latter by modelling the environment as a one-dimensional continuum of modes b_k with linear dispersion relation $\omega_k = c|k|$. Having chosen a one-dimensional bath instead of a three-dimensional one simplifies the discussion without affecting the physical interpretation of the system. We further assume that both the atom and the cavity mode are coupled linearly to the external bosonic field with a coupling almost frequency independent (white noise environment). The total Hamiltonian reads

$$H_{JC-E} = H_{JC} + H_E + \frac{g_c}{\sqrt{2\pi}}\int dk(a^\dagger b_k + \text{H.c}) + \frac{g_a}{\sqrt{2\pi}}\int dk(\sigma_+ b_k + \text{H.c}), \tag{1.24}$$

where H_E is the environment Hamiltonian. Applying again the Born-Markov approximation and assuming the environment to be in the vacuum state is possible

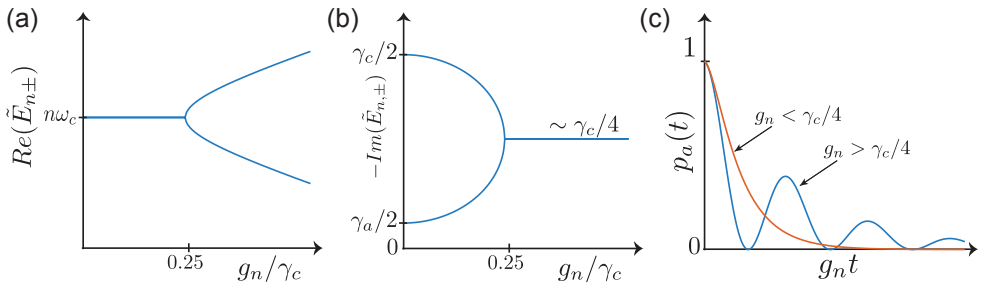

Figure 1.3: (a) and (b) Real and imaginary part of (1.28) in the limit $\gamma_c \gg \gamma_a$. (c) Time evolution of the excited state population of an atom inside a dissipative cavity. In all the plots the atom and the cavity are assumed to be on resonance, $\delta = 0$.

to obtain a master equation describing the time evolution of the reduced density operator for the atom-cavity system $\rho(t)$:

$$\frac{d}{dt}\rho(t) = -i[H_{\text{eff}}\rho - \rho H_{\text{eff}}^{\dagger}] + \gamma_a \sigma_- \rho \sigma_+ + \gamma_c a \rho a^{\dagger}, \tag{1.25}$$

where the last two terms assure the trace conservation of the density operator while the first presents the non-hermitian effective Hamiltonian:

$$H_{\text{eff}} = H_{JC} - i\frac{\gamma_a}{2}\sigma_+\sigma_- - i\frac{\gamma_c}{2}a^{\dagger}a. \tag{1.26}$$

The decay rates were obtained after evaluation of the field correlation functions:

$$\gamma_\eta = \frac{g_\eta^2}{\pi}\int_0^\infty d\tau \int dk e^{i(\omega_a - \omega_k)\tau}\langle bb^{\dagger}\rangle = \frac{g_\eta^2}{c}, \tag{1.27}$$

where we assigned $\eta = a, c$. This last expression is true under the assumption that the dynamics of the environment field is much faster compared to the slow system dynamics: $\omega_k \gg g$ or, in other words, that the interaction between the atom and the cavity does not affect their dissipation mechanism. Equation (1.26) shows that one can account for the dissipation by introducing imaginary terms in the atomic and cavity frequencies: $\omega_a \to \omega_a - i\frac{\gamma_a}{2}$ $\omega_c \to \omega_c - i\frac{\gamma_c}{2}$ making the Jaynes-Cumming spectrum complex. In the simple resonant case, $\delta_{JC} = 0$, the eigenvalues of (1.26) are given by:

$$\tilde{E}_{n,\pm} = n\hbar\omega_c - i\hbar\frac{\gamma_a + \gamma_c}{4} \pm \hbar\sqrt{g_n^2 - \left(\frac{\gamma_a - \gamma_c}{4}\right)^2}. \tag{1.28}$$

The real part of the eigenvalues describes the coherent dynamics and oscillatory behaviour while the imaginary part describes the damping of the atom-cavity system [see Fig. 1.3(a)-(b)]. In most of the Cavity QED implementations the main source of dissipation arises from the cavity damping $\gamma_a \ll \gamma_c$. In this limit we can distinguish between two qualitatively different regimes.

- For $4g_n < \gamma_c$ the Rabi splitting does not arise anymore and the two eigenvalues of (1.28) have the same real parts, i.e, $\tilde{E}_a \simeq n\hbar\omega_c - i\hbar(\gamma_a/2 + 2g^2/\gamma_c)$ and $\tilde{E}_c \simeq n\hbar\omega_c - i\hbar\gamma_c/2$. The first eigenvalue can be associated with the atomic degree of freedom while the second corresponds to the cavity mode. In Fig. 1.3(c) we can see how the oscillatory behaviour in the excited state population is suppressed and an exponential decay is instead observed. In this limit of strong damping, the atom-cavity interaction still plays a role by introducing an additional damping rate $\sim g^2/\gamma_c$. This effect is known as Purcell effect [91] and, which for not too small cavity loss can lead to an atomic damping that exceed the free space spontaneous emission decay rate given in (1.16).

- If the cavity damping is weak,

$$4g_n > \gamma_c, \tag{1.29}$$

  the Rabi splitting occurs and the two eigenvalues given in Eq. (1.28),

$$E_{n,\pm} \simeq n\hbar\omega_c \pm \hbar\sqrt{g_n^2 - \gamma_c^2/16} - -i\hbar\gamma_c/4, \tag{1.30}$$

  are still associated with the atom-cavity dressed states. In Fig. 1.3(c) we can see that when condition (1.29) is satisfied the excited state population presents a damped oscillatory behaviour given by: $p_a(t) \simeq \cos^2(g_n t)e^{-\gamma_c/2}$. This means that the atom is able to reabsorb the photon multiples times before the excitation decays completely. The condition (1.29) not only rules the dynamics, but can also be considered as the minimal requirement to achieve a nonlinear spectrum. The regime when such condition is satisfied is referred in literature as "strong-coupling regime".

1.3.2 Multiple atoms

Let us now consider the case of N_a identical atoms interacting with the same cavity mode. For simplicity we can further assume that the atoms are located at anti-nodes of the electromagnetic field where the coupling is maximum $g := g(z_i)$. The physics of the system is described by the Tavis-Cumming Hamiltonian [92]:

$$H_{TC} = \sum_{i=1}^{N_a} \hbar\delta|e\rangle_i\langle e| + \hbar\sum_{i=1}^{N_a} g(\sigma_+^i a + \sigma_-^i a^\dagger). \tag{1.31}$$

In the single excitation subspace and for $N_a = 2$ atoms Hamiltonian (1.31) gives the following eigenvalue equation:

$$(\delta - E)[E(\delta - E) + 2g^2] = 0. \tag{1.32}$$

When the interaction is on resonance, $\delta = 0$, the eigenstates of the system consist of two states $|2\pm,1\rangle = 1/\sqrt{2}|g,g,1\rangle \pm 1/2(|e,g,0\rangle + |g,e,0\rangle)$ separated by $2\sqrt{2}g$, and a singlet state $|2d,1\rangle = 1/\sqrt{2}(|e,g,0\rangle - |g,e,0\rangle)$ on resonance with the bare cavity

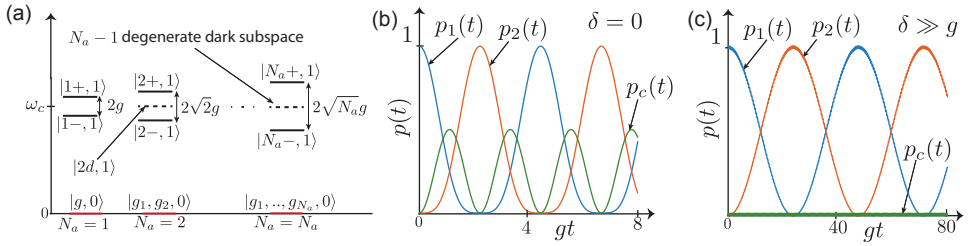

Figure 1.4: (a) Level structure of multiple atoms in a cavity. For $N_a > 1$ a $N_a - 1$ degenerate dark subspace is formed. (b)-(c) Evolution of the population of the excited state of two atoms, p_1 and p_2, and of the cavity photon, p_c, as function of time. The plot in (b) shows the resonant case, $\delta = 0$, while (c) shows the case the atoms are far detuned, $\delta \gg g$.

frequency at ω_0. The first two states present both a photonic and an atomic component and they are referred to as bright states because they radiate into the cavity field. The third state instead is purely atomic and is completely decoupled from the cavity mode. This means that this state cannot emit or absorb photons: it is a dark state. The same reasoning can be extended to the N_a atom case where the eigenstates consists always of two bright states separated by $g\sqrt{N_a}$ and a $N_a - 1$ fold degenerate subspace of dark states. A sketch of the eingevalues structure is shown in Fig. (1.4)(a). The splitting of the dark states suggest that the atomic ensemble, similarly to the free space case, reacts collectively to the field with an effective coupling $G = g\sqrt{N_a}$. This scaling was observed in both optical and microwave cavities and is largely used to explore strong light-matter interactions in cavity QED [93, 94, 95, 96].

Let us now focus our attention on the dynamics described by (1.31) and in particular on the exchange of excitations between the atoms. On resonance an atom can emit a real photon in the cavity that can be subsequently coherently re-absorbed by another atom, as shown in Fig. (1.4)(b) for $N_a = 2$. An interesting regime is when the atoms are off resonance, i.e., $\delta \gg g$. In this limit the atom-cavity eigenstates are weakly dressed by the photons that can be adiabatically eliminated. This leads to an effective Hamiltonian [97] for the atoms:

$$H_{\text{eff}} = \frac{\hbar g^2}{\delta} \sum_{ij} \sigma_+^i \sigma_-^j. \tag{1.33}$$

Here the exchange of excitation occurs at the second order in the coupling strength g and it is associated with a longer time-scale compared to the resonant case, as shown in Fig. (1.4)(c). Note that the interaction does not depend on the atomic distances because and it is mediated by virtual photons that are extend over the entire cavity.

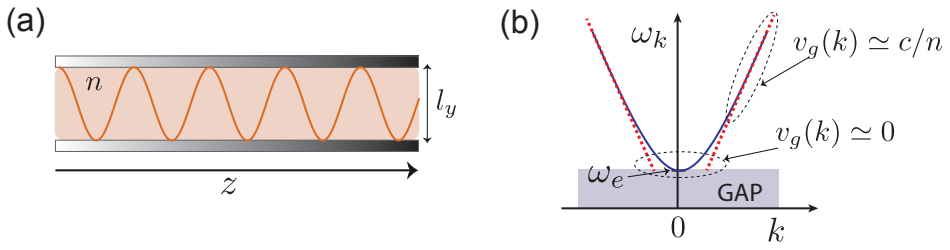

Figure 1.5: (a) Sketch of a rectangular metallic waveguide. (b) Dispersion relation for a metallic waveguide. The linear and the quadratic regime are highlighted.

1.4 QED in one dimension

Let us now consider the most relevant scenario for this thesis: the confinement of the electromagnetic field in one dimension. In this case the field modes are infinitely extended along the z direction, but strongly confined in the transversal xy plane to a cross section A. The free space linear dispersion relation can be rewritten separating the transversal and the longitudinal components as:

$$\omega_k = \frac{c}{n}\sqrt{k_T^2 + k_z^2}, \tag{1.34}$$

where n is the refractive index of the confining medium. While along the z-axis the field modes are plane waves and form a mode continuum, the transverse modes are quantized, due to the confinement.

To simplify the discussion let us assume that the field is confined inside a rectangular metallic waveguide with sides l_x and l_y as sketched in Fig. 1.5(a). This waveguide implementation is for waves in the microwave domain, but captures also the essential physics of optical waveguides. The perfectly reflecting boundary conditions for the field in the transverse directions lead to transverse wavevectors with discrete values $k_T(n,m) = n\pi/l_x + m\pi/l_y$. For each of these transverse modes there is a branch of frequencies continuously spanned by the longitudinal wavevector $k := k_z$. In the limit of strong confinement the transversal modes $\omega_{n,m} = \frac{c}{n}k_T(n,m)$ are well separated from each other and we can assume to address only one of them with frequency ω_e. The dispersion relation associated with this specific transverse mode is given by:

$$\omega_k = \omega_e\sqrt{1 + \left(\frac{c}{n\omega_e}\right)^2 k^2}, \tag{1.35}$$

and the transverse mode frequency ω_e plays the role of a low frequency cut-off as sketched in Fig. (1.5)(b). In order to characterize the propagation of the photons inside the waveguide we can use the group velocity $v_g(k) = \partial\omega_k/\partial k$, which usually depends on the wave vector k. The dispersion relation can be separated in three different regimes depending on their propagation properties.

- For frequencies far above ω_e the dispersion relation is almost linear and can be approximated as: $\omega_k \simeq (c/n)|k|$. In this regime the photons propagate with a

finite group velocity, $v_g(k) \simeq c/n$, which is just given by the speed of light in vacuum divided by the refractive index of the waveguide medium.

- For frequencies close to the cut-off frequency the dispersion becomes flatter and approximately quadratic

$$\omega_k \simeq \omega_e + \frac{\hbar k^2}{2m^*}. \tag{1.36}$$

  Here we introduced the effective photon mass $m^* = \omega_e n^2 \hbar / c^2$. In this regime the photons behave as effective massive particles and their propagation speed slows down, i.e., $v_g(k) \simeq (\hbar/m^*)k$ for $k \to 0$.

- For frequencies below the cut-off frequency, there are no solutions of the Helmholtz equation with real eigenvalues. Note that here equation (1.35) does no provides the full dispersion of the waveguide but only one specific transversal branch so we cannot properly refer to this range of frequencies as photonic gap. This is because in general the full dispersion presents also other transversal branches that lie below the cut-off. Proper band gaps can be realized in photonic structures such as photonic crystal and coupled cavity arrays and will be discussed in chapter 3.

In the first two cases the mode functions of the electromagnetic field have the form

$$\vec{\Phi}_k(x, y, z) = \vec{e} \frac{1}{\sqrt{2\pi}} \Phi_T(x, y) e^{ikz}, \tag{1.37}$$

where as before $\vec{e}$ indicates the polarization of the field and

$$\Phi_T(x, y) = \sqrt{\frac{4}{A}} \sin\left(\frac{n\pi}{l_x} x\right) \sin\left(\frac{m\pi}{l_y} y\right) \tag{1.38}$$

is the normalized transverse mode function. If we now consider the coupling of TLA to the waveguide, the coupling strength of the k-th mode to the i-th atom is

$$g_k(z_i) = \frac{g_i}{\sqrt{2\pi}} e^{ikz_i}. \tag{1.39}$$

where $g_i = \vec{d}^i_{eg} \cdot \vec{e} \sqrt{\frac{\hbar\omega_e}{2\epsilon_0}} \Phi_T(x_i, y_i)$. The coupling strength depends inversely on the cross section. Thus by considering small confinement it is possible to achieve strong light-matter interaction. The essential difference compare to the cavity QED setup is that in this waveguide configuration the field is not trapped inside a limited region of space. Instead, it can propagate away leading to the possibility of carry information over long distances and to achieve long-range interactions among the atoms.

The light-matter coupling (1.39) was presented for the simple example of a metallic waveguide but it can be used in most of the waveguide implementations when the dispersion relation is approximately linear in the ranges of frequencies

under interest. In these cases the only parameter that is affected by the specific setup is the strength g_i that in any case does not affect the full model itself.

A difference arises in the quadratic regime that, as we previously mentioned, can be properly realized in periodic photonic structure. In such structures the coupling (1.39) is not complete because the model function of the field are not anymore plane waves but Bloch functions and an additional modulation along z should be taken into account.

Chapter 2

Waveguide QED

The realization of cavity QED experiments [98, 99, 100, 101, 102] in the strong coupling regime was an important milestone for the field of quantum optics. For the first time it was possible to achieve coherent interactions between individual atoms and photons and to realize basic quantum gates and quantum information protocols. These experiments are now the basis for building larger quantum networks.

A quantum network is composed of many nodes and channels and has the goal of generating, processing and distributing quantum information. In this sense the atom-cavity systems could play the role of the nodes where the quantum states are processed and stored. The distribution instead requires flying qubits that can transfer quantum states between distant nodes with high fidelity. A natural choice for flying qubits are optical photons, which can travel over long distances without loosing their coherence. However, photons emitted into in free space quickly spread into all directions and for two nodes separated by only several wavelengths, the ability to deterministically exchange photons becomes vanishingly small. An optimal choice for the quantum channels are 1D waveguides where photons can connect separated nodes over very large distances, limited only by photon absorption.

With this idea in mind, there has been a lot of interest over the past years on studying the interface between emitters (the nodes) and photons in optical waveguides (the channels). This field is now commonly known as "waveguide QED". Besides the final goal of implementing large quantum network, many intriguing phenomena and applications have been discovered along the way such as single photon switches and mirrors [6, 7, 8], single and correlated photon scattering [9, 10, 11, 12, 13, 14], self-organized atomic lattices [15, 16, 17], or the dissipative generation of long-distance entanglement [18, 19, 20, 21, 22, 23, 24, 25, 26, 27] and new realizations of quantum gates [30, 31, 32].

Today there are already many experimental platforms where such a 1D configuration can be realized to a very good approximation. In Fig. 2.1 we illustrate a few of the most relevant implementations.

- In the optical domain an interesting and successful implementation are optical nanofibers [103, 104, 105, 106, 107, 108]. These are silica fibers that are

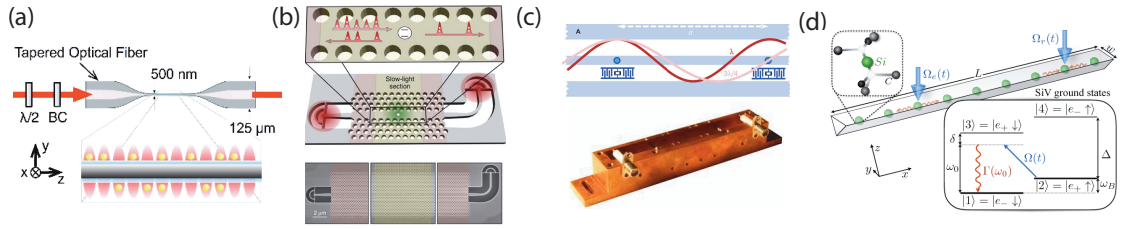

Figure 2.1: Waveguide QED platforms. (a) Ensembles of cold atoms coupled to the evanescent field of a nanofiber. [103]. (b) Qunatum dots coupled to waveguides embedded into 2-dimensional photonic crystal slab [110]. (c) Superconducting qubits coupled to transmission lines [113] and rectangular waveguides [115] are a promising implementation for the microwave regime. (d) Diamond defects coupled to phononic waveguide are an alternative route to the photonic implementations [116].

pulled to reach a diameter smaller or comparable to the optical wavelength as shown in Fig. 2.1(a). In this regime there is still a considerable evanescent electromagnetic field that surrounds the fiber. Ensembles of atoms can then be coupled via this evanescent component to the propagating guided modes.

- An other exciting optical platform is shown in Fig. 2.1(b) and it consists of quantum dots efficiently coupled to a line defect embedded in a 2 dimensional photonic crystal slab [109, 110, 40]. As we will discuss in more detail in chapter 3 the periodicity in the photonic structure creates band gaps that allow to isolate the guided modes and to suppress emission into non-guided modes.

- The optical domain is not the only regime where waveguide QED system can be implemented. With the developments of circuit QED it has become possible to exploit the microwave regime and to couple superconducting qubits to open transmission lines or to rectangular waveguides as shown in Fig. 2.1(c) [111, 112, 113, 114, 115].

- Finally, a different but complementary route consists in not consider the photonic degree of freedoms as flying qubits but phonons [116]. In Fig. 2.1(d) is shown an example of a phononic waveguide made out of diamond that is a convenient material choice due to its high speed of sound $v_g \sim 10^4$. In this context there are several well studied candidates for the emitters, like the nitrogen-vacancy (NV) or the silicon-vacancy (SiV) centers, which are ideally suited for quantum information processing applications [117, 118, 119, 122, 121, 122, 123].

An extremely interesting feature of the two optical implementations mentioned above is that in such nanostructures the light confinement creates a link between the polarization and propagation direction of the field. Such polarization-direction connection can be exploited to achieve a directional emission. In particular, by coupling the field to a specific polarized dipole transition of a quantum emitter, photons can be emitted into one or the other direction of the waveguide. In the

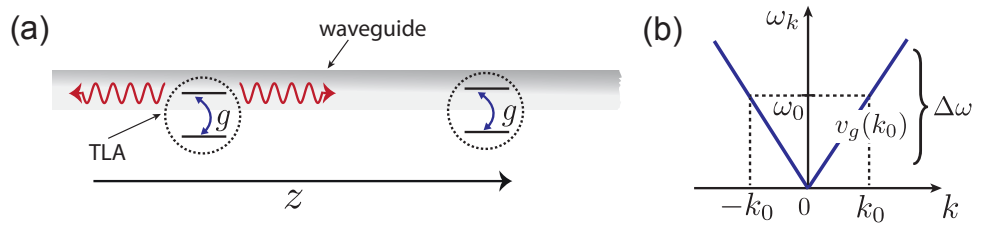

Figure 2.2: (a) A typical waveguide QED setup. (b) Linear dispersion relation for a waveguide.

ideal case the emission and absorption process can become unidirectional. This chiral coupling has been experimentally observed in several setting [124, 125, 126, 127].

In the remainder of this chapter we will provide an overview about the theoretical framework and a few of the basic properties of waveguide QED systems. The formalism developed here will be used in the remainder of the thesis. In section 2.1 we briefly introduce the Hamiltonian that describes the atom-light interaction in a waveguide. In section 2.2 we use the Born-Markov approximation to derive a master equation for an ensemble of atoms that interact trough the waveguide. In particular we will show that this tool can describe the system both in the bidirectional and unidirectional case. In the last section section 2.3 we exactly solve the waveguide QED Hamiltonian in the single excitation sector. The advantage of the exact solution is the possibility to describe scattering process and to explore the limits of validity of the Born-Markov approximation.

2.1 Model

Let us consider a setup where N_a two level atoms are coupled to the electromagnetic field confined inside a one dimensional photonic structure and located at positions z_i along the longitudinal direction. In particular, in this chapter we will concentrate on the case where the photonic structure is invariant for any translation along the z axis and we will refer to it as a waveguide. A sketch of the setup is shown in Fig. 2.2(a).

As we discussed in Sec. 1.4, when the light is confined in one dimension the dispersion relation can in principle become non-linear. Nevertheless, in many relevant cases it can be simplified. Let us assume that the dispersion relation of the waveguide is approximate linear within a frequency region $[\omega_0 - \Delta\omega, \omega_0 + \Delta\omega]$. If $\Gamma \ll \Delta\omega$, with Γ being the decay rate of a two level system in the waveguide, the atom will just experience a linear dispersion relation simply given by $\omega_k = v_g(k_0)|k|$, with k_0 being the positive resonant wavevector associated with ω_0 [see Fig. 2.2(b)].

In the continuum limit we can write down the Hamiltonian describing the interaction between the atoms and field confined in the waveguide:

$$H = \sum_{i=1}^{N_a} \hbar\omega_i |e\rangle_i\langle e| + \int dk\, \hbar\omega_k a_k^\dagger a_k + \hbar \sum_{i=1}^{N_a} \frac{g_i}{\sqrt{2\pi}} \int dk \left[e^{-ikz_i} a_k^\dagger \sigma_-^i + e^{ikz_i} a_k \sigma_+^i \right]. \quad (2.1)$$

2.2 Waveguide QED master equation

The interaction of many atoms with the waveguide field is a complex problem and in general can be exactly solved only in the few-excitation subspaces. Nevertheless, similarly as in Sec. 1.2.1, it is still possible to get an effective description for the reduced atomic system. Among all the different possible techniques we will focus here on the master equation approach to describe the waveguide mediated interaction between the atoms.

In many waveguide QED implementations, it is possible to couple the atoms to the left (L) and to the right (R) propagating modes with different strengths [124, 125, 126, 127]. In order to take this asymmetry into account, we separate the left and the right contributions by introducing two different coupling constant for the i-th atom: g_R^i and g_L^i. We will further assume that all the atoms are coupled to the left and to the right modes with the same strength $g_R^i = g_R$ and $g_L^i = g_L$. By changing into the interaction picture, Hamiltonian (2.1) can then be rewritten as

$$H_I(t) = \hbar \sum_{i=1}^{N_a} \left[\left(g_R F_R^\dagger(z_i,t) + g_L F_L^\dagger(z_i,t) \right) \sigma_-^i e^{-i\omega_i t} + \text{H.c.} \right], \tag{2.2}$$

where we defined the field operators for the right- and left-propagating fields,

$$F_\eta(z,t) = \frac{1}{\sqrt{2\pi}} \int_{\substack{k>0 \\ k<0}} dk\, e^{i(kz-\omega_k t)} a_k. \tag{2.3}$$

Here the sum over the positive and negative wavevectors is for the right and left propagating modes, respectively. By proceeding as in Sec. 1.2.1 we end up with a master equation governing the time evolution of the atom's reduced density operator $\rho(t)$:

$$\dot{\rho} = \sum_{ij} (A_{ij}^R + A_{ij}^L) \left(\sigma_-^j \rho \sigma_+^i - \sigma_+^i \sigma_-^j \rho \right) e^{i(\omega_i-\omega_j)t} + (B_{ij}^R + B_{ij}^L) \left(\sigma_-^i \rho \sigma_+^j - \rho \sigma_+^j \sigma_-^i \right) e^{-i(\omega_i-\omega_j)t}, \tag{2.4}$$

where we introduced the correlation functions:

$$A_{ij}^\eta = g_\eta^2 \int_0^\infty d\tau \, \langle F_\eta(z_i,t) F_\eta^\dagger(z_j,t-\tau) \rangle e^{i\omega_j \tau} \tag{2.5}$$

and

$$B_{ij}^\eta = g_\eta^2 \int_0^\infty d\tau \, \langle F_\eta(z_j,t-\tau) F_\eta^\dagger(z_i,t) \rangle e^{-i\omega_j \tau}. \tag{2.6}$$

Note that here we assumed the field to be in initially in the vacuum state, i.e., $\langle a_k^\dagger a_k \rangle = 0$ and $\langle a_k a_k^\dagger \rangle = 1$. Let us start evaluating the term A_{ij}^R:

$$\begin{aligned} A_{ij}^R &= \frac{g_R^2}{2\pi} \int_0^\infty d\tau \int_{k>0} dk\, e^{ik(z_i-z_j)} e^{i(\omega_j-\omega_k)\tau} \\ &\simeq \frac{g_R^2}{2\pi} e^{ik_0(z_i-z_j)} \int_0^\infty d\tau \int_{k>0} dk\, e^{-iv_g(k_0)(k-k_0)[\tau - \frac{(z_i-z_j)}{|v_g(k_0)|}]}, \end{aligned} \tag{2.7}$$

where between the first and the second line we expanded the dispersion relation around the positive resonant solution of $\omega_j = \omega_k$ given by $k = k_0$. The previous expression can be computed using a Markov approximation

$$\begin{aligned} A_{ij}^R &\simeq \frac{g_R^2}{|v_g(k_0)|} e^{ik_0(z_i - z_j)} \int_0^\infty d\tau \delta\left(\tau - \frac{(z_i - z_j)}{|v_g(k_0)|}\right) \\ &\simeq \Gamma_R e^{ik_0(z_i - z_j)} \theta[z_i - z_j], \end{aligned} \tag{2.8}$$

where we defined the decay rate

$$\Gamma_R = \frac{g_R^2}{|v_g(k_0)|} \tag{2.9}$$

associated with the exponential spontaneous emission of right propagating photons. Similarly we get for the other coefficients:

$$A_{ij}^L = \Gamma_L e^{-ik_0(z_i - z_j)} \theta[z_j - z_i], \tag{2.10}$$

with $\Gamma_L = g_L^2/|v_g(k_0)|$ determining the emission of left propagating photons, and $B_{ij}^R = (A_{ij}^R)^*$, $B_{ij}^L = (A_{ij}^L)^*$. As we already discussed in Sec. 1.2.1 the coefficients A_{ij}^η contain information about correlated decay and photon-mediated interaction processes. It is important to note that in contrast to the free space case these coefficients do not decay with the distance. This is a peculiar situation that depends crucially on the one dimensional confinement of the light and has the great advantage to allow effectively "infinite long range interactions" between the atoms. This feature can be qualitatively explained by keeping in mind that when a photon is emitted by one atom it propagates only along one direction without any attenuation until it reaches a second atom, leading to an interaction that depends only on the relative phases between the emitters.

The derivation of A_{ij}^η relies on the validity of the Born-Markov approximation that requires two different conditions. For a single atom the main requirement is that the correlation time of the field, given essentially by $\tau_c \sim 1/\Delta\omega$, is much shorter than the relevant time scales of the atomic dynamics. This condition is satisfied as long as $\Gamma \ll \Delta\omega$ where $\Gamma = \Gamma_R + \Gamma_L$ is the total decay rate.

For multiple atoms there is an additional requirement to consider that relies on the collective behaviour of the emitters. In particular, the single atom dynamics should occur on a time scale, which is longer than the minimal time it takes a photon to propagate between the atoms. This is evident for the validity of equation (2.8) that holds as long as $\tau \geq |z_j - z_i|/|v_g(k_0)|$. More generally, for the validity of a time-local master equation for N_a-atoms with spacing d we must ensure that the maximal retardation time $\tau_R \sim (N_a - 1)d/|v_g(k_0)|$ is short compared to the system evolution determined by the single-atom spontaneous-emission time Γ^{-1}. This yields

$$g \ll \frac{|v_g(k_0)|}{\sqrt{(N_a - 1)d}} \tag{2.11}$$

as a slightly more stringent condition for large systems. Under this requirement the system can be described in terms of atomic excitations, which interact via a quasi-instantaneous exchange of photons. The breaking of this condition and its physical meaning will be addressed in more detail in Sec. 2.3.4 and is extensively discussed in Ref. [14, 19].

Coming back to the master equation (2.4), we can now extend it to a more general case assuming to drive each of the qubits with a laser at frequency ω_L^i and with strength $\mathcal{E}_i$. Going back to the Schrödinger picture with respect to the atomic frequencies we get the generic waveguide QED master equation [26]:

$$\dot{\rho} = -\frac{i}{\hbar}[H_S, \rho] + \sum_{ij} \left(A_{ij}^R + A_{ij}^L\right)\left(\sigma_-^j \rho \sigma_+^i - \sigma_+^i \sigma_-^j \rho\right) + \left((A_{ij}^R)^* + (A_{ij}^L)^*\right)\left(\sigma_-^i \rho \sigma_+^j - \rho \sigma_+^j \sigma_-^i\right), \tag{2.12}$$

where

$$H_S = \sum_i \hbar\omega_i |e\rangle_i\langle e| + \sum_i \hbar(\mathcal{E}_i e^{i\omega_L^i t} + \text{H.c.}). \tag{2.13}$$

In this general form, the master equation describes waveguides with an arbitrary degree of chirality. In the following we will present the two limiting cases of a bidirectional waveguide, $g_R = g_L$, and a fully unidirectional one where $g_L = 0$ and $g_R \neq 0$.

2.2.1 Bidirectional waveguide

When the symmetry between the left and the right emission is not broken, i.e. $g_R = g_L = g$ we can rewrite (2.12) in the usual form [18, 15, 20]:

$$\dot{\rho} = -\frac{i}{\hbar}[H_S + \sum_{i,j} \frac{U_{ij}}{2}\sigma_+^i \sigma_-^j, \rho] + \sum_{ij} \frac{\Gamma_{ij}}{2}\left(2\sigma_-^i \rho \sigma_+^j - \sigma_+^i \sigma_-^j \rho - \rho \sigma_+^i \sigma_-^j\right), \tag{2.14}$$

where

$$\begin{aligned} U_{ij} &= \frac{2g^2}{|v_g(k_0)|}\sin\left(k|z_i - z_j|\right), \\ \Gamma_{ij} &= \frac{2g^2}{|v_g(k_0)|}\cos\left(k|z_i - z_j|\right). \end{aligned} \tag{2.15}$$

The coefficients U_{ij} and Γ_{ij} describe the collective coherent and dissipative dipole-dipole interaction between the atoms, respectively. This exchange of excitation is infinite in range and depends sinusoidally on the atom-atom distance. We observe that, due to the reflection symmetry of the system, the order of the qubits does not matter in contrast with the more general chiral situation.

In order to understand the effect of this collective behaviour let us first concentrate on the case of $N_a = 2$ atoms. In particular, let us assume that the external driving, $\mathcal{E}_i = 0$, is turned off and that one of the atoms is prepared in the excited state. Given the out-of-phase variation of the coefficients U_{ij} and Γ_{ij} we can distinguish between two different cases.

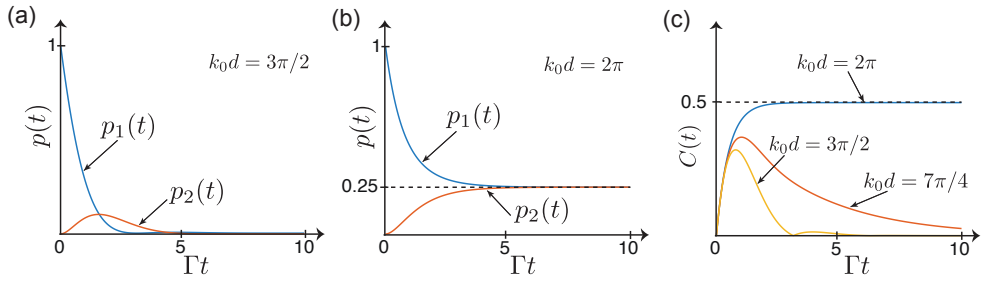

Figure 2.3: Excited state populations $p_{1,2}(t)$ and concurrence $C(t)$ as a function of time for the case where the first atom is initially prepared in the excited state. Different atomic distances are considered, as shown in the plot.

- For atomic distances $k_0 d = (2n+1)\pi/2$ with $n \in \mathbb{N}$ the dissipative interaction between the atoms is suppressed, i.e. $\Gamma_{ij} = 0$, and only the U_{ij} term persist. In this case there is a damped coherent exchange of excitation between the two atoms as shown in Fig. 2.3(a). This interaction is reminiscent of the case of a dissipative cavity where each atom decays independently with the rate

$$\Gamma = 2g^2/|v_g(k_0)|. \tag{2.16}$$

- When the atoms are placed at distances commensurate with the resonant wavelength, $k_0 d = n\pi$ with $n \in \mathbb{N}$, the coherent contribution vanishes and only a dissipative coupling between the qubits is allowed. In this limit the master equation (2.14) describes the Dicke model of super-radiance [76] presented in Sec.1.2.1. In this limit the adequate basis to represent the dynamics is the one depicted in Fig.1.1(b) where the super- and sub-radiant states $|\pm\rangle = 1/\sqrt{2}(|e_1 g_2\rangle \pm |g_1 e_2\rangle)$ play a crucial role. When the first atom decays the system relax with probability $P_- = 1/2$ to the dark state $|-\rangle$ as shown in Fig. 2.3 (b). Another way to explain this behaviour comes from the fact that the two qubits, when on resonance, behave as a Fabry-Perot-like cavity where the photon can be trapped forming a standing wave between the two atoms. We will discuss this interpretation again in the next sections where we will take into account also the photonic degree of freedom.

The state $|-\rangle$ is an entangled state. To better quantify the entanglement produced in the spontaneous emission process we introduce an entanglement measurement that will be useful for our later discussion: the Wootters concurrence [128]. The concurrence for the density operator of a two qubits system is defined as:

$$C(\rho) = \max(0, \lambda_1 - \lambda_2 - \lambda_3 - \lambda_4) \tag{2.17}$$

where λ_i are the eigenvalues in decreasing order of the operator: $R = \sqrt{\sqrt{\rho}\tilde{\rho}\sqrt{\rho}}$ with $\tilde{\rho} = (\sigma_y \otimes \sigma_y)\rho^*(\sigma_y \otimes \sigma_y)$. This measurement ranges from 0 for non-entangled states to 1 for maximally entangled configurations.

For the spontaneous emission case the concurrence expression is really simple. If we decompose the two-atoms density matrix in the bare basis $|1\rangle = |e_1, e_2\rangle$, $|2\rangle = |e_1, g_2\rangle$, $|3\rangle = |g_1, e_2\rangle$, $|4\rangle = |g_1, g_2\rangle$, the concurrence is just given by twice the atomic coherences $C(t) = 2|\rho_{23}(t)|$. In Fig. 2.3 (c) we plotted $C(t)$ as function of time for different atomic distances. We can see that when the qubits separation approaches the superradiant one, a steady state concurrence of 0.5 is achieved [18, 27]. The upper bound of the concurrence is an unavoidable in the bidirectional waveguide where only half of the photons emitted by the first atom reach the second allowing to build quantum correlation among them [see Fig. 2.2(a)]. The same steady subradiant state can also be reached in a configuration where both the atoms are initially in the ground state and only one of them is continuously pumped by an external laser (see [18]).

Finally, let us mention that for the case of $N_a \gg 1$ equally driven atoms in the Dicke super-radiant configuration the competition between the collective dissipation and the driving leads to a non-equilibrium phase transition in the steady-state at the critical driving $\mathcal{E}_c = N\Gamma/2$. Above this threshold the N_a qubits behave as a collective spin and switch their orientation from $\langle S_z/N\rangle = -0.5$ to $\langle S_z/N\rangle \to 0$ where $S_z = \sum_i \sigma_z^i$ is the collective spin operator [20].

2.2.2 Unidirectional waveguide

An interesting situation occurs when the waveguide is fully chiral and the atoms are coupled only to the right propagating mode $g_L = 0$ (the opposite case with $g_R = 0$ is equivalent). In this case each atom can only interact with other atoms to the right without receiving any back action from them. Systems of that type are known as cascaded quantum systems [129, 21, 25, 26]. The master equation (2.12) can then be rewritten as:

$$\dot{\rho}(t) = -\frac{i}{\hbar}[H_{\text{eff}}\rho - \rho H_{\text{eff}}^{\dagger}] + J(\rho), \tag{2.18}$$

where the effective Hamiltonian reads:

$$H_{\text{eff}} = H_S - i\frac{\hbar\Gamma_R}{2}\sum_j \sigma_j^{\dagger}\sigma_j - i\hbar\Gamma_R\sum_{j>i}\sigma_j^{\dagger}\sigma_i \tag{2.19}$$

and the recycling term that assures the conservation of the density operator trace is given by:

$$J(\rho) = \Gamma_R\sum_{ij}\sigma_-^i\rho\sigma_+^j. \tag{2.20}$$

Note that in Eq. (2.18) only the spatial order of the atoms and not the specific positions matters. This is true only in the strict case where the waveguide is fully chiral. Indeed, in such situations it is is possible, without loss of generality, to absorb the position dependent phases in the qubit operators, $\sigma_j \to \sigma_j e^{ikz_j}$, and in the driving amplitudes $\mathcal{E}_j \to \mathcal{E}_j e^{-ikz_j}$. Equation (2.19) describes a unidirectional interaction where the excitation is transferred only to the right without any back

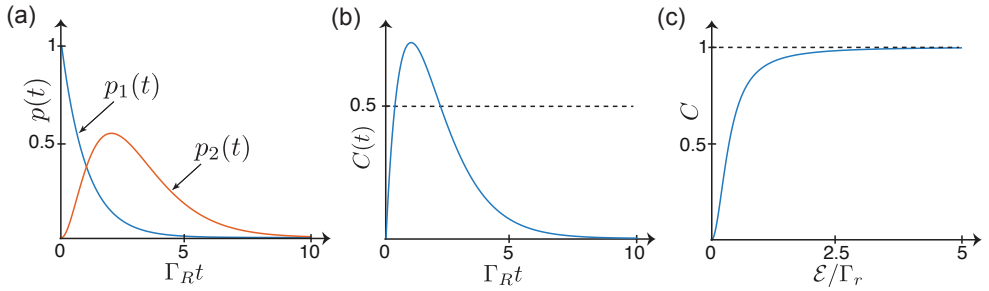

Figure 2.4: (a)-(b) Excited state population and concurrence as function of time when just one of the two qubits is initially excited. For the unidirectional waveguide the transfer is independent of the distance between the atoms. (c) Steady-state concurrence as a function of the driving strength. A maximum value is reached in the limit of $\mathcal{E}/\Gamma_R \gg 1$.

action. The theoretical framework and the consequent experimental implementation developed to describe this kind of physics is know as "Chiral waveguide QED"[127].

To understand the main features of the system, it is convenient to start by considering two atoms in the absence of external driving and with only one of the two initially excited. As shown in Fig. 2.4(a) the population transfer is bigger compare to the bidirectional case where half of the emission is always lost. On the other hand, even in this unidirectional case, the exchange of excitations is not complete. A perfect transfer could be achieved if the photon emitted from the first atom and received by the second would have been the same of the time reversal packet emitted by the second atom. This is never the case without including additional dynamical control [130, 131].

The increase in the excitation transfer is reflected as well in the spontaneously generated concurrence where, as shown in Fig. 2.4(b), an enhanced concurrence ($C \sim 0.7$) compare to the bidirectional case is achieved. We remark again that in the unidirectional waveguide, compare to the bidirectional case, there is not an optimal separation for the excitation transfer because the master equation (2.18) does not depend on the distance.

The concurrence and transferred excitation shown in Fig. 2.4(a)-(b) both decay in the long time limit in contrast with the resonant case of the bidirectional waveguide where a steady subradiant state is achieved. One could ask, if it is possible to obtain a dark steady state also for the unidirectional configuration. The answer is positive if a driving of the qubits is taken into account. The requirements to observe such a state are the following. It should be an eigenstate of the coherent part of the driven-dissipative dynamics described by Hamiltonian (2.19) that reads:

$$H_{\text{cas}} = H_S - i\hbar\Gamma_R\left(\sum_{j>i}\sigma_j^\dagger\sigma_j - \sigma_i^\dagger\sigma_i\right) \tag{2.21}$$

and should be annihilated by the collective jump operator $S_- = (\sigma_-^1 + \sigma_-^2)$. It is possible to show that both these conditions are satisfied if the two qubits are driven

with the same strength $\mathcal{E}_1 = \mathcal{E}_2 = \mathcal{E}$ and if they have opposite detuning from the laser frequency: $\delta_L^1 = -\delta_L^2 = \delta_L$ with $\delta_L^i = \omega_i - \omega_L$. Under these conditions there is a unique pure steady state $|D\rangle$ given by [21, 25, 26]:

$$|D\rangle = \frac{1}{\sqrt{1+|\alpha|^2}} \left(|g_1, g_2\rangle + \alpha|-\rangle\right), \tag{2.22}$$

where $\alpha = \sqrt{2}\mathcal{E}/(\delta_L - i\Gamma_R)$. This means that for strong driving ($\alpha \gg 1$) the dark state $|D\rangle$ approaches the antisymmetric state $|-\rangle$ that is a pure entangled state as we have shown in the previous sections. This is clearly shown in Fig. 2.4(c) where we plotted the steady-state concurrence as function of the driving strength. We can see that in the strong driving limit it approaches its maximum value meaning that a dark entangled state can be prepared. Note that this preparation scheme is very sensitive to imperfections such as offsets in the detuning or additional dissipation channels. We will briefly mention these effects in Sec. 2.3.5 and we refer to [21, 25, 26] for a more extensive discussion.

Finally, it is worth mentioning that in the case of an arbitrary even number of atoms N_a, it is still possible to find pure dark steady states of the driven-dissipative dynamics. The conditions are similar to that one for the two atoms case with the difference that by choosing different detunings is possible to achieve different multipartite entanglement patterns such as dimers, tetramers or octamers [21, 25, 26]. Such many body dark states are of crucial importance to implement quantum communication protocol or to perform quantum simulation of many-body systems.

2.3 Exact solutions: position space description

The master equation description adapted in the previous section is a powerful tool to describe the multi-qubit dynamics. On the other hand, besides being limited only to the markovian evolution, it also does not provide any insight on the photonic degrees of freedom. Indeed the scattering problem of one or multiple photons impinging on an atomic ensemble can be really interesting in the context of quantum nonlinear optics [88]. To achieve this goal we need to solve exactly the model given in Eq. (2.1). This can be done in both momentum and position space. Here we will present the latter that is more common in the literature.

Let us first rewrite (2.1) separating the right- and left-propagating contributions:

$$\begin{aligned} H = &\sum_{i=1}^{N_a} \hbar\omega_i |e\rangle_i\langle e| + \int dk_R\, \hbar\omega_{k_R} a_{k_R}^\dagger a_{k_R} + \int dk_L\, \hbar\omega_{k_L} a_{k_L}^\dagger a_{k_L} \\ &+ \hbar \sum_{i=1}^{N_a} \frac{g_i}{\sqrt{2\pi}} \left[\left(\int dk_R\, e^{-ik_R z_i} a_{k_R}^\dagger \sigma_-^i + \text{H.c.} \right) + \left(\int dk_L\, e^{-ik_L z_i} a_{kL}^\dagger \sigma_-^i + \text{H.c.} \right) \right], \end{aligned} \tag{2.23}$$

where the operators $a_{k\eta}^\dagger$ create a right or left propagating photon, respectively. To

represent (2.23) in position space we can perform the Fourier transform:

$$a_{k\eta} = \frac{1}{\sqrt{2\pi}} \int dz\, e^{ikz} a_\eta(z), \tag{2.24}$$

where $a_\eta^\dagger(z)$ creates a left/right propagating photon at position z. Using these transformations we end up with the "waveguide QED" Hamiltonian in real space [6, 7, 9, 11]:

$$\begin{aligned} H =& \sum_{i=1}^{N_a} \hbar\omega_i |e\rangle_i\langle e| + i\hbar v_g(k_0) \int dz \left(a_L^\dagger(z) \frac{\partial}{\partial z} a_L(z) - a_R^\dagger(z) \frac{\partial}{\partial z} a_R(z) \right) \\ &+ \hbar \sum_{i=1}^{N_a} g_i \int dz \left[\left(a_L^\dagger(z) + a_R^\dagger(z) \right) \sigma_-^i + \text{H.c.} \right] \delta(z - z_i). \end{aligned} \tag{2.25}$$

Hamiltonian (2.25) conserves the total number of atomic and photonic excitations

$$\hat{N}_e = \int dz \left[a_L^\dagger(z) a_L(z) + a_R^\dagger(z) a_R(z) \right] + \sum_i |e\rangle_i\langle e|. \tag{2.26}$$

Therefore, the eigenstates can be evaluated in each excitation subspace separately.

2.3.1 Single excitation subspace with a single atom

Let us start with the single excitation subspace and $N_a = 1$ atom. A generic eigenstate in this sector is a dressed state of the atom with the field and has the form (we set $\sigma_\pm^1 := \sigma_\pm$):

$$|\phi\rangle = \left(b\sigma_+ + \int dz \left[\phi_{k_R}(z) a_R^\dagger(z) + \phi_{k_L}(z) a_L^\dagger(z) \right] \right) |0, g\rangle, \tag{2.27}$$

where $|0, g\rangle$ is the vacuum state with the atom in the ground and no photons in the waveguide. We denote by b the excited state amplitude of the atom while by $\phi_{k_\eta}(z)$ the amplitude of left- and right-propagating photons. Having assumed for a waveguide an infinite dispersion relation implies, for a single atom, the existence of only scattering states. The photonic wavefunctions for these states are plane waves associated with the propagation of photons in the waveguide. In particular, if we consider a photon incident from the left, we can make the following ansatz for the scattering wave function [6]:

$$\begin{aligned} \phi_{k_R}(z) &= \left(e^{ikz}\theta(-z) + te^{ikz}\theta(z) \right), \\ \phi_{k_L}(z) &= re^{-ikz}\theta(-z), \end{aligned} \tag{2.28}$$

where t and r are the transmission and reflection amplitudes. Note that for a waveguide with finite bandwidth another class of states should be taken into account, i.e. the bound states, that we will discuss in chapter 3.

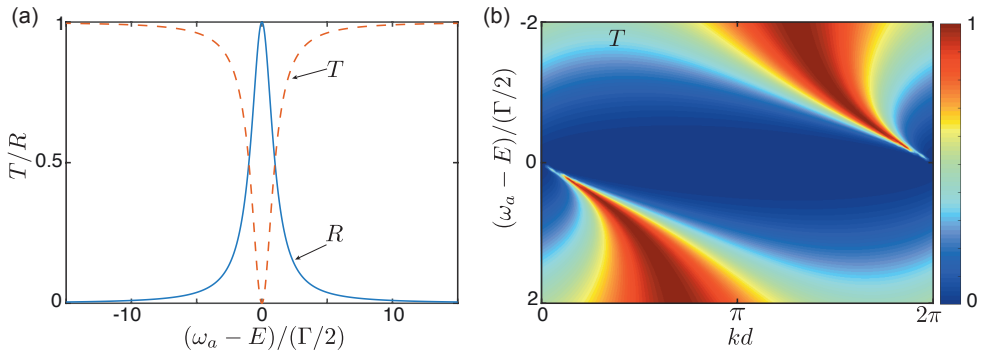

Figure 2.5: (a) Transmission and reflection coefficients for the case of a single TLA in a waveguide. (b) Color map of the transmission coefficient as function of the atom-field detuning and the wavevector for the case of two atoms in a waveguide.

Plugging the ansatz (2.27) into the stationary Schrödinger equation $H|\phi\rangle = \hbar\omega|\phi\rangle$ yields the following set of equations:

$$\begin{aligned} \pm iv_g \frac{\partial}{\partial z}\phi_{k_\eta}(z) + bg\delta(z) &= \omega\phi_{k_\eta}(z) \\ g\left[\phi_{k_R}(0) + \phi_{k_L}(0)\right] &= (\omega - \omega_a)b \end{aligned} \tag{2.29}$$

where $\pm$ corresponds to $\eta = L$ and $\eta = R$, respectively. From Eq.(2.29) it is easy to compute the expression for the amplitudes:

$$b_k = -\frac{v_g}{g}\sin(\varphi)e^{i\varphi}, \qquad r = i\sin(\varphi)e^{i\varphi}, \qquad t = \cos(\varphi)e^{i\varphi} \tag{2.30}$$

where

$$\varphi = \arctan\left[\frac{\Gamma}{2(\omega_a - \omega)}\right] \tag{2.31}$$

is the phase shift and Γ is the single atom decay rate given in (2.16). The reflection (R) and transmission (T) coefficients, plotted in Fig. 2.5(a), are then simply given by

$$R = |r|^2 = \frac{\left(\frac{\Gamma}{2}\right)^2}{(\omega_a - \omega)^2 + \left(\frac{\Gamma}{2}\right)^2} \qquad T = |t|^2 = \frac{(\omega_a - \omega)^2}{(\omega_a - \omega)^2 + \left(\frac{\Gamma}{2}\right)^2}. \tag{2.32}$$

We observe that when the photon is in resonance with the atomic frequency it is completely reflected with no loss by the TLA that acts as a perfect mirror. This property is a peculiarity of the one-dimensional confinement and disappears in higher dimensions.

2.3.2 Single excitation subspace with two atoms

Let us now consider the case of two identical atoms with frequencies $\omega_i = \omega_a$ and coupling strengths $g_i = g$ located at positions $z_1 = -d/2$ and $z_2 = d/2$. Under these

conditions the system is symmetric with respect to the middle point $z = 0$ and can be described in terms of even ($s = e$) and odd ($s = o$) symmetry operators:

$$a_s = \frac{1}{\sqrt{2}}(a_R(z) \pm a_L(-z)), \qquad \sigma_-^s = \frac{1}{\sqrt{2}}(\sigma_-^1 \pm \sigma_-^2). \tag{2.33}$$

Using this basis we can rewrite Hamiltonian (2.25) as a sum of two uncoupled contributions $H = H_e + H_o$ where:

$$\begin{aligned} H_s =& \hbar\omega_a \sigma_+^s \sigma_-^s - i\hbar v_g(k_0) \int dz\, a_s^\dagger(z) \frac{\partial}{\partial z} a_s(z) \\ &+ \hbar g \int dz \left(a_s^\dagger(z)\sigma_-^s + a_s(z)\sigma_+^s\right) \left[\delta(z + d/2) \pm \delta(z - d/2)\right], \end{aligned} \tag{2.34}$$

where $\pm$ is associated to $s = e$ and $s = o$, respectively. Proceeding as before in the single excitation subspace we can find the eigenstates of the system by using an ansatz similar to (2.27):

$$|\phi_s\rangle = \left(b\sigma_+^s + \int dz \phi_{k_s}(z) a_s^\dagger(z)\right)|0, g\rangle, \tag{2.35}$$

where now the photonic wave function is defined in three separated sectors according:

$$\phi_{k_s}(z) = e^{ikz} \begin{cases} , \alpha_s & \text{for } z < -d/2 \\ t_{1,s} & \text{for } -d/2 < z < d/2, \\ t_{2,s} & \text{for } z > d/2. \end{cases} \tag{2.36}$$

This ansatz yields to the following set of equations for the atomic and photonic amplitudes:

$$\begin{aligned} &(\omega - \omega_a) b^s = \frac{g}{2}\left(\pm(t_{2,s} + t_{1,s})e^{ikd/2} + (\alpha_s + t_{1,s})e^{-ikd/2}\right), \\ &iv_g(t_{2,s} - t_{1,s})e^{ikd/2} = g b^s, \\ &iv_g(t_{1,s} - \alpha_s)e^{-ikd/2} = \pm g b^s. \end{aligned} \tag{2.37}$$

The solutions of this system can be classified by the value of the coefficient α_s. When $\alpha_s \neq 0$ the complete set of solutions is given by scattering states extended over the whole waveguide. The amplitudes in this case read [22, 19]:

$$\begin{aligned} t_{1,s} &= \frac{E - \omega_a}{E - \omega_a + i\Gamma/2(1 \pm e^{ikd})}, \\ t_{2,s} &= \frac{E - \omega_a - i\Gamma/2(1 \pm e^{ikd})}{E - \omega_a + i\Gamma/2(1 \pm e^{ikd})}, \\ b^s &= g\frac{e^{-ikd/2} \pm e^{ikd/2}}{E - \omega_a + i\Gamma/2(1 \pm e^{ikd})}. \end{aligned} \tag{2.38}$$

From these amplitudes it is possible to evaluate the photon transmission, which is plotted in Fig. 2.5(b). Compare to the single atom case, where a perfect transmission

is reached only for far off-resonant photons, in the two atom case there are frequency windows with large transmission, $T \sim 1$, even for frequencies detuned by just the resonance linewidth ($\sim \Gamma$). This effect is caused by the destructive interference of the photons reflected by the two atoms. Furthermore, the transmitted photon can acquire, for frequencies always within the resonance linewidth, a considerable phase shift. This feature can be used to implement photon-atom and photon-photon phase gates and open the possibility to waveguide QED based quantum computation [22].

2.3.3 Bound states in the continuum

If we set $\alpha_s = 0$ in (2.37) the scattering solutions do not form a complete basis set and an additional class of states should be taken into account. These states have eigenvalues in resonance with the atomic frequencies $\omega = \omega_a$ and exist only for specific atom-atom distances

$$k_0 d = n\pi, \tag{2.39}$$

where $n \in \mathbb{N}$ and $k_0 = \omega_a / v_g$ is the resonant wave vector. From the system of equations (2.37) it is possible to derive an expression that relates the atomic amplitude with the coefficient $t_{1,s}$:

$$t_{1,s} = \mp i \; b^s \sqrt{\frac{\Gamma}{2v_g}} e^{ik_0 d/2}, \tag{2.40}$$

while the transmission coefficient $t_{2,s}$ turns out to be always zero. This is related to the fact that on resonance a photon is perfectly reflected by a TLA, as shown in Fig. 2.5(a), so the regions inside and outside the two emitters are completely decoupled. This means that, while incident photons cannot enter in the inter-atomic region, photons on resonance that are already between the two atoms cannot escape. For each specific system configuration that respects condition (2.39), there exists only one of these states. In particular, for even resonant separations, $d = 2n\pi/k_0$, this bound state has odd symmetry while for odd resonant separations, $d = (2n+1)\pi/k_0$, it exists only in the even subspace. It can be explicitly written as

$$|\phi_b\rangle = b\left(\frac{1}{\sqrt{2}}[\sigma_+^1 \pm \sigma_+^2] + \sqrt{\frac{\Gamma}{v_g}} \int_{-d/2}^{d/2} dz \, \sin\left(k_0(z + d/2)\right) a^\dagger(z)\right)|0, g\rangle, \tag{2.41}$$

where the atomic amplitude is defined up to a global phase factor, $|b|^2 = 1/(1+\Gamma\tau/4)$, and the photonic wavefunction corresponds to a stationary wave localized between the atoms. The delay time $\tau = 2d/v_g$ corresponds to the time that a photon takes to make the round-trip between the two atoms. These localized states are known as bound states in the continuum (BIC) [19, 27, 28, 29, 64, 65, 66, 68] due to the fact that they have energies that lie inside the photonic spectrum in contrast with the most common bound states that have energies inside a gap. Instead, the existence of a BIC is a consequence of the "colored" atom-field interaction. Due to the orthogonality of the unbound states and the BIC subspaces the latter states do not play any role in scattering processes where the atoms are initially in the ground state. On the other hand, if some of the atoms are initially excited, the BIC can have

an important role in the dynamics. The importance of these states can be easily visualized in the case in which one of the two atoms is initially excited. During the spontaneous emission the amount of population that relaxes into the bound state can be easily evaluated from (2.41) and is also given by $p_{\rm BIC} = \frac{1}{(1+\Gamma\tau/4)}$. This equation shows that the BIC population becomes significant in the limit of small couplings and short distances and implies that these states play a fundamental role in the Markovian regime. Indeed condition (2.39) is the same as the one obtained in Sec. 2.2.1 and these states correspond basically to the sub-radiant states of the bidirectional waveguide master equation. If bigger couplings or longer distances are considered, the Markov approximation breaks down and the contribution of these states decreases. What happens is that retardation effects start to play an important role in the dynamics as we will see in the next section.

Before we proceed we point out that a BIC can also occur for a single atom placed in front of a mirror. In this case the resulting BIC is equivalent to the two atoms case with the only difference that the photonic population is twice as big. This case will be considered in chapter **??**.

2.3.4 Effects of retardation

One of the advantages of having found exact analytic solutions for the scattering states is the possibility to go beyond the Markov approximation and to study in more detail the effect of time delay on the atom dynamics. To have a comparison with the previous results, let us consider again a spontaneous emission process where the first atom is initially excited $|\phi(0)\rangle = |eg0\rangle$. The evolution of the state can be computed as usual and it is given by the sum of the scattering states and BIC contributions:

$$|\phi(t)\rangle = \sum_s \frac{1}{2\pi} \int dk\, e^{-i\omega_k t} |\phi_{s,k}\rangle\langle\phi_{s,k}|\phi(0)\rangle + e^{-i\omega_b t}|\phi_{BIC}\rangle\langle\phi_b|\phi(0)\rangle, \tag{2.42}$$

where the index s runs over the even and odd subspaces. Using equation (2.42) it is possible to evaluate the exact evolution of the excited state population of the first qubit for different atomic distances as plotted in Fig. 2.6(a). We observe that when the atom-atom distance increases the exact results deviate more and more from the predictions obtained from the master equation. For short distances the qubit decays in a time Γ^{-1} much longer than the time required by the photon to travel from one atom to the other. This allows to build rapidly the BIC standing wave that mediates an instantaneous effective interaction between the atoms. In this regime the exact solution is perfectly described by the master equation in which the BIC contributions are implicitly considered.

If we increase the atom-atom distance we gradually enter in a regime where the first atom decay faster than the photon travel time. This means that the first atom decays as a single emitter (with decay rate Γ) for a time $\sim \tau$ until it receives back the photon reflected by the second atom that restores the collective emission [14, 19, 68]. This effect can be even better visualized in Fig. 2.6(b) where we plotted the concurrence to quantify the entanglement between the atoms. We observe that

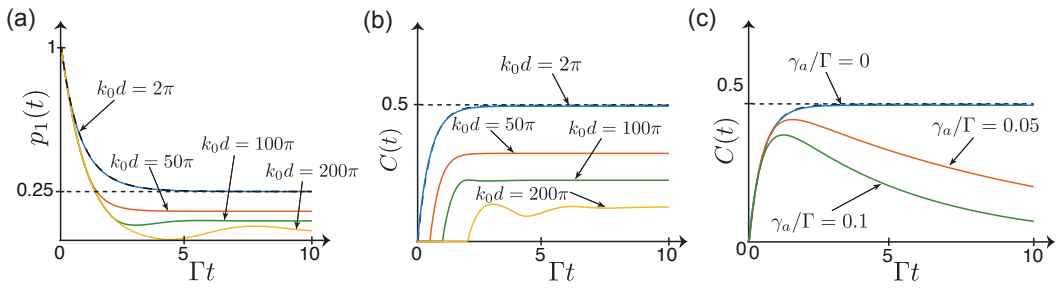

Figure 2.6: (a)-(b) Excited state population and concurrence as function of time for different atom-atom distances. As the atom-atom distance becomes larger and larger the predictions based on the Markov approximation (black dashed line) deviate more and more from the exact results. (c) Concurrence as a function of time for different atomic decay rates. The photonic decay enters in only for stronger values and is not plotted here. In this the atom-atom distance is fixed to $k_0 d = 2\pi$.

an increase of the distance affects the concurrence in two different way. First, it raises up at a retarded time as a consequence of the delayed activation of the collective emission. Second, it reaches a lower value due to the fact that a considerable part of the excitation is lost during the single emission of the first atom. In the limit of very large distances, $\tau \gg \Gamma^{-1}$, the first atom decays completely before receiving feedback from the second atom and there is no entanglement formation at all. Note that the same behaviour is observed if the distance is kept fixed and the atom-field coupling is instead increased. In this case we reach the counter-intuitive result that a strong atom-field coupling leads to a smaller amount of entanglement than what can be established in the weak-coupling limit.

2.3.5 Effect of dissipation

So far we have considered the ideal situation where the photonic modes of the confined field are the only bosonic degrees of freedom in the system. In real implementations the waveguide and atoms are embedded in a 3D environment, which provides additional decay channels. The loss of excitations can occur through spontaneous emission of the atoms into the environment or through losses in the waveguide. In both cases the loss can significantly affect the dynamics. To account for these effects we can proceed as in Sec. 1.3.1 and model the environment as a Markovian bath. For most purposes, it is enough to account for the losses into other modes by considering an effective non-Hermitian Hamiltonian [7, 22, 132]:

$$H_{\text{diss}} = H - i\hbar\frac{\gamma_a}{2}\sum_{i=1}^{N_a}\sigma_+^i\sigma_-^i - i\hbar\frac{\gamma_c}{2}\int dk\, a_k^\dagger a_k, \tag{2.43}$$

where γ_a and γ_c are the atomic and photonic decay rates. In the case of a single atom this allows us to evaluate how the dissipation affects the transmission coefficient,

which is now given by:

$$T = \frac{(\omega_a - \omega)^2 + \left(\frac{(\gamma_a - \gamma_c)}{2}\right)^2}{(\omega_a - \omega)^2 + \left(\frac{\Gamma + (\gamma_a - \gamma_c)}{2}\right)^2} \quad . \tag{2.44}$$

We observe that, if the photonic leakage rate is equal to the atomic decay rate, the two dissipation mechanisms combine together (see also the case of the dissipative cavity treated in Sec. 1.3.1) and the photon transmission is still suppressed on resonance. Note that, compared to the non-dissipative case, even on resonance the reflection is not perfect because part of the reflected field gets lost in the environment.

For more than one atom the effective Hamiltonian (2.43) still describes very well scattering process, but it is not enough to correctly treat the behaviour of the BIC in presence of external dissipation. By doing a more careful analysis that explicitly includes the interaction with the environment [19], it turns out that there still exists a subspace of localized eigenstates orthogonal to the scattering states. Compared to the non-dissipative case for a given system configuration this subspace is spanned by a continuum of states. These states are still localized within the two atoms but they are not anymore bound. Indeed they decay into the reservoir loosing completely their localization in the long-time limit. Therefore, they are known as quasi-bound or quasi-localized states. This loss of excitations manifests itself in the plot of the concurrence that, as shown in Fig. 2.6(c), does not reach a steady-state, but decays in time.

Finally, it is worth mentioning an important figure of merit largely used in the waveguide community to quantify the effects of dissipation on the system: the β factor [133, 33]. The β factor quantifies the fraction of radiation that is spontaneously emitted into the waveguide modes and is defined as:

$$\beta = \frac{\Gamma}{\Gamma + \gamma_a + \gamma_{nr}}. \tag{2.45}$$

Here we also included the decay rate γ_{nr} associated with coupling to non-guided or non-radiative modes. This factor clearly shows that, in order to avoid loss of excitation into undesired decay channels, it is fundamental to enhance the emission in the guided modes, or in other words, it is necessary to reach the regime $\Gamma \gg \gamma_a, \gamma_{nr}$. The atomic emission rate into the waveguide Γ is given in (2.16) and depends directly on the coupling strength and inversely on the photonic group velocity. While increasing the coupling is often more challenging and strongly depends on the particular implementation, decreasing the group velocity is something that is achievable by properly engineering the photonic waveguide. Indeed, following this route a beta factor of $\beta \sim 0.98$ was reached in a photonic crystal waveguide [109].

On the other hand when the decay rate is enhanced we start to enter in a regime where non-Markovian effects should be considered. In the last section we discussed the retardation effects that can be often avoided by taking distances short enough.

When waveguides with slow-light propagation are considered a new plethora of non-Markovian effects arises. This is the regime of "slow-light waveguide QED" that we will discuss in the next chapter.

Chapter 3

Slow-light waveguide QED

In the previous chapter we introduced the field of waveguide QED, discussing how the nature of atom-light interactions changes when the field is confined to one dimension. For this discussion we had focused on a purely linear dispersion relation and on the resulting Markovian dynamics. However, there are other interesting regimes to explore where the dispersion can be non-linear or can exhibit photonic band gaps.

In this chapter we will show how non-trivial band structures can arise by properly engineering the photonic medium. In particular, by applying a periodic modulation to the waveguide it is possible to generate a finite bandwidth for the light and highly decrease the group velocity of the propagating photons. This gives rise to an exciting new regime for atom-light interactions, which we refer to as "slow-light waveguide QED".

In section 3.1 we review the concept of photonic crystals focussing on the one-dimensional case. Here the presence of photonic gaps leads to the existence of localized atom-photon bound states that can mediate coherent atom-atom interactions.

In section 3.2 we will then show with a simple model that it is possible to decrease even further the width of the photonic band. This small finite bandwidth definitively promotes the bound states as elementary excitations of the system and imposes an upper bound for the photons group velocity that can become comparable to the speed of moving atoms or acoustic waves. This is the exactly the scenario, which is considered in the first three project of this thesis discussed in chapters 4-6.

3.1 Photonic crystal waveguides

The theoretical and experimental basis for photonic crystals (PC) were laid at the end of the 80s and the beginning of the 90s [34, 33, 41, 42, 44] with the purpose of achieving an higher level of control for light. The basic idea behind a PC comes from usual crystals in condensed matter physics. In solids, a periodic structure of atoms yields a periodic potential for the electrons, which leads to a modification of

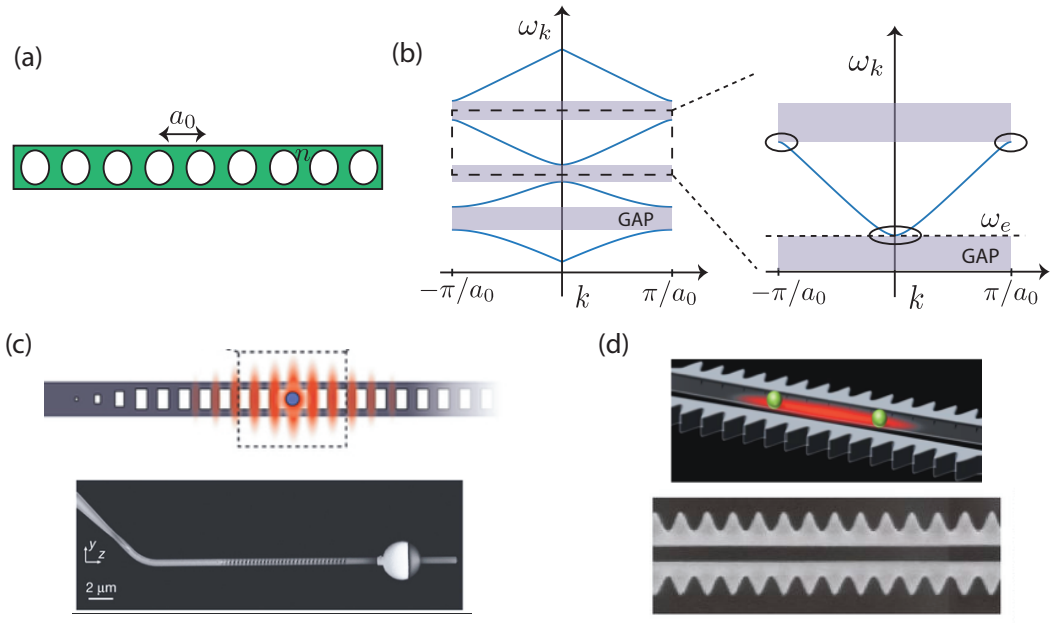

Figure 3.1: (a) Sketch of a 1D photonic crystal waveguide where the refractive index is spatially modulated with lattice constant a_0. (b) Example of a band structure induced by the periodic modulation. On the right side a zoom of a specific band and the adjacent gaps is shown. The black circles represent the frequencies ranges where the dispersion can be approximated as quadratic. (c) High Q-factor nanocavities fabricated in photonic crystal waveguides [36]. (d) Alligator photonic crystal waveguides [38].

the dispersion relation, of the density of states, and to the formation of forbidden energy gaps for the electrons.

Similarly, a photonic crystal is a material characterized by a spatially periodic modulation of some structure parameter, usually the refractive index [see Fig. 3.1(a)], where the length of the modulation is comparable to the wavelength of the light. The wave nature of the electromagnetic field and the periodicity of the medium leads to the formation of a photonic band structure as sketched in Fig. 3.1(b). In particular, this results in frequency ranges, the bands, where the field can propagate and frequency ranges, the gaps, where photons cannot propagate. This means that, for example, a light beam incident on a photonic crystal, with a frequency inside the band gap region, will be backscattered from the material. Even if at the beginning many papers were published trying to investigate the atom-light interaction in this kind of structures [42, 43, 45, 44, 46, 134] with the time the research on PC has been focussing mainly on controlling the light propagation in 3 and 2 dimensional media [135]. Recently, the success achieved in waveguide QED in interfacing ensembles of atoms with confined light has stimulated again a lot of interest on PC structures, in particular also in the quantum optics community. Indeed the physics of light-matter interactions in 1D becomes even more involved

when the waveguide is engineered to have non-trivial dispersion relations, such as band edges and band gaps. This has led to the development of experiments where ensembles of real or artificial atoms can be coupled to photonic crystal waveguides.

Besides the use of 2 dimensional photonic crystal slabs to protect a one-dimensional waveguide embedded between them [see Fig. 2.1], one dimensional PC waveguides have been implemented. Nowdays such structures are used to realized optical cavities with extremely high Q-factor [122, 117, 36, 35, 136, 137], as shown in Fig. 3.1(c), or to investigate long-range coherent atom-atom interactions mediated by the PC waveguide. In particular, with this purpose the group of Jeff Kimble at Caltech has developed a new platform called alligator photonic crystal waveguides (APCW) illustrated in Fig. 3.1(d) [37, 38, 39]. It consists of two parallel SiN nanobeams modulated periodically at the outer edges. This peculiar design allows to trap atoms along the longitudinal direction and at the same time to couple them to the photonic band structure generated by the periodicity.

These experimental activities have also renewed the theoretical interest in studying atom-light interaction in confined band gap media, in particular with the final purpose of studying many-body physics [49, 48, 50, 51]. In the following we are going to present the main features of photonic crystal waveguides and we will show how they can lead to new forms of atom-atom interactions mediated by atom-photon bound states.

3.1.1 Dispersion relation

A simple photonic crystal model was introduced by John and Wang [41, 42, 43] and assumes a 3D isotropic and non-dissipative media. The isotropy assumption makes this model basically equivalent to a one dimensional one. In our case we are interested in confined structures so here we will review directly the simpler 1D version of this model.

Let us a consider a waveguide of length L with a longitudinal spatial modulation of its dielectric constant $\epsilon(z) = n^2(z)$ given by:

$$\epsilon(z) = \epsilon_0 + \delta\epsilon(z), \tag{3.1}$$

where the dielectric constant was separated into an average value ϵ_0 and a spatial dependent part $\delta\epsilon(z)$. A similar treatment can be applied also for other kinds of modulations. The Helmholtz equation given in (1.2) for the longitudinal field $\Phi(z)$ reads:

$$\left(-\frac{\partial^2}{\partial z^2} - \epsilon_f(z)\frac{\omega^2}{c^2}\right)\Phi(z) = \epsilon_0\frac{\omega^2}{c^2}\Phi(z). \tag{3.2}$$

Equation (1.2) is formally equivalent to the Schrödinger equation for an electron in a spatially varying potential. Therefore, the term $\epsilon_f(z)\frac{\omega^2}{c^2}$ plays the of role of an effective potential for the photons.

Let us assume the potential to be periodic with lattice constant a_0. The periodic potential slows down the photons by Bragg-reflection [34, 33, 41, 42, 43, 45, 44, 46, 134] and separates the spectrum into individual bands ω_k^n, where n is the band

index. Each of these bands can be described within the first Brillouin zone, $k \in (-\pi/a_0, \pi/a_0]$, as sketched in Fig. 3.1(b). In most of the cases the system dynamics is governed by frequencies scales that are small compared to the width of individual bands and gaps. In optical implementations these bandwidths have usually widths on the order of several THz. This is much bigger than the typical atom-field coupling strengths achievable in these kind of systems, which are in the MHz-GHz scale. With this argument it is often possible to restrict the analysis to a single band. If we focus on frequencies in the proximity of one of the band edges, it is possible to approximate the dispersion relation as quadratic

$$\omega_k = \omega_e \pm \alpha(k - k_0)^2, \tag{3.3}$$

where ω_e is the frequency at the band edge and k_0 the wavenumber at which the gap occurs [see right side of Fig. 3.1(b)]. The quantity α is a positive constant that characterizes the band curvature and the sign plus or minus refers to frequencies close to the lower or upper edge, respectively. The assumption (3.3) is known as effective mass approximation because it allows to associate a "mass" $m^* = \hbar/(2\alpha)$ to the photons. For optical implementations this mass is on the order of $m^* \simeq 10^{-36}$kg. Note that with this approximation we recover the same dispersion obtained for the metallic waveguide in (1.35). The main difference compared to the previous case is that in a photonic crystal there are no modes that lie in the frequency gaps. In a metallic waveguide instead there can be propagating modes below a cut off associated to the other transversal branches.

An important consequence of the quadratic dispersion is that the group velocity of the photons $v_g(k)$ approaches zero when $k \to k_0$. When a photon propagates in the photonic crystal it is continuously reflected back and forth by the dielectric array, which effectively reduces its group velocity. This slowing down of the photons, which is most effective near the band edges, can dramatically affect the emission behaviour. Indeed, the atomic decay rate given in Eq. (2.16) is inversely proportional to the group velocity and could be infinitely enhanced at the edges. Such divergence of the decay rate is of course not physical and the explanation for this prediction relies on the approximations assumed for the decay rate derivation. To better understand this point let us look at the photonic density of states that is given by:

$$\rho(\omega) = \frac{L}{2\pi}\frac{dk}{d\omega}\theta(\omega - \omega_e) = \frac{L}{2\pi}\frac{\theta(\omega - \omega_e)}{2\sqrt{\alpha}\sqrt{\omega - \omega_e}}, \tag{3.4}$$

where the Heaviside function $\theta(\omega - \omega_e)$ indicates the presence of a gap below ω_e. From (3.4) we observe that the density of states has a divergence at the band edge, due to the existence of many photonics modes at this frequency. Such a divergence implies that it is not possible anymore use the Born-Markov approximation to describe the atom-light interaction. This means that the expression for the decay rate derived in (2.16) does not hold anymore for frequencies close to the band edge and an exact treatment of the problem is necessary.

3.1.2 Spontaneous emisssion

In this section we will investigate in more detail the nature of the atom-light interaction in a photonic crystal. With this goal in mind it is important to note that the refractive index modulation not only affects the dispersion relation but also changes the shape of the electric field. Indeed, the periodicity of the system implies that the longitudinal electric field, solution of Eq. (3.2), is a Bloch wave of the form $\Phi(z) = e^{ikz}u_{nk}(z)$, where $u_{nk}(z + a_0) = u_{nk}(z)$ are the Bloch functions of the n-th band. This also changes the form of the interaction term of Hamiltonian (2.1) describing the coupling between one or multiple emitters and the field. Nevertheless, in most of the cases, the Bloch functions can be approximated by their value at the resonant wavevector, $u_{nk}(z) \simeq u_{n_0k_0}(z)$. This means that the model given in (2.1) can still be used by just rescaling the coupling strength: $g_i := g_i u_{n_0k_0}(z_i)$. With this assumption the main difference with respect to the waveguide case relies only on the dispersion relation.

Let us a first consider the simple case of a spontaneous emission process for a single atom. A perturbative solution of the problem can capture some features and gives some intuition about the process. However, such an approximation is not able to fully and correctly describe the atomic emission close to the band edge or inside the band gap. The reason was previously mentioned and relies on the rapid change of the density of states when the atomic transition frequency is close to the band edge. In this regime the atom-light interaction becomes too strong for applying perturbation theory and we need to look for the exact solutions of the problem.

To evaluate the dynamics we use the Hamiltonian (2.1) in interaction picture and we solve the time-dependent Schrödinger equation using the ansatz:

$$|\phi(t)\rangle = \left(b(t)\sigma_+ + \int dk\, \phi_k(t) a_k^\dagger\right)|0, g\rangle. \tag{3.5}$$

This leads to the following coupled differential equations:

$$\begin{aligned} \frac{db(t)}{dt} &= -i\frac{g}{\sqrt{2\pi}}\int dk\, \phi_k(t) e^{i(\omega_a-\omega_k)t}, \\ \frac{d\phi_k(t)}{dt} &= -i\frac{g}{\sqrt{2\pi}} b(t) e^{-i(\omega_a-\omega_k)t}. \end{aligned} \tag{3.6}$$

By formally integrating the second term we get the integro-differential equation for the atomic excitation amplitude:

$$\frac{db(t)}{dt} = -\frac{g^2}{2\pi}\int dk \int dt' e^{i(\omega_a-\omega_k)(t-t')} b(t'). \tag{3.7}$$

Under effective mass approximation the momentum integral can be performed in the frequency range $[k_0, \infty]$ and gives the kernel:

$$K(t-t') = \frac{g^2}{2\pi}\int_{k_0}^{\infty} dk e^{i(\omega_a-\omega_k)(t-t')} = \beta^{3/2} e^{-i\pi/4}\frac{e^{i(\omega_a-\omega_g(t-t'))}}{\sqrt{\pi(t-t')}}, \qquad t > t', \tag{3.8}$$

where $\beta^{3/2} = g^2/(4\sqrt{\alpha})$ is the β factor [43] (note that it should not be confused with the β factor of waveguide QED given in Eq. (2.45)). This kernel shows the non-Markovian character of the reservoir. Indeed, there are contributions to the dynamic of the system not only from the state at the current time, but also from states at earlier times. In order to solve the integro-differential equation (3.7) we can perform the Laplace transform on both sides

$$s\bar{b}(s) - 1 = \beta^{3/2} e^{-i\pi/4} \int_0^\infty e^{-st} dt \int_0^t dt' \frac{b(t') e^{i\delta_e (t-t')}}{\sqrt{\pi (t-t')}}, \tag{3.9}$$

where $\delta_e = \omega_a - \omega_e$. After performing the time integral

$$\int_{t'}^\infty \frac{e^{-(s-i\delta_e)t}}{\sqrt{\pi (t-t')}} dt = \frac{e^{-(s-i\delta_e)t'}}{\sqrt{s-i\delta_e}} \tag{3.10}$$

and by changing the order of the integrations, we obtain the Laplace transform of the excited state amplitude,

$$\bar{b}(s) = \frac{(s-i\delta_e)^{1/2}}{s(s-i\delta_e)^{1/2} - (i\beta)^{3/2}}. \tag{3.11}$$

The atomic amplitude is obtained by the inverse Laplace transformation

$$b(t) = \frac{1}{2\pi i} \int_{\epsilon - i\infty}^{\epsilon + i\infty} e^{st} \bar{b}(s) ds. \tag{3.12}$$

The integration domain of this integral is parallel to the imaginary axis and passes through the point $s = \epsilon$. The real number ϵ is such that the integration domain is at the right of the poles and of the branch cut due to the square root in $\bar{b}(s)$. The inverse Laplace transform yields [41, 42, 43, 45, 44, 46]:

$$b(t) = 2a_1 x_1 e^{\beta x_1^2 t + i\delta_e t} + a_2 (x_2 + y_2) e^{\beta x_2^2 t + i\delta_e t} - \sum_{j=1}^{3} a_j y_j [1 - \Phi(\sqrt{\beta x_j^2 t})] e^{\beta x_j^2 t + i\delta_e t}, \tag{3.13}$$

where

$$x_1 = (A_+ + A_-) e^{i\pi/4}, \tag{3.14}$$

$$x_2 = (A_+ e^{-i\pi/6} - A_- e^{i\pi/6}) e^{-i\pi/4}, \tag{3.15}$$

$$x_3 = (A_+ e^{i\pi/6} - A_- e^{-i\pi/6}) e^{i3\pi/4}, \tag{3.16}$$

$$A_\pm = \left[\frac{1}{2} \pm \frac{1}{2} \left[1 + \frac{4\delta_e^3}{27\beta^3} \right]^{1/2} \right]^{1/3}, \tag{3.17}$$

$$a_j = \frac{x_j}{(x_j - x_i)(x_j - x_k)} \quad (j \neq i \neq k; j, i, k = 1, 2, 3), \tag{3.18}$$

$$y_j = \sqrt{x_j^2} \quad (j = 1, 2, 3), \tag{3.19}$$

and $\Phi(x)$ is the error function defined by:

$$\Phi(x) = \frac{2}{\sqrt{\pi}} \int_0^x e^{-t^2} dt. \tag{3.20}$$

The squared modulus of the amplitude $b(t)$ gives the probability of finding the atom in the excited state. In Fig. 3.2(a) this probability is shown as a function of time for different values of δ_e. We see that, while for atomic frequencies near the middle of the band an exponential Markovian decay is still obtained, the spontaneous emission gets strongly modified when the atomic frequency is close to the edge or in the gap.

- First we observe that there is no divergence of the decay rate at the edge frequency as predicted by the Markov approximation. Nevertheless, the atom indeed experiences a big enhancement of the spontaneous emission rate. This decay takes place on time scales of the order of $1/\beta$,which are much shorter than the corresponding decay time that occurs for frequencies in the band.

- For frequencies close to the edge or inside the gap the excited state population does not decay exponentially but exhibits an oscillator behaviour. The frequency of these oscillations is given by β, which plays a role similar to the Rabi frequency in cavity QED. This is a manifestation of the non-Markovian character of the reservoir and in particular of the non-linearity of the dispersion relation. It can be interpreted as a consequence of the low group velocity of the emitted photon, which that can be reabsorbed by the atom before it propagates away.

- Finally, we note that, while for atomic frequencies inside the band the probability of finding the atom in the excited state is vanishing at long times, for frequencies close to the edge or in the gap a substantial fraction of the atomic population remains trapped in the excited state even at $t \to \infty$. This effect relies on the existence of a photonic band gap and on the localization of the emitted photon around the atomic position. This trapping can be analytically estimated for the case of $\delta_e = 0$ where the steady-state population of the excited state can be obtained by taking the $t \to \infty$ limit:

  $$P = \lim_{t\to\infty} |b(t)|^2 = 4|a_1 x_1|^2 = \frac{4}{9}. \tag{3.21}$$

  A deeper understanding of this localization phenomenon can be obtained in terms of the atom-photon bound states, which will be discussed in the next section.

3.1.3 Atom-photon bound states

The trapping of atomic excitation and the localization of photons presented in the previous section originate from the existence of atom-photon bound states. This is

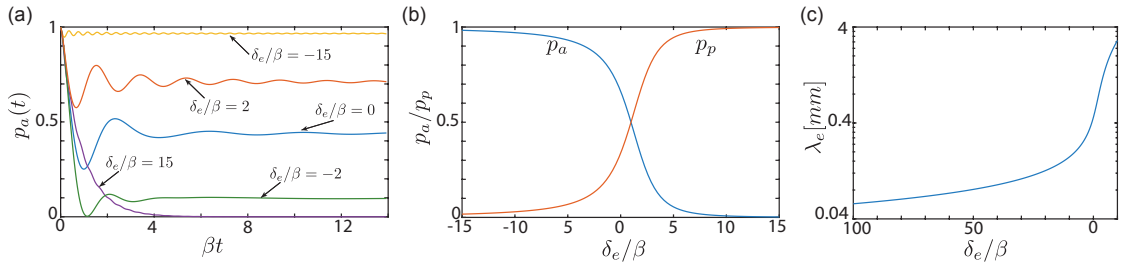

Figure 3.2: (a) Population of the excited state as a function of time for different values of the atom edge detuning. (b) Atomic (p_a) and photonic population (p_p) of the atom-photon bound state as function of the atom-edge detuning δ_e. (c) Localization length in logarithmic scale as function of δ_e. For this plot we assumed a band edge frequency of $\omega_e/(2\pi) \sim 300$THz, an atom field coupling strength of $g/(\sqrt{\lambda_0}2\pi) = 10$GHz with λ_0 being the optical wavelength at the edge, and a band edge curvature of $\alpha = 400$ Hz m^2.

not surprising because, similarly to what happen in solid-state physics, the atom acts as a defect for the photonic crystal breaking the spatial periodicity of the refractive index and causes a discrete energy level in the photonic gap. When the atom decays, part of its excitation relaxes to this state that, being decoupled from the propagating band, traps the excitation forever (assuming and ideal situation without additional decay channels).

To better discuss this kind of states, let us look for the solutions of the stationary Schrödinger equation $H|\phi\rangle = E|\phi\rangle$, with H given in (2.1). If we use the ansatz:

$$|\phi\rangle = \left(b\sigma_+ + \int dk\, \phi_k a_k^\dagger\right)|0, g\rangle \tag{3.22}$$

and concentrate only on the solutions with an energy below the band edge, $E = \hbar\omega < \hbar\omega_e$ (the other solutions are scattering states similar to that one shown in chapter 2), we end up with the following eigenvalue equation:

$$\omega - \omega_a = \Sigma(\omega), \tag{3.23}$$

where

$$\Sigma(\omega) = \frac{g^2}{2\pi}\int dk \frac{1}{\omega - \omega_k} \tag{3.24}$$

is the self energy. To prove that equation (3.23) admits a solution that lies below the bath spectrum we can define the function $F(\omega) = \omega - \omega_a - \Sigma(\omega)$. This function is monotonically increasing and $F(\omega) \to -\infty$ as $\omega \to -\infty$. Thus, if $F(\omega_e) > 0$ there must be only one solution with $\omega < \omega_e$. This means that, if the self energy evaluated at the band edge i.e. $\Sigma(\omega_e)$ is negatively divergent, a unique bound state exists. This is indeed always the case for a quadratic dispersion relation in one and two dimensions while in three dimensions a bound state exists only under more specific conditions involving the system parameters [66, 61]. In our case the self energy can

be computed exactly, $\Sigma(\omega) = \frac{\beta^{3/2}}{\sqrt{\omega_e - \omega}}$, and the real negative solution of equation (3.23) can be explicitly written as [41, 42, 43, 45, 46, 49]:

$$\delta_\omega = \frac{2}{3}\delta_e - \frac{\beta}{2^{2/3}}\left(a_+^{1/3} + a_-^{1/3}\right), \qquad a_\pm = \left(1 \pm \sqrt{1 + 2^{2/3}\left(\frac{\delta_e}{3\beta}\right)^3}\right)^2, \tag{3.25}$$

where $\delta_\omega = \omega - \omega_e$. The corresponding eigenstate is given by:

$$|\phi\rangle = b(\omega)\left(\sigma_+ + \frac{g}{\sqrt{2\pi}}\int dk \frac{e^{ikx_a}}{\delta_\omega - \alpha k^2} a_k^\dagger\right)|0, g\rangle, \tag{3.26}$$

where

$$b(E) = \left(1 + \frac{1}{2}\left(-\frac{\beta}{\delta_\omega}\right)^{3/2}\right)^{-1/2}, \tag{3.27}$$

is the excited state amplitude. The excited state population, $p_a = |b(\omega)|^2$, and the photonic population, $p_p = 1 - p_a$, are shown in Fig 3.2(b) as function of the atom-edge detuning. We can identify three different regimes.

- For atomic frequencies in the band the bound state is mainly composed by a photonic excitation and its eigenfrequency is tangent to the band edge.
- For atomic frequencies in the gap the bound state energy moves away from the band edge and the atom becomes weakly dressed by the photon.
- For frequencies close to the edge the state is highly hybridized between the atomic and the photonic component.

It is also interesting have a look at the spatial distribution of the photonic wavefunction. An expression for the bound state in position space can be obtained by making a Fourier transform of equation (3.26):

$$|\phi\rangle = b(\omega)\left(\sigma_+ + g\int dz \frac{e^{-\frac{|z - z_a|}{\lambda_e}}}{\sqrt{-4\delta_\omega \alpha}} a_z^\dagger\right)|0, g\rangle. \tag{3.28}$$

We immediately see that in real space the photon is exponentially localized around the atomic position with a localization length given by $\lambda_e = \sqrt{-\alpha/\delta_\omega}$. This localization can be interpreted as an evanescent electromagnetic field inside the gap that does not propagate in the crystal.

It is instructive to estimate the behaviour of this localization length using some typical parameters in optical photonic crystal implementations [49, 37, 38]. In Fig 3.2(c) we plotted the localization length as function of δ_e for a band edge frequency of $\omega_e/(2\pi) \sim 300$THz, an atom field coupling strength of $g/(\sqrt{\lambda_0}2\pi) \sim 10$ GHz with λ_0 being the optical wavelength at the edge, and a bandedge curvature of $\alpha \sim 400$ Hz×m^2. We first observe that the photonic cloud is more localized for

atomic frequency in the gap while it becomes more and more extended for atomic frequency closer or inside the band. For the parameters considered here the cloud is extended over a millimetre scale, which is comparable with the length of typical photonic crystal waveguides. This explains why these state were never directly observed so far in optical photonic crystal implementations. Nevertheless, when the atomic frequency is deep in the gap, the localization length can be decreased down to a micrometre scale. In this regime the bound state basically consists of an atomic excitation weakly dressed by the photons and the remaining field can be adiabatically eliminated.

3.1.4 Atom-atom interactions in a photonic crystal

The long-term interest in interfacing nanophotonics structures with quantum emitters goes beyond simple spontaneous emission. Indeed, the final goal is to engineer interactions between multiple emitters trough the photonic structure. The photonic crystal waveguides in this sense have recently attracted a lot of interest for the purpose of controlling and simulating many-body physics [49, 37, 38]. In this section we show how the atom-atom interactions are affected by the photonic band structure and that in certain limits an effective spin model can be derived. In the rest of this section we will just consider a resonant interaction where all the atomic frequencies are the same, i.e. $\omega_i = \omega_a$.

Excitation transfer

Let us consider a simple excitation transfer process between two atoms embedded in a photonic crystal waveguide where one of the two emitters is initially excited. The two-atoms dynamics in the single excitation subspace can be exactly solved by going to Laplace space, similarly as we presented for the spontaneous emission in the previous section. Here we do not show this exact solution, which can be found in [44, 46, 47, 48, 138], but we summarize the main results. Similarly to the single atom case we can distinguish different regimes by considering different atom-edge detunings.

- For atomic frequencies deep in the band, $\delta_e \gg \beta$, the qubit dynamics resembles that one of two atoms in a waveguide and is mainly Markovian. In this case the excitation transferred to the second qubit never exceeds the value of $p_2 \simeq 0.25$, which occurs at resonant distances when the collective behaviour becomes important [see discussion in Sec. 2.2.1].

- For atomic frequencies close to the band edge, $\delta_e \simeq 0$, the excitation transfer process changes dramatically. From Fig. 3.3 (a) we observe that, after an initial transient where the excited atom rapidly decays loosing part of its population, on a longer time scale the rest of excitation is resonantly exchanged between the atoms. This transfer of excitation occurs in an oscillatory and non-dissipative manner and is caused by the beating between two atom-photon bound states

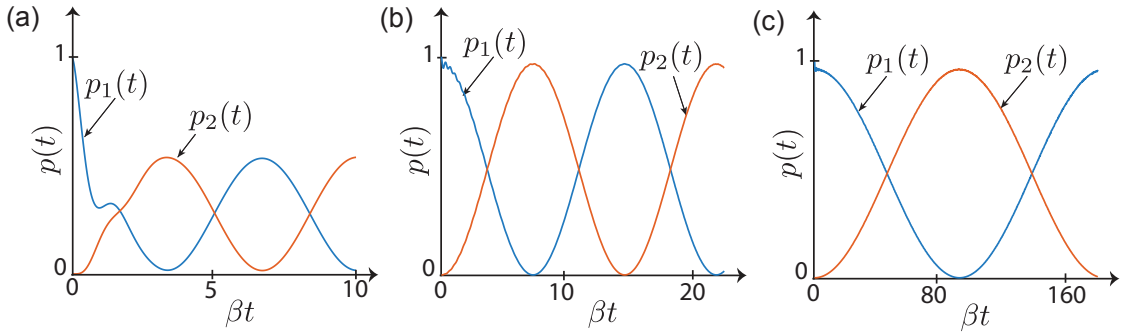

Figure 3.3: (a)-(c) Excitation transfer between two atoms as function of time for the case where one of the atoms is initially excited. We fixed $\delta_e/\beta = 0$, $d/\lambda_e \simeq 1$(a), $\delta_e/\beta = -15$, $d/\lambda_e \simeq 1$, (b) and $\delta_e/\beta = -15$, $d/\lambda_e \simeq 4$(c).

with frequency in the gap (note that these two-atom bound states will be discussed in more detail in the similar CCA case presented in Sec. 4.3). This allows a dispersive interaction between the atoms mediated by the localized photonic cloud surrounding each of them.

- For atomic frequencies deep in the gap, $\delta_e < 0$ and $|\delta_e| \gg \beta$, the dispersive interaction becomes dominant and the amount of excitation that goes trough dissipative dynamics becomes negligible as shown in Fig. 3.3(b). In this limit the dynamics resembles that one observed in the dispersive regime of cavity QED discussed in Sec. 1.3.2 where the atom-field states are weakly dressed by the photons and consist of mainly atomic excitations.

The last point seems to suggests that, similarly to cavity QED, it should be possible to write down an effective model where the photonic degree of freedom is traced out and an effective atom-atom interaction is obtained. However, this mapping fails because, compared to a cavity, in a photonic crystal the atom-atom distance d still plays a role. This is clear in Fig. 3.3(c) where we observe that by increasing the qubits separation the interaction occurs in a much longer time scale. In the next section we will derive the correct effective Hamiltonian that takes in account this distance dependence.

Effective dipole-dipole interaction

In the limit where $\delta_e < 0$ and $|\delta_e| \gg \beta$, the atom-field bound states are weakly dressed by the photonic modes that can be eliminated to obtain a description only in terms of the atomic degree of freedoms [48, 49]. In this limit, where the atomic frequency is detuned from the band edge, it is still possible to use the Born-Markov approximation and to get a master equation similar as we did in Sec. 2.2.1 for multiple atoms in a waveguide. In particular let us consider the correlation function:

$$A_{ij} = \frac{2g^2}{\pi}\int_0^\infty d\tau \int_{k_0}^t dk\, e^{ik(z_i-z_j)}e^{i\delta_k\tau} = \frac{2g^2}{\pi}\int_{k_0}^\infty dk\, \frac{1}{i\delta_k}\left(e^{i\delta_k t}-1\right), \tag{3.29}$$

where $\delta_k = \omega_a - \omega_k$ and between the LHS and RHS we performed the time integration. In the limit of $|\delta_e| \gg \beta$ the exponential term on the RHS of (3.30) is fast oscillating compared to the rest of the system dynamics, which occurs on a time scale given by β, and can be adiabatically eliminated. The correlation function can thus be simplified to:

$$A_{ij} \simeq \frac{ig^2}{\sqrt{|\delta_e|\alpha}} e^{-\frac{|z_i - z_j|}{\lambda_e}}, \tag{3.30}$$

where $\lambda_e = \sqrt{\alpha/|\delta_e|}$ is the localization length of a single atom-photon bound state. We immediately notice that, in the limit of interest, the correlation function A_{ij} is always imaginary. This means that the atom dynamics is never dissipative but only coherent and can be fully described by a unitary effective Hamiltonian. If we define the effective coupling $g_c = g/\sqrt{\lambda_e}$ we can write the effective Hamiltonian describing the atom-atom interaction as:

$$H_{\text{eff}} = \frac{g_c^2}{\delta_e} \sum_{ij} e^{-\frac{|z_i - z_j|}{\lambda_e}} \sigma_+^i \sigma_-^j. \tag{3.31}$$

This kind of interaction resembles the dispersive interaction in cavity QED described by Eq. (1.33) where the photonic cloud associated to the atom-photon bound state plays the role of the cavity mode. The main difference arises from the extended multi-mode dressing of the atom compare to the single localized mode that hybridizes with an emitter in cavity QED. This difference manifests itself in the exponentially localized suppression of the interaction with the distance. The physical interpretation is that the interaction among the atoms is mediated by the exponential photonic cloud surrounding each of them. When the atoms are too far apart the clouds do not overlap and the interaction is suppressed. Nevertheless, as we pointed out in Sec. 3.1.3, in optical implementations the photonic cloud can be largely extended and for frequencies deep in the gap they can still have a length of the order of $\sim 100\mu m$. This means that it is possible to implement long-range dispersive interactions between atoms that are protected from decay.

This kind of interactions recently attracted a lot of attention. In particular, it was suggested to exploit them to establish long-distance entanglement among atoms and to simulate many-body physics and spin models [48, 49, 50, 51]. This last idea relies on the possibility of controlling and engineering the properties of the interaction. This is indeed possible for the strength of the coupling that can be tuned through the photon localization length and the shape of the Bloch function. The scaling with the atomic distance can also be modified to a power law by effectively coupling the atoms with more than one band edges [49]. These theoretical proposals have led to a significant experimental effort in this direction [38, 39, 139, 140].

3.2 Narrow bandwidth waveguide

In the last section we have shown how the reduction of the photon group velocity that occurs in a photonic crystal waveguide can drastically affect the interaction

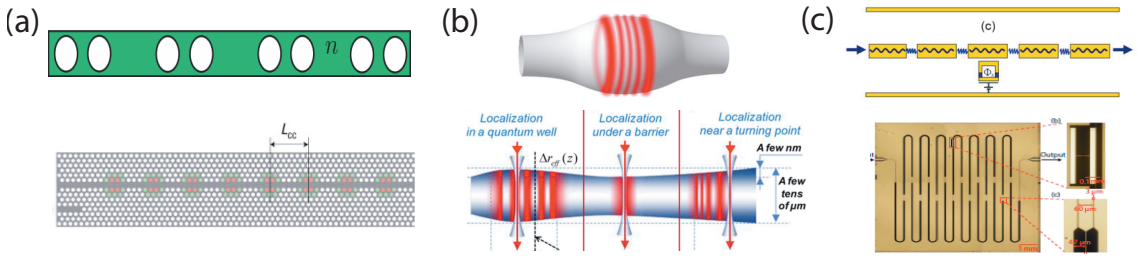

Figure 3.4: Implementations of a narrow bandwidth waveguide. (a) An array of defects in a photonic crystal waveguide creates an effective array of coupled resonators [141, 142]. (b) A sketch of a bottle resonator and a SNAP waveguide [143, 146].(c) An array of mircrowave resonators coupled to superconducting qubits [56, 139].

of one or multiple emitters with the field. In spite of these results for some of the effects that we are going to present in this thesis the speed of the light is still not slow enough.

In a photonic crystal waveguide, even if the group velocity approaches zero close to the band edge, the maximum speed is still given by the linear part of the dispersion relation shown in Fig. 3.1(b). This maximum speed scales with the photonic band as $\bar{c} \sim Ba$, with a being the lattice constant. In most of the photonic implementations this bandwidth is on the order of $B \sim$THz and and the maximum speed of light, $\bar{c} = \max\{v_g(k)\}$, is around $\bar{c} \gtrsim 10^6$m/s. In order to enter in a regime where the maximum speed of the photons is even slower we need to further decrease the width of the band.

The bandwidth of a waveguide can be narrowed by implementing a stronger spatial modulation of the medium. Effectively, this means that we pass from a weakly-perturbed waveguide to a tight-binding model. In a photonic crystal this can be done by considering a periodic arrangement of defects, as shown in Fig. 3.4(a), that creates an effective coupled-cavity array with a GHz "miniband", where the group velocity of the photon is strongly reduced. This kind of structures are know in the literature as Coupled Resonator Optical Waveguides (CROW) [141, 142]. Another possible optical implementation consists in creating a periodic modulation of the radius of an optical fiber. The modulation effectively generates an array of bottle resonators [143, 144, 145] as shown in Fig. 3.4(b). This is possible with the recent development of surface nanoscale axial photonic (SNAP) waveguides where a high level of control on the disorder can be achieved [146, 147]. Besides the nano-photonic implementations another promising route to engineer narrow bandwidth waveguides consists in considering arrays of microwave resonators coupled to superconducting qubits as sketched in Fig. 3.4(c) [56, 148]. Here the great advantage relies on the higher control on the system fabrication that recently has allowed to experimentally explore this slow-light regime, as we will discuss in more detail in chapter 4 [139, 140].

The possibility to narrow and engineer the bandwidth of the waveguides opens new interesting regimes where the atoms can interact with very slow photons. Here

we summarize a few of these aspects that will be investigated in the remainder of the thesis.

First, as we explained in Sec. 3.1.3, in a photonic crystal waveguide the bound states play an important role in the dynamics only when the atomic frequencies are deep in the photonic gap and consist of atomic excitation weakly dressed by the photonic bath. When the bandwidth is further decreased we enter in a regime where the bound states get strongly hybridized between the atomic and photonic components with a small localization length. In this limit the width of the photonic band is almost comparable to the typical atomic decay rate in the waveguide $\Gamma \sim B$ and, as we will show in chapter 4, the bound states become the main elementary excitations of the system and play a crucial role even when the atomic frequency is inside the band.

Second, in such narrow bandwidth waveguides it is possible to highly decrease the maximum speed of propagation of the photons to a value of the order of $\bar{c} \sim 10^4$ m/s. This means that we can enter a regime where the light can propagate with velocities similar to that one of atomic beams or to the propagation speed of acoustic waves in phononic waveguides. These effects will be discussed in chapters 5 and 6.

In this section in order to introduce the physics of these slow light waveguides we will first present a simple model that captures the transition from a photonic crystal to a narrow bandwidth waveguide. We will then introduce the tight binding model that encodes most of the effects that we are going to discuss.

3.2.1 A simple model: from photonic crystals to slow light waveguides

In this section we present a model that captures the transition from a photonic crystal of the kind shown in Sec. 3.1 to a narrow bandwidth waveguide. Let us consider one or multiple TLA coupled close to the band edge of a photonic crystal waveguide. As previously discussed, close to the band edge ω_e the dispersion relation is approximately quadratic [see Fig. 3.5(b)] and has an effective photon mass m^*. To further decrease the photonic bandwidth we add an effective periodic potential $V(z)$ for the photons, as shown in Fig. 3.5(a). This potential can be induced by creating an additional spatial modulation of the waveguide, for example, by a periodic arrangement of defects. We then obtain an Hamiltonian in position space, which can be considered the "slow light" version of the waveguide QED Hamiltonian presented in (2.25):

$$H = \sum_i^{N_a} \hbar\delta_i \sigma_+^i \sigma_-^i + \hbar g \sum_{i=1}^{N_a} \left[a^\dagger(z_i)\sigma_-^i + \sigma_+^i a(z_i) \right] + \int_0^L dz\, a(z)^\dagger \left(-\frac{\hbar^2 \partial^2}{2m^* \partial z^2} + V(z) \right) a(z), \tag{3.32}$$

where $\delta_i = \omega_i - \omega_e$ and L is the length of the waveguide. Let us consider the case of a periodic potential with spatial grating a. Without affecting too much the generality of the discussion we can choose a potential shape of the form $V(z) = V\cos(\Delta k z)$, where $\Delta k = 2\pi/a$ is the lattice vector. Note that the model presented here is analogous to the one of neutral atoms in optical lattices. Here the effect of

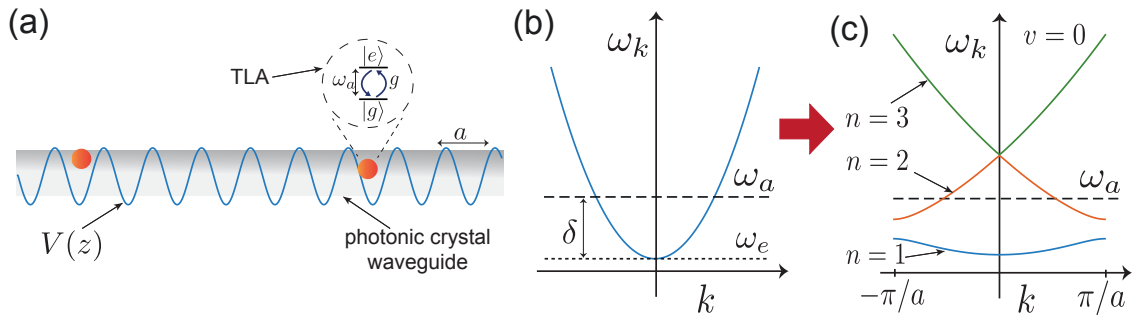

Figure 3.5: (a) Sketch of the setup where an ensemble of two-level atoms is coupled to a 1D photonic crystal waveguide spatial modulated by an effective photonic potential $V(z)$. (b) Original quadratic dispersion associated with the PC-waveguide with effective photon mass m^*. (c) Band structure formation arising from an effective potential with strength $V/E_r = 0.2$.

the spatial modulation consists in separating the original quadratic dispersion into individual bands.

We can diagonalize the photonic part of Hamiltonian (3.32) by decomposing the field in momentum space as

$$a(z) = \frac{1}{\sqrt{L}} \sum_{nk} e^{ikz} u_{nk}(z) a_{nk}, \tag{3.33}$$

where a_{nk} are the annihilation operators that destroy a field excitation of the n-th band with momentum $k \in (-\pi/a, \pi/a]$. The $u_{nk}(z + a) = u_{nk}(z)$ are the periodic Bloch functions satisfying the eigenvalues equation

$$\omega_n(k) u_{nk}(z) = -\frac{i}{\hbar}\left[\frac{\hbar^2}{2m^*}\left(\frac{\partial}{\partial z} + ik\right)^2 + V(z)\right] u_{nk}(z). \tag{3.34}$$

These functions can be decomposed as

$$u_{nk}(z) = \sum_{\ell=-\infty}^{\infty} u_{nk}^{(\ell)} e^{i(\Delta k z)\ell}. \tag{3.35}$$

By inserting this decomposition into Eq. (3.34) we obtain an equation for the coefficients

$$\sum_{l} H_{\ell\ell'} u_{nk}^{(\ell)} = \hbar\omega_n(k) u_{nk}^{(\ell)}, \tag{3.36}$$

where

$$H_{\ell\ell'} = \begin{cases} E_r(\ell + \frac{k}{\Delta k})^2, & \ell = \ell' \\ \frac{V}{2}, & |\ell - \ell'| = 1 \\ 0, & \text{otherwise.} \end{cases} \tag{3.37}$$

In this equation $E_r = \hbar^2 \Delta k^2/(2m^*)$ is the photonic recoil energy. The solution of (3.36) provides the band structure ω_{kn} and the Bloch coefficients $u_{nk}(z)$. The

width of the band is determined by the ratio of the potential strength V and the recoil energy. When $V/E_r > 0$ the original quadratic dispersion starts to get split into several bands that get flatter and more separated as much as the ratio V/E_r increases as shown in Fig. 3.5(c). This means that by properly engineering the strength of this additional modulation that we impose on the waveguide we can achieve the slow-light regime that we are aiming. In particular, in the limit of strong modulation, $V \gg E_r$, a tight binding approximation (TBA) can be applied on the specific band under study and the band can be described approximately by a dispersion of the form $\omega_n(k) \simeq \omega_{cn} \mp (B/2)\cos(ka)$ where ω_{cn} is the frequency in the center of the n-th band and the $\mp$ depends on the curvature of the band. This tight binding picture will be properly discussed in the next section.

3.2.2 Tight binding limit: coupled-cavity array

In this section we model a "slow-light" waveguide with finite bandwidth as a Coupled-Cavity Array (CCA): a one dimensional arrangement of optical resonators with nearest-neighbour coupling. In the absence of any emitters, such a system forms a finite propagating band with an effective speed of light that is fully controlled by the tunnel coupling between neighboring cavities, and thus can in principle be made arbitrarily small. An elegant feature of the CCA system is that in various parameter regimes one can recover the behavior of other systems previously discussed (such as single-mode cavity QED, infinite-bandwidth waveguides and one dimensional photonic crystal). Coupled cavity arrays (CCA) received a lot of attention in the context of quantum simulation of many-body physics with light with the purpose of observing quantum phase transitions [53, 54, 55, 149, 150]. At the same time many people became interested also in photon scattering processes in this finite-bandwidth scenario with a special focus the transmission properties [56, 57, 58, 59, 151, 152, 153, 154, 155, 156]. In presence of a finite bandwidth there is indeed the appearance of localized photonic bound states similar to that one discussed in section 3.1.3 [57, 151, 156, 60, 62]. These bound states can lead to unusual two-photon scattering processes, where, e.g., one photon can remain bound to an atom [58, 59, 151], while the other one escapes. Such processes are absent in free space or infinite-band waveguides.

In chapter 4 of this thesis we will make a detailed analysis on the nature and on the main features of these bound states. Here we will start to introduce in more detail the CCA setup presenting the basic properties and the single excitation dynamics.

Model

The model that we are going to use is illustrated in Fig. 3.7 (a), where a set of N_a two-level atoms is coupled to an array of $N \to \infty$ optical resonators with center frequency ω_c and nearest-neighbor tunnel coupling J. For atoms located at sites x_i

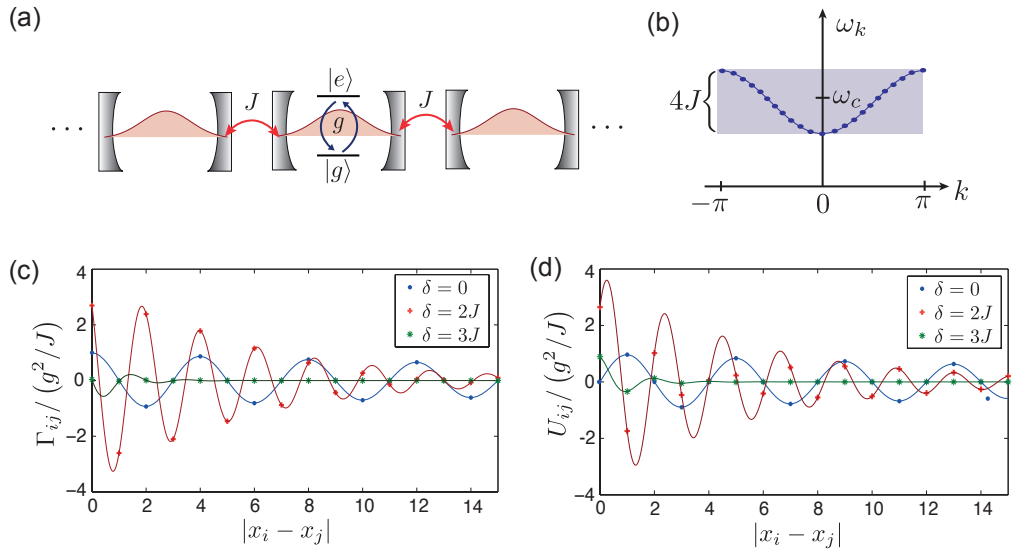

Figure 3.6: (a) Sketch of a slow-light waveguide modelled as a large array of coupled cavities with nearest-neighbor coupling J. (b) Band structure of the waveguide without atoms. (c) Correlated decay rates Γ_{ij} as a function of the (discrete) interatomic distance $|x_i - x_j|$ and (d) coherent dipole-dipole interactions U_{ij} versus $|x_i - x_j|$ for different detunings $\delta = \omega_a - \omega_c$. The solid lines are a guide to the eye obtained from a continuous interpolation of Eq. (3.43). In both plots, the photon loss rate has been set to $\gamma_c/(2J) = 0.14$.

the total Hamiltonian for this system is ($\hbar = 1$)

$$H = \omega_c \sum_x a_x^\dagger a_x - J \sum_x (a_x^\dagger a_{x-1} + a_{x-1}^\dagger a_x) + \sum_{i=1}^{N_a} \omega_a |e\rangle_i\langle e| + g \sum_{i=1}^{N_a} \sum_x \left(a_x \sigma_+^i + a_x^\dagger \sigma_-^i \right) \delta_{x,x_i}, \quad (3.38)$$

where a_x ($a_x^\dagger$) are bosonic annihilation (creation) operators for the individual cavity modes. This Hamiltonian can be considered the discrete version of the waveguide QED Hamiltonian presented in (2.25) with the coupling strength rescaled to have the dimension of a frequency, i.e. $g \to g/\sqrt{a}$, where a is the longitudinal size of a cavity. We can eliminate the absolute optical frequencies by changing into a rotating frame with respect to ω_c, and the resulting system dynamics depends only on the atom-photon detuning $\delta = \omega_a - \omega_c$. To account for atomic emission into other radiation modes as well as the loss of waveguide photons, we introduce a bare atomic decay rate γ_a and a photon loss rate γ_c for each cavity as additional phenomenological parameters.

The first line of Eq. (3.38) represents the tight-binding Hamiltonian H_c of the waveguide. By introducing the momentum operators $a_k = \frac{1}{\sqrt{N}} \sum_x e^{ikx} a_x$, with $k \in]-\pi, \pi]$ (note that here we are implicitly rescaling the wave-vector $k := ka$), we can write (3.38) in a diagonal form $H_c = \sum_k \omega_k a_k^\dagger a_k$, where the mode frequencies

$$\omega_k = \omega_c - 2J\cos(k), \quad (3.39)$$

form a band of total width $B = 4J$ centred around the bare cavity frequency ω_c [see Fig. 3.7 (b)]. The propagation of photons inside the waveguide is characterized by the group velocity

$$v_g(\omega) = \left.\frac{\partial \omega_k}{\partial k}\right|_{\omega_k=\omega} = \sqrt{4J^2 - (\omega - \omega_c)^2}, \tag{3.40}$$

which vanishes for $J \to 0$ or when operating at frequencies close to the band edges, i.e., $\omega \approx \omega_c \pm 2J$. In the limit $J = 0$ the cavities are completely decoupled, each site being thereby described by a single-mode Jaynes-Cummings model [3] with coupling constant g and detuning δ. In this sense the present model captures well finite-bandwidth and bandedge features over a wide range of parameters.

Large bandwidth limit

Let us consider the weak-coupling or broadband limit $g/J \to 0$. In this regime the CCA is equivalent to a photonic waveguide and simply acts as a collective reservoir for the atoms. In particular, it is possible to derive, by using a Born-Markov approximation, the same master equation given in (2.14) for the bidirectional waveguide:

$$\dot{\rho} = -i[H_a, \rho] + \sum_{i,j} \frac{\Gamma_{ij}}{2}\left(2\sigma_-^j \rho \sigma_+^i - \sigma_+^i \sigma_-^j \rho - \rho \sigma_+^i \sigma_-^j\right), \tag{3.41}$$

where in the rotating frame with respect to ω_c,

$$H_a = \sum_i \delta |e\rangle_i\langle e| + \frac{1}{2}\sum_{i,j} U_{ij}\left(\sigma_+^i \sigma_-^j + \sigma_-^i \sigma_+^j\right). \tag{3.42}$$

Similarly to section 2.2.1, Γ_{ij} and U_{ij} represent the correlated decay rates and the coherent dipole-dipole interactions, respectively, which arise from virtual or real photons propagating along the waveguide. Compared to what we have done in the previous chapter, here we generalize the ME including small atomic and photonic losses [see App. A.1]. This allows us to still capture some features of the system even for frequencies close to the band edge. We thus obtain $\Gamma_{ij} = 2\mathrm{Re}\{A_{ij}\} + \gamma_a$ and $U_{ij} = 2\mathrm{Im}\{A_{ij}\}$, where

$$A_{ij} = \frac{g^2}{\tilde{v}_g(\delta)} e^{iK|x_i - x_j|}, \tag{3.43}$$

and

$$K = \pi - \arccos\left[\frac{\delta + i\gamma_c/2}{2J}\right]. \tag{3.44}$$

Here we have introduced a generalized (complex) group velocity

$$\tilde{v}_g(\delta) = \sqrt{4J^2 - \left(\delta + i\frac{\gamma_c}{2}\right)^2}. \tag{3.45}$$

For $\gamma_c \to 0$ and for atomic frequencies within the photonic band this quantity reduces to the conventional group velocity given in Eq. (3.40). In this case $\sim 1/|v_g(\delta)|$

determines the density of photonic modes, or equivalently, the correlation time of the waveguide. In a system with losses this correlation time is now replaced by $1/|\tilde{v}_{\rm g}(\delta)|$, which is well-defined and non-diverging even at or beyond the band edges (for a related study of the group velocity in lossy waveguides see also Ref. [157]). Therefore, the Born-Markov approximation, which requires

$$g \ll |\tilde{v}_{\rm g}(\delta)|, \tag{3.46}$$

can be used for all atomic frequencies provided that the coupling g is sufficiently weak and photon propagation times are negligible [see App. A.1 for additional details on the validity of the Born-Markov approximation].

Figure 3.7(c)-(d) illustrates the dependence of Γ_{ij} and U_{ij} on the interatomic distance for different atom-photon detunings, δ, and a non-vanishing photon loss rate γ_c. If instead cavity losses are negligible, Eqs. (3.42)-(3.44) reproduces the same results for two-level atoms coupled to an infinite-bandwidth waveguide discussed in Sec. 2.2.1. In particular for frequencies within the propagating band, K is purely real and the dipole-dipole interactions become infinite in range, with a phase factor $e^{iK|x_i-x_j|}$ that reflects the propagation phase of photons at the atomic resonance frequency that mediate the interaction. This behaviour can be seen in Fig. 3.7(c)-(d) for $\delta = 0$ (blue curve), with the deviation from infinite-range interaction due to the finite cavity losses γ_c. As expected, by going from the center of the band towards the edge, $\delta \approx 2J$ (red curve), both the coherent couplings as well as the correlated decay rates increase due to a reduction of the group velocity. However, slow propagation also means that the photons have more time to decay and for a finite γ_c and large atom-atom distances, there is a trade-off between an enhanced coupling and a larger propagation loss. For atomic frequencies outside the band there are no longer waveguide modes into which the atom can emit. Therefore, for $\gamma_c \to 0$, the real part of A_{ij} vanishes and the atoms interact predominantly in a coherent way via a virtual exchange of photons. The exponential decay of interactions directly reflects the exponential attenuation of fields propagating through a band gap (see green curve of Fig. 3.7 (c)-(d)). This is the regime where the atom-atom interactions are mediated by the atom-photon bound states as discussed in Sec. 3.1.4 in the context of photonic crystal waveguides.

In summary, Eq. (3.41) shows that for sufficiently weak couplings the dynamics of the waveguide QED system can be described in terms of atomic excitations, which interact via a quasi-instantaneous exchange of photons. In this regime it is preferential to work near the band edge or to reduce the waveguide bandwidth all together in order to enhance waveguide mediated atom-atom interactions (coherent or dissipative) compared to the bare atomic decay. However, eventually the Markov condition given by Eq. (3.46) breaks down and for larger couplings the photons emitted by an atom can be coherently reabsorbed before they decay or propagate along the fiber. In this strong coupling regime photons and atoms can be bound together and form atom-photon bound states that will be discussed in chapter 4.

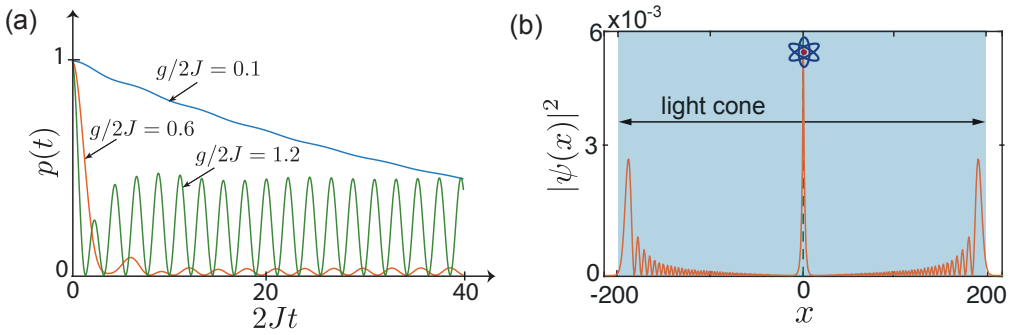

Figure 3.7: (a) Atomic population as function of time for different values of the coupling strength. Here we assumed $\delta = 0$. (b) Photonic wave function emitted by the atom for $g/2J = 0.6$ and $\delta = 0$.

Single-photon dynamics

To have a first idea about the physics beyond the Markov approximation is instructive to consider the simple case of the spontaneous emission of a single TLA in a CCA. This problem can be exactly solved in the same way as we did in section 3.1.2, but here we will just focus just on describing the overall behaviour. A detailed discussion of the exact analytic solution of this problem can be found in Ref. [60].

Compare to the cases analysed so far here the coupling strength plays a crucial role. Increasing the coupling has consequences not only on the decay rate, but also allows the atom to "see" all the band modes, which strongly modifies its spontaneous emission.

To visualize the process we plotted in Fig. 3.7(a)(b) the atomic population as function of time for different coupling strengths. We identify the following regimes.

- For low coupling values $g \ll J$ and atomic frequency in the band the emitter does not feel the finiteness of the band and the atom excitation exhibits a purely exponential decay as shown in Fig. 3.7(a). Note that in this limit, if the atomic frequency is tuned to one of the band edges, the CCA is equivalent to a photonic crystal waveguide and the usual fractional decay is observed.

- When the coupling is increased, secondary oscillations start to arise but still, as long the ratio $g/2J$ is not too large, the majority of the excitation still gets emitted into propagating modes.

- For coupling comparable to the photon bandwidth $g \sim 2J$ the oscillatory behaviour becomes dominant and a big amount of the excitation remains trapped or long times. This behaviour is even more clearly shown in 3.7(b) where a considerable part of the emitted photonic wave function remains localized around the atom. The physical explanation of this effect relies on the atom-field bound states that will be extensively discussed in the next chapter.

- We finally note that in the limit of $g \gg J$ the atom effectively feels just a single mode and the usual Jaynes-Cumming model with Rabi oscillation is recovered.

Chapter 4

Atom-field dressed states in slow-light waveguide QED

In the last chapter we introduced the coupled cavity array as a simple and elegant model which is able to capture, in different parameter regimes, the physics of single-cavities, infinite-bandwidth waveguides and photonic crystals. In a CCA, similar to a photonic crystal, an important role on the system dynamics is played by the atom-photon bound states that emerge in the moderate and strong coupling regime as the the elementary excitations of the system. These states can be written as a continuum generalization of the dressed-states of the Jaynes-Cummings model for a single cavity.

In this chapter we go beyond the single-atom and single-photon configuration by extending the discussion to the multi-photon and multi-atom cases. In particular, we introduce a variational ansatz to characterize the multi-photon dressed states and we discuss their spectral features. For these states, we identify the crossover from a linear regime, where the bound state energies are proportional to the number of excitations, N_e, to a nonlinear regime where the splitting of the bound-state energies from the photonic band scales like $\sim \sqrt{N_e}$.

In the last part of the chapter, we show how the usual long-range dipole-dipole interactions between multiple atoms coupled to broadband waveguides are modified in the presence of bound photonic states. Here we observe the formation of meta-bandstructures for delocalized dressed states as well as a partial "melting" of these bands back into the continuum, when specific coupling conditions are met.

All the results presented in this chapter have been obtained in collaboration with Francesco Ciccarello, Darrick Chang and Peter Rabl and were published in Physical Review A 93, 033833 (2016). In this work I contributed as a leading author and performed all the analytic and numerical calculations under the supervision of Peter Rabl.

4.1 Atom-photon bound states

Let us consider the model given in Eq. (3.38). In the absence of other decay channels, the atom-light coupling conserves the total number of excitations, $N_e = \sum_x a_x^\dagger a_x + \sum_i |e\rangle_i\langle e_i|$, and the eigenstates of H can be discussed separately within each subspace of given excitation number. For a given value N_e, the Schrödinger equation $H|\phi\rangle = E|\phi\rangle$ then has two types of solutions. First, there are scattering states, which are spatially extended over the whole waveguide and have an energy $E/N_e \in [-2J, 2J]$ within the free N_e-photon band. Second, there are states with energy $|E|/N_e > 2J$. These states are energetically separated from the N_e-photon continuum and represent bound states with an exponentially localized photonic component. While both types of states are atom-photon dressed states, here we are primarily interested in the latter type, namely in *bound* dressed states. Note that these bound states exist also in photonic crystal waveguides, as discussed in Sec. 3.1.3. The main difference here is that in a narrow bandwidth setup these states can be highly hybridized and have a small localization length of the photonic cloud. This gives rise to new interesting effects such as multi-photon bound states and interactions among the dressed states that will be discussed respectively in Sec. 4.2 and Sec. 4.3.

In this section we will concentrate on the case of a single atom in the single-excitation sector. We will first derive the expression of the single-photon bound state and we will discuss its main properties. Then, we will discuss a more realistic implementation taking into account the effect that dissipation has on these states by presenting the excitation spectrum and deriving the minimal conditions on the parameters to spectroscopically distinguish these states. Finally, we will make some estimates about the impact of disorder on these states.

Note that these single photon bound states were experimentally observed for the first time few months after we published this work. The results, obtained in an array of microwave resonators coupled to a transmon qubit, can be found in [139].

4.1.1 Single photon bound states

Let us first consider the simple case of a single photon, N_e=1, coupled to a single atom located at position x_a. In order to find the eigenstates we need to solve the stationary Schrödinger equation $H|\phi\rangle = E|\phi\rangle$. The solutions of this problem can be found both in the position and momentum space. Let us use the latter approach by rewriting Hamiltonian (3.38) in k space as (in a frame rotating with frequency ω_c)

$$H = -2J\sum_k \cos(k) a_k^\dagger a_k + \delta|e\rangle\langle e| + \frac{g}{\sqrt{N}}\sum_k \left(a_k^\dagger \sigma_- e^{ikx_a} + a_k \sigma_+ e^{-ikx_a}\right). \tag{4.1}$$

In the single-excitation sector a generic state can be written as a superposition of an atomic excitation $|e,0\rangle$ and a single photon states $|g,1_x\rangle \equiv a_x^\dagger|g,0\rangle$:

$$|\phi\rangle = \left(b\,\sigma_+ + \sum_k c_k a_k^\dagger\right)|g,0\rangle\,. \tag{4.2}$$

Plugging this ansatz into the stationary Schrödinger equation yields the coupled equations

$$\begin{aligned} b(E-\delta) &= \frac{g}{\sqrt{N}}\sum_k c_k\, e^{-ikx_a}, \\ c_k(E+2J\cos k) &= \frac{g}{\sqrt{N}}\, b\, e^{ikx_a}. \end{aligned} \tag{4.3}$$

Using the second equation to eliminate c_k in the first one, we end up with the eigenvalue equation

$$E-\delta = \Sigma_1(E)\,, \tag{4.4}$$

where the self-energy $\Sigma_1(E)$ (in the continuum limit) is given by

$$\Sigma_1(E) = \frac{1}{2\pi}\int_{-\pi}^{\pi} dk\, \frac{g^2}{E+2J\cos k} = \frac{g^2}{E\sqrt{1-\frac{4J^2}{E^2}}}\,, \tag{4.5}$$

where in the last identity we calculated the integral explicitly using that $|E| > 2J$ [158]. Replacing the self-energy in Eq. (4.4) we end up with the following expression:

$$E-\delta = \frac{g^2}{E\sqrt{1-\frac{4J^2}{E^2}}}\ . \tag{4.6}$$

This equation has two real solutions $E_\pm$, where E_+ (E_-) lies above (below) the continuum of scattering states $E \in [-2J, 2J]$. Figure 4.1(a) shows the resulting energy spectrum as function of the coupling strength. The corresponding bound states can be worked out with the help of Eq. (4.3) as

$$|\phi_\pm\rangle = b(E_\pm)\left[\sigma_+ + \frac{1}{\sqrt{N}}\sum_k \frac{g e^{ikx_a}}{E_\pm + 2J\cos k} a_k^\dagger\right]|g,0\rangle, \tag{4.7}$$

where, using that the state must be normalized,

$$b(E) = \left(1 + \frac{g^2}{E^2\left(1-\frac{4J^2}{E^2}\right)^{\frac{3}{2}}}\right)^{-\frac{1}{2}}. \tag{4.8}$$

By going back in the real space, the bound state can be rewritten as

$$|\phi_\pm\rangle = b(E_\pm)\left[\sigma_+ + \frac{g\sum_x (\mp 1)^{|x-x_a|} e^{-\frac{|x-x_a|}{\lambda}} a_x^\dagger}{E_\pm\sqrt{1-\frac{4J^2}{E_\pm^2}}}\right]|g,0\rangle, \tag{4.9}$$

where the parameter $\lambda_\pm = \lambda(E_\pm)$ is a function of the corresponding bound state energies and is given by:

$$\frac{1}{\lambda} = \operatorname{arccosh}\left(\frac{|E|}{2J}\right). \tag{4.10}$$

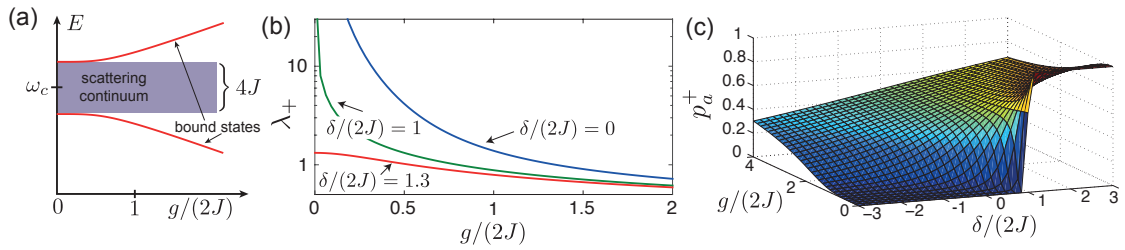

Figure 4.1: (a) Single-photon (i.e., single-excitation) spectrum as a function of the atom-photon coupling g in the case of a single atom (with $\omega_a = \omega_c$) coupled to a cavity array according to Hamiltonian (3.38). (b) The width of the photonic wavepacket in the upper bound state, λ_+, is plotted as a function of g and for three different detunings δ. (c) Atomic population $p_a^+ = \cos^2(\theta_+)$ in the upper bound state as function of the coupling constant g and the atom-field detuning δ.

We see that the bound states show an exponential localization of the photons around the atomic position with a localization length given by $\lambda_\pm$. In order to make a direct connection with the cavity QED formalism we can define the normalized bosonic creation operator

$$a^\dagger_{\lambda,\pm}(x_a) = \sum_x \frac{(\mp 1)^{|x-x_a|} e^{-\frac{|x-x_a|}{\lambda_\pm}}}{\sqrt{\coth\frac{1}{\lambda_\pm}}} a^\dagger_x, \tag{4.11}$$

which creates a photon in the localized wavepacket around the atom. This allows us to rewrite the bound states in the form

$$|\phi_\pm\rangle = \left[\cos\theta_\pm \sigma_+ \pm \sin\theta_\pm a^\dagger_{\lambda,\pm}(x_a)\right]|g,0\rangle \equiv D^\dagger_\pm(x_a)|g,0\rangle, \tag{4.12}$$

where we introduced the mixing angles:

$$\cos\theta = \left(1 + \frac{g^2}{E^2\left(1-\frac{4J^2}{E^2}\right)^{\frac{3}{2}}}\right)^{-\frac{1}{2}}. \tag{4.13}$$

The form used in Eqs. (4.12) to rewrite the bound states has the advantage of establishing a direct connection to the more familiar dressed states of a single mode cavity model [3][see Sec 1.3]. Indeed, in the limit of single cavity, $J \to 0$, the bound states energies approach the value of the Jaynes-Cumming model given in (1.21), i.e. $E_\pm = \frac{\delta}{2} \pm \frac{1}{2}\sqrt{\delta^2 + 4g^2}$. Moreover the extended photonic cloud reduces to a single cavity mode $\lambda_\pm \approx 0$ [see Fig.4.1 (b)] and the dressed states become fully hybridized $\theta_+ = \theta_- - \pi/2$ [see Fig.4.1 (c)]. On the other hand Eqs. (4.6)-(4.10) also reproduce various results that we have been previously presented for photonic bound states near band edges or in coupled cavity arrays [41, 42, 46, 57, 59, 151, 156, 60, 62][see Chap. 3]. The nice aspect of the form of the wavefunction given in Eq. (4.12) is that

provides a unified description of all those cases in terms of the mixing angles $\theta_\pm$ and the wavepacket lengths $\lambda_\pm$.

For a finite and large J the single-cavity picture is modified in different ways depending on whether the atomic frequency lies inside or outside of the band.

- For atomic frequencies inside the band the photonic component is extended over multiple sites and becomes more and more delocalized the weaker the coupling g gets [see Fig. 4.1 (b)]. This delocalization of the bound states is associated to a progressive decreasing of the total atomic contribution of both bound states, $\cos^2(\theta_+) + \cos^2(\theta_-) < 1$. This quantity is indeed always smaller than one and for $|\delta| < 2J$ it vanishes as $g/J \to 0$ [see Fig. 4.1 (c)]. In this limit the bound state energies get really close to the band edge [see Fig. 4.1(a)] and, although a bound state solution always exists, both dressed states become more photon-like as g/J decreases and eventually become indistinguishable from the propagating waveguide modes. This regime approaches exactly the broadband waveguide limit [see Sec. 3.2.2] where the bound states do not play any role in the dynamics that is instead entirely ruled by the scattering states.

- For atomic frequencies outside the band, e.g., $\delta > 2J$, the upper bound state becomes more atom-like as $g/J \to 0$, but the residual photonic cloud remains localized. This is the limit where the system is equivalent to a photonic crystal waveguide [see Sec. 3.1.3] where the photonic component of the bound states can be adiabatically eliminated and can eventually enable virtual photon mediated atom-atom interactions.

- When the coupling strength and the bandwidth are comparable, $g \sim J$, the CCA really differs from the systems discussed so far. In this limit the bound states are extended over more than a lattice sites but, compared to the photonic crystal case, a strong hybridization between atomic and photonic states can be achieved with a localization length that entirely lie inside the waveguide. This means that the system have interesting non-linear features, typical of cavity QED systems, in an extended setup where such non-linearities could be probed by propagating waves.

We finally notice that the simplified model described in section 3.1.4 [49], where the waveguide is replaced by an effective cavity of size λ, is incomplete. In particular, such a description misses the fact that for $\delta \neq 0$ photonic wavefunctions associated with the two dressed states can significantly differ, i.e., $\lambda_+ \neq \lambda_-$ and $\theta_+ \neq \theta_-$.

4.1.2 Effect of dissipation: excitation spectrum and strong coupling conditions

In the last section we derived the atom-photon bound states in the absence of dissipation. In realistic implementations additional decay channels should be taken into account and could affect the spectral properties and even the existence of the bound

states. In this context, an experimentally relevant quantity to probe the properties of atom-photon bound states in presence of dissipation is the atomic excitation spectrum $S_a(\omega)$. It can be obtained by weakly exciting the atom with a laser of frequency ω and recording the total emitted light. In the weak driving limit the excitation spectrum is given by

$$S_a(\omega) = \frac{\gamma_a^2}{4}\left|\langle e,0|\frac{1}{H_{\text{eff}}-\omega\mathbb{1}}|e,0\rangle\right|^2, \tag{4.14}$$

where

$$H_{\text{eff}} = H - i\frac{\gamma_a}{2}|e\rangle\langle e| - i\sum_x \frac{\gamma_c}{2}a_x^\dagger a_x, \tag{4.15}$$

and the normalization has been set such that $S(\omega=\omega_a)=1$ for $g=0$. Figure 4.2

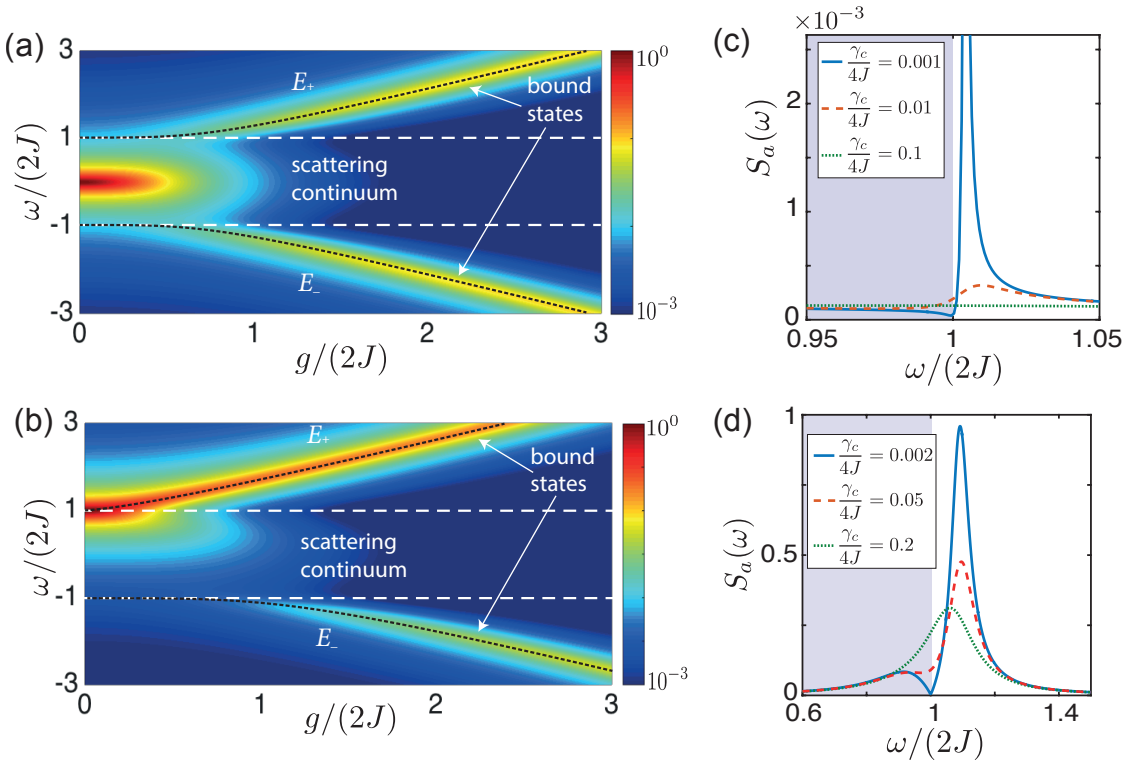

Figure 4.2: (a)-(b) Atomic excitation spectrum $S_a(\omega)$ (in logarithmic scale) as function of g and for an atom-cavity detuning (a) $\delta = 0$ and (b) $\delta = 2J$. The dotted lines show the bound-state energies $E_\pm$ in the absence of loss, while the dashed lines correspond to the waveguide band edges. In either case, we have set $\gamma_a/(2J) = 0.1$ and $\gamma_c/(2J) = 0.2$. (c)-(d) Dependence of the atomic excitation spectrum $S_a(\omega)$ near the band edge and for (c) $\delta = 0$ and (d) $\delta = 2J$. In (c) the values $g/(2J) = 0.3$ and $\gamma_a/(4J) = 0.02$ and in (b) the values $g/(2J) = 0.2$ and $\gamma_a/(4J) = 0.05$ have been assumed and in both cases the spectrum is plotted for different cavity decay rates γ_c.

shows the results for $S_a(\omega)$ for different coupling strengths g and for the two relevant

cases $\delta = 0$ (center of the band) and $\delta = 2J$ (upper-band edge). For $\delta = 0$ we observe three different regimes.

- For very weak couplings there is only a single peak at the atomic frequency with a width $\sim \gamma_a + 2g^2/J$ due to the enhanced emission into the waveguide (recall that in the broadband limit the atom emission rate into the waveguide is $2g^2/J$ [see Section 3.2.2].
- At intermediate couplings $g/(2J) \sim 1$ the spectrum is completely smeared out. The atom is now partially hybridized with all the waveguide modes and there is no longer a well defined frequency associated with the atomic excitation.
- At larger couplings two dominant resonances at the dressed-state energies $E_\pm$ appear. As the coupling increases the width of the two bound-state resonances approaches
$$\bar{\gamma} = \frac{\gamma_a + \gamma_c}{2}, \tag{4.16}$$
as expected from an equal superposition of atomic and photonic excitations.

For $\delta = 2J$ a significant hybridization between atom and photon is already observed at small g, consistent with the atomic population $p_a^+ \approx 0.67$ predicted for the dressed state exactly at the band edge [see Sec. 3.1.2]. However, in this case the transition from waveguide-enhanced decay to atom-photon hybridization is not so clear and requires a more detailed discussion.

To clarify this point and, more generally, to understand better how dissipation affects the bound-state physics it is useful to identify the "strong coupling" conditions for this slow-light waveguide system. In cavity QED the "strong coupling" regime, where the coherent interaction between atoms and photons dominates over the relevant decay processes, is achieved when

$$g > \frac{\gamma_a + \gamma_c}{4}, \tag{4.17}$$

as we discussed in 1.3.1 [note that here we also added the atomic dissipation]. Our goal is now to identify an equivalent condition for the waveguide QED system, by taking a closer look at the spectral features for $g \ll J$. The atomic excitation spectrum (4.14) can be explicitly written as [43, 154]

$$S_a(\omega) = \frac{\gamma_a^2}{4} \frac{1}{\left|\omega - \delta + i\frac{\gamma_a}{2} - \tilde{\Sigma}(\omega)\right|^2}, \tag{4.18}$$

where $\tilde{\Sigma}(\omega) = -ig^2/\tilde{v}_g(\omega)$ is the self energy in the presence of dissipation. To bring this result into a more useful form we define

$$\Delta_\pm(\omega) = \left(\omega - \delta + i\frac{\gamma_a}{2}\right)\tilde{v}_g(\omega) \pm ig^2. \tag{4.19}$$

The product $\Delta_+(\omega)\Delta_-(\omega)$ is a forth order polynomial in ω with two roots given by the complex eigenenergies $\tilde{E}_\pm$ of H_{eff}. We can use this property to further rewrite the spectrum as

$$S_a(\omega) = \frac{\gamma_a^2}{4} \frac{|\tilde{v}_g(\omega)\Delta_-(\omega)|^2}{|(\omega - \tilde{E}_+)(\omega - \tilde{E}_-)L(\omega)|^2}. \tag{4.20}$$

Here $L(\omega)$ is a quadratic polynomial, which for the limits discussed below has two roots with real parts inside the photonic band, and thus describes the atomic emission into the waveguide continuum. Overall the structure of the spectrum consists of two external poles with a position and a width given by the real and imaginary parts of $\tilde{E}_\pm$ and a broader emission peak inside the band. Note that for $\gamma_c \to 0$ the generalized group velocity, $\tilde{v}_g(\omega)$, and therefore also the spectrum vanishes exactly at the bandedge, $\omega = \pm 2J$. This is due to a destructive interference between the excitation laser and the long-lived band-edge mode and leads to a Fano-like profile for $S_a(\omega)$. For non-vanishing γ_c this interference effect is washed out.

We first consider the case $\delta = 0$, where we obtain to lowest order in g

$$\tilde{E}_\pm \simeq \pm 2J \pm \frac{g^4}{16J^3[1 \pm i(\gamma_a - \gamma_c)/(2J)]} - i\frac{\gamma_c}{2}, \tag{4.21}$$

which shows that for not too large decay rates, the position of the external peaks essentially follows the bare energy levels $E_\pm$ and their width is mainly determined by photon loss. For the polynomial determining the internal peaks we obtain

$$L(\omega) = \left(\omega + i\frac{\gamma_a}{2}\right)^2 + \left(\frac{g^2}{2J}\right)^2, \tag{4.22}$$

which therefore contributes with two purely imaginary poles at $\omega = -i(\gamma_a \pm g^2/J)/2$. Figure 4.2 (c) shows a zoom-in on the resulting spectrum near the band edge and for different values of γ_c. First, we observe that for large γ_c the external peak is completely buried within the tail of the broad internal peak and a closer inspection shows that a minimal coupling of

$$g > \sqrt{J\gamma_c}, \tag{4.23}$$

is required to spectrally resolve the existence of an external bound state. This condition is equivalent to the requirement that the atomic emission rate into the waveguide exceeds the cavity loss rate. Once this condition is fulfilled we can define strong coupling by the requirement that the separation of the external peak from the band edge, $\text{Re}\{\tilde{E}_+ - 2J\}$, exceeds its half-width given by $\text{Im}\{\tilde{E}_+\}$. Again for $\gamma_c, \gamma_a \ll 2J$ we obtain

$$g > \sqrt[4]{8J^3\gamma_c}, \tag{4.24}$$

as the strong coupling condition for a resonantly coupled waveguide QED system. Note that since in the present regime the bound states are mainly photonic in nature the atomic decay is relevant only for higher-order corrections.

The second important limit is $\delta = 2J$, which for $g/J \ll 1$ corresponds to the quadratic dispersion relation assumed for photonic bound states near the band edge of a photonic crystal waveguide described in chapter 3. Note that in this regime the initial scaling of the bound state energy in the absence of losses ($\gamma_a = \gamma_c = 0$) is given by

$$E_+ \simeq 2J + \left(\frac{g^4}{4J}\right)^{\frac{1}{3}}, \tag{4.25}$$

where the splitting $\beta = \sqrt[3]{g^4/(4J)}$ can be directly identified with the beta factor introduced in section 3.1.2. In the presence of decay and for $g < |\gamma_c - \gamma_a|$ we obtain the modified result

$$\tilde{E}_+ \simeq 2J - i\frac{\gamma_a}{2} + \frac{g^2}{2\sqrt{J|\gamma_c - \gamma_a|}}(1 \mp i), \tag{4.26}$$

where the minus (plus) sign is for the case $\gamma_c > \gamma_a$ ($\gamma_c < \gamma_a$). This result shows that the effect of the dissipation is not only restricted to a modification of the initial scaling of the bound state energy. Indeed Eq. (4.26) also predicts that at the band edge and for small g the atom is critically damped, i.e., the coupling induced losses are exactly of the same magnitude as the coherent shift of the bound state energy. By increasing the coupling further the imaginary part of the eigenvalue $\tilde{E}_+$ will eventually saturate at a value $\bar{\gamma}/2$ [see Eq. 4.16] corresponding to a fully hybridized state. This hybridized regime is reached for coupling strengths

$$g > \sqrt[4]{\frac{J|\gamma_c - \gamma_a|^3}{4}}. \tag{4.27}$$

Under this condition the separation of the bound-state from the bandedge is then given by β from which we obtain the strong coupling condition $\beta > \bar{\gamma}/2$, or

$$g > \sqrt[4]{J\bar{\gamma}^3/2}. \tag{4.28}$$

Figure 4.2 (d) shows a zoom-in of the atomic spectrum $S_a(\omega)$ for $\delta = 2J$ and for three different values of the photon decay, which correspond to the critically damped, intermediate and strong coupling regime. Note that for $\delta = 2J$ the internal poles associated with $L(\omega)$, i.e., $\omega_1 = 2J - i\frac{\gamma_c}{2}$ and $\omega_2 = 2J - i\frac{\gamma_a}{2} - g^2(1 \mp i)/(2\sqrt{J|\gamma_c - \gamma_a|})$ provide an additional background, but do not play a significant role.

In conclusion we underline that in this work we are mainly interested in coherent effects and from now on for the sake of clarity we will only present results for idealized systems where $\gamma_a = \gamma_c = 0$. Therefore, the validity of these results in particular requires that the strong-coupling conditions identified in Eqs. (4.23), (4.24), (4.27) and (4.28) are fulfilled in the respective limits.

4.1.3 Disorder induced localization

All the results discussed for this project are based on the model of a perfectly regular cavity array. In real systems disorder in the cavity frequencies or tunnel

couplings introduces an additional localization mechanism, even in the absence of the emitters. Here we do not want to extensively treat this topic and for a more accurate treatment of localization in waveguides we refer the reader to Ref. [159, 160] and the supplementary material of [49].

Nevertheless, we can still make a rough estimate to identify a minimal requirement for the maximum disorder that can be tolerated in order to observe the bound-state physics. Let us consider a simple impurity model, where we add an energy offset ϵ to one of the lattice sites, $H_c \to H_c + \epsilon a_{x_d}^\dagger a_{x_d}$. This model is well known in literature [158] and it exhibits a purely photonic bound state with a localization length given by

$$\frac{1}{\lambda_\ell} = \operatorname{arcsinh}\left(\frac{|\epsilon|}{2J}\right). \tag{4.29}$$

This means that random energy offsets of typical strength ϵ will create bound states that are localized over $\lambda_\ell \sim 2J/|\epsilon|$ lattices sites. While atom-photon bound states will also exist in such disordered waveguides, in order to still be able to distinguish them from the disorder induced localization we will assume in this project that λ_ℓ is large compared to the size of the atom-induced bound states, $\lambda_\pm$.

4.2 Multi-photon bound states

In Sec. 1.3.1 we discussed how the quantum nature of cavity QED systems arises when more than a single excitation is considered. Indeed, when a TLA atom is coupled to a single cavity mode, the mode splitting presents a non-linear scaling with the number of excitations, $\sim g\sqrt{N_e}$, that allows to generate highly non-classical photon states. The question that we want to address in this section is, if this non-linear features of the spectrum persist in the context of slow-light waveguides where both cavity and waveguide QED aspects must be considered. In contrast to the single excitation case, the Schrödinger equation for $N_e > 1$ no longer permits explicit analytic solutions [61] and for exact results one is restricted to numerical methods in real or momentum space [58, 59, 151, 154]. In this chapter we perform such calculations by an approximate variational approach, which provides additional intuition on the nature of the multi-photon dressed states. This allows us to evaluate the corresponding bound-state energies for excitation numbers that are no longer trackable by standard numerical methods. With this approach then we discuss and quantify the non-linear properties of the spectrum that still persist in the extended waveguide system.

4.2.1 Two-photon dressed states

Let us first evaluate the spectrum in the simplest case of the two-excitation subspace. A general eigenfunction of Hamiltonian (3.38) can be written in the form

$$|\phi\rangle = \sum_x b(x) a_x^\dagger |e,0\rangle + \frac{1}{\sqrt{2}} \sum_{x,y} u(x,y) a_x^\dagger a_y^\dagger |g,0\rangle. \tag{4.30}$$

By assuming that the atom is located at $x_a = 0$ the inversion symmetry of the Hamiltonian and the bosonic symmetry of the wavefunction require $u(x,y) = u(y,x)$, $u(-x,y) = u(x,y)$ and $b(-x) = b(x)$. Applying the stationary Schrödinger equation to this ansatz we get the set of coupled equations

$$-J\left[u(x+1,y)+u(x-1,y)+u(x,y+1)+u(x,y-1)\right]+\frac{g}{\sqrt{2}}\left[b(x)\delta_{0,y}+b(y)\delta_{0,x}\right]=Eu(x,y), \tag{4.31}$$

and

$$-J\left[b(x+1)+b(x-1)\right]+\frac{g}{\sqrt{2}}\left[u(0,x)+u(x,0)\right]=Eb(x)\,. \tag{4.32}$$

These equations can be considered as the discrete extension of the continuous waveguide expressions in the 2-excitation subspace given in [7]. They can be solved numerically and the resulting eigenvalue spectrum is shown in Fig. 4.3 together with the single excitation energy band discussed in Sec. 4.1.1. For our numerical calculations an array of $N = 120$ coupled resonators with periodic boundary conditions has been assumed. We can identify three different classes of states.

- In line with the single-excitation case there is a band of two-photon scattering states with energies $E \in [-4J, 4J]$. As before these states are extended in nature and they are associate to propagating photons.
- In addition, there are two bands with energies $E \in [E_\pm - 2J, E_\pm + 2J]$. These bands can be simply interpreted as the combination of a single-atom bound state with energy $E_\pm$ and an additional free photon with energy ω_k. In this configuration one photon remains localized around the atom while the other propagates in the waveguide.
- Finally, we observe two isolated lines at energies $E_\pm^{(N_e=2)}$ above and below all other states. These discrete energy levels represent the true two-photon bound states in the $N_e = 2$ sector. It is possible to show both numerically and analytically [61] that in general multi-photon bound states always exists in 1 and 2 dimensions for gapped system with quadratic or cosine-like dispersion relation. In three dimensions instead their existence is limited to specific parameters regimes.

Before proceeding with a more detailed discussion on the two-photon bound states, let us briefly point out another interesting feature of Fig. 4.3, namely the overlap region between the continuum of states with a single bound photon (shaded in green) and the two-photon continuum (shaded in purple). In this region, which extends up to a coupling strength of about $g/(2J) \simeq 3$ scattering processes of the form

$$|2_{\text{in}}\rangle \leftrightarrow |1_{\text{out}}\rangle|1_{\text{bound}}\rangle, \tag{4.33}$$

are energetically allowed, meaning in particular that scattering processes where two incoming photons evolve into a bound photon and an outgoing one are allowed.

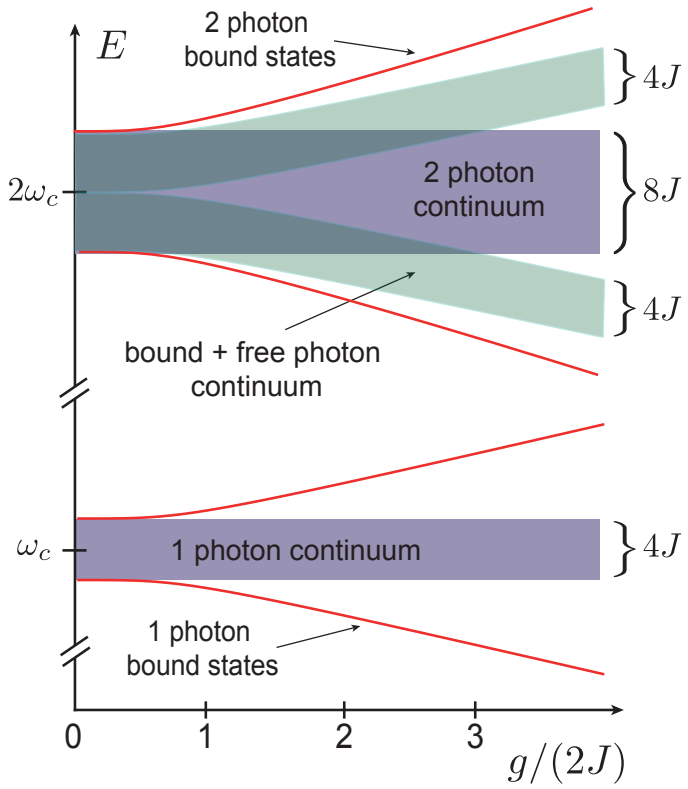

Figure 4.3: Sketch of the single- and two-excitation spectrum in a finite-bandwidth waveguide coupled to an atom for $\delta = 0$.

Such processes have previously been observed in numerical studies [58, 59, 151] and further investigated in Refs. [154, 155]. The energy level diagram shown in Fig. 4.3 provides simple energetic arguments to determine under which conditions such processes can occur.

Finally, we note that all the qualitative considerations made so far can be extended to the N_e-excitation subspace. For example the $N_e = 3$ band structure consists of three-photon continuum of width $12J$, two bands of one bound and two free photons of width $8J$, two bands with two bound and one free photons of width $4J$ and two true three-photon bound states, and so on. Therefore, the complete energy spectrum of a single atom waveguide QED system can be constructed from the knowledge of the N_e-photon bound states energies $E_{\pm}^{(N_e)}$.

4.2.2 Variational ansatz

While the exact eigenstates can be still found numerically in the $N_e = 2$ excitation subspace, solving the problem for excitation subspaces higher than $N_e \geq 4$ can be challenging even with modern numerics technique such as matrix product states

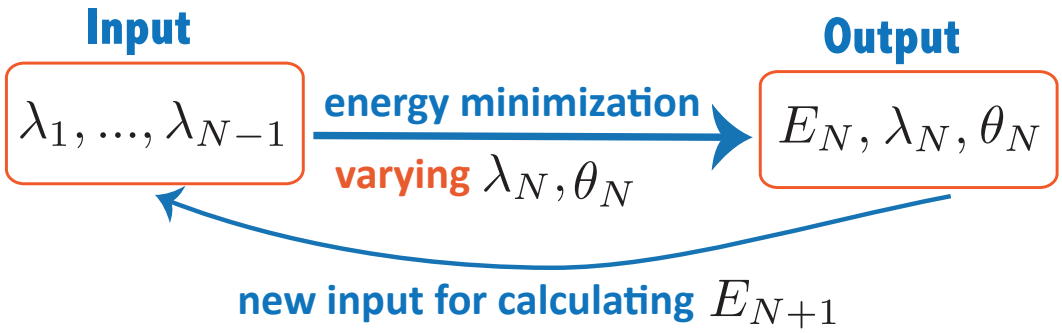

Figure 4.4: Sketch of the variational asnatz protocol to find the multi-photon bound states.

(MPS) [61]. To tackle this problem here we present a variational approach that allows us to estimate the bound states energies for arbitrary excitation subspaces. Note that a different and more complex ansatz to solve the same problem has been proposed in [61]. The advantage of our approach relies on its effectiveness and simplicity and provides an additional intuition about the nature of multi-photon bound states.

To explain the method let us first consider the two excitation case. Within this subspace the lower energy two-photon bound state corresponds to the ground state and this allows us to use a variational approach. The state can be generically written as

$$|\Psi_-^{(2)}\rangle = \left(\cos(\theta)\sigma_+ A_1^\dagger - \sin(\theta) B_2^\dagger\right)|g,0\rangle, \tag{4.34}$$

where A_1 and B_2 are single and two-photon operators, respectively. Based on the discussion in Sec. 4.2.1 a suitable ansatz for the two-photon state is

$$B_2^\dagger = \frac{1}{\mathcal{N}_u}\tilde{a}_{\lambda_1}^\dagger \tilde{a}_{\lambda_2}^\dagger, \tag{4.35}$$

where $\tilde{a}_\lambda = \sum_x e^{-\frac{|x|}{\lambda}} a_x^\dagger$ and the normalization constant $\mathcal{N}_u$ is chosen such that $\langle 0|B_2 B_2^\dagger|0\rangle = 1$. Note that this trial is equivalent to a Bethe-like ansatz having the 2-photon wavefunction of the form:

$$u(x,y) \propto \left(e^{-\frac{|x|}{\lambda_1}-\frac{|y|}{\lambda_2}} + e^{-\frac{|x|}{\lambda_2}-\frac{|y|}{\lambda_1}}\right). \tag{4.36}$$

This two-photon wavepacket is an exact solution of the Schrödinger equation for $x, y \neq 0$ with an energy

$$E_-^{(2)} = -2J\cosh(1/\lambda_1) - 2J\cosh(1/\lambda_2). \tag{4.37}$$

For the single-photon operator we demand that the wavefunction also satisfies the first boundary condition, Eq. (4.31), at $x = 0$ and $y \neq 0$. This leads to

$$A_1^\dagger = \frac{1}{\mathcal{N}_b}\left[\sinh\left(\frac{1}{\lambda_2}\right)\tilde{a}_{\lambda_1}^\dagger + \sinh\left(\frac{1}{\lambda_1}\right)\tilde{a}_{\lambda_2}^\dagger\right], \tag{4.38}$$

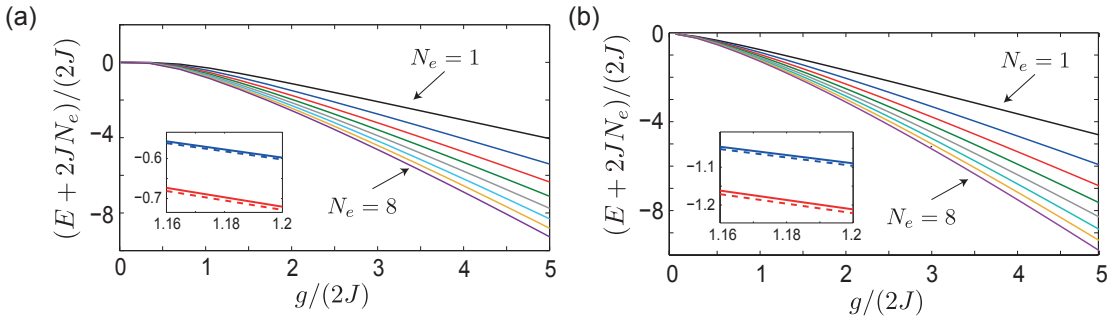

Figure 4.5: The N_e-photon bound-state energies $E_-^{(N_e)}$ obtained from a variational approach are plotted for $N_e = 1, \ldots, 8$ in descending order and for (b) $\delta = 0$ and (c) $\delta = -2J$. The dashed lines in the insets show the exact numerical results for $N_e = 2$ and $N_e = 3$.

where $\mathcal{N}_b$ is again a normalization constant. By using this ansatz we can now find an upper bound for the two-photon bound state by minimizing $E_{\rm var} = \langle \Psi_-^{(2)}|H|\Psi_-^{(2)}\rangle$ with respect to θ and $\lambda_{1,2}$. To further reduce the parameter space, it is reasonable to assume that the wavepacket size of the first photon, λ_1, is approximately given by the value of λ_-, which we determined for the single-photon bound state in Sec. 4.1.1. The variational ansatz is then based on the physical picture of a two-photon dressed state consisting of the single-photon dressed state plus an additional photon, which is more weakly bound and thus less localized, $\lambda_2 > \lambda_1$.

An important aspect of our variational wavefunction approach is that it can be extended to higher excitation numbers N_e in a systematic way. To do so we write the wavefunction for the lowest energy state within the N_e-excitation subspace as

$$|\Psi_-^{(N_e)}\rangle = \left(\cos(\theta)\sigma_+ A_{N_e-1}^\dagger - \sin(\theta)B_{N_e}^\dagger\right)|g,0\rangle. \tag{4.39}$$

Based on analogous arguments as above, we make the ansatz

$$B_{N_e}^\dagger = \frac{1}{\mathcal{N}_u}\tilde{a}_{\lambda_1}^\dagger \tilde{a}_{\lambda_2}^\dagger \ldots \tilde{a}_{\lambda_{N_e}}^\dagger, \tag{4.40}$$

and

$$A_{N_e-1}^\dagger = \frac{1}{\mathcal{N}_b}\left[\sinh\left(\frac{1}{\lambda_{N_e}}\right)\tilde{a}_{\lambda_1}^\dagger \ldots \tilde{a}_{\lambda_{N_e-1}}^\dagger \ldots + \sinh\left(\frac{1}{\lambda_1}\right)\tilde{a}_{\lambda_2}^\dagger \ldots \tilde{a}_{\lambda_{N_e}}^\dagger\right], \tag{4.41}$$

where $\mathcal{N}_u$ and $\mathcal{N}_b$ are chosen to normalize each photonic component of the state. To reduce the variational parameter space, the problem can be solved in an iterative manner, i.e., by using the values of $\lambda_1, \ldots \lambda_{N_e-1}$ as input for minimizing the energy $E_-^{(N_e)}$ with respect to θ and λ_{N_e}. In Fig. 4.4 we summarized the iterative variational protocol used to numerically evaluate the bound state energies.

To probe the validity of our ansatz we compared in figure 4.5 the bound-state energies $E_-^{(N_e)}$ obtained from our variational approach with the energies obtained from the exact numerical diagonalization. In the insets the $N_e = 2, 3$ cases in the crossover regime $g/(2J) \sim 1$ are shown. The excellent agreement within $\sim 1\%$ (for

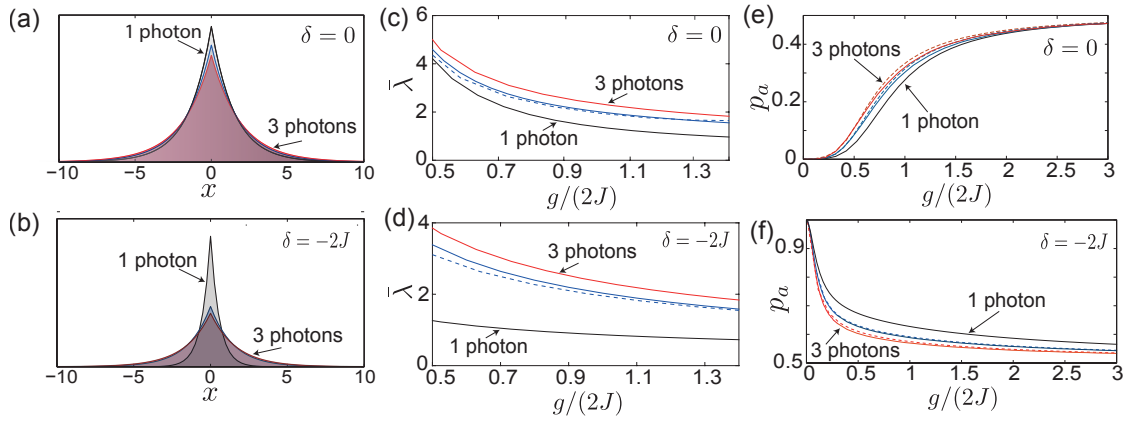

Figure 4.6: Sketch of the first three photonic wavefunctions that appear in the variational ansatz, Eq. (4.40), for the multi-photon bound states. Here, we have set $g = 0.6$, (a) $\delta = 0$ and (b) $\delta = -2J - 0^+$. Figures (c) and (d) show the exponential decay length $\bar{\lambda}_{N_e}$ as a function of g, for $N_e = 1, 2$, and 3 photons and for $\delta = 0$ and $\delta = -2J - 0^+$, respectively. The dotted line shows the result for $\bar{\lambda}$ obtained numerically for the case $N_e = 2$. In Figs. (e) and (f) the atomic population $p_a = \cos^2(\theta(E_-^{N_e}))$ is plotted against g for $\delta = 0$ and $\delta = -2J - 0^+$, respectively.

smaller or larger values of g the agreement is even better) demonstrates that our variational ansatz captures the essential features of the exact wavefunction. Based on this confirmation, we then plot in the main part of figure 4.5 the bound-state energies $E_-^{(N_e)}$ for up to $N_e = 8$ excitations, a subspace that would not be accessible with standard numerical techniques.

4.2.3 Properties of the multi-photon dressed states

In this section we use the variational ansatz previously developed to discuss the main features of the multi-photon bound states and to estimate the associated non-linearity. As discussed in the previous section, in our ansatz the photonic cloud surrounding the atom plays a role similar to that one of an electronic orbital in a molecule. It is interesting to investigate if the size of this cloud depends on the number of excitations involved in the system.

With this purpose, we plot in Fig. 4.6 (a) and (b) the shape of the individual photonic wavepackets associated with the operators $\tilde{a}^\dagger_{\lambda_i}$ in Eq. (4.40) for $N_e = 1, 2, 3$. We see that in particular near the band edge there is a significant difference between λ_1 and λ_2, while the differences between the λ_{N_e} are less pronounced for higher excitation numbers. This dependence on the number of photons seems to suggest that there is some non-linearity in the system. This is indeed the case and will be discussed in more details in a moment. Before it should be noted that the variational approach, which is constructed to minimize the energy, is not very sensitive to the exponential decay of the wavefunction $\langle 0, \ldots, 0, x_{N_e} | \Psi_-^{(N_e)} \rangle \sim e^{-|x_{N_e}|/\bar{\lambda}_{N_e}}$. For physical

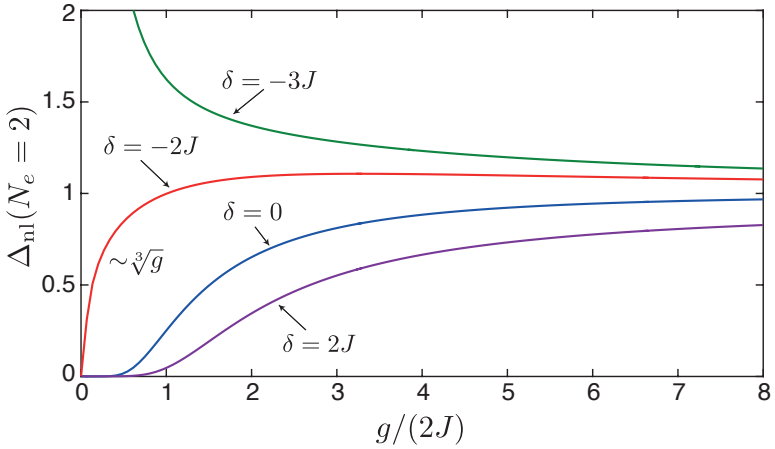

Figure 4.7: The non-linearity parameter $\Delta_{\rm nl}(N_e)$ as defined in Eq. (4.43) is plotted for $N_e = 2$ and different atom-photon detunings δ.

effects that rely on more accurate predictions for the exponential decay we can, instead of simply setting $\bar{\lambda}_{N_e} = \lambda_{N_e}$, make use of the exact energy relation [see Eq. (4.37) for $N_e = 2$]

$$\frac{E_-^{(N_e)}}{2J} = \sum_{n=1}^{N_e} \cosh\left(\frac{1}{\bar{\lambda}_n}\right), \tag{4.42}$$

valid at distances far away from the atom. Therefore, from the exact result for $\lambda_1 \equiv \bar{\lambda}_1$ and the set of bound state energies $E_-^{(N_e)}$ obtained from our variational calculations, one can iteratively apply Eq. (4.42) to also calculate values for the asymptotic decay lengths $\bar{\lambda}_{N_e}$. For $N_e = 2$ the results of this procedure are shown in Fig. 4.6 (c) and (d) and compared with the asymptotic decay length extracted from the numerical solution of the two-photon wavefunction $u(x, y)$. We observe the same general trend as already mentioned above, but at the same time the use of Eq. (4.42) provides more accurate quantitative results.

It is also interesting to analyze how the atomic population varies with the number of excitations. In Fig. 4.6 (e) and (f) we plot the atomic population for $N_e = 1, 2, 3$ for different atom-cavity detuning. In both cases we observe an increase of the hybridization for higher excitation numbers. Indeed, for $\delta = 0$ the state is mainly photonic and the atomic component increases when higher excitations are considered. Reversely, when $\delta = -2J$, the state is mainly atomic and becomes more dressed by the photons when further excitations are added. This behaviour similarly to cavity QED relies on an effective increasing of the coupling with the number of photons that leads to an higher hybridization of the dressed states.

From the discussion on the localization length and on the atomic population it seems that our slow-light waveguide QED setup presents indeed non-linear properties. This is even more clear by observing Fig. 4.5, where we see that for large couplings, $g/(2J) \gg 1$, the bound-state energies exhibit a splitting from the bare

energy by an amount $\sim \sqrt{N_e}$, characteristic of the scaling in conventional cavity QED [see Sec.1.3.1]. In this limit all bound photons are essentially localized on the atom site and the single-mode physics is recovered. To characterize the non-linearity of the spectrum also in the weak and moderate coupling regime we define the non-linearity parameter

$$\Delta_{\rm nl}(N_e) = \frac{|N_e E_-^{(1)} - E_-^{(N_e)}|}{g|N_e - \sqrt{N_e}|}. \tag{4.43}$$

With this definition $\Delta_{\rm nl}(N_e) \simeq 1$ implies that the excitation spectrum is as nonlinear as cavity QED under resonance conditions, $\delta = 0$, while the opposite limit $\Delta_{\rm nl}(N_e) \simeq 0$ indicates a harmonic spectrum. In Fig. 4.7 we plot $\Delta_{\rm nl}(N_e = 2)$ for different values of g and different atomic detunings. We see that, as expected, in the strong coupling limit, $g \gg \{J, |\delta|\}$, the waveguide QED system approaches asymptotically the nonlinear behaviour of the single-mode Jaynes-Cummings model. For small values of g the amount of non-linearity strongly depends on the atomic frequencies and we can identify the following regimes.

- For detunings in the band or close to the upper edge (we recall that in Fig. 4.5 we focussed on the lowest dressed state) the non-linearity approaches zero because the states becomes completely photonic and exhibits a harmonic spectrum.

- For $\delta = -2J$, although $\Delta_{\rm nl}(2)$ vanishes at small g, it is still much stronger than for the resonant case $\delta = 0$. This is consistent with the observation that for $\delta = -2J$ the wavelength of the second photon, λ_2, can be much larger than the wavelength of the first bound photon, λ_1, in contrast with the $\delta = 0$ case where $\lambda_1 \approx \lambda_2$. Note that the approximate scaling of the nonlinearity parameter for $g \to 0$ can be understood from the simplified assumption $E_-^{(2)} \approx E_-^{(1)} - 2J$, which would correspond to a single photon bound state plus an additional very loosely bound photon at the bandedge. By recalling that $E_-^{(1)} \simeq -2J - [g^4/(4J)]^{1/3}$ [see Eq.(4.25)] we obtain $\Delta_{\rm nl}(2) \sim \sqrt[3]{g}$.

- Finally for $\delta = -3J$, which for $g \to 0$ corresponds to a two-level atom-like state inside the bandgap, the nonlinearity parameter diverges. Note that this divergence is a consequence of the chosen normalization for $\Delta_{\rm nl}(N_e)$ and can again be understood from the approximation $E_-^{(2)} \simeq \delta - 2J$ for small g.

4.3 Dipole-dipole interactions between dressed states

Our analysis so far has focused on the bound states of a single atom. However, a key element of waveguide QED are the photon-mediated interactions between two or multiple separated emitters. So far in this thesis we presented two different examples of such interactions. In the weak-coupling regime discussed in Sec. 2.2.1

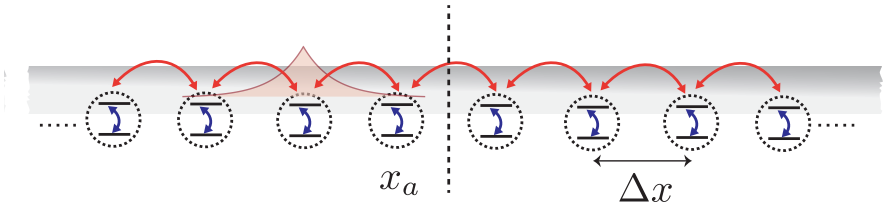

Figure 4.8: Sketch of the setup where an ensemble of atoms with equidistant spacings, $x_{i+1} - x_i = \Delta x$, is coupled to a slow-light waveguide. Here we set $x_a = x_{N_a/2}$.

and Sec. 3.2.2 we have identified effective dipole-dipole interactions between individual atoms, which are both dissipative and dispersive in nature and which can be *infinite-range*, scaling like $\Gamma_{ij}, U_{ij} \sim g^2/J$. In Sec. 3.1.4 instead we have shown how in a photonic crystal waveguide the atom-atom interactions become fully dispersive, but remain long-range due to the long extension of the bound states. In both cases we were able to eliminate the photonic degree of freedom and to obtain an effective interaction in terms of the only atomic operators. In the following section we are interested in the nature of the interactions between dressed bound states which, in the strong coupling regime, represent the elementary excitations of our slow-light waveguide setup. Compared to usual photonic crystal waveguide here the hybridized polaritonic nature of these states plays an important role and leads to a different physics compared to that one commonly used in the gap of photonic structure.

4.3.1 General solution

Here we present a generic method to solve the stationary Schrödinger equation for the case of $N_a > 1$ atoms. In the single excitation subspace, $N_e = 1$, the problem can be solved analytically. At higher excitation a numerical approach is needed and we refer to [161] for further details.

Let us consider an ensemble of $N_a > 1$ atoms placed along the waveguide with equidistant spacings, $x_{i+1} - x_i = \Delta x$, as sketched in Fig. 4.8. This system is reflection symmetric with respect to the center of the atomic array. A possible way to derive the multi-atoms bound states is to exploit this mirror symmetry. For the sake of argument, here we focus on bound states below the continuum, i.e., such that $E < -2J$. In accordance with the mirror symmetry, we define the pair of collective atomic operators

$$\mathcal{S}_{s=e,o} = \sum_{n=1}^{N_a} (\pm 1)^{|n+1|} \sigma_-^n \,, \tag{4.44}$$

where the + (-) sign holds for $s = e, o$. Above the band, the reasoning is analogous, but an extra phase factor $(-1)^{|x_n - x_a|}$ needs to be included in the definition of the collective operators (4.44), i.e.,

$$\mathcal{S}_s = \sum_{n=1}^{N_a} (\pm 1)^{|n+1|} (-1)^{|x_n - x_a|} \sigma_-^n . \tag{4.45}$$

Note that in the case $N_a = 2$, the operators (4.44) reduce to the (unnormalized) symmetric and antisymmetric combinations of σ_-^1 and σ_-^2. Based on this definition, here we look for bound states of the form

$$|\phi_s^{(N_a)}\rangle = \left(b\,\mathcal{S}_s^\dagger + \sum_k c_k a_k^\dagger\right)|g,\ldots,g,0\rangle\,. \tag{4.46}$$

Imposing the ansatz (4.46) to be an eigenstate of Hamiltonian (4.1) with eigenvalue E yields an eigenvalue equation analogous to Eq. (4.4) with the self-energy now given by

$$\Sigma_s(E) = \sum_n (\pm 1)^{|n+1|}\frac{1}{2\pi}\int_{-\pi}^{\pi} dk\,\frac{g^2 e^{ik(x_n - x_a)}}{E + 2J\cos k} = \Sigma_1(E)\; f_{N_a,s}(E), \tag{4.47}$$

where $\Sigma_1(E)$ is the single-atom self-energy given in Eq. (4.5). Here we have defined the function

$$f_{N_a,s}(E) = \sum_n (\pm 1)^{|n+1|} e^{-\frac{|x_n - x_a|}{\lambda}}, \tag{4.48}$$

where the localization length $\lambda = \lambda(E)$ has the same energy dependence as given in Eq. (4.10). The atomic position x_a set the choice of placing the atomic ensemble in the array and will be specified later in the derivation of $f_{N_a,s}(E)$. As in the one-atom case, in deriving the last identity of Eq. (4.47) we used $E < -2J$ to calculate the integral over k through standard methods [158].

The self-energy, hence the eigenvalue equation, is thus determined by the function $f_{N_a,s}(E)$ in Eq. (4.48). In the next sections we will explicitly derive this function for the paradigmatic cases $N_a = 2$ and $N_a \gg 1$ and we will discuss the properties of the corresponding bound states.

4.3.2 Two-atom dressed states

Derivation of the states

We first consider the case of two atoms located at positions x_1 and x_2. In this case we set $x_a = x_1$ and Eq. (4.48) simply yields

$$f_{2,e} = e^{-\frac{\Delta x}{2\lambda}}\cosh\left(\tfrac{\Delta x}{2\lambda}\right),\quad f_{2,o} = e^{-\frac{\Delta x}{2\lambda}}\sinh\left(\tfrac{\Delta x}{2\lambda}\right), \tag{4.49}$$

for the even- and odd-parity states, respectively (recall that $\Delta x = |x_1 - x_2|$). This provides the self-energy function that explicitly reads

$$\Sigma_s(E) = \frac{g^2}{E\sqrt{1-\frac{4J^2}{E^2}}}\left[1 \pm \left(\frac{|E|}{2J} - \frac{|E|}{2J}\sqrt{1-\frac{4J^2}{E^2}}\right)^{|x_1 - x_2|}\right], \tag{4.50}$$

where the + (−) sign holds for $s = e$ ($s = o$). In close analogy to what we did for the single atom case in Sec. 4.1.1, the bound states energies are given by the solution of the eigenvalue equation $E - \delta = \Sigma_s(E)$ in the domain $|E| > 2J$. The resulting

energy spectrum has up to four solutions [see discussion below and appendix A.2] with energies $E_{\pm,s=e,o}$ outside the waveguide continuum given by the real solutions of

$$E_{\pm,e} - \delta = \frac{2g^2 e^{-\frac{|x_1-x_2|}{2\lambda}} \cosh\left(\frac{|x_1-x_2|}{2\lambda}\right)}{E_{\pm,e}\sqrt{1-\frac{4J^2}{E_{\pm,e}^2}}} \tag{4.51}$$

for the even parity states and

$$E_{\pm,o} - \delta = \frac{2g^2 e^{-\frac{|x_1-x_2|}{2\lambda}} \sinh\left(\frac{|x_1-x_2|}{2\lambda}\right)}{E_{\pm,o}\sqrt{1-\frac{4J^2}{E_{\pm,o}^2}}} \tag{4.52}$$

for the odd parity states, where $\lambda \equiv \lambda(E_{\pm,s})$ has the same energy dependence as for the single atom case in Eq. (4.10). For concreteness and notational simplicity, we restrict the following discussion to the two lower bound states with energies $E_{-,s} < -2J$ below the continuum and even ($s = e$) or odd ($s = o$) symmetry of the atom-field system. The corresponding bound states can be derived in terms of $E_{-,s}$ in a way essentially analogous to that one used in Sec. 4.1.1 and in momentum space read:

$$|\phi_{-,s}\rangle = b(E_{-,s})\left[\sigma_+^1 \pm \sigma_+^2, + \frac{1}{\sqrt{N}}\sum_k \frac{g(e^{ikx_1} \pm e^{ikx_2})}{E_{-,s} + 2J\cos k} a_k^\dagger\right]|g_1, g_2, 0\rangle\,, \tag{4.53}$$

where the function $b(E)$ follows from the normalization constraint

$$b(E) = \left(2 + \frac{g^2\mathcal{N}_s^2}{2J^2 \sinh^2\frac{1}{\lambda}}\right)^{-\frac{1}{2}}, \tag{4.54}$$

and

$$\mathcal{N}_{e,o} = \sqrt{\coth\frac{1}{\lambda}\left(1 \pm e^{-\frac{|x_1-x_2|}{\lambda}}\right) \pm |x_1 - x_2| e^{-\frac{|x_1-x_2|}{\lambda}}}, \tag{4.55}$$

is the corresponding normalization constant (again, the + (−) sign holds for the even (odd) case). In position space, the state (4.53) can be rewritten as

$$|\phi_{-,s}\rangle = b(E_{-,s})\Big[\sigma_+^1 \pm \sigma_+^2 + \frac{g}{E_{-,s}\sqrt{1-\frac{4J^2}{E_{-,s}^2}}}\sum_x \Big(e^{-\frac{|x-x_1|}{\lambda}} \pm e^{-\frac{|x-x_2|}{\lambda}}\Big) a_x^\dagger\Big]|g_1, g_2, 0\rangle. \tag{4.56}$$

In analogy to the single-atom case, one can express such bound states in terms of the polaritonic operators

$$|\phi_{s=e,o}\rangle = \frac{1}{\sqrt{2}}\left[D_s^\dagger(x_1) \pm D_s^\dagger(x_2)\right]|g_1, g_2, 0\rangle, \tag{4.57}$$

where the dressed-state creation operators $D_{e,o}^\dagger(x_i)$ are defined as

$$D_{s=e,o}^\dagger(x_i) = \cos(\theta_s)\sigma_+^i + \sin(\theta_s)\frac{\tilde{a}_{\lambda,s}^\dagger(x_i)}{\mathcal{N}_s}, \tag{4.58}$$

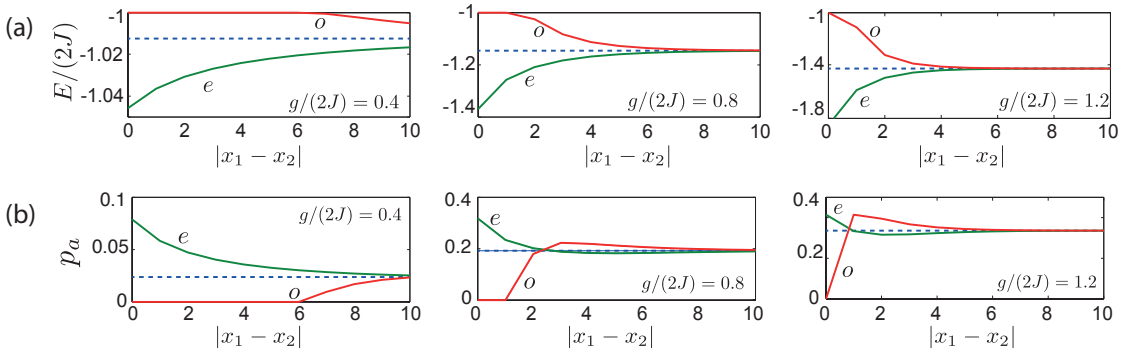

Figure 4.9: The bound-state energy levels $E_{-,s}$ (a) and the corresponding atomic populations $p_a = \cos^2(\theta(E_{-,s}))$ (b) are plotted as a function of the interatomic distance for the case of two atoms and for three representative values of $g/(2J)$. For all plots $\delta = 0$ is assumed. For comparison, in each panel the dashed line indicates the corresponding bound-state energy or atomic population for a single atom.

with $\tilde{a}^\dagger_{\lambda,s}(x_i) = \sum_x e^{-\frac{|x-x_i|}{\lambda}} a^\dagger_x$ being an unnormalized photonic creation operator. Here the mixing angle θ is given by

$$\cos\theta_s = \left(1 + \frac{g^2 \mathcal{N}_s^2}{4J^2 \sinh^2 \frac{1}{\lambda}}\right)^{-\frac{1}{2}}, \tag{4.59}$$

which depends on both the bound-state energy and the distance between the atoms.

Before we proceed with the discussion of the bound state properties, it is important to make a few remarks. First, regarding the bound states above the band, one can follow an analogous reasoning by taking into account the different definition of operators $\mathcal{S}_s$ given in (4.45). While this affects the expression of the bound states, namely the counterparts of (4.53) and (4.56), (4.47), the self-energy turns out to be unaffected both above and below the continuum.

Second, while our approach based on the collective atomic operators (4.44) is devised to easily tackle the $N_a \gg 1$ limit, in the $N_a = 2$ case an equivalent method would be to block-diagonalize H with the blocks corresponding to even- and odd-parity sectors of the entire single-excitation Hilbert space (including the field). In the even (odd) subspace, the problem is reduced to an effective single atom coupled to the cosine-shaped (sine-shaped) field modes. This approach was followed in Ref. [67], where however the authors focused only on the bound states in the continuum (BIC) discussed in Sec. 2.3.3. The effective Hamiltonian in each parity-definite subspace differs from the model in Eq. (4.1) (case $N_a = 1$) in that the atom-mode couplings are k-dependent. Such "coloured" Fano-Anderson model is investigated in Ref. [66] in the case of sine-shaped couplings.

Discussion

Figure 4.9 shows the dependence of the two-atom dressed state energies $E_{-,s}$ on the atomic separation Δx. For distances which are large compared to λ both energies are approximately equal to the single-atom bound state, $E_{-,e} \simeq E_{-,o} \simeq E_-$ and the two atoms do not interact. At a large but finite separation $|x_1 - x_2| \gtrsim \lambda(E_-)$ the photonic wavefunctions associated with the single-atom bound states start to overlap and induce a splitting of the energies such that $E_{-,e} < E_- < E_{-,o}$. As long as this splitting is still small and the two atoms not too close the dressed-states dynamics can be described by the Hamiltonian

$$H \approx \sum_{i=1,2} E_- D_i^\dagger D_i + \frac{U_{\rm dd}}{2}\left(D_1^\dagger D_2 + D_1 D_2^\dagger\right). \tag{4.60}$$

Here the $D_i \equiv D(x_i)$ are the single-atom dressed state operators introduced in Eq. (4.12) that follow the commutation rules

$$[D(x_1), D(x_1)^\dagger] = [D(x_2), D(x_2)^\dagger] = \mathbb{I} \tag{4.61}$$

and in the approximated model in Eq. (4.60) these operators are treated as independent and mutually commuting degrees of freedom, i.e,

$$[D(x_1), D(x_2)^\dagger] \propto e^{-\frac{|x_1-x_2|}{\lambda}} \sim 0. \tag{4.62}$$

Hamiltonian (4.60) describes a dipole-dipole like coupling between distant dressed states as sketched in Fig. 4.10(a). The effect of the interaction is that the initially almost degenerate states split in two distinct energy levels according [see also [162]]:

$$E_{e,o} \simeq E \pm U_{dd}, \tag{4.63}$$

where

$$U_{dd} \approx \frac{4J\cosh\frac{1}{\lambda} - |\delta|}{1 + \coth^2\frac{1}{\lambda} - \frac{|\delta|}{2J}\frac{1}{\cosh\frac{1}{\lambda}\sinh^2\frac{1}{\lambda}}} e^{-|x_1-x_2|/\lambda} \tag{4.64}$$

gives the strength of the interaction. Note that in this approximate regime the localization length λ used in (4.64) is that one of the single atom bound state. This clearly shows the localized nature of the interactions when $g/(2J) \gtrsim 1$, in contrast with the long-range coupling obtained in the weak-coupling regime. Note that here, even at large distances, the interaction involves the fully hybridized dressed states and not only the atomic degrees of freedoms as it occurs for the photonic crystal waveguides discussed in Sec. 3.1.4.

This point is even clearer when the atoms get closer. Indeed, as the atom-atom separation decreases further, the mutual distortion of the wavepackets must be taken into account. As illustrated in Fig. 4.10(b) and (c), the even bound state, corresponding to the lower level $E_{-,e}$ in Fig. 4.9(a), is a "bonding'" state such that the photon becomes more and more localized between the atoms and the corresponding

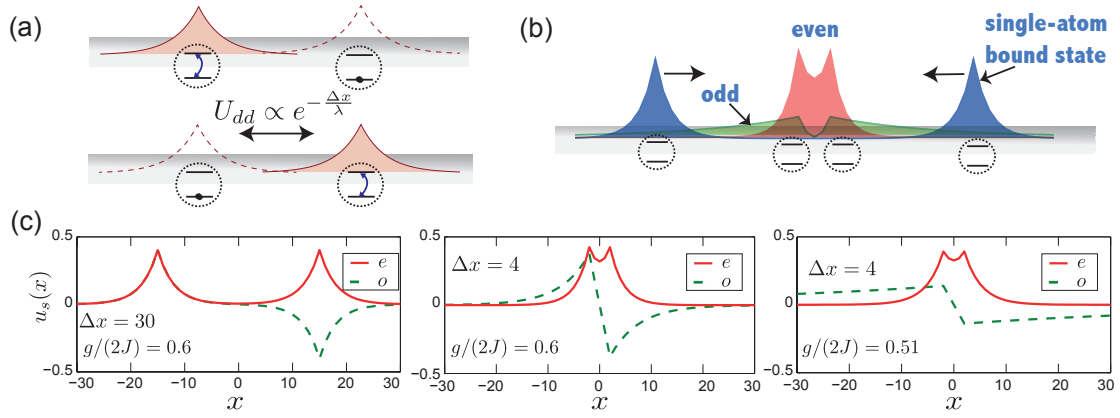

Figure 4.10: (a) Sketch of the long-distance regime where the atom-atom interactions can be described by a dipole-dipole like coupling between the unperturbed dressed states. (b) Sketch of the photonic cloud distortion that arises when the dressed states become closer. A bonding (even) and an antibonding (odd) wavepackets are formed. (c) Spatial profile of the photonic wave function $u_s(x) = \langle x|\Phi_s\rangle$ corresponding to the even (red solid line) and odd (green dashed line) lower band bound states in the case of two atoms for different coupling strengths and interatomic distances. For all plots $\delta = 0$ is assumed.

atomic population increases [see Fig. 4.9(b)]. In contrast, the odd state, corresponding to the upper level $E_{-,o}$, behaves as an "anti-bonding" state such that the photon becomes more and more delocalized as the atomic spacing decreases with the states that eventually becomes completely photon-like [see Fig. 4.9(b)].

In general two regimes can be distinguished.

- For $g > g_m$ and $\delta > -2J$, where

$$g_m = 2J\sqrt{1 + \frac{\delta}{2J}}, \tag{4.65}$$

  both $E_{-,e}$ and $E_{-,o}$ solutions exist for all $\Delta x \geq 1$ [see App. A.2]

- In the opposite case, $g < g_m$, we find that there is a finite distance $x_m = (g_m/g)^2 > 1$ below which the upper bound state $E_{-,o}$ reaches the band edge and disappears [see Fig. 4.9](a). This "melting" of one of the bound states into the waveguide continuum is related to a progressive delocalization of the photonic wavepacket that eventually becomes completely delocalized along the array [see for instance the dashed green line in Fig. 4.10(c)].

This effect is most relevant for resonantly coupled atoms, $\delta \approx 0$, and for moderate coupling strengths, while for frequencies in the gap, $\delta \leq -2J$, both the two-atom bound states always exist. Note that the current discussion has been restricted to the two lower dressed states $E_{-,s} < -2J$, but analogous results are obtained for the two-atom bound states above the photonic band, $E_{+,s} > 2J$ with the sign of δ reversed. See App. A.2 for more details.

In conclusion we mention that recently, for two qubits coupled to a superconducting microwave photonic crystal, an avoided crossing of the bound states energies has been observed. This result confirms the prediction illustrated in this section and can be found in [140].

4.3.3 Multi-atom dressed states

Let us now consider the case of multiple atoms, where for $N \gg N_a \gg 1$ and equidistant spacings, $|x_{i+1} - x_i| = \Delta x$, function $f_{N_a,s}(E)$ (4.48) can be written in a compact form. Here we assume to have an even number of atoms and we set $x_a = x_{N_a/2}$. Note that an analogous reasoning with a slightly different choice for x_a can be made if N_a is odd. By expressing in Eq. (4.48) each atomic position as $x_n = x_a + (n - N_a/2)\Delta x$, the function $f_{N_a,s}(E)$ reduces to a geometric series and we end up with

$$f_{N_a\gg1,e} = \coth\left(\frac{\Delta x}{2\lambda}\right), \quad f_{N_a\gg1,o} = \tanh\left(\frac{\Delta x}{2\lambda}\right), \tag{4.66}$$

which provide the eigenvalue equation for the bound states $|\phi_s^{(N_a\gg1)}\rangle$. Here the coupling between neighbouring atoms leads to the formation of a meta-bandstructure for propagating dressed-state excitations below and above the bare photonic band. This is illustrated in Fig. 4.11 where the single-photon bound-state energies for $N_a = 40$ atoms are shown as a function of Δx. For large Δx we see that the bound states form a narrow band around the single-atom energies E_+ and E_- with a width of $\Delta E \approx U_{\rm dd}$. For smaller atomic spacings, the bandwidth grows and, depending on the parameters, it can either partially melt into the waveguide continuum or remain energetically separated.

As shown in App. A.2, the meta-band is bounded by an upper and lower energy E_u and E_l, which obey the equations

$$E_u - \delta = \frac{g^2 \coth\left(\frac{\Delta x}{2\lambda}\right)}{E_u\sqrt{1 - \frac{4J^2}{E_u^2}}} \tag{4.67}$$

and

$$E_l - \delta = \frac{g^2 \tanh\left(\frac{\Delta x}{2\lambda}\right)}{E_l\sqrt{1 - \frac{4J^2}{E_l^2}}}, \tag{4.68}$$

respectively. We confirmed numerically that the metaband-edge levels [see Fig. 4.11] for growing N_a converge to the numerical solutions of the eigenvalue equation $E - \delta = \Sigma_1(E) f_{N_a\gg1,s}(E)$. Specifically, above the continuum ($E > 2J$) the solution for $s = e$ ($s = o$) gives the upper (lower) metaband edge, while below the continuum $s = e$ ($s = o$) corresponds to the lower (upper) metaband edge.

Similarly to the previous section, it is possible to define a critical coupling

$$g_m^{(N_a\gg1)} = \sqrt{2} g_m\,, \tag{4.69}$$

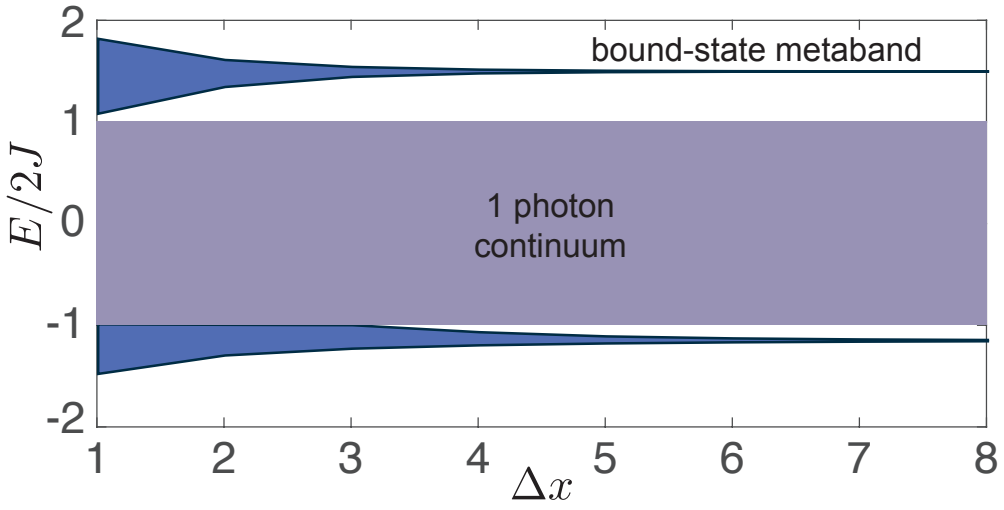

Figure 4.11: Single-excitation energy spectrum in the case of $N_a = 40$ equally spaced atoms as a function of the atomic nearest-neighbour distance Δx. Note the appearance of upper and lower metabands of bound states. For this plot $\delta/(2J) = 0.6$ and $g/(2J) = 1$ have been assumed.

for the multi-atom band, which only differs by a factor $\sqrt{2}$ from the two-atom case g_m given in Eq. (4.65). For $g > g_m^{(N_a)}$ and $|\delta|/(2J) < 1$, the meta-band is separated from the photonic continuum regardless of Δx. In the opposite case, $g < g_m^{(N_a)}$, a fraction of the dressed-state band disappears in the waveguide continuum and, unlike in a usual band-structure, only a fraction of the k-modes are available.

Chapter 5

Strong coupling between moving atoms and slow-light Cherenkov photons

In the last chapter we have shown how narrow bandwidth waveguides can lead to different physical effects compared to usual waveguides and photonic crystals. In particular, we focussed on the fact that the atom-field coupling strength and the associated decay rate can be comparable to the waveguide bandwidth and in this "strong coupling" regime the atom-field bound states emerge as the elementary excitations of the system.

Here we want to address another remarkable feature of the slow-light waveguides that relies on the existence of a maximum value for the photonic group velocity, which can be highly decreased and approach, match or even go below typical atomic velocities in cold atom experiments. In this chapter we exploit this effect by considering a slow-light waveguide coupled to atoms that move with a speed comparable to the velocity of propagation of the photons.

The study of the emission of particles moving close to the speed of light it is not a new problem. Indeed, it was first addressed by Cherenkov [163, 164] and it is usually considered in the context of relativistic and high-energy physics [165]. On the other hand, in quantum optics, the motion of neutral atoms and molecules coupled to classical or quantized fields is usually investigated when particle velocities are low and mainly affects the emission and absorption of photons via a small Doppler shift of the transition frequency. This effect had a crucial role for the development of laser cooling [166] and successive atom trapping techniques [167], which enabled the study of strong light-matter interactions even at the single photon level [36, 106, 168, 169].

In this chapter we merge these two opposite scenarios and we show that moving atoms coupled to a slow-light waveguide give rise to a new intriguing regime for atom-light interactions where atoms and photons move at comparable velocities while still interacting *strongly* with each other. In particular, the existence of an upper bound for the photonic group velocity introduces a velocity-induced di-

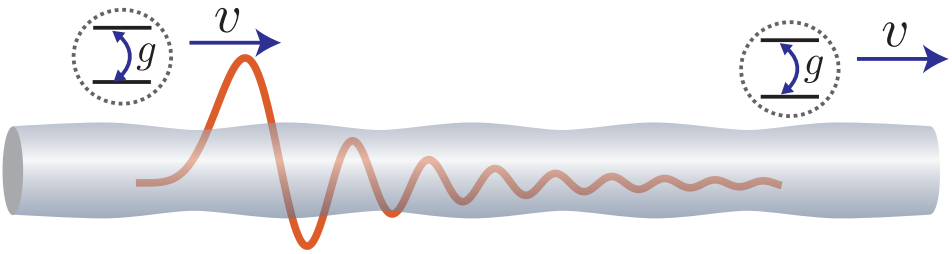

Figure 5.1: Sketch of the setup where two-level atoms moving at a velocity v are strongly coupled to the evanescent field of a 1D waveguide. By introducing a sufficiently strong spatial modulation with periodicity a, photons are slowed down by Bragg-reflection and can propagate with a maximal group velocity comparable to typical atomic velocities.

vergence in the photonic density of states that goes beyond the usual Cherenkov emission [163, 170, 171] and that is not present for static atoms. This divergence, which is associated with a strong resonant coupling between the moving atoms and individual co-propagating Cherenkov photons, leads to a non-Markovian spontaneous emission of the atoms and can be used to enhance the excitation transfer between separated emitters.

To describe this new regime of light-matter interactions we develop an effective model that correctly describes the dynamics for the relevant range of parameters and we also discuss its validity. In the last section we finally propose a potential realization of this system that consists of Rydberg atoms flying across a coupled array of planar microwave resonators [148, 172, 173, 174, 175].

All the results presented in this chapter have been published in Physical Review A 95, 043824 (2017). In this work I contributed as a main author and I performed all the analytic and numerical calculations under the supervision of Peter Rabl.

5.1 Model

5.1.1 Atoms moving close to a slow-light waveguide

In this chapter we consider a setup as shown in Fig. 5.1, where N_a two-level atoms with mass M are coupled to the field of a 1D waveguide while moving along the longitudinal direction $\vec{e}_z$. In conventional waveguides and within the relevant frequency range the dispersion relation is usually linear $\omega_k \simeq (c/n)|k|$, where c is the speed of light in vacuum and $n \sim \mathcal{O}(1)$ is the refractive index of the material. Therefore, in this case the photonic group velocity, $v_g(k) = \partial\omega_k/\partial k \sim 10^8$ m/s, is much larger than typical velocities $v \lesssim 10^4$ m/s of neutral atoms.

To achieve the condition $v \sim v_g$, we again consider a slow-light waveguide setup of the form presented in 3.2.1. In particular, we assume a spatially periodic modulation of the waveguide (for example, of its width, refractive index, etc.) with lattice constant a, that slows down the propagation of the photons and separates

the spectrum into individual bands. For this specific work we further assume that all the relevant time-scales of the system dynamics are slow compared to the inverse frequency separation between individual bands, $\sim a/c$. This allows us to restrict our analysis to a single band and to approximate the dispersion relation using the tight binding model introduced in 3.2.2, i.e. $\omega_k \simeq \omega_0 - 2J\cos(ka)$ where ω_0 is the central frequency and $4J = B$ the total width of the band. Within the single band of interest, the periodic modulation introduces an upper bound for the maximal propagation velocity of the photons given by the effective speed of light

$$\bar{c} = \max\{v_g(k)\} = 2Ja. \tag{5.1}$$

The interesting point is that the maximal photon speed can be tuned close to zero by taking the limiting case of a weakly tunnel-coupled array of localized resonator modes, making the regime $v \sim \bar{c}$ experimentally accessible. Note, however, that the required reduction of the photonic group velocity by many orders of magnitude goes significantly beyond what is possible in conventional photonic crystal structures [134]. In Sec. 5.4 below we will discuss in more detail, how this extreme slow-light condition can be realized in practice. With these assumptions the Hamiltonian for this system reads

$$H = \sum_{i=1}^{N_a}\left(\frac{p_i^2}{2M} + \hbar\omega_a|e\rangle_i\langle e|\right) + \sum_k \hbar\omega_k\, a_k^\dagger a_k + \sum_{i=1}^{N_a}\sum_k \hbar g\left[\psi_k(z_i)a_k\sigma_+^i + \psi_k^*(z_i)a_k^\dagger\sigma_-^i\right], \tag{5.2}$$

where z_i and p_i are the atomic position and momentum operators and in this definition the coupling has the dimension of a frequency ([g]=Hz). As explained in 3.2.1, here a_k and $a_k^\dagger$ are the bosonic annihilation and creation operators for photons obeying $[a_k, a_{k'}^\dagger] = \delta_{k,k'}$, with Bloch-wavefunctions

$$\psi_k(z) = \sqrt{\frac{a}{L}}u_k(z)e^{ikz}, \tag{5.3}$$

where $L \gg a$ is the waveguide length, $k \in (-\pi/a, \pi/a]$ and the $u_k(z) = u_k(z+a)$ are periodic functions. Compared to the usual waveguide Hamiltonian given in (2.1), by introducing a periodic modulation for slowing down the photons we have changed to a Bloch-wave description, which also results in a periodic variation of the coupling, $g \to g(z) \sim u(z)$. For atoms moving along classical trajectories, i.e., $z_i(t) = z_i + v_i t$, this translates into a time-periodic modulation of the coupling with frequency $\Omega_i = 2\pi|v_i|/a$, which makes the dynamics of the system in general quite involved. However, it turns out that for a large range of parameters, in particular for the relevant case of high velocities, $v \sim \bar{c}$, and atomic frequencies ω_a inside the propagation band a simple effective model can be derived as we will present in the next section.

5.1.2 Effective model

Hamiltonian (5.2) is time dependent and in general not easy to treat. To solve the problem we exactly simulated numerically the full time-dependent Schrödinger

equation. Before we present and discuss the results, we first introduce an effective model that captures well the physics in the regime of interest and provides a simpler and clearer picture of the system dynamics.

Let us start by rewriting the full model given in Eq. (5.2) in the interaction picture with respect to the bare atom and photon Hamiltonian:

$$H_I = \hbar \sum_{i=1}^{N_a} \sqrt{\frac{a}{L}} \sum_k \left[g_k(z_i(t)) e^{ikz_i(t)} e^{i\delta_k t} a_k \sigma_+^i + g_k^*(z_i(t)) e^{-ikz_i(t)} e^{-i\delta_k t} a_k^\dagger \sigma_-^i \right], \tag{5.4}$$

where $\delta_k = \omega_a - \omega_k$ and $g(z) = g u_k(z)$. To proceed we assume that at time $t = 0$ the i-th atom is located at the left border of one of the unit lattice cells, i.e., $z_i(0) \equiv z_i = (n_1 - 1/2)a$, and the atom then traverses l lattice sites following a classical trajectory $z_i(t) = z_i + v_i t$. We here consider the case of very fast atoms where $\Omega_i = 2\pi/T_i = 2\pi|v_i|/a \gg g$. The integrated coupling between the atom and mode a_k is given by

$$G_k^l := \int_0^{lT_i} dt' \, g_k(z_i(t')) e^{ikz_i(t')} e^{i\delta_k t'} = \frac{g}{v_i} \int_{z_i}^{z_i + la} dz \, u_k(z) e^{ikz} e^{i\delta_k (z - z_i)/v_i}. \tag{5.5}$$

We now use the fact that in the tight-binding limit,

$$u_k(z) \simeq \bar{u}(z) e^{-ikz} \qquad \text{for} \quad -a/2 < z < a/2, \tag{5.6}$$

where $\bar{u}(z)$ is approximately k-independent. Then, by discretizing the position variable we can rewrite Eq. (5.5) as

$$G_k^l = \left[\frac{gT_i}{a} \int_{-\frac{a}{2}}^{\frac{a}{2}} dz \, \bar{u}(z) e^{i\delta_k z/v_i} \right] \sum_{n=n_1}^{n_1+l-1} e^{ikan} e^{i\delta_k T_i (n+\frac{1}{2})}. \tag{5.7}$$

To proceed we neglect the variation $\sim e^{i\delta_k z/v_i}$ in the integral in Eq. (5.7). This is valid for small detunings, $\delta_k \ll \Omega_i$, for strongly peaked $\bar{u}(z)$ and under the already taken assumption that the system dynamics is slower compared to the modulation frequency $g \ll \Omega_i$. Under these approximations we can introduce the average coupling

$$\bar{g} = \frac{g}{a} \int_0^a dz \, \bar{u}(z), \tag{5.8}$$

and obtain

$$G_k^l \simeq \bar{g} T_i \times \sum_{n=n_1}^{n_1+l-1} e^{ikan} e^{i\delta_k T_i (n+1/2)}. \tag{5.9}$$

We see that this result is just the discretized version of the integral

$$G_k^l \simeq \bar{g} \int_0^{lT_i} dt' \, e^{ikz_i(t')} e^{i\delta_k t'}. \tag{5.10}$$

We now observe that the exactly same result could have been obtained by starting with the effective model (going back from the interaction picture):

$$H(t) \simeq \sum_{i=1}^{N_a} \hbar\omega_a |e\rangle_i\langle e| + \sum_k \hbar\omega_k \, a_k^\dagger a_k + \sum_{i=1}^{N_a} \sqrt{\frac{a}{L}} \sum_k \hbar\bar{g} \left[e^{ikz_i(t)} a_k \sigma_+^i + e^{-ikz_i(t)} a_k^\dagger \sigma_-^i \right], \tag{5.11}$$

where the time periodic modulation induced by the Bloch functions is averaged over one unit cell and only the effective coupling $\bar{g}$ appears. This effective model, mimics very closely the coupling of fast moving atoms to arbitrarily slow photons in a 1D continuum and will be used to describe the atom-light interaction properties in the the following sections.

In Hamiltonian (5.11) the only remaining time-dependence arises in the phase factor $e^{ikz_i(t)}$. To achieve a full time independent description and to obtain a better intuition of the atomic emission it is convenient to change into a frame, which is co-moving with the atom. This is achieved by the unitary transformation $\tilde{H} = UHU^\dagger + i\hbar\dot{U}U^\dagger$, where

$$U(t) = e^{i\sum_k vka_k^\dagger a_k t}. \tag{5.12}$$

In this new representation the time-dependence in the exponentials in Eq. (5.11) is eliminated, $z(t) \to z$, and we obtain the following tilted dispersion relation

$$\omega_k \to \tilde{\omega}_k = \omega_k - kv. \tag{5.13}$$

This means that, within the validity of our approximations, we can effectively describe the system as an ensemble of atoms at rest coupled to a waveguide with the tilted dispersion relation given in (5.13). In Fig. 5.2 we illustrate the effect of the atomic velocity on the dispersion relation. When the atoms are moving there is a range of frequencies where only photons with negative (positive if $v < 0$) group velocity can be emitted [see Fig. 5.2(b)]. This suggests that we can achieve a velocity induced directional emission. Most surprising is the case when the atoms are moving at the maximal group velocity of the photon. In this limit the dispersion gets completely tilted, as shown in Fig. 5.2(c) and a saddle point appears in the middle of the band. This divergence of the density of states inside the band is quite unusual and leads to a directional and non-Markovian emission that we will discuss in the next section 5.2. For a detailed analysis on the range of validity of the effective model see section 5.3.

5.2 Atoms and photons interacting at the speed of light

Based on the effective model given in Eq. (5.11), we now investigate in this section, how basic atom-photon processes are modified when atoms and photons move at comparable velocities. We first consider the simple spontaneous emission of a moving atom and we show the arising of a velocity-induced directional emission. Then we extend the results to describe the exchange of excitations between multiple atoms.

5.2.1 Spontaneous emission of a moving atom

Let us first consider the process where a photon is emitted from a single atom moving at a constant velocity $v > 0$. By assuming that at time $t = 0$ the atom is in state $|e\rangle$ and the waveguide in the vacuum state $|\text{vac}\rangle$, the state of the whole system can be

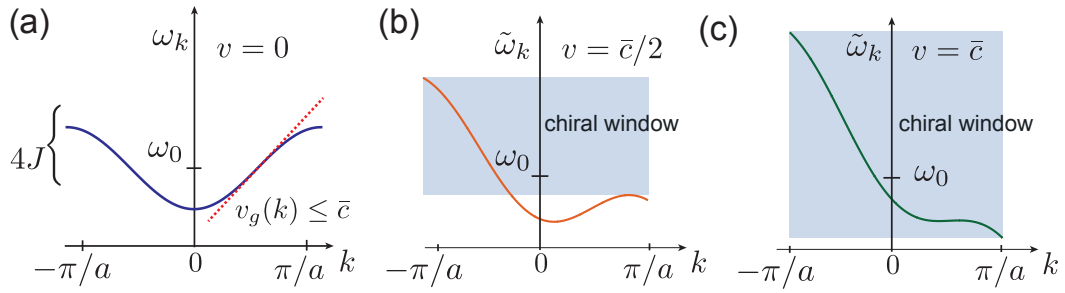

Figure 5.2: Tilting of the dispersion relation for different values of the atomic velocity v. (a) When the atom is at rest we have the usual tight binding cosine dispersion $\omega_k \sim 2J\cos ka$ with band width $B = 4J$. (b) For atomic speed $v = \bar{c}/2$ the dispersion gets tilted and there is a range of frequency where only left propagating photons can be emitted. (c) For atoms moving at the speed of light $v = \bar{c}$ the dispersion is completely tilted and a plateau arises in the middle of the band.

written as

$$|\psi(t)\rangle = \left[c_e(t)\sigma_+ + \sum_k \psi(k,t)a_k^\dagger\right]|g\rangle|\text{vac}\rangle, \tag{5.14}$$

where $p_e(t) = |c_e(t)|^2$ is the excited state population and $\psi(k,t)$ is the wavefunction of the emitted photon in k-space. For frequencies ω_a inside this tilted band, away from the divergencies of the density of states, and for sufficiently small $\bar{g} < 4J$, the coupling to the continuum of modes in the waveguide can be described by using a Born-Markov approximation. This will result in an approximately exponential decay of $p_e(t)$ with total rate $\Gamma = \Gamma_L + \Gamma_R$, where

$$\Gamma_{L,R} = \frac{\bar{g}^2 a}{|\tilde{v}_g(k_{L,R})|} \tag{5.15}$$

is the decay rate that now depends on the modified group velocity $\tilde{v}_g(k) = v_g(k) - v$ in the co-moving frame. Here $k_L < 0$ and $k_R > 0$ are left- and right-propagating [in the lab frame] wavevectors defined by the resonance condition $\tilde{\omega}_k = \omega_a$.

In the usual case, where the dispersion is linear, $v_g(k) \simeq \pm\bar{c}$ and $v \ll \bar{c}$, Eq. (5.15) implies that photons are emitted with Doppler-shifted wavevectors $k_{L,R} = \mp\omega_a/(\bar{c}\pm v)$, but with the same group velocity in the laboratory frame and approximately the same rates $\Gamma_L \simeq \Gamma_R$.

When $v \sim \bar{c}$, this picture changes significantly. This is summarized in Fig. 5.3, where we plot the directionality parameter [127, 24]

$$D = \frac{\Gamma_L - \Gamma_R}{\Gamma_L + \Gamma_R}, \tag{5.16}$$

for a range of atomic velocities and atom-waveguide detunings $\delta = \omega_a - \omega_0$. This parameter indicates if the emission occurs to the left or to the right in the lab frame. Note that for this plot we have assumed a finite decay rate $\gamma_p/J = 0.01$ for

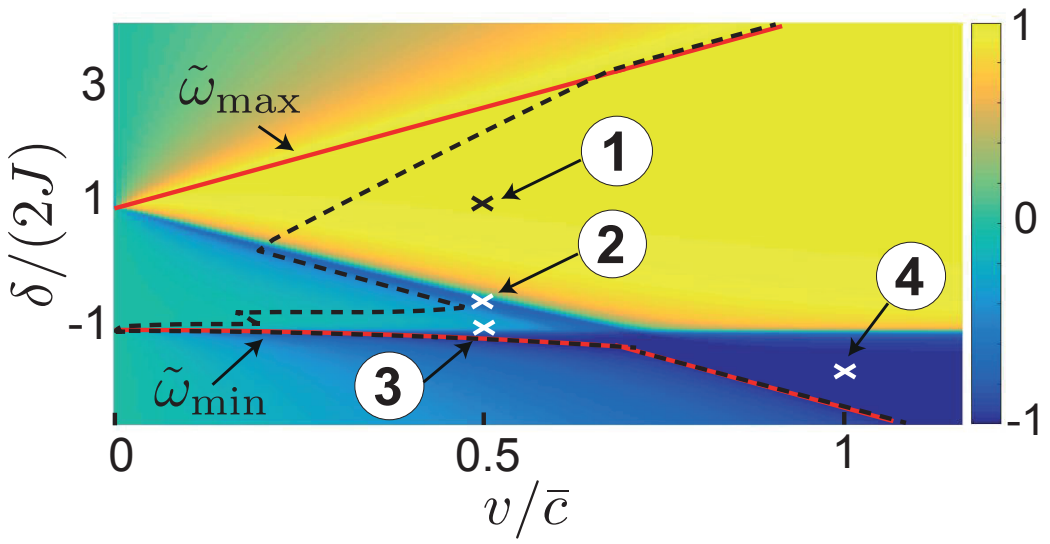

Figure 5.3: Plot of the directionality parameter D defined in Eq. (5.16) as a function of δ and v. The crosses mark the parameter values assumed in the corresponding plots in Fig. 5.4. The solid red lines indicate the minimal ($\tilde{\omega}_{\min}$) and maximal ($\tilde{\omega}_{\max}$) frequency of the tilted band. For each detuning, the dashed line shows the minimal velocity $v_{\min}(\delta)$, above which the effective model (5.11) provides an accurate description of the dynamics (see Sec. 5.3 for more details).

the photons, which allows us to generalize Eq. (5.15) to frequencies outside the band and to avoid unphysical divergences, similarly as done in Sec. 3.2.2. In Fig. 5.3 we point out different regimes that will be discussed in the following sections.

Velocity-induced directional emission of light

Fig. 5.3 shows a large parameter range (in yellow) where mainly left propagating photons are emitted. The black dashed line indicates the area of validity of our effective model [see Sec. 5.3]. Let us consider as an illustrative example the parameters indicated by ①. In this case the tilting of the finite propagation band opens a frequency window, within which only backward propagating modes exist. This is more clear in Figures 5.4(a)-(b) where we show snapshots of the photonic wavefunction in the discretized position space, $\psi(z,t)$, and the atomic population as function of time. Note that these results are obtained by using the effective model (5.11) and agree with the numerical simulation of the full model [see Sec. 5.3]. Figures 5.4(a)-(b) show a purely unidirectional emission opposite to the atomic motion associated with an exponential (Markovian) decay of the atom. This regime is formally equivalent to the chiral waveguide QED scenario discussed in Sec. 2.2.2 with the only difference that here the time reversal symmetry breaking is induced by the atomic motion. It is interesting to see that a fully directional emission already occurs at velocities $v < \bar{c}$, where photonic wavepackets travelling faster than the atom would

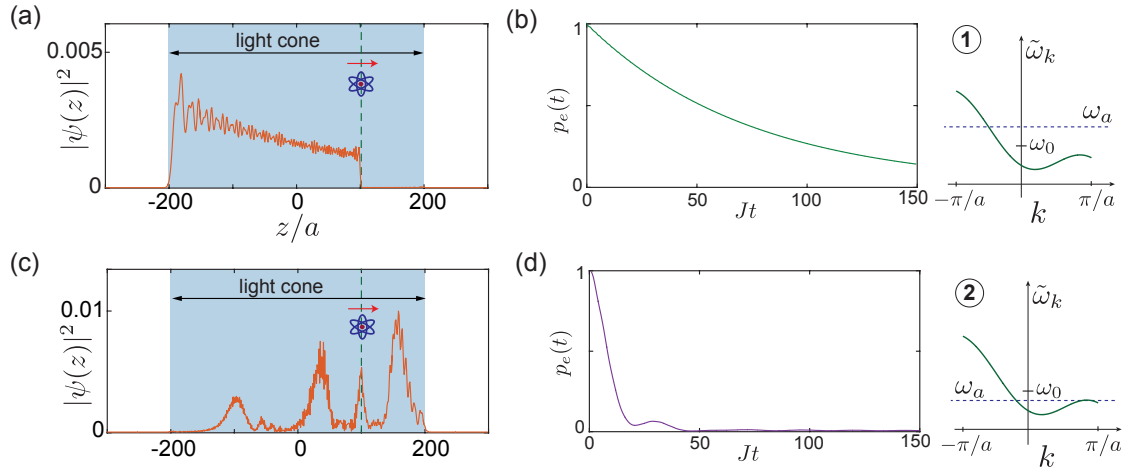

Figure 5.4: Snapshots of the emitted photon wavepacket (evaluated at a time $t = 100/J$) and corresponding excited state population $p_e(t)$ for different sets of parameters. In (a)-(b) $v = \bar{c}/2$, $\delta/(2J) = 1$ while in (c)-(d) $v = \bar{c}/2$, $\delta/(2J) = -0.5$. In all plots a coupling of $\bar{g}/(2J) = 0.1$ is assumed. The blue shaded area indicates the light cone, $|z| \leq \bar{c}t$. For each set of parameters we also show the position of the atomic transition frequency within the tilted photonic propagation band in the co-moving frame.

still be allowed. This would not be the case for an infinite band where a directional emission could be reached only for $v > \bar{c}$.

A different mechanism for directionality arises for the parameters chosen in example ② and shown in Fig. 5.4(c)-(d). To understand the emission in this case let us discuss it in the frame co-moving with the atom. In this frame the atom is coupled to a linear branch of the dispersion, associated with a fast photon emitted in the backward direction [see the small propagating peak on the left side of Fig. 5.4(c)], and to a divergence in the photonic density of states associated with the right edge of the tilted propagation band. This divergence leads to an enhanced emission of slows photons, i.e. $\tilde{v}_g(k_R) \simeq 0$, in both directions. These slow photons in the lab frame will move in the same direction of the atom contributing mainly to the emission to the right. This explains the blue color around ② in Fig. 5.3. Here it is important to notice that although the emission into backward-propagating modes is still allowed, this band-edge effect leads to a strong asymmetry, $\Gamma_R \gg \Gamma_L$, as well as a substantially increased total emission rate. Overall, the combination of both of these mechanisms, related to either the absence or divergence of the photonic density of states, can give rise to strong variations in the direction, the rate and the group velocity of the emitted photons. This would be even more evident in the cases that we are going to discuss in the next section.

Atom-photon bound states at finite velocities

To derive the exponential decay with rates $\Gamma_{L,R}$ given in Eq. (5.15) we have assumed a perturbative treatment of the photon emission process, which is strictly valid only in the weak-coupling limit $\bar{g} \ll |\tilde{v}(k_{L,R})|/a$. As we showed in chapter 3 for static atoms it is well known that even for $\bar{g} \ll J$, such a description breaks down near the edges of the propagation band. In this regime a vanishing group velocity results in a highly non-Markovian, oscillatory decay and a non-decaying photonic fraction. This behaviour is caused by the atom-photon bound states that we largely discussed both in chapter 3 and chapter 4.

It is interesting to ask if these states can still exist when the atom is moving, or in other words, if a flying atom can drag the photon along. The example ③ in Fig. 5.3 and in Fig. 5.5 (a)-(b) show that such effects remain even at very high velocities. In both examples, a large fraction of the photon is coherently reabsorbed and remains bound to the moving atom for a long time.

We emphasize that in contrast to the static case, the photons in this example are only quasi-bound to the moving atoms and will eventually decay at very long times [see Fig. 5.5(b)]. According our effective model (5.11) the eigenvalue equation that gives the bound states is similar to that one written for the static atom case, (4.6), and reads:

$$\omega_\pm - \delta = \frac{\bar{g}^2 a}{2\pi} \int_{-\pi/a}^{\pi/a} \frac{dk}{\omega_\pm - \tilde{\omega}_k}. \tag{5.17}$$

This equation always predicts two non-decaying bound states with eigen-frequencies $\omega_\pm$ outside the propagation band. This is in contrast to the long-time decay observed in Fig. 5.5(b) and moreover such an analysis would also predict the existence of atom-photon bound states at velocities $v > \bar{c}$, which are clearly unphysical.

These paradoxical predictions are a consequence of the effective model approximation used in Eq. (5.11). They disappear when the full time dependence of $g(t)$ is taken into account. As we will extensively discuss in section 5.3 these bound states can decay via additional channels at the sideband frequencies $\omega_a \pm l\Omega$, $l \in \mathcal{N}$ [171]. What happens is that when the atom is moving the bound states associated to the static Hamiltonian are not anymore eigenstates and they becomes quasi-bound state [see [176] for a related discussion]. We emphasize though that all the results shown in Fig. 5.3, Fig. 5.4 and Fig. 5.5 are not artifacts of the approximation and are accurately reproduced by the full model on the timescales of interest.

Photon emission at the speed of light

A new and very unique situation occurs when the atomic velocity matches the maximum speed of light, $v = \bar{c}$. In this case the dispersion relation presents a plateau in the middle of the band with $\tilde{v}_g(k) \simeq 0$ as shown in Fig. 5.13(c). The dispersion relation can then be approximated as cubic

$$\tilde{\omega}_k \simeq -\pi J - \frac{Ja^3}{3}(k - k_c)^3, \tag{5.18}$$

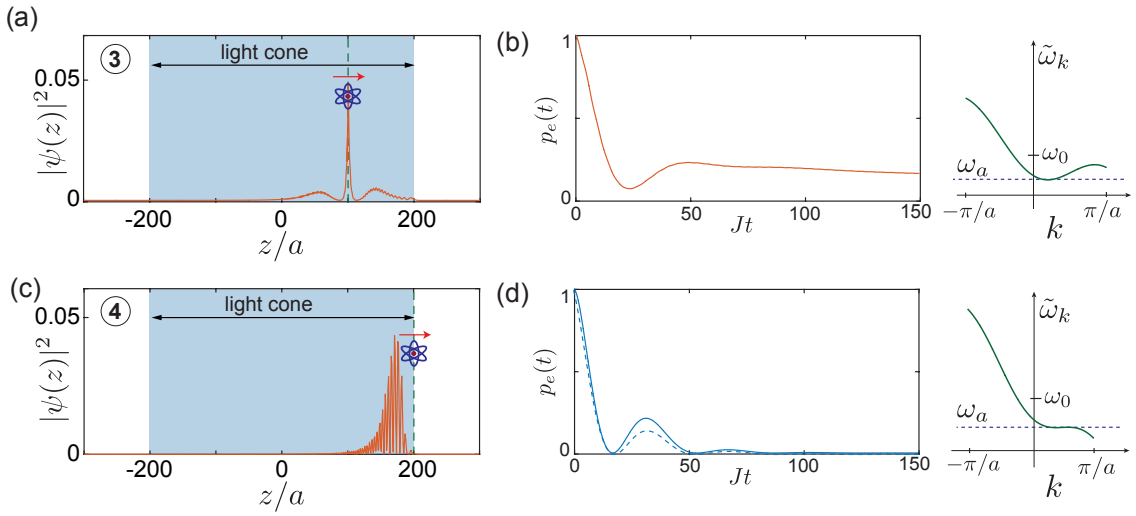

Figure 5.5: Same plots as in Fig. 5.4 with different parameters. In (a)-(b) $v = \bar{c}/2$, $\delta/(2J) = -1.1$ while in (c)-(d) $v = \bar{c}$, $\delta/(2J) = -\pi/2$. In (d) the dashed line indicates the approximate analytic result given in Eq. (5.35) for $v = \bar{c}$ and $\delta = -\pi J$.

for wavevectors around $k_c = \pi/(2a)$. This results in a higher order divergence $\sim (\omega - \pi J)^{-2/3}$ in the effective photonic density of states. However, in contrast to usual band-edge effects, this velocity-induced singularity lies in the middle of the propagation band and for moderate $\bar{g}$ there is no bound state associated with it. This regime is fully described by the effective model [as underlined by ④ in Fig. 5.3], and the corresponding dynamics is shown in Fig. 5.5 (c)-(d). Here the divergence results in strong non-Markovian interactions between the moving atom and the co-propagating Cherenkov photon with group velocity $v_g(k_c) = v$. We emphasize that this regime exists only for finite bandwidth where the photon group velocity is bounded.

Let us analyze this case in more detail. Here the advantage of the effective model is that it allows us to map this problem to that one of a stationary atom coupled to a photonic band with a cubic dispersion relation (5.18). To simplify the notation we can set $k_c = 0$ and assume the dispersion to be infinite, $k \in (-\infty, \infty)$. This last assumption is valid as long as the coupling strength is smaller than the bandwidth $\bar{g} \ll 4J$. Since the bandwidth of this cubic model is infinite, all eigenstates are scattering states of the form:

$$|\phi_k\rangle = \left[c_e^k \sigma_+ + \int dk'\, \psi_k(k') a_{k'}^\dagger\right]|g\rangle|\text{vac}\rangle, \tag{5.19}$$

with energy $E_k = \hbar\tilde{\omega}_k$. From the Schrödinger equation $\tilde{H}|\phi_k\rangle = E_k|\phi_k\rangle$ we obtain

$$c_e^k(\tilde{\omega}_k - \omega_a) = \bar{g}\sqrt{\frac{a}{2\pi}} \int dk' \psi_k(k')\,, \tag{5.20}$$

while the Lippmann-Schwinger equation for the photonic wavefunction reads [60,

158]

$$\psi_k(k') = \sqrt{\frac{a}{2\pi}}\frac{\bar{g}c_e^k}{\tilde{\omega}_k - \tilde{\omega}_{k'} + i\epsilon} + \delta(k-k'). \tag{5.21}$$

Here the limit $\epsilon \to 0^+$ is assumed to obtain the correct boundary conditions. By inserting Eq. (5.21) back into Eq. (5.20) the atomic amplitude can be written in a closed form as

$$c_e^k = \sqrt{\frac{a}{2\pi}}\frac{\bar{g}}{\tilde{\omega}_k - \omega_a - \bar{g}^2\mathcal{I}_0(\tilde{\omega}_k)}. \tag{5.22}$$

Here we have introduced the integral

$$\begin{aligned}\mathcal{I}_z(\tilde{\omega}_k) = \frac{a}{2\pi}\int \frac{e^{ik'z}dk'}{\tilde{\omega}_k - \tilde{\omega}_{k'} + i\epsilon} = -\frac{\mathrm{sgn}(k)\sqrt{3}+i}{2Ja^2k^2} \\ \times\left(e^{-i\frac{kz}{2}-\frac{\sqrt{3}}{2}|kz|} + \theta(-z)e^{i\frac{2}{3}\pi\mathrm{sgn}[k]+ikz}\right),\end{aligned} \tag{5.23}$$

where $\mathrm{sgn}(k)$ is the sign function and $\theta(z)$ is the Heaviside function with $\theta(z=0)=0$. The scattering states can then be written in momentum space as

$$|\phi_k\rangle = \left[c_e^k\sigma_+ + a_k^\dagger + \sqrt{\frac{a}{2\pi}}\int dk'\frac{\bar{g}c_e^k a_{k'}^\dagger}{\tilde{\omega}_k - \tilde{\omega}_{k'} + i\epsilon}\right]|g\rangle|\mathrm{vac}\rangle. \tag{5.24}$$

Finally, to evaluate the photonic wavefunction $\psi_k(z) = \frac{1}{\sqrt{2\pi}}\int dk'\psi_k(k')e^{ik'z}$ in position space, we make again use of the integral in Eq. (5.23) and we obtain

$$\psi_k(z) = \frac{1}{\sqrt{2\pi}}\left[e^{ikz} + \gamma_k\left(e^{-i\frac{kz}{2}-\frac{\sqrt{3}}{2}|kz|} + \theta(-z)e^{i\frac{2}{3}\pi\mathrm{sgn}[k]+ikz}\right)\right], \tag{5.25}$$

with the scattering amplitude

$$\gamma_k = \frac{\bar{g}^2 I_0(\tilde{\omega}_k)}{\tilde{\omega}_k - \omega_a - \bar{g}^2 I_0(\tilde{\omega}_k)}. \tag{5.26}$$

These scattering states are very a-typical compared to usual linear or quadratic dispersion [see Sec.2.3] since independent on the direction of the incoming wavevector k. This means that the scattered wave vanishes at $z \to +\infty$, while it is finite at $z \to -\infty$. This can be understood from the particularity of the assumed dispersion relation, which always leads to negative group velocities.

Using the exact scattering solutions we can investigate the spontaneous emission of an initially excited atom. In this case the atom-field dressed state $|\psi(t)\rangle = \left[c_e(t)\sigma_+ + \int dk\,\psi(k,t)a_k^\dagger\right]|g\rangle|\mathrm{vac}\rangle$ can be expressed in terms of the eigenstates of the system according to

$$|\psi(t)\rangle = \int dk\,(c_e^k)^* e^{-i\tilde{\omega}_k t}|\phi_k\rangle, \tag{5.27}$$

and we obtain $c_e(t) = \langle e|\psi(t)\rangle$ and the emitted photonic wave packet

$$\psi(z,t) = \langle z|\psi(t)\rangle = \int dk\,\psi_k(z)(c_e^k)^* e^{-i\tilde{\omega}_k t}, \tag{5.28}$$

in terms of integrals over k. These results perfectly agree with the numerics presented in Fig. 5.5 (c)-(d).

To derive a simpler approximate result for the atomic population it is more convenient to consider instead directly the equations of motion for $c_e(t)$ and $\psi(k,t)$. In a frame rotating with $\omega_c = \omega_a - \delta$ they are given by

$$\dot{c}_e^k = -i\delta c_e(t) - i\bar{g}\sqrt{\frac{a}{2\pi}}\int dk'\psi_k(k',t), \tag{5.29}$$

$$\dot{\psi}(k,t) = i\frac{J}{3}(ka)^3\psi(k,t) - i\bar{g}\sqrt{\frac{a}{2\pi}}c_e(t). \tag{5.30}$$

By performing a Laplace transformation we obtain for the atomic amplitude

$$c_e(s) = \frac{1}{s + i\delta + \bar{g}^2\mathcal{I}(s)}, \tag{5.31}$$

where

$$\mathcal{I}(s) = i\frac{a}{2\pi}\int \frac{dk}{J(ka)^3/3 + is} = (9Js^2)^{-1/3}. \tag{5.32}$$

For vanishing detuning, i.e., $\omega_a = \omega_c$, we can further rewrite $c_e(s)$ as

$$\begin{aligned} c_e(s) = &\frac{1}{s + i\bar{g}\left(\frac{s}{9J}\right)^{1/6}} + \frac{1}{s - i\bar{g}\left(\frac{s}{9J}\right)^{1/6}} \simeq \\ &\frac{1}{s + i\Omega_c + \Gamma_c/2} + \frac{1}{s - i\Omega_c + \Gamma_c/2}, \end{aligned} \tag{5.33}$$

where in the last step we made a single pole approximation introducing the effective rates that describe the coherent atom-photon oscillations and the overall decay

$$\Omega_c = \frac{\sqrt{5+\sqrt{5}}}{2\sqrt{2}}\left(\frac{\bar{g}^6}{9J}\right)^{\frac{1}{5}}, \qquad \Gamma_c = \frac{\sqrt{5}-1}{2}\left(\frac{\bar{g}^6}{9J}\right)^{\frac{1}{5}}. \tag{5.34}$$

Under this approximation the inverse Laplace transform of $c_e(s)$ results in a damped cosine function

$$p_e(t) \simeq \cos^2(\Omega_c t)e^{-\Gamma_c t}, \tag{5.35}$$

which approximates well the the non-Markovian decay of the atomic population as shown by the dashed line in Fig. 5.5 (d). The oscillatory dependence of $p_e(t)$ and the unusual scaling, $\Omega_c, \Gamma_c \sim \bar{g}^{6/5}$, demonstrate that atom-light interactions in this critical parameter regime are highly non-perturbative and show a clear strong coupling behavior already at the level of individual photons. For a given $\bar{g} \ll J$, Γ_c is also the fastest rate at which the atom can be completely deexcited by emitting a highly localized photonic wave packet [see Fig. 5.5 (c)], which closely follows the atom in forward direction.

At even higher velocities, $v > \bar{c}$, the density of states, and therefore also the emission rate, decreases again. As shown in Fig. 5.3, the directionality of the emitted photon in the laboratory frame is then only determined by the condition $\delta \lessgtr -2J$. For the specific detuning $\delta = -2J$, a very extended and essentially stationary photonic wavepacket is produced.

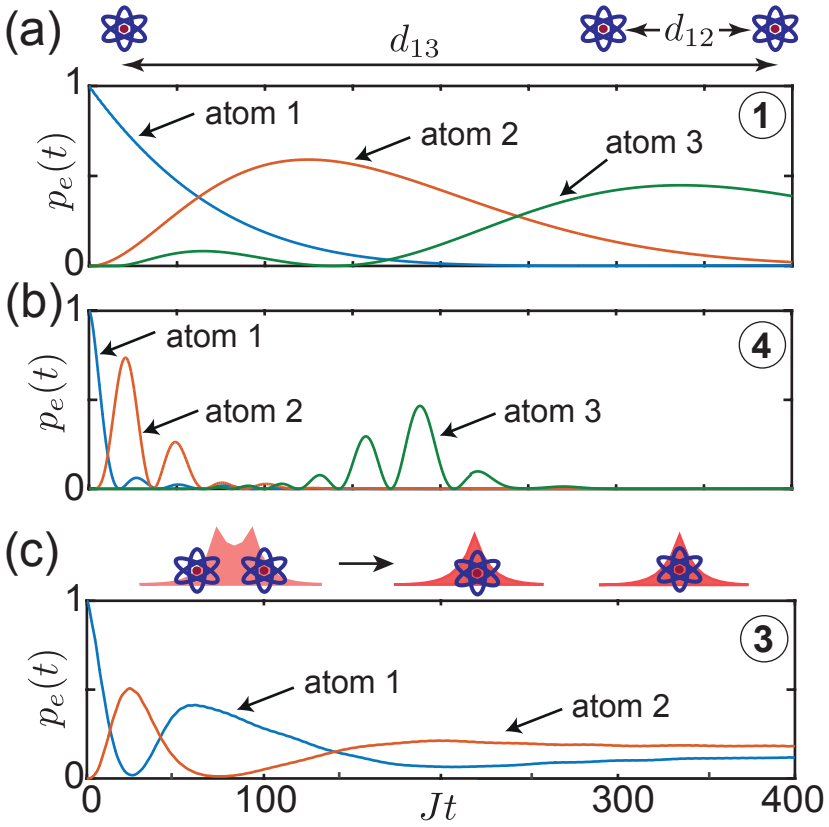

Figure 5.6: Excitation transfer between moving atoms. In the first two plots three atoms moving with the same velocity $v > 0$ and relative separations $d_{12}/a = 2$ and $d_{13}/a = 45$ are considered. The parameters in (a) are $v = \bar{c}/2$ and $\delta/(2J) = 1$ and in (b) $v = \bar{c}$ and $\delta = -\pi J$. For the plot in (c) two atoms with $z_1(0) = z_2(0)$, slightly different velocities $v_1 = 0.5\bar{c}$ and $v_2 = 0.53\bar{c}$ and a detuning of $\delta/(2J) = -1.1$ have been assumed. In all plots $\bar{g}/(2J) = 0.1$.

5.2.2 Excitation transfer processes

Compared to conventional Cherenkov radiation studied in higher dimensional structures [170, 171], a key feature of the current setting is that all emitted photons are confined to one dimension and can thus be efficiently reabsorbed by other atoms. For conventional waveguides with static atoms, this emission and reabsorption of photons gives rise to almost instantaneous, long-range and bidirectional dipole-dipole interactions, which depend only on the relative atomic positions $|z_i - z_j|$, as discussed in 2.2.1. In our narrow-bandwidth waveguide setup with moving atoms this picture changes qualitatively and different excitation transfer processes arise, depending strongly on the velocities and detunings of the involved atoms.

To illustrate this point we first consider in Fig. 5.6 (a) and (b) the case of $N_a = 3$ atoms moving at the same speed $v > 0$, with the first atom to the right being initially prepared in the excited state. For this plot we have solved the evolution of

the generalized wavefunction $|\psi(t)\rangle = \big[\sum_{i=1}^{N} c_e^i(t)\sigma_+^i + \sum_k \psi(k,t)a_k^\dagger\big]|g\rangle|\text{vac}\rangle$ under the action of Hamiltonian (5.11).

With all the atoms at rest, under the usual Markov approximation, and assuming that the propagation time of the photons can be neglected, the maximal population transfer from atom 1 to atoms 2 and 3 is limited to $p_e^{(2,3)}(t) < 0.25$. This result, discussed in sections 2.2.1 and 2.3.3, can be understood from a decomposition of the initial atomic excitation into super- and sub-radiant states and depends in detail on the exact atomic positions.

This limit no longer applies at moderate and fast velocities, where the emission becomes highly directional and therefore also results in a much more efficient transfer of excitations from the right to the left. This is shown in Fig. 5.6 (a), where the same parameters as in example ① in Fig. 5.4 for a completely unidirectional photon emission have been assumed. In this regime the excitation transfer process is the same as that one described in chiral waveguide QED systems [see Sec. 2.2.2]. Note that for these parameters the retardation time $\tau_{13} = |d_{13}/(v_g(k_L) - v)|$ is still short compared to the timescale of the transfer dynamics ($\sim \Gamma_L^{-1}$) and the whole process can be well described by a unidirectional Markovian master equation [21, 26] in the co-moving frame.

This is no longer the case for the critical condition $v = \bar{c}$ and $\delta/J = -\pi$ assumed in Fig. 5.6 (b) when the atom is moving at the maximum speed of light. Here we observe a very rapid transfer of the initial excitation from atom 1 to atom 2, which is mediated by the highly compressed Cherenkov photon shown in example ④ in Fig. 5.5(c). This photon then slowly falls behind and at a much later time overlaps with the third atom. The resulting oscillations between the photon and atom 3 with roughly the same Rabi frequency Ω_c as identified in Eq. (5.35), are again a clear signature of the highly non-Markovian nature of the transfer process.

Finally, in Fig. 5.6 (c) we consider the example of the kind described by ③ [see Sec. 5.2.1]. Here two initially co-propagating atoms exchange excitations via a co-moving bound photon which remains exponentially localized around the atomic positions $z_i(t)$. By introducing a small velocity difference, i.e. $v_1 \neq v_2$, the atoms slowly separate and gradually decouple. Depending on the detailed choice of parameters, the photon may remain with one of the atoms or be split into two separated atom-photon bound states.

5.3 Validity of the effective model

Our discussion so far has been based on the approximate model given in Eq. (5.11), which ignores the time-periodic modulation of the coupling with multiples of the frequency $\Omega = 2\pi|v|/a$. To understand more precisely, under which conditions this description is meaningful let us consider again the evolution of the generic state

$$|\psi(t)\rangle = \Big[\sum_i c_e^i(t)\sigma_+^i + \sum_k \psi(k,t)a_k^\dagger\Big]|g\rangle|\text{vac}\rangle \tag{5.36}$$

under the full Hamiltonian (5.2). We obtain the following set of equations

$$\begin{aligned}\frac{dc_e^i(t)}{dt} &= -ig\sqrt{\frac{a}{L}}\sum_k \psi(k,t)u_{ki}(t)e^{i\tilde{\delta}_k^i t}e^{ikz_i},\\ \frac{d\psi(k,t)}{dt} &= -ig\sqrt{\frac{a}{L}}\sum_j c_e^j(t)u_{kj}^*(t)e^{-i\tilde{\delta}_k^j t}e^{-ikz_j},\end{aligned} \tag{5.37}$$

where $\tilde{\delta}_k^i = \omega_a - (\omega_k - v_i k)$ and $u_{ki}(t) \equiv u_k(z_i(t))$. After inserting the second equation into the first we obtain the following integro-differential equation

$$\frac{dc_e^i(t)}{dt} = -\frac{g^2 a}{L}\sum_j\sum_k e^{ik(z_i-z_j)}u_{ki}(t)e^{i\tilde{\delta}_k^i t}\times\int_0^t dt' u_{kj}^*(t')e^{-i\tilde{\delta}_k^j t'}c_e^j(t'). \tag{5.38}$$

The $u_{ki}(t)$ are periodic in time and can be expanded in a Fourier series $u_{ki}(t) = \sum_n u_{ki}^n e^{i\Omega_i n t}$. The resulting expression can be written as

$$\begin{aligned}\frac{dc_e^i(t)}{dt} &= -\frac{g^2 a}{L}\sum_j\sum_k\sum_{n,m} u_{ki}^n[u_{kj}^m]^* e^{ik(z_i-z_j)}e^{i(\tilde{\delta}_k^i-\tilde{\delta}_k^j)t}e^{i(\Omega_i n-\Omega_j m)t}\int_0^t dt' e^{i\tilde{\delta}_k^j(t-t')}e^{i\Omega_j m(t-t')}c_e^j(t')\\ &= -\frac{g^2 a}{L}\sum_j\sum_k u_{ki}^0[u_{kj}^0]^* e^{ik(z_i-z_j)}e^{i(\tilde{\delta}_k^i-\tilde{\delta}_k^j)t}\int_0^t dt' e^{i\tilde{\delta}_k^j(t-t')}c_e^j(t') + \text{rest}.\end{aligned} \tag{5.39}$$

When evaluated in the stroboscopic limit $\Omega_i \gg g$, the first term in the second line of this equation simply corresponds to the evolution under the effective model given in Eq. (5.11). A first set of corrections arises from terms with $n \neq 0$, but $m = 0$. Such terms lead to additional oscillating contributions to $c_e^i(t)$. However, as long as $g \ll \Omega_i$, these corrections remain small and do not affect the long time behavior of $c_e^i(t)$.

More crucial are terms with $n = m \neq 0$, which can generate non-oscillating contributions that affect the slowly varying dynamics of $c_e^i(t)$. To see this more explicitly, let us consider a single atom and a specific correction term

$$\begin{aligned}\left.\frac{dc_e(t)}{dt}\right|_{n=m} &= -\frac{g^2 a}{L}\sum_k |u_k^n|^2\int_0^t dt' e^{i\tilde{\delta}_k(t-t')}e^{i\Omega n(t-t')}c_e(t')\\ &\approx -\left[\frac{\pi g^2 a}{L}\sum_k |u_k^n|^2\delta\left(\tilde{\delta}_k^i + \Omega_i n\right)\right]c_e(t),\end{aligned} \tag{5.40}$$

where in the second line we have made a Markov approximation and replaced the integral over t by a δ-function in frequency. From this estimate we see that the higher order correction terms introduce additional decay channels with rates $\Gamma^{(n)}$ proportional to the density of states evaluated at the modulation frequencies $\omega_a - (\omega_k - vk) + n\Omega$, where $n = \pm 1, \pm 2, \ldots$. To ensure that such corrections do not affect the dynamics, all sidebands $\omega_a + n\Omega$ must lie outside the tilted propagation band, as illustrated in Fig. 5.7 (a). This condition can be recast into the form

$$\Omega = \frac{2\pi|v|}{a} > \max_k\left|\frac{\delta + 2J\cos(ka)}{1 - \frac{ak}{2\pi}}\right|, \tag{5.41}$$

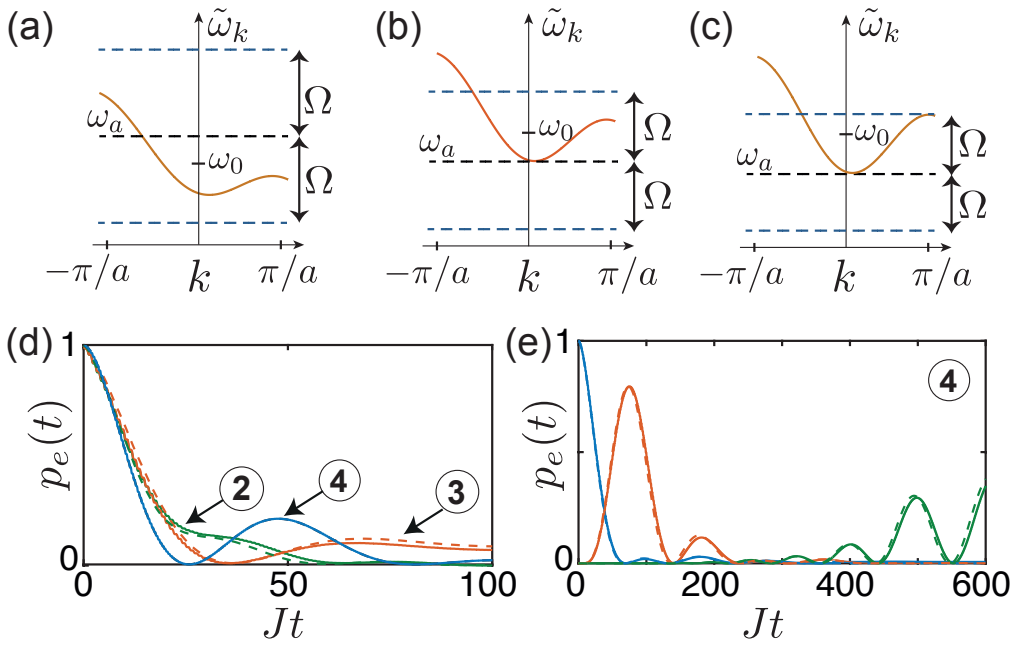

Figure 5.7: (a)-(c) The positions of the modulation frequencies $\omega_a \pm \Omega$ are shown in relation to the tilted photonic band for (a) $v/\bar{c} = 0.5$ and $\delta/(2J) = 1$, (b) $v/\bar{c} = 0.3$ and $\delta/(2J) = -1.05$ and (c) $v/\bar{c} = 0.22$ and $\delta/(2J) = -1$. In (d) and e) the evolution of the excited state population as predicted by the full model in Eq. (5.2) (continuous line) is compared with the corresponding evolution under the effective continuum model in Eq. (5.11) (dashed line). (d) Decay of the excited state population corresponding to the cases: $v = \bar{c}/2$ and $\delta/(2J) = -0.5$, $v = \bar{c}/2$ and $\delta/(2J) = -1.1$ and $v = \bar{c}$ and $\delta/(2J) = -\pi/2$.(e) Excitation transfer between three atoms with $v = \bar{c}$ and $\delta/(2J) = -\pi/2$. In all the plots $g/(2J) = 0.1$ and $z_0/a = 0.1$ is assumed. All the other parameters are the same as in the respective examples in Fig. 5.4 and Fig. 5.6.

and implies that our effective description for the slow-light waveguide is only possible for high enough velocities, $|v| \gtrsim 0.25\bar{c}$, and for atomic frequencies inside the tilted propagation band. This simple picture also explains why there are no bound states, e.g., in the gap above the upper band edge, $\omega_+ \gtrsim \tilde{\omega}_{\max} = \omega_0 + 2J + \Omega/2$. In this case the sideband $\omega_+ - \Omega$ is necessarily inside the propagation window and leads to a rapid decay.

While Eq. (5.41) captures very well the main region of validity of Eq. (5.11), it is too strict in certain regimes. In particular, this is the case for moderately slow atoms tuned to the lower band edge, $\omega_a \simeq \tilde{\omega}_{\min}$. As indicated in Fig. 5.7 (b), for these parameters the condition (5.41) can be violated, but the dynamics is still well approximated by the effective model. The reason is that the additional decay $\Gamma^{(1)}$ associated with the sideband $\omega_a + \Omega$ is simply very slow compared to the dominant evolution determined by the high density of states near the band edge. This explains why quasi-bound states near the lower band edge can be observed at finite velocities.

However, since $\Gamma^{(1)}$ is non-zero, these bound states still decay on longer timescales.

To verify the validity of our analytic estimates we compare directly the predictions from the effective model (5.11) with a numerical simulation of the full model (5.2), which accounts for the exact time-dependence of the couplings. To do so we consider the specific example, where the local mode at each lattice site is represented by a Gaussian wavepacket

$$\bar{u}(z) = \frac{1}{\pi^{1/4}}\sqrt{\frac{a}{z_0}}e^{-\frac{z^2}{2z_0^2}}, \tag{5.42}$$

with a width $z_0 \ll a$. This results in an averaged coupling $\bar{g} \simeq g\sqrt{\frac{2z_0}{a}}\pi^{1/4}$. For the simulation of the full model we assume $g/(2J) = 0.1$ and $z_0/a = 0.1$. This corresponds to $\bar{g}/(2J) \simeq 0.06$. For these parameters we compare in Fig. 5.7 (d) and (e) the excited state population predicted by the effective model and the full model for some of the values of δ and v assumed in Fig. 5.4, Fig. 5.5 and Fig. 5.6. For all these cases we see an excellent agreement between the exact and the effective evolution. More generally, we evaluate the evolution of the excited state population $p_e(t)$ for a single atom up to a final time $T_\mathrm{f} = 50/J$ for a wide range of parameters δ and v. Then, the discrepancy parameter

$$d = \max\{|p_e^{\mathrm{eff}}(t) - p_e^{\mathrm{full}}(t)|, 0 < t < T_f\}, \tag{5.43}$$

can be used to quantify the validity of the effective model. The black dashed line in Fig. 5.3 exactly indicates the boundary set by the requirement $d \leq 0.1$. For most parameters, this boundary reproduces the condition identified in Eq. (5.41). However, near $\delta \approx -2J$ the region of validity extends to very low velocities, which can be explained by the qualitative arguments given above. We also see an additional kink at $v/\bar{c} \simeq 0.22$ and $\delta/(2J) = -1$. As shown in Fig. 5.7 (c), in this case also the $(\omega_a + \Omega)$ sideband hits a divergence in the photonic density of states and therefore induces a significant perturbation. In conclusion, we find that, within the region of parameters delimited by the dashed line in Fig. 5.3, the effective model (5.11) provides an accurate description of the dynamics and we can replace the modulated couplings $g(z_i(t))$ by the coupling $\bar{g}$ averaged over one period, $T = 2\pi/\Omega$.

5.4 Implementation

While the approach described so far for realizing the slow-light Hamiltonian (5.11) is very generic and can in principle be implemented with various photonic waveguide structures, the conditions for achieving a strong coupling between moving atoms and co-propagating photons are in practice very demanding. In particular, for atomic velocities $v < 10^4$ m/s and lattice constants of $a > 10\,\mu$m, the condition $\bar{c} \sim v$ restricts the maximal bandwidth to $J/(2\pi) \approx v/(4a\pi) < 80$ MHz, while it must still exceed the level of on-site disorder to avoid localization [159, 160, 49]. In addition, the atoms must be guided close to the surface of the waveguide such that the rate of

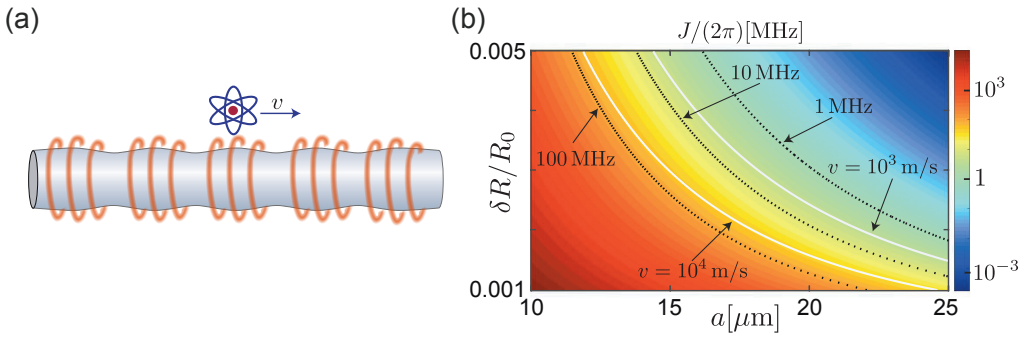

Figure 5.8: a) Realization of an optical slow-light waveguide QED system using atoms coupled to the evanescent field of a silica fiber with a periodically modulated radius. Note that in this setup a natural reduction of the photonic speed already arises from the fact that the light does not propagate in a straight line, but rather around the circumference of the fiber. b) The tunneling amplitude $J/(2\pi)$ is plotted (in a logarithmic scale) as a function of the lattice constant a and the radial variation $\delta R/R_0$. The white continuous lines indicate the condition $v = \bar{c} = 2Ja$. For this plot a cutoff frequency of $\omega_e/(2\pi) \simeq 350$ THz ($\ell = 180$) and a radius $R_0 = 17.5\,\mu$m has been assumed. In order to avoid mixing with the neighboring transverse branches, the radial variation has been limited to $\delta R_0/R_0 < 1/\ell \simeq 0.0056$.

emission into the waveguide, Γ, exceeds the decay rate into free space, γ_a, as well as the photon loss rate, γ_c.

In the following we first show in Sec. 5.4.1 how such extreme slow-light conditions can in principle be achieved in the optical regime. As example we focus on the whispering gallery modes of a periodically modulated optical fiber. This setup was introduced in Sec. 3.2 and recently SNAP waveguides [146] with a high level of disorder control have been demonstrated [147]. In Sec. 5.4.2 we then describe an alternative setup in the microwave regime, where many of the remaining experimental difficulties can be overcome by simply working with much larger wavelengths.

5.4.1 Modulated optical waveguides

We consider a cylindric silica fiber with radius R_0 and refractive index n. As illustrated in Fig. 5.8 (a), the fiber supports optical modes, where light is guided around the circumference of the waveguide [146, 143] and couples evanescently to nearby atoms [104, 105]. We assume in addition a small periodic modulation of the fiber radius,

$$R(z) = R_0 + \delta R \cos\left(\frac{2\pi z}{a}\right), \tag{5.44}$$

with a period a that is large compared to the wavelength $\lambda_e = 2\pi c/(n\omega_e)$. This modulation $R(z)$ results in a variation of the cutoff frequency, $\omega_e(z) = \omega_e R_0/R(z)$, which corresponds to an effective potential

$$V(z) = \hbar\omega_e(\delta R/R_0)\cos(2\pi z/a) \tag{5.45}$$

for the photons propagating along z.

The eigenmodes $\vec{\Phi}_k(\vec{r})$ of the electric field in the waveguide with frequency ω_k and wavevector k along the z direction are solutions of the Helmholtz equation

$$\left[\Delta + n^2(\vec{r})\frac{\omega_k^2}{c^2}\right]\vec{\Phi}_k(\vec{r}) = 0, \tag{5.46}$$

where $n(\vec{r})$ is the refractive index that assumes the values $n(\vec{r}) = n \simeq 1.47$ inside the fiber and $n(\vec{r}) = 1$ outside. In view of the cylindrical symmetry we change to polar coordinates and make the ansatz $\vec{\Phi}_k(\vec{r}) = \vec{\chi}_\ell(r,z)\psi_k(z)e^{i\ell\phi}$, where ℓ is the azimuthal mode index. The radial component $\vec{\chi}_\ell(r,z)$ satisfies the radial Helmholtz equation for a given $R(z)$ and corresponding eigenfrequency $\omega_e(z) = \frac{\ell c}{\bar{n}c_r R(z)}$. Here $\bar{n}$ denotes the effective refractive index averaged over the radial mode profile and c_r is a correction factor that accounts for the finite radial width of the mode function [144]. For a TM mode, i.e., $\vec{\chi}_\ell = \chi_{\ell,z}\vec{e}_z$, the unnormalized radial mode functions are given by [143, 144, 145, 179]

$$\begin{aligned}
\chi_{\ell,z}(r,z) &= J_\ell\left(k_0(z)nr\right),\ r \le R(z),\\
\chi_{\ell,z}(r,z) &= \left(\frac{J_\ell(k_0(z)nR(z))}{Y_\ell(k_0(z)R(z))}\right)Y_\ell\left(k_0(z)r\right),\ r > R(z),
\end{aligned} \tag{5.47}$$

where $J_\ell(x)$ and $Y_\ell(x)$ are Bessel functions of the first and second kind and $k_0(z) = \omega_e(z)n/c$. Given a certain frequency ω_e the fiber radius and the azimuthal number ℓ are related by the resonance condition

$$n\frac{J_\ell'(k_0(z)nR(z))}{J_\ell(k_0(z)nR(z))} - \frac{Y_\ell'(k_0(z)R(z))}{Y_\ell(k_0(z)R(z))} = 0. \tag{5.48}$$

By making a paraxial approximation, valid for $\delta R/a \ll 1$, we neglect the derivatives of $\vec{\chi}_\ell(r,z)$ with respect to z and we obtain

$$\left[\frac{\partial^2}{\partial z^2} + \frac{\bar{n}^2}{c^2}(\omega_k^2 - \omega_e^2(z))\right]\psi_k(z) = 0. \tag{5.49}$$

By introducing the eigenenergies $E_k = \hbar(\omega_k - \omega_e)$ and the effective potential $V(z)$ definition used in (5.45) this equation can be re-arranged as an effective Schrödinger equation:

$$\left[-\frac{\hbar^2}{2m^*}\frac{\partial^2}{\partial z^2} + V(z)\right]\psi_k(z) = E_k\psi_k(z), \tag{5.50}$$

This means that for a given branch with a cutoff frequency $\omega_e = \frac{\ell c}{nR_0}$ determined by the azimuthal quantum number ℓ, the dispersion relation for small wavevektors k along the z-direction is approximately given by

$$\omega_k \simeq \omega_e + \frac{\hbar k^2}{2m^*}, \tag{5.51}$$

where $m^* = \omega_e n^2 \hbar / c^2 \sim 10^{-36}$ kg is the effective photon mass. This effective description is along the same line of the simple slow-light model presented in section 3.2.1. The solution of Eq. (5.50) provides the dispersion relation E_k and the Bloch waves $\psi_k(z)$ entering the model in Eq. (5.2). In the tight-binding limit J can be numerically estimated from the width of the first energy band, i.e., $J = (\max\{\omega_k\} - \min\{\omega_k\})/4$. For the specific example of a fiber with radius $R_0 = 17.5\,\mu$m and $\omega_e/(2\pi) \simeq 350$ THz [144, 145] the resulting range of values for J is plotted in Fig. 5.8 (b) for varying parameters a and δR.

From Fig. 5.8 (b) we see that for lattice constants in the range of $a \sim 10 - 20\,\mu$m we can obtain by this approach a tunnel coupling of $J/(2\pi) \approx 80$ MHz together with an effective speed of light of $\bar{c} = 10^4$ m/s.

To estimate the atom-photon coupling let us consider the absence of the periodic modulation. The atom field coupling strength evaluated at the surface of the fiber reads

$$g = d\sqrt{\frac{\omega_k}{2\hbar\epsilon_0 a A}}|\vec{\chi}_\ell(R_0)|. \tag{5.52}$$

Here ϵ_0 is the vacuum permittivity, $d \simeq 2 \times 10^{-29}$ Cm is the dipole moment of a ^{133}Cs atom and A is the mode area defined as [143, 144]

$$A = \pi\left(n^2 \int_0^{R_0} dr r J_\ell^2(k_0 n r) + \frac{J_\ell^2(k_0 n R_0)}{Y_\ell^2(k_0 R_0)} \int_{R0}^{\infty} dr r Y_\ell^2(k_0 r)\right). \tag{5.53}$$

The radial modulation gives an approximate quadratic potential for the photons in each lattice site. Thus, the local modes can be represented by Gaussian wavepackets of the form given in Eq. (5.42). This leads to an effective coupling $\bar{g} \simeq g\pi^{1/4}\sqrt{2z_0/a}$ as assumed for all our estimates.

For the same fiber parameters used to determine J we can estimate an atom-photon coupling of $g/(2\pi) \simeq 30 - 40$ MHz , in agreement with coupling constants measured for bottle resonators of similar dimensions [145]. This translates into an averaged coupling of $\bar{g}/(2\pi) \approx 10 - 20$ MHz, consistent with the requirements for the derivation of the effective model. At the same time, this coupling can exceed both the atomic decay rate, $\gamma_a/(2\pi) \simeq 2$ MHz, as well as photonic losses, $\gamma_p/(2\pi) \simeq 0.5$ MHz [145].

On the other end an ubiquitous problem of slow-light waveguides and coupled resonator arrays are unintented, fabrication-related variations of the local frequency, $\omega_e \to \omega_e(z)$. This additional random potential leads to localization of photons, when the bandwidth J becomes too small. In Section. 5.4.3 we present a numerical study of our model in the presence of random on-site energies of magnitude ϵ. From this study we estimate a tolerable level of disorder of $\epsilon/(2J) \leq 0.1$. This translates into maximal variations of the effective fiber radius of $\delta r \simeq R_0\epsilon/\omega_e \simeq 0.05\dot{A}$. Even if this seems a pretty demanding requirement that this level of disorder control is achievable with in-situ tuning techniques, which have already been implemented for tunnel-coupled bottle resonator arrays [147], similar to the setup considered here.

On the other hand maintaining this amount of control on the fabrication could be challenging for an extended waveguide.

In summary, these estimates show that, although challenging, a strong coupling of atoms and photons under the condition $\bar{c} \approx v$ can in principle be realized with modulated photonic waveguide structures. A remaining difficulty is the guiding of atoms at rather high velocities [177, 178] and at a distance of less then the optical wavelength above the waveguide. To overcome this problem it might be more favorable to consider waveguide QED systems in a much lower frequency regime.

5.4.2 Slow-light waveguide QED with microwave photons and Rydberg atoms

Let us now describe an alternative implementation shown in Fig. 5.9 (a), where flying Rydberg atoms [172, 173, 174, 175] are coupled to an array of coplanar waveguide (CPW) resonators.

A CPW resonator consists of a central superconducting track placed between two ground planes printed onto a dielectric substrate as sketched in Fig 5.9. If the coplanar track is cut along the longitudinal direction the edges of the cut act like a mirror and we get a microwave resonator. Here we assume that the resonators are arranged in an array, implementing the coupling between the different sites by additional capacitors, as shown in Fig. 5.9(a).

The electric field of the fundamental mode of this resonator can be written as

$$\vec{E}(x,y,z) = [E_z(z,y)\vec{e}_z + E_y(z,y)\vec{e}_y]\cos\left(\frac{\pi x}{L_x}\right). \tag{5.54}$$

To estimate the transverse electric field profile we consider the limit of an infinitely flat CPW resonator with an additional ground plate located at a distance h below the central track. Further, if the width of the two outer ground planes is larger than twice the gap between them, they can be treated as infinitely extended [180]. With this assumption, an exact solution for the electric field above the central electrode of the CPW resonator can be obtained using conformal mapping techniques [181]. In particular, the two transverse field components are given by $E_z(z,y) = \mathrm{Im}\{E(t)\}$ and $E_y(z,y) = \mathrm{Re}\{E(t)\}$, where $t = z + iy$ and for $y > 0$

$$E(t) = \frac{E_0}{\sqrt{\left(\frac{t^2}{l_1^2} - 1\right)\left(\frac{t^2}{l_2^2} - 1\right)}}. \tag{5.55}$$

For the evaluation of the coupling strength g we need the electric field per photon, $E_0 = \sqrt{\frac{\hbar\omega}{2\epsilon_0 V_r}}$, where V_r the mode volume of the resonator which can be found by imposing the normalization condition

$$\epsilon_0 \frac{L_x}{2}\left[\int_{-\infty}^{\infty} dz \int_{-h}^{\infty} dy \left(E_z^2(z,y) + E_y^2(z,y)\right)\right] = \frac{\hbar\omega}{2}. \tag{5.56}$$

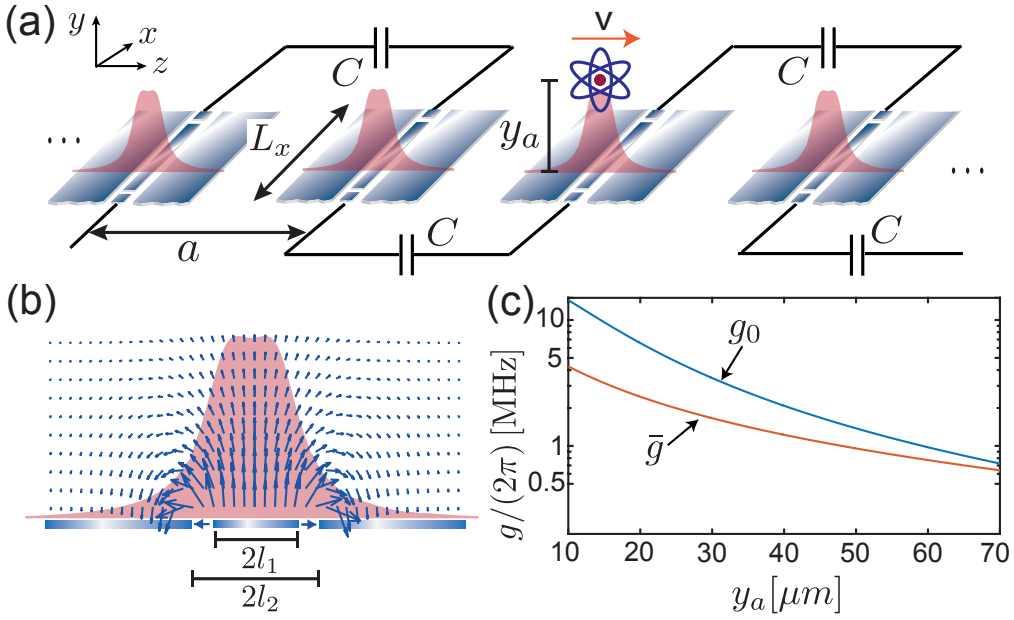

Figure 5.9: Slow-light waveguide QED with Rydberg atoms. (a) Rydberg atoms fly at a distance y_a above an array of parallel CPW resonators coupled by capacitances C. (b) Cross section of a single resonator and sketch of the transverse field distribution. (c) Atom-field coupling strength as a function of the atom-surface distance y_a for the example described in the text. Here g_0 denotes the maximal coupling evaluated at $z = 0$ and $\bar{g}$ the corresponding averaged coupling, which is used in the effective model (5.11).

For the parameters considered in the main text and $h < 5\mu$m, the volume below the central electrode is negligible compare to the mode volume above and only the latter must be considered for the evaluation of the field strength E_0.

With these analytic expressions we can make the following estimates. For a length of $L_x \sim 1$ cm each the CPW resonator exhibits standing wave modes with frequencies $\omega_0 = c\pi/L_x$ in the GHz regime, while in z-direction the electric field is strongly confined to a few tens of μm determined by the size of the middle electrode, $2l_2$ [see Fig. 5.9 (b)]. By considering an array of parallel resonators separated by $a \sim 100\,\mu$m, we obtain a closely spaced resonator array with a tunnel coupling J that can be fully adjusted by additional capacitive couplings at the end-points [139, 148].

As a specific example, we consider a microwave resonator with dimensions $L_x = 0.5$ cm, $l_1 = 10\,\mu$m, $l_2 = 15\,\mu$m and $\omega_0/(2\pi) \approx 30$ GHz. For $a = 200\,\mu$m and an atomic beam of velocity $v = 10^4$ m/s [173] we choose a capacitive coupling $J/(2\pi) = 4$ MHz to obtain $v/\bar{c} \approx 1$. This bandwidth is still considerably above the level of on-site disorder achievable in large arrays of coupled microwave resonators [148]. By identifying two Rydberg states with neighboring principle quantum numbers n, i.e. $|g\rangle = |n\rangle$ and $|e\rangle = |n+1\rangle$, we obtain a resonant coupling $\omega_a = \omega_{n+1} - \omega_n \simeq \omega_0$ for $n \simeq 50$. The resulting maximal atom-field coupling $g_0 = d_{n,n+1}E_0(y_a)/\hbar$ [172, 173], as well as the corresponding averaged coupling, $\bar{g}$, are plotted in Fig. 5.9 (c) where

$d_{n,n+1}$ is the transition dipole moment. We see that already at convenient distances of $y_a \approx 50\,\mu$m we obtain $\bar{g} \sim J/4$ and for the validity of the effective model we can choose any smaller value, e.g. $\bar{g}/J \simeq 0.1$, by adjusting the position of the beam along the x-direction.

On the relevant timescale set by $\Gamma_c/(2\pi) \approx 400$ kHz, both the decay rate of the Rydberg states, $\gamma_a/(2\pi) \simeq 1$ kHz, and the photon loss rate $\gamma_p/(2\pi) \simeq 30$ kHz of a high-Q microwave resonator [182] are still negligible. For an array of ~ 500 resonators with a total length of $L = 10$ cm, the condition on the transverse spread during the flight time, $\Delta y/y_a < 1$, requires a transverse cooling of the atom beam to a few mK, or alternatively, on-chip guiding systems for Rydberg atoms [183].

Finally, regarding the disorder, in Sec. 5.4.3 we estimate a maximum tolerable cavity offset of the order of $\epsilon/(2J) \simeq 0.1$. In the CPW resonators array implementation this would corresponds a variation in the frequency of each resonator of about $\epsilon \simeq 0.8$ MHz. This accuracy is achievable with the state of the art fabrication technology [148]. This shows that all the requirements for slow-light waveguide QED systems can be achieved in the microwave regime, using fabrication and atom-guiding techniques that are currently developed.

5.4.3 Disorder

In this last section we evaluate the influence of disorder on the present slow-light waveguide system. Compare to the analysis performed in 4.1.3, where we were interested in estimating the localization length of a single cavity defect, here we consider a random frequency offset $\delta\omega_l$ at each lattice site l. In momentum space this corresponds to the Hamiltonian

$$H_{\rm dis} = \hbar \sum_{k,k'} f_{k,k'} a_k^\dagger a_{k'}, \tag{5.57}$$

where $f_{k,k'} = \frac{L}{a} \sum_l e^{i(k-k')l} \delta\omega_l$, which we add in our numerical simulation to the original Hamiltonian given in Eq. (5.11). For numerical simulations the $\delta\omega_l$ are chosen randomly from a uniform distribution within the interval $[-\epsilon/2, \epsilon/2]$.

In Fig. 5.10 (a) and (b) we plot the atomic population and the wave function of the emitted photon for the case $v/\bar{c} = 0.5$ and $\delta/(2J) = -0.5$ and for different values of the disorder strength ϵ. From the plots we see that the system dynamics is almost unaffected by the disorder up to values of about $\epsilon/(2J) = 0.1$. Above this value the signatures of a co-moving bound state are washed out. In Fig. 5.10 (c) and (d) we plot the analogue results for the critical coupling conditions $v/\bar{c} = 1$ and $\delta = -\pi J$. Here we find that the atomic decay is even less affected by disorder. However, for $\epsilon/(2J) > 0.1$ the emitted wavefunction is becomes again significantly distorted, which would affect the dynamics of excitation transfer processes. Therefore, we find that all the effects described in Sec. 5.2 are robust with respect to disorder up to a strength of the order of $\epsilon/(2J) \simeq 0.1$.

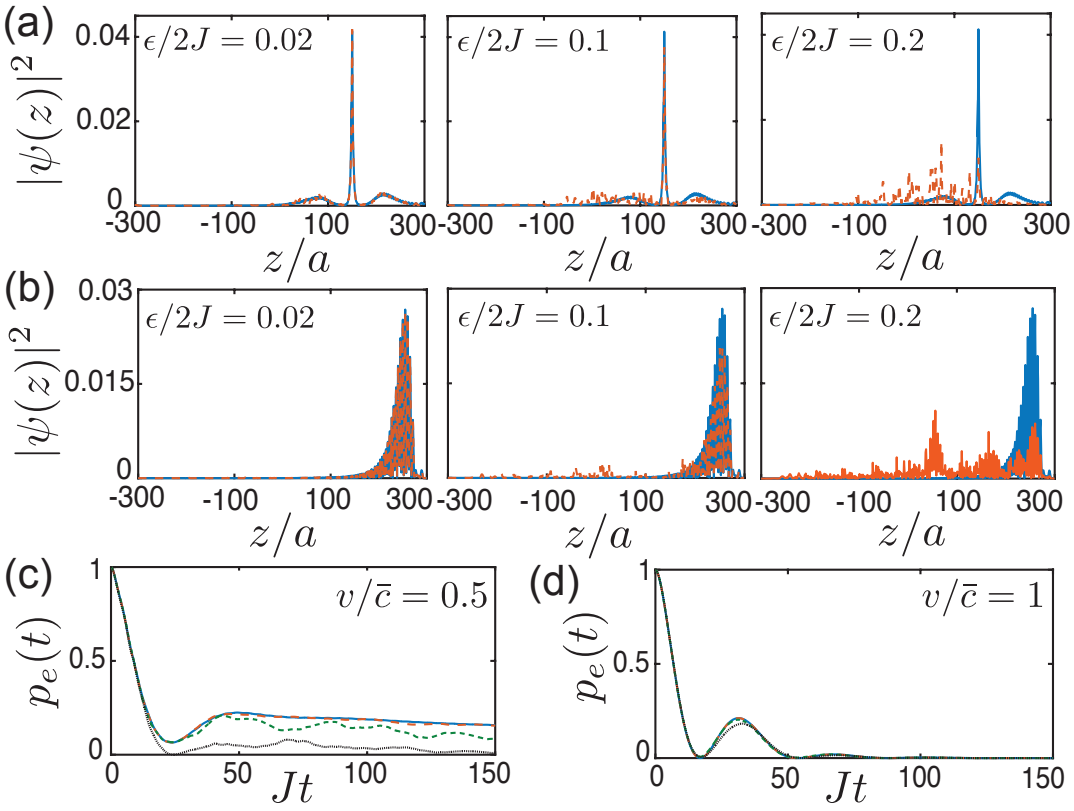

Figure 5.10: The effect of disorder on the system dynamics. The red dashed lines in the plots in (a) and (b) show the emitted photon wavepacket (evaluated at $t = 110/J$) for increasing levels of disorder and for the parameters (a) $v/\bar{c} = 0.5$, $\delta/(2J) = -0.5$ and (b) $v/\bar{c} = 1$, $\delta/(2J) = -\pi/2$. For comparison the case without disorder is represented by the blue solid line. The plots in (c) and (d) show the decay of the excited state population for $\epsilon/(2J) = 0$ (continuous line), $\epsilon/(2J) = 0.02$ (long dashes), $\epsilon/(2J) = 0.1$ (short dashes) and $\epsilon/(2J) = 0.2$ (dotted line). In all plots a coupling of $\bar{g}/(2J) = 0.1$ is assumed.

Chapter 6

Acoustic control of emitter-photon interactions in slow-light waveguide QED

In the last chapter we have seen how in slow-light waveguides the photonic group velocity can be significantly decreased, and we have exploited this effect to study the interaction between moving atoms and co-propagating photons. Here we make a step further by noticing that such a reduced photonic group velocity can even be comparable to the speed of propagating acoustic waves. This effect opens new possibilities where acoustic waves can be used to control the atom-light interaction.

Usually sound and light do not interact strongly with each other due to the difference in frequencies and propagation speed. Nevertheless, under specific conditions, Brillouin scattering, where photons are scattered into orthogonal modes by simultaneously emitting or absorbing phonons, can occur. Recently, many ideas have been proposed to turn such effect around and to use acoustic waves for controlling the propagation of optical fields [184, 185, 186, 187, 188, 189, 190] or for affecting the emission rate of an atom coupled to a photonic crystal [191]. A major limitation to these proposals lies in the fact that, for large photonic bandwidth, the Brillouin scattering occurs only at specific resonances. The situation is much different in a slow-light waveguide modulated by strong acoustic waves. In this case the photonic band, due to its finite width, can be deformed and tilted by the acoustic wave giving rise to scenarios that go beyond usual Brillouin scattering.

Here we consider atomic or solid-state emitters coupled to such an acousto-optical waveguide. When the photonic group velocity becomes comparable to the speed of sound, a full directional emission of the atoms can occur for a wide range of frequencies. Moreover, similar to the moving atoms case analyzed in the previous chapter, the acoustic modulation can induce divergencies of the density of states, which can affect the emission rates of the emitters.

A crucial point of this setup is that the directional emission can be controlled by properly tuning the acoustic wave parameters. This effect provides a flexible tool

for controlling emitter-emitter interactions in extended optical networks, and it can be used, for example, for the generation of stationary entanglement or the shuttling of quantum states via phononic conveyor belts.

This idea of modulating photonic structures with acoustic waves brings even more interesting results when the model is extended to two dimensional photonic lattices. In particular we show how, by modulating a 2D photonic structure with propagating acoustic waves, it is possible to obtain a new type of chiral quantum optics in two dimensions, where photons are emitted into a single, highly focused beam with a slow radial decay.

In the last part of the chapter, we discuss the general conditions to implement and observe all these effects. In particular, we propose a possible implementation consisting of solid-state defects coupled to a photonic crystal structure modulated by a propagating surface acoustic wave.

For this work I performed all the analytic and numerical calculations under the supervision of P. Rabl. A publication of these results is currently under preparation.

6.1 Model

In this chapter we consider a setup similar to the one presented in 3.2.1, where N_a two-level atoms or solid-state emitters are coupled to the field of a modulated photonic crystal waveguide. We assume that the emitters are dominantly coupled to photons of a single propagation band with a quadratic dispersion relation $\omega(k) \simeq \omega_e + \hbar k^2/(2m^*)$ as shown in Fig. 6.1(b). To keep the discussion as simple as possible we will primarily focus on homogeneous waveguides, where ω_e is the cutoff frequency of a given transverse mode and $m^* \approx \omega_e \hbar/c^2$ the effective mass. However, as will be discussed in more detail in Sec. 6.5, our analysis can be generalized to narrow bandwidth waveguides, where very strong couplings and much smaller group velocities, i.e., much larger values of m^*, can be realized.

Compared to Sec. 3.2.1 here we assume that the waveguide is subject not only to a spatial modulation but also to a time-dependent one. Specifically, we will focus on refractive index modulations, $n(z,t) = n + \delta n(z,t)$, induced by propagating acoustic waves via acousto-optical or optomechanical interactions [188, 189, 192, 193, 194], as shown in Fig. 6.1(a). However, all of the following results can be generalized to other electro-optical or Kerr-modulation schemes as well. The refractive index modulation creates an effective potential for the photon $V(z,t) \sim \delta n(z,t)$ that leads to the following time-dependent Hamiltonian:

$$H = \sum_i^{N_a} \hbar\delta |e\rangle_i\langle e| + \hbar g \sum_{i=1}^{N_a} \left[a^\dagger(z_i)\sigma_-^i + \sigma_+^i a(z_i) \right] + H_f(t), \tag{6.1}$$

where $\delta = \omega_a - \omega_e$ with ω_a being the transition frequency of the emitters and

$$H_f(t) = \int_0^L dz\, a^\dagger(z) \left(\hbar\omega_e - \frac{\hbar^2\partial^2}{2m^*\partial z^2} + V(z,t) \right) a(z), \tag{6.2}$$

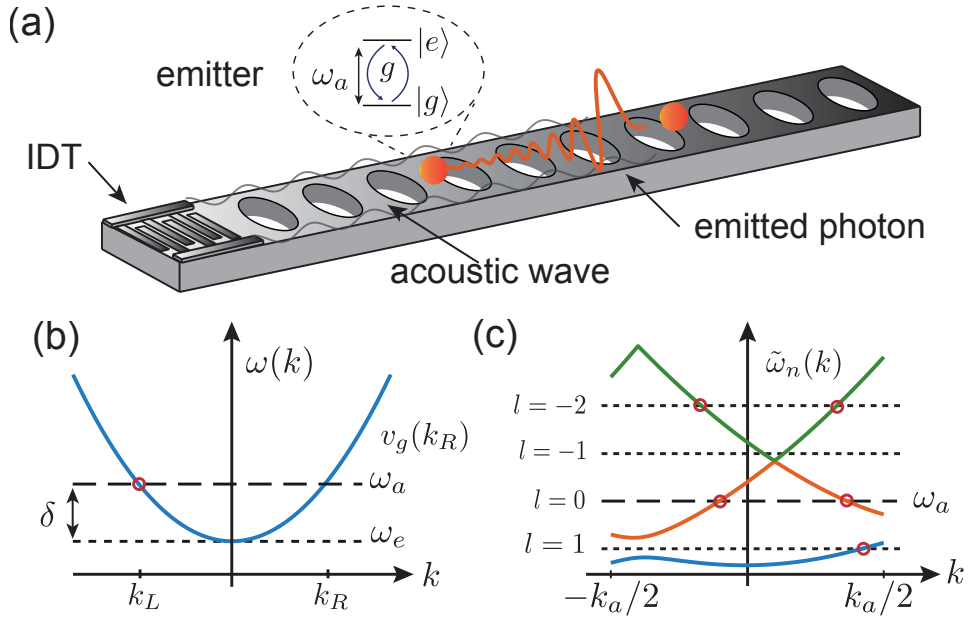

Figure 6.1: Sketch of a waveguide QED setup with multiple two-level emitters coupled to photons inside a 1D photonic channel. A strong acoustic wave creates a modulation of the refractive index, which propagates along the waveguide with velocity v and modifies the emission properties. (b) Dispersion relation $\omega(k)$ of the unperturbed waveguide, which is assumed to be approximately quadratic above the edge frequency of the propagation band, ω_e. (c) In the presence of the acoustic wave, the photon emission is determined by the tilted Floquet quasi-energy bandstructure $\tilde{\omega}_n(k)$, which is plotted for $V_a/E_r = 0.2$ and $\Omega/\Omega_r = 0.4$. In (b) and (c) the circles indicate the resonance conditions given in Eq. (6.18), which determine the set of wavevectors k_α that contribute to the overall emission rate.

is the Hamiltonian of the acousto-optical waveguide of total length $L \to \infty$. In (6.1) we further assumed that the coupling strength $g(z_i) \simeq g$ is approximately the same for all emitters, which are located at positions z_i along the waveguide (note that here g has dimension $[g] = \mathrm{Hz}\, m^{1/2}$).

Throughout this chapter we will consider the case of a perturbation of the form $V(z,t) = V(z - vt)$, that propagates at constant velocity $v > 0$ along the positive longitudinal direction of the waveguide. This means that Hamitonian (6.1) can be tackled not only in the lab frame at rest with the emitters but also in the frame co-moving with the propagating potential. This description will be particular useful for the case of a moving localized potential that will be discussed in section 6.3.2. The change to the co-moving frame can be done by using the unitary transformation $\tilde{H} = THT^\dagger + i\hbar \dot{T} T^\dagger$, where

$$T = e^{i\hat{p}vt} = e^{\hbar v t \int dz a(z)^\dagger \frac{\partial}{\partial z} a(z)} \tag{6.3}$$

transforms the bosonic operators according $Ta(z)T^\dagger = a(z - vt)$. Applying such

transformation and relabelling the integration variable we get the following Hamiltonian in the co-moving frame,

$$H = \sum_{i=1}^{N_a} \hbar\delta|e\rangle_i\langle e| + \int_0^L dz\, a^\dagger(z)\left(-\frac{\hbar^2\partial^2}{2m^*\partial z^2} + V(z) + i\hbar v\frac{\partial}{\partial z}\right)a(z) + \hbar g\sum_{i=1}^{N_a}\left[a^\dagger(z_i - vt)\sigma_-^i + \text{H.c.}\right]. \tag{6.4}$$

We note that in this frame the system is similar to the case considered in chapter 5 where we had quantum emitters moving close to a waveguide. The difference with respect to this case is the presence of an additional drift term in the photonic part of the Hamiltonian, which can lead to different results, as we will see later below.

6.2 Photon emission in an acousto-optical waveguide

In a first step we are interested in the spontaneous emission of photons from a single emitter, which is initially prepared in the excited state $|e\rangle$. In the absence of the acoustic perturbation, i.e $V = 0$, and for not too strong coupling g it is possible to use the Markov approximation to derive an effective equation for the decay of the excited state amplitude. In particular, as we derived in 2.2.1, the resulting decay rates are given by: $\Gamma_R = \Gamma_L = g^2/|v_g(k_{R/L})|$ where $v_g(k) = \partial\omega(k)/\partial k$ is the group velocity and the two wavevectors $k_R = -k_L$ are determined by the resonance condition $\omega_{eg} = \omega(k_{R/L})$. In this section we will derive the corresponding emission rates for the model (6.1) and we will show that the time modulation of the waveguide can lead to a dynamical control of the atomic emission both in rate and direction.

6.2.1 Bloch-Floquet theory of spontaneous emission

Bloch-Floquet decomposition

Let us consider the case of a propagating periodic potential $V(z,t) = V_a\cos k_a(z - vt)$ induced by a right-propagating acoustic wave with wavelength $\lambda = 2\pi/k_a$ and frequency $\Omega = vk_a$. Note that this specific choice for the potential does not affect the generality of the results. The problem is similar to that one treated in Sec. 3.2.1 but the time-dependent modulation of the Hamiltonian makes the solution more involved. In order to tackle the problem let us work in the lab frame at rest with the emitters but similar results can be also obtained in the co-moving frame. In this case it is convenient to change into the interaction picture with respect to the decoupled Hamiltonian $H_0 = \hbar\omega_a|e\rangle\langle e| + H_f(t)$. In this new representation, the field operator $a(z,t) = U^\dagger(t)a(z)U(t)$, where $U(t) = \mathcal{T}e^{-\frac{i}{\hbar}\int_0^t dsH_0(s)}$, can be written in terms of a Bloch-Floquet expansion as

$$a(z,t) = \frac{1}{\sqrt{L}}\sum_{n,k} e^{ikz}u_{nz}(z,t)a_{nk}, \tag{6.5}$$

where n is the band index, $k \in [-k_a/2, k_a/2]$ lies within the Brillouin zone defined by the phonon wavevector k_a and the a_{nk} ($a_{nk}^\dagger$) are bosonic annihilation (creation)

operators. The $u_{nk}(z+\lambda, t+2\pi/\Omega) = u_{nk}(z,t)$ are periodic functions satisfying the differential equation

$$\dot{u}_{nk}(z,t) = -\frac{i}{\hbar}\left[\hbar\omega_c - \frac{\hbar^2}{2m^*}\left(\frac{\partial}{\partial z} + ik\right)^2 + V(z,t)\right]u_{nk}(z,t), \tag{6.6}$$

and can be decomposed as

$$u_{nk}(z,t) = e^{-i\tilde{\omega}_n(k)t}\sum_{\ell=-\infty}^{\infty} u_{nk}^{(\ell)} e^{i(k_a z - \Omega t)\ell}, \tag{6.7}$$

where ℓ is the Floquet index. The decomposition (6.7), once inserted in (6.6), leads to the following eigenvalues equation for the coefficients $u_{nk}^{(\ell)}$:

$$\sum_l H_{\ell\ell'} u_{nk}^{(\ell)} = \tilde{\omega}_n(k) u_{nk}^{(\ell)}, \tag{6.8}$$

where

$$H_{\ell\ell'} = \begin{cases} \Omega_r(\ell + \frac{k}{k_a})^2 - \Omega\ell, & \ell = \ell', \\ \frac{V_a}{2\hbar}, & |\ell - \ell'| = 1, \\ 0, & \text{otherwise}, \end{cases} \tag{6.9}$$

and $\Omega_r = \hbar k_a^2/(2m^*)$. The numerical solution of this eigenvalues problem gives us the Bloch-Floquet coefficients $u_{nk}^{(\ell)}$ and the quasi-energies bands $\tilde{\omega}_n(k)$ shown in Fig. 6.1(c), which for a static potential just correspond to the usual Bloch bands. As we discussed in Sec. 3.2.1 for $V_a/E_r \gtrsim 1$, where $E_r = \hbar\Omega_r$ is the photonic recoil energy, the lowest bands become well separated and more and more flat. For finite propagation velocity v, we observe an additional asymmetric distortion, and in particular, $\tilde{\omega}_n(k) \neq \tilde{\omega}_n(-k)$. By using the decomposition (6.7) and assuming $z_1 = 0$, the remaining interaction Hamiltonian can be written as

$$H_I(t) = \frac{\hbar g}{\sqrt{L}}\sum_{kn\ell} u_{nk}^{(\ell)} e^{-i(\tilde{\omega}_n(k) + \Omega l - \omega_a)t} a_{nk}\sigma_+ + \text{H.c.}. \tag{6.10}$$

Before we proceed, in order to be consistent with the derivation and in particular with the interaction picture description, we prove that the commutation rules

$$\begin{aligned} &[a(z,t), a(z',t)] = 0,\ [a^\dagger(z,t), a^\dagger(z',t)] = 0, \\ &[a(z,t), a^\dagger(z',t)] = \delta(z - z'), \end{aligned} \tag{6.11}$$

are fulfilled at each time t. The first equation comes directly from the standard bosonic commutation relations $[a_{nk}, a_{n'k'}] = 0$. The second equation is also satisfied, as shown in the following:

$$\begin{aligned} [a(z,t), a^\dagger(z',t)] &= \frac{1}{L}\sum_{nn'kk'} e^{ik(z-z')} u_{nk}(z,t) u_{nk}^*(z',t)[a_{nk}, a_{n'k'}^\dagger] = \\ &= \frac{1}{L}\sum_{nk} e^{ik(z-z')}\sum_{\ell\ell'} u_{nk}^{(\ell)} u_{nk}^{*(\ell')} e^{ik_a(\ell z - \ell' z')} e^{-i\Omega(\ell-\ell')t} = \frac{1}{L}\sum_{k\ell} e^{i(k+\ell k_a)(z-z')} = \delta(z - z'). \end{aligned} \tag{6.12}$$

Here between the first and the second line we have used $[a_{nk}, a^\dagger_{n'k'}] = \delta_{k,k'}\delta_{n,n'}$ and between the second and the third line we used the orthogonality of the Bloch coefficients, $\sum_n u^{(\ell)}_{nk} u^{(\ell')}_{nk} = \delta_{\ell\ell'}$.

Evaluation of the decay rates

The interaction Hamiltonian (6.10) allows us to solve the dynamics of the spontaneous emission process. The generic time-dependent state can be written as

$$|\Psi(t)\rangle = \left[c_e(t)\sigma_+ + \sum_{nk} \phi_n(k,t) a^\dagger_{nk}\right]|g\rangle|\text{vac}\rangle \tag{6.13}$$

and its evolution is determined by the time dependent Schrödinger equation, which gives the following equations of motion:

$$\dot{c}_e(t) = -i\tfrac{g}{\sqrt{L}} \textstyle\sum_{nk} \phi_n(k,t) u_{nk}(z_1,t) e^{i\omega_a t} \tag{6.14}$$

$$\dot{\phi}_n(k,t) = -i\tfrac{g}{\sqrt{L}}\, c_e(t) u^*_{nk}(z_1,t) e^{-i\omega_a t}. \tag{6.15}$$

After inserting the second equation into the first we obtain the integro-differential equation:

$$\dot{c}_e(t) = -\frac{g^2}{L} \sum_{nk}\sum_{\ell\ell'} u^{(\ell)}_{nk} [u^{(\ell')}_{nk}]^* e^{-i\Omega(\ell-\ell')t} \int_0^t dt' e^{i(\delta^n_k - \Omega\ell')(t-t')} c_e(t'), \tag{6.16}$$

where $\delta^n_k = \omega_a - \tilde{\omega}_n(k)$. This expression can be simplified by observing that, similarly as done in section 5.1.2, the terms $\ell \neq \ell'$ are fast oscillating compared to the system dynamics and can be neglected if $g/\sqrt{\lambda} \ll \Omega$. We thus obtain the following simplified expression for the time evolution of the atomic amplitude:

$$\dot{c}_e(t) = -\frac{1}{L} \sum_{nk\ell} |g u^{(\ell)}_{nk}|^2 \int_0^t dt' e^{i(\delta^n_k - \Omega\ell)(t-t')} c_e(t'). \tag{6.17}$$

This expression shows that resonant interactions between the emitter and the field can occur at multiple wavevectors k_α, which satisfy the condition

$$\omega_{eg} = \tilde{\omega}_{n_\alpha}(k_\alpha) + \Omega\ell_\alpha, \tag{6.18}$$

for a band index n_α and a Floquet index ℓ_α [see Fig. 6.1(c)]. The emission rate into modes around k_α will depend on the coupling $\bar{g}_\alpha = g u^{(\ell_\alpha)}_{n_\alpha k_\alpha}$ and the quasi group velocity $\tilde{v}_{g\alpha} = v_g(k_\alpha, n_\alpha) = \partial\tilde{\omega}_{n_\alpha}(k)/\partial k|_{k=k_\alpha}$. If we assume that the atomic frequency lies inside the n-th band away from edges or divergences in the density of states, we can perform a Born-Markov approximation in the limit $g/\sqrt{\lambda} \ll B_n$, where B_n is the width of the n-th band. This can be done by linearising the dispersion relation around each resonant solution of (6.18) and in this way equation (6.16) reads in the continuum limit:

$$\begin{aligned}\dot{c}_e(t) &\simeq -\sum_{\alpha n} \frac{|\bar{g}_\alpha|^2}{2\pi} \int_0^\infty d\tau \int_{-\pi/a}^{\pi/a} dk\, e^{-i\tilde{v}_{g\alpha}(k-k_\alpha)\tau} (\theta[\tilde{v}_g] + \theta[-\tilde{v}_g]) c_e(t) \\ &= -\sum_{\alpha l} \frac{|\bar{g}_\alpha|^2}{\tilde{v}_{g\alpha}} \int_0^\infty d\tau\, \delta(\tau)(\theta[\tilde{v}_{g\alpha}] + \theta[-\tilde{v}_{g\alpha}]) c_e(t) = -\left(\frac{\Gamma_R}{2} + \frac{\Gamma_L}{2}\right) c_e(t).\end{aligned} \tag{6.19}$$

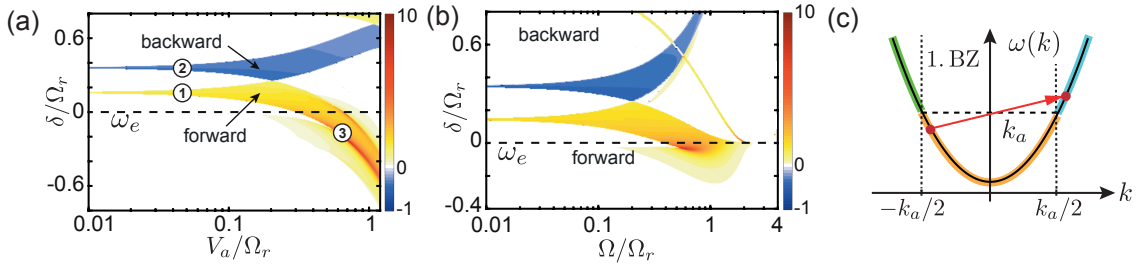

Figure 6.2: (a)-(b) Directional parameter D as a function of δ and V_a in (a) and Ω in (b). In (a) we fixed $\Omega/\Omega_r = 0.2$ while in (b) $V_a/E_r = 0.2$. In both plots the dashed black lines represent the band edge frequency. (c) Sketch of the bandstructure $\omega_n(k)$ in the unperturbed case. Here the red arrow indicates the Brillouin scattering resonances.

In this derivation we have separated the total emission rates into right- and left-propagating modes that are obtained by summing over all resonant k-vectors:

$$\Gamma_{R,L} = \sum_{\alpha} \frac{|\bar{g}_\alpha|^2}{|\tilde{v}_g(k_\alpha)|}\theta[\pm\tilde{v}_g(k_\alpha)], \tag{6.20}$$

where $\theta(x)$ denotes the Heaviside step function. In the next section we will show how the dynamical modulation of the waveguide can lead to a directional and controlled emission.

6.2.2 Photon dragging and directionality

In order to understand the modification in the emission process induced by the presence of a strong acoustic wave we can define the following directionality parameter

$$D = (\Gamma_R - \Gamma_L)/\Gamma_0, \tag{6.21}$$

which quantifies the difference between the emission rates into right (positive values of D) and left (negative values of D) propagating modes. Note that, compared to the analogous parameter defined in (5.16), here D is normalized respect to the characteristic decay rate $\Gamma_0 = g^2/|v_g(k_a/4)| = 2g^2k_a/\Omega_r$. In figure 6.2(a)-(b) we plot this parameter as a function of the potential depth (a) and the acoustic wave frequency (b). Both plots show the appearance of two frequency windows with opposite directional emission.

For a weak perturbation and low frequencies, $V_a, \hbar\Omega \ll E_r$, directional emission occurs only at two specific resonances

$$\delta = \omega_a - \omega_e \simeq \frac{\Omega_r}{4} \mp \frac{1}{2}\sqrt{\Omega^2 + \left(\frac{V_a}{\hbar}\right)^2}. \tag{6.22}$$

In particular, in the limit of $V_a \to 0$, $\delta \simeq \frac{\Omega_r}{4} \mp \frac{\Omega}{2}$ and these resonances can be understood from a regular Brillouin scattering process between modes k and $k' =$

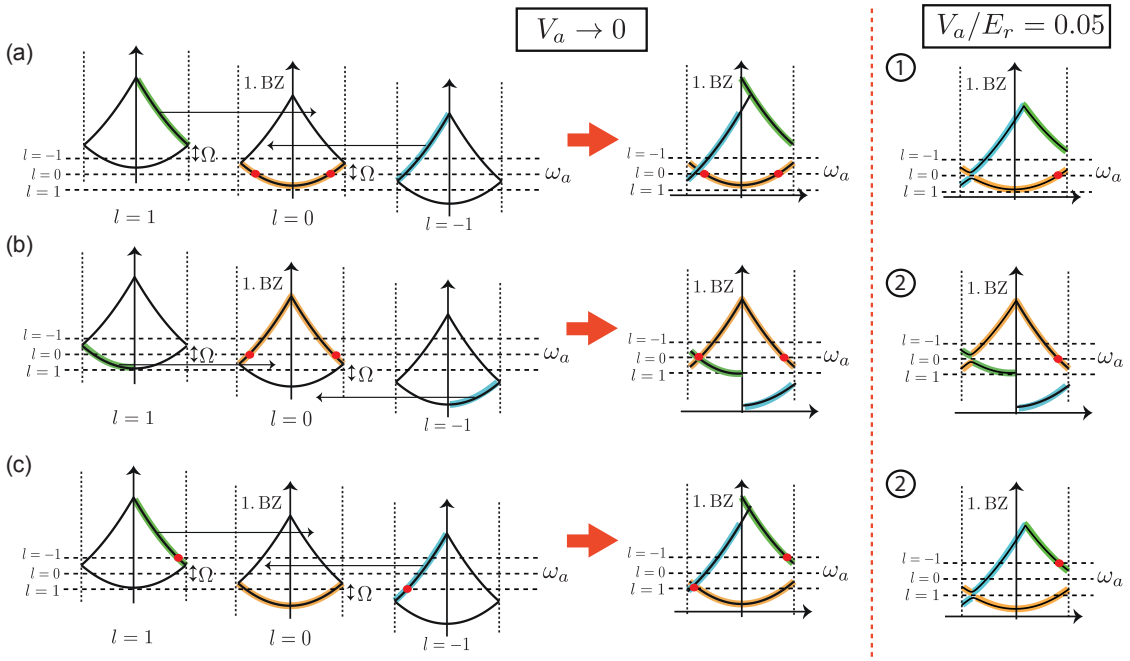

Figure 6.3: Construction of the quasi bandstructure $\tilde{\omega}_n(k)$. The left plot shows the bandstructure, (mapped to the first BZ) in different Floquet sectors. The acoustic potential couples dispersion branches in different Floquet sectors and in different Bloch bands. When mapping the coupled branches into a single BZ, the different BZ of the original bandstructure must be simultaneously shifted in frequency by $\pm\Omega$. In the right part of the plot is shown the effect that a finite perturbation, $V_a/E_r = 0.05$, has on the band structure. In (a) we explain the forward emission process. (b) and (c) is illustrate the backward emission process with two different mapping. The mapping illustrated in (b) clearly indicates the main resonances while in (c) is shown the mapping implicitely used in the Floquet decomposition. In all the plots we considered $\Omega/\Omega_r = 0.2$.

$k + k_a$ of the unperturbed waveguide. This scattering process is resonant only for wavevectors that conserve the energy of the process, i.e. $\omega(k) + \Omega = \omega(k')$. This is the transition of the kind indicated by the red arrow in Fig. 6.2(c) which leads to an avoided crossing (band gap opening) for finite V_a. When either k_R or k_L lies within this avoided crossing, the corresponding left- or right-propagating emission channel is suppressed and the emission becomes directional.

This mechanism can also be understood by looking at the resonances in the quasi-energy band-structure, which is defined within the first Brillouin zone (BZ) associated with acoustic wavevector k_a. The left part of figure 6.3 graphically shows how the quasi-energy bands are built from the static one. Here we considered the $V_a \to 0$ limit to better visualize the connection of this representation with the original dispersion. Compared to the static case, where the branches of the dispersion are mapped to the first BZ by applying a momentum shift multiple of k_a, in the time-dependent case the branches are simultaneously shifted in frequency by $\pm\Omega, \pm 2\Omega, \ldots$.

Figure 6.3(a) explains the forward emission process indicated in Fig. 6.2(a) by ①. Here, in correspondence of the main resonance, $\ell = 0$, there is a crossing of the left branches of the first two bands that becomes a gap when the perturbation strength V_a is not negligible. In this case only right propagating photons can be emitted. The same argument can be used also to explain the backward emission indicated by ② in Fig. 6.2(a). In this case the main resonance intersects the second band and the gap arises in correspondence of the right propagating branch, as shown in Figure 6.3(b). Note that in our Floquet decomposition the two branches of the second band are labelled by $\ell \pm 1$. Thus, we are implicitly folding the dispersion relation in the first BZ by using the mapping shown in Figure 6.3(c) and not that one illustrated in Figure 6.3(b). In this case the the two main resonances are in correspondence of $\ell = \pm 1$ and, when V_a is not negligible, the right propagating one is suppressed by the gap.

For a stronger potential, $V_a/E_r \gtrsim 0.1$ the simple Brillouin scattering picture does no longer apply and the emission characteristics changes substantially. In this regime the photons become strongly confined by the potential and therefore they are dragged along rather than being scattered by the acoustic wave. As a result, the two narrow resonances evolve into broad windows, where strong directional emission occurs. Interestingly, even in this photon-dragging regime a preferred emission in the direction opposite to the acoustic wave can occur, although this effect is less pronounced than the forward emission.

Importantly, the presence of the acoustic wave can not only lead to a directional, but also to a significantly enhanced rate of emission [see ③ in Fig. 6.2(a)]. This enhancement arises, first of all, from an overall reduction of the quasi group velocity $\tilde{v}_g$. In addition, for $\Omega > 0$ the tilting of the quasi energy bands can introduce new divergencies in the effective photonic density of states $\sim 1/\tilde{v}_g$, which have no analogue in static lattices. Physically, such divergencies occur when the original photonic group velocity matches the speed of sound, in which case the emitted photons reside in the vicinity of the emitter for a very long time.

This effect is closely related to the emission of Cherenkov photons by atoms moving close to slow-light waveguides discussed in chapter 5. Note, however, that the process of photons being emitted from a moving atom into a periodic structure and the emission of photons into a moving photonic lattice are not the same, since the presences of a periodic structure breaks Galilean invariance (see also [176]) as also confirmed by the appearance of the additional drift term in the co-moving frame Hamiltonian (6.4). A limit that shows the difference between the two cases is when the acoustic wave is propagating at very high velocities, i.e. $\Omega \gtrsim \Omega_r$. In this situation, compared to the moving atom case, all the directional emission features vanish and the perturbation is not able anymore to drag the photons along.

6.2.3 Acoustic emission control

One remarkable property of our setup is that by tuning the shape and the strength of the acoustic wave we can achieve a control over the emission of the atom. To make

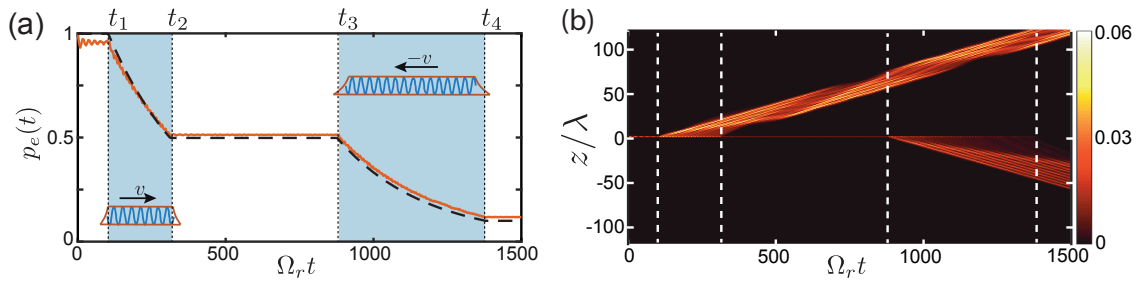

Figure 6.4: (a) Plot of the excited state probability $p_e(t)$ for an emitter with a frequency ω_a slightly below the band edge. During the time interval $\Delta T_R = t_2 - t_1$ a right-propagating acoustic wave passes the emitter and induces a strong decay. After the acoustic wave has passed the emission is again inhibited until a second left-propagating acoustic packet induces again a decay for a time interval $\Delta T_L = t_4 - t_3$. The solid red line shows the results from a numerical simulation of the full Hamiltonian and the dashed line the results obtained from a Markovian theory with time-dependent decay rates $\Gamma_{R,L}(t)$ evaluated from Eq. (6.20). (b) Plot of the emitted photon wavepacket $|\phi(z,t)|^2$, which shows that during the two time intervals the photon is emitted into different directions. The parameters for both plots are $V_a/E_r = 0.4$, $\Omega/\Omega_r = 0.6$, $\delta/\Omega_r = -0.3$ and $g/(\sqrt{\lambda}\Omega_r) = 0.05$.

this point clearer let us consider an emitter with a frequency $\omega_a < \omega_e$ well within the band gap, such that initially the emission is strongly suppressed. Figure 6.2 shows that for large enough V_a the acoustic wave can open up an emission window for frequencies below the edge ω_e, where otherwise no propagating photonic modes exist. The example shown in Fig. 6.4 illustrates, how this feature can be used to achieve full acoustic control over the emission dynamics. At time t_1 a right-propagating acoustic wave of finite length is sent through the waveguide and induces a decay into right-propagating photons during the time interval $\Delta T_R = t_2 - t_1$. Once the acoustic wavepacket has passed the emitter, the decay process stops half way in between. After a certain waiting time a second wavepacket propagating in the opposite directions leads to a decay of the remaining population by emitting photons to the left. Note that in the absence of other decay channels, the whole process is fully coherent and produces a superposition between a right- and a left-propagating photon.

In Fig. 6.4 (a) the evolution of $p_e(t)$ is calculated from Eq. (6.20) with rates $\Gamma_{R,L}(t) \sim V_a(t)$ that simply follow the slowly-varying envelop of the modulation. This approximate Markovian theory is compared with an exact simulation of the emission process based on the full Hamiltonian (6.1). We see that within the regime of validity, $g/\sqrt{\lambda} \ll \Omega_r$, the system dynamics is captured very well by the Markovian model, which justifies the extension of this theory to multiple atoms as will be discussed below. The main discrepancy actually arises from the initial preparation step, where the system quickly evolves into an atom-photon bound state with a residual photonic component [see chapter 3]. This bound-state physics is not captured by the Markov approximation, but can be taken into account by a more accurate modelling

of the initial preparation step.

6.3 Quantum networking applications

In the previous section we have shown how a controlled directional emission can be achieved in acousto-optical waveguides. This can already be useful for enhancing the detection efficiency of photons emitted from a single atom or defect. On the other hand in section 2.2.2 we discussed how such directionality becomes an essential ingredient for various quantum communication schemes, where propagating photons are used to distribute quantum states or to generate entanglement between multiple emitters along the waveguide [127, 21, 23, 25, 26]. In this context it is not only important to emit photons into a preferred direction, but also to efficiently reabsorb the photons by a second emitter. In the following we will show in terms of two basic examples, the new possibilities that are offered by acoustic control schemes for optical quantum networking applications.

6.3.1 Steady-state entanglement

Master equation formalism

Here we derive a master equation for the reduced density operator ρ of N_a emitters located at position z_i along the waveguide. Similarly as done in section 2.2 we write the total Hamiltonian (6.1) in interaction picture and we separate the contributions corresponding to the right (R) and left (L) propagating modes:

$$H_I(t) = \hbar g \sum_i \left(\left[F_R(z_i,t) + F_L(z_i,t) \right] \sigma_+^i + \text{H.c.} \right), \tag{6.23}$$

where we defined the right- and left-propagating field operators:

$$F_\eta(z) = \frac{1}{\sqrt{L}} \sum_{n,k} u_{nk}(z,t) e^{ikz} a_{nk} \theta[\pm \tilde{v}_g(k,n)] \tag{6.24}$$

and in the Heaviside function we assigned the values $\pm$ to $\eta = R, L$. Note that here we have identified the direction of propagation of the modes through the sign of the group velocity because in this case, compared to section 2.2, it does not coincide with the sign of the wavevector.

If we assume the field to be initially in the vacuum state we can proceed as done in section 2.2 and evaluate the correlation functions A_{ij}^η and B_{ij}^η given respectively in (2.5) and (2.6). By using again the Bloch-Floquet decomposition (6.7) the term A_{ij}^R in the continuous limit reads

$$\begin{aligned} A_{ij}^R &= \frac{g^2}{2\pi} \int_0^\infty d\tau \sum_{n\ell\ell'} \int_{-\pi/a}^{\pi/a} dk u_{nk}^{(\ell)} [u_{nk}^{(\ell')}]^* e^{ik(z_i - z_j)} e^{ik_a(z_i\ell - z_j\ell')} e^{-i\Omega(\ell-\ell')t} e^{i(\delta_k^n - \Omega\ell')\tau} \theta[\tilde{v}_g(k,n)] \\ &\simeq \frac{g^2}{2\pi} \int_0^\infty d\tau \sum_{n\ell} \int_{-\pi/a}^{\pi/a} dk |u_{nk}^{(\ell)}|^2 e^{i(k+k_a\ell)(z_i - z_j)} e^{i(\delta_k^n - \Omega\ell)\tau} \theta[\tilde{v}_g(k,n)], \end{aligned} \tag{6.25}$$

where $\delta_k^n = \omega_a - \tilde{\omega}_n(k)$. Between the second and the third line we neglected the fast oscillating terms $\ell \neq \ell'$ under the assumption $g/\sqrt{\lambda} \ll \Omega$. As before we can linearise the dispersion relation around the resonant solutions of (6.18) and the previous equation reduces to

$$\begin{aligned} A_{ij}^R &= \sum_\alpha \frac{|g_\alpha|^2}{|\tilde{v}_{g\alpha}|} e^{i(k_\alpha + k_a \ell_\alpha)(z_i - z_j)} \int_0^\infty d\tau \delta(\tau - \frac{(z_i - z_j)}{\tilde{v}_{g\alpha}}) \theta[\tilde{v}_{g\alpha}] \\ &= \sum_\alpha \frac{|g_\alpha|^2}{|\tilde{v}_{g\alpha}|} e^{i(k_\alpha + k_a \ell_\alpha)(z_i - z_j)} \theta[z_i - z_j] \theta[\tilde{v}_{g\alpha}]. \end{aligned} \tag{6.26}$$

Similarly we get for the other coefficients:

$$A_{ij}^L = \sum_\alpha \frac{|g_\alpha|^2}{|\tilde{v}_{g\alpha}|} e^{i(k_\alpha + k_a \ell_\alpha)(z_i - z_j)} \theta[z_j - z_i] \theta[-\tilde{v}_{g\alpha}], \tag{6.27}$$

$B_{ij}^R = A_{ij}^{*R}$ and $B_{ij}^L = A_{ij}^{*L}$. Here the index α runs again over all resonant wavevectors k_α and band indices n_α in the quasi-energy band structure. Going back to the Schrödinger picture with respect to the atomic frequencies we finally get the master equation:

$$\dot{\rho} = -\frac{i}{\hbar}[H_a, \rho] + \sum_{ij} (A_{ij}^R + A_{ij}^L) \left(\sigma_-^j \rho \sigma_+^i - \sigma_+^i \sigma_-^j \rho\right) + (A_{ij}^{*R} + A_{ij}^{*L}) \left(\sigma_-^i \rho \sigma_+^j - \rho \sigma_+^j \sigma_-^i\right), \tag{6.28}$$

where $H_a = \sum_i \hbar \omega_a |e\rangle_i \langle e|$ is the atomic Hamiltonian.

Discussion

We want to study the generation of stationary entangled states between two distant emitters located at positions $z_1 < z_2$ along the waveguide. For this purpose, we assume that both emitters are continuously driven by an external laser with frequency $\omega_L = \omega_{eg} + \delta_L$ and exchange photons via the waveguide. In this case the master equation (6.28) can be rewritten in the form:

$$\dot{\rho}(t) = -\frac{i}{\hbar} \left(H_{\text{eff}} \rho - \rho H_{\text{eff}}^\dagger\right) + \mathcal{J}(\rho). \tag{6.29}$$

Here the first term describes the system evolution under the effective (non-Hermitian) Hamiltonian H_{eff}. In the frame rotating with the laser frequency ω_L it reads

$$\begin{aligned} H_{\text{eff}} = &\sum_{i=1,2} \hbar \left[-\delta_L |e\rangle_i \langle e| + \frac{\mathcal{E}}{2} \left(e^{i\phi_i} \sigma_+^i + e^{-i\phi_i} \sigma_+^i\right)\right] \\ &- i\frac{\hbar\Gamma}{2} |e\rangle_1 \langle e| - i\frac{\hbar\Gamma}{2} |e\rangle_2 \langle e| - i\hbar A_R \sigma_+^2 \sigma_-^1 - i\hbar A_L \sigma_+^1 \sigma_-^2, \end{aligned} \tag{6.30}$$

where $\mathcal{E}$ is the Rabi frequency, ϕ_i are locally adjustable laser phases and we set $A_R = A_{21}^R$ and $A_L = A_{12}^L$. Eq. (6.30) shows that each individual emitter decays with rate $\Gamma = \Gamma_R + \Gamma_L + \Gamma_{\text{ng}}$, where $\Gamma_{R,L}$ are the same as defined in Eq. (6.20) and Γ_{ng}

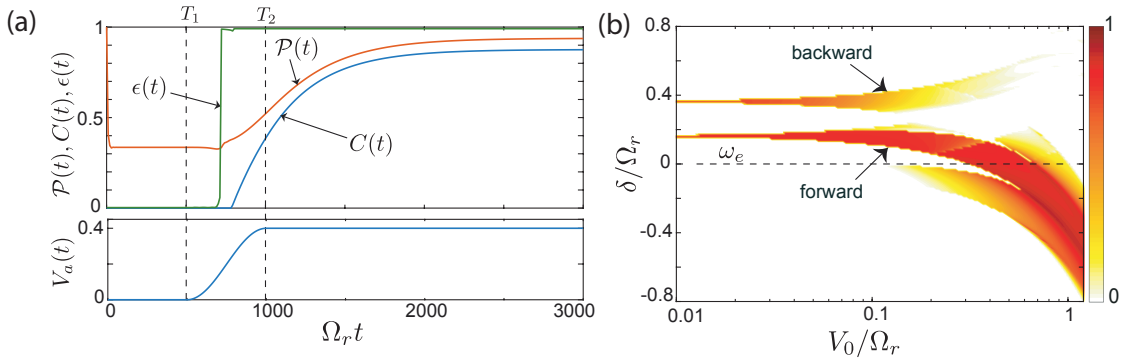

Figure 6.5: (a) Plot of the ϵ parameter, concurrence C and purity $\mathcal{P}$ of the atomic state as function of time. Here we keep the acoustic potential off until the time T_1. During the time interval $T_2 - T_1$ the potential is switched on until it reach the value $V_a/E_r = 0.4$ and it is kept constant until the end of the protocol. Here we assumed $\delta/\Omega_r = 0.08$, $\Omega/\Omega_r = 0.2$, $g/\sqrt{\lambda} = 0.08$, $\Gamma_{bg}/\Gamma_0 = 0.001$. (b) Steady state concurrence C_s as function of δ and V_a for $\Omega/\Omega_r = 0.2$. Here we fixed the Rabi frequency to be always $\mathcal{E} = 1.3\Gamma$ and we included the residual decay $\Gamma_{bg}/\Gamma_0 = 0.002$.

accounts for residual decay into non-guided modes. In addition, there are correlation effects $\sim \sigma_+^2\sigma_-^1$ and $\sim \sigma_+^1\sigma_-^2$, which arise from the coherent emission and reabsorption of photons that are mediated by the coefficients $A_{R,L}$. The last term in Eq. (6.29) is the recycling term introduced in Sec. 2.2.2. It ensures that probabilities are conserved, and is given by

$$J(\rho) = \sum_{i=1,2} \Gamma_i \sigma_-^i \rho \sigma_+^i + (A_R + A_L^*)\sigma_-^1 \rho \sigma_+^2 + (A_R^* + A_L)\sigma_-^2 \rho \sigma_+^1. \tag{6.31}$$

For the ideal case of a fully directional, single channel waveguide we obtain $A_R = \Gamma_R e^{ik_R(z_2-z_1)}$ and $A_L = 0$. In this limit the system is equivalent to the unidirectional waveguide shown in section 2.2.2 and the master equation (6.29) has a unique pure steady state, $\rho(t \to \infty) = |D\rangle\langle D|$, where the dark state $|D\rangle$ obeys $H_{\text{eff}}|\psi_0\rangle = 0$. For $\delta_L = 0$ and setting $\phi_i = -ik_R z_i$ to compensate for the propagation phase, this state is the same as the one given in (2.22):

$$|D\rangle = \sqrt{\frac{\Gamma_R^2}{\Gamma_R^2 + 2\mathcal{E}^2}} \left(|gg\rangle - i\frac{\sqrt{2}\mathcal{E}}{\Gamma_R}|S\rangle \right), \tag{6.32}$$

where $|S\rangle = (|ge\rangle - |eg\rangle)/\sqrt{2}$ is the maximally entangled singlet state. Therefore, for $\mathcal{E} \sim \Gamma$, the system evolves by itself into a highly entangled steady state without any precise switching of control pulses. As we discussed in Sec. 2.2.2 this method can also be generalized for the generation of more complex entangled states between multiple emitters.

Under non-ideal conditions $\Gamma_L \neq 0$ and $|A_R| < \Gamma_R$ the dark state condition $H_{\text{eff}}|D\rangle = 0$ can no longer be fulfilled perfectly and the purity, $\mathcal{P} = \text{Tr}\{\rho^2\}$, as well

as the degree of entanglement of the steady state is degraded. While in principle a pure entangled state can also exist for finite Γ_L, it relies on an exact interference between right-and left-propagating modes and becomes very sensitive to the exact positioning of the emitters. By requiring that the protocol to be insensitive to the exact positions z_1 and z_2, we identify a single parameter

$$\varepsilon = \frac{||A_R| - |A_L||}{\Gamma}, \tag{6.33}$$

which takes all the relevant deviations from an ideal unidirectional waveguide into account. In Fig. 6.5(a) we consider the current acousto-optical waveguide setting and we implement the previously mentioned entanglement protocol. Here we assume that the atomic frequency lies initially in the band and we gradually switch on the acoustic potential [see lower plot of Fig. 6.5(a)]. We plot the ε parameter together with the purity and the concurrence C [see section 2.2.1] of the atomic state. We see that once we enter in the ideal unidirectional regime, $\varepsilon \sim 1$, it is possible to prepare the steady state (6.32) and to generate entanglement among the qubits. This is also confirmed in Fig. 6.5(b) where the steady state concurrence averaged over different distances $d = |z_2 - z_1|$ is plotted in terms of the system parameters. This figures shows that the protocol works efficiently when a strong forward emission for a single emitter occurs. On the other hand in the backward emission window this is only partially the case and the concurrence reaches a maximum value of $C \sim 0.6$ only in the small perturbation limit.

6.3.2 An acoustic conveyor belt for light

In all the examples discussed so far we have studied the effects of continuous acoustic waves in the regime, where the emitter-field coupling is sufficiently weak. Under these conditions a Markovian treatment of the emission and reabsorption process is valid and determined by the structure of the quasi-mode continuum $\tilde{\omega}_n(k)$. However, due to the tight transverse confinement, this weak coupling assumption can be violated in nanophotonic waveguides, when the atomic frequency is close to a divergence of the density of states or in the band gap as discussed in chapter 3. In this section we consider a case where these features, combined with a strong and localized acoustic modulation, give rise to a non-Markovian mechanisms for manipulating the interaction between emitters and photons. In particular, we focus on the case, where the frequency of the emitters lies within the band gap, $\omega_a < \omega_e$, and we assume a short acoustic pulse of the form:

$$V(z,t) = -V_a \cos[k_a(z - vt)] e^{-\frac{(z-vt)^2}{2\Delta z^2}}, \tag{6.34}$$

where Δz is in the order of a few wavelengths. As shown in Fig. 6.6(a), this wavepacket creates a localized potential well, which for sufficiently strong V_a can drag along photons with it. In the following we will present an effective model to describe this configuration and we will then discuss its potential for quantum networking applications.

Effective model

To study this problem it is more convenient to work in the frame co-moving with the acoustic pulse. The co-moving frame Hamiltonian (6.4) provides an effective Schrödinger equation for the photons

$$(E-\hbar\omega_e)\Phi(z)=\left[-\frac{\hbar^2}{2m^*}\frac{\partial^2}{\partial z^2}+V(z)+i\hbar v\frac{\partial}{\partial z}\right]\Phi(z). \tag{6.35}$$

The photonic eigenstates consist of unbound states $\Phi_k(z)$ with $k\in[-\infty,+\infty]$ and energies $E_k=\hbar\omega_k$ inside the band and bound states $\Phi_n(z)$ with energies $E_n=\hbar\omega_n$ below the band edge ω_e. These eigenstates can be modelled respectively by a continuum and a discrete set of photonic modes, i.e. a_k and a_n, and allow us to decompose the field operator as a linear combination of these modes:

$$a(z)=\int dk\,\Phi_k(z)a_k+\sum_n\Phi_n(z)a_n. \tag{6.36}$$

Let us considering the interaction of a single emitter located at position z_1 with a frequency below the band edge. The previous field decomposition allows us to rewrite Hamiltonian (6.4) in the interaction picture as:

$$H_I(t)=\hbar g\int dk(\Phi_k(z_1(t))e^{i\delta_k t}a_k\sigma_+ + \text{H.c.})+\hbar g\sum_n(\Phi_n(z_1(t))e^{i\delta_n t}a_n\sigma_+ + \text{H.c.}) \tag{6.37}$$

where $z_1(t)=z_1-vt$, $\delta_k=\omega_a-\omega_k$ and $\delta_n=\omega_a-\omega_n$. Proceeding as usual we can use this Hamiltonian to evaluate the evolution of the atomic amplitude $c_e(t)$, which is described by the following integro-differential equation

$$\begin{aligned}\dot{c}_e(t)=&-g^2\int dk'\int_0^t dt'\Psi_k(z_1(t))\Psi_k^*(z_1(t'))e^{i\delta_k(t-t')}c_e(t')\\&-g^2\sum_n\int_0^t dt'\Psi_n(z_1(t))\Psi_n^*(z_1(t'))e^{i\delta_n(t-t')}c_e(t').\end{aligned} \tag{6.38}$$

Let now assume in addition that the emitter is tuned close to the resonance of the lowest bound state with energy $E_0=\hbar\omega_0$. In the limit where all the other modes are off resonance, i.e. $g/\sqrt{\lambda}\ll|\delta_{n,k}|$ $n\neq 0$, we can isolate the 0-th mode from the sum in (6.38) and integrate by parts all the rest. We thus end up with;

$$\dot{c}_e(t)\simeq -i\Sigma(t)c_e(t)-g^2\int_0^t dt'\Psi_0(z_1(t))\Psi_0^*(z_1(t'))e^{i\delta_0(t-t')}c_e(t'), \tag{6.39}$$

where the effect of all the other modes is just restricted to a frequency shift given by the self energy

$$\Sigma(t)=g^2\left[\int dk\frac{|\Psi_k(z_1(t))|^2}{\delta_k}+\sum_{n\neq 0}\frac{|\Psi_n(z_1(t))|^2}{\delta_n}\right]. \tag{6.40}$$

To get this expression we neglected all the other contributions coming from the integration by parts assuming that not only $g/\sqrt{\lambda}\ll|\delta_{n,k}|$, but also $\Omega\ll|\delta_{n,k}|$. This

last assumption comes from terms of the form $\sim \dot{\Psi}_{k,n}(z_1(t))$ in the integration. In most of the relevant cases the effect of frequency renormalization given by the self energy is negligible and we can approximate $\omega_a + \Sigma(t) \simeq \omega_a$. We notice that this procedure of adiabatic elimination of the off resonant field is closely related to that one used in section 3.1.4 to derive the dipole-dipole interaction in a photonic band gap.

Finally, by going back to the Schrödinger picture, we observe that equation (6.39) can be directly obtained by an effective moving cavity model. In particular, after generalizing this result to many emitters with the same frequency ω_a, we obtain that the effective Hamiltonian

$$H_{\rm mc}(t) = \hbar\omega_a|e\rangle\langle e| + \hbar\omega_0 a_0^\dagger a_0 + \hbar\sum_i g_i(t)(a_0^\dagger\sigma_-^i + a_0\sigma_+^i). \tag{6.41}$$

Here $g_i(t) = g|\Phi_0(z_i - vt)|$ is the effective coupling strength between the bound photon and the i-th emitter. This means that for a finite speed of sound, these photonic states can be dragged along by the acoustic wave and mediate interactions between different emitters. In the following we are going to discuss an excitation transfer application for this model.

Discussion

An interesting feature of the effective Hamiltonian (6.41) is its formal equivalence to models that were used for a long time in the context of atomic cavity QED to describe the interaction of multiply Rydberg atoms flying through a single resonator [195, 196, 197]. However, here the roles are reversed, allowing the successive interaction of fixed emitters with a common cavity mode that is carried by the acoustic wavepacket along the waveguide. The fact that it is the "cavity" and not the emitters that is moving is much more interesting and promising for quantum networking applications.

In Fig. 6.6(b) we show how this acoustic conveyor belt can be used for implementing a state transfer protocol between two emitters located at positions $z_2 > z_1$. In this example, the first emitter is initially prepared in the excited state $|e\rangle$ and we are interested in the excitation probability of the second emitter, $p_e^{(2)}(T_f)$, at a final time T_f, once the acoustic wave has left the interaction region. The frequencies of both emitters are set to $\omega_a = \omega_0$, which matches the frequency of the lowest photon bound state for a potential depth of $V_a/E_r = 0.5$. From the plot we see an almost perfect transfer of the excitation between the two emitters, where the delay between photon emission and re-absorption just corresponds to the propagation time $(z_2 - z_1)/v$. We also find a very good agreement between the numerical simulation and the effective theory as expected in the limit $g/\sqrt{\lambda} \ll |\delta_{n,k}|$.

In the example shown in Fig. 6.6(b) the potential parameters V_a and Δz have been chosen to achieve perfect resonance conditions, $\omega_a = \omega_0$, and to obtain a coupling $g_i(t)$ satisfying $\int_0^{T_f} g_i(t)dt = \pi$, in order to realize a complete transfer between the photon and the emitter. It is important to underline that for given ω_a is possible to shape the acoustic wavepacket in order to match the atomic resonances. In

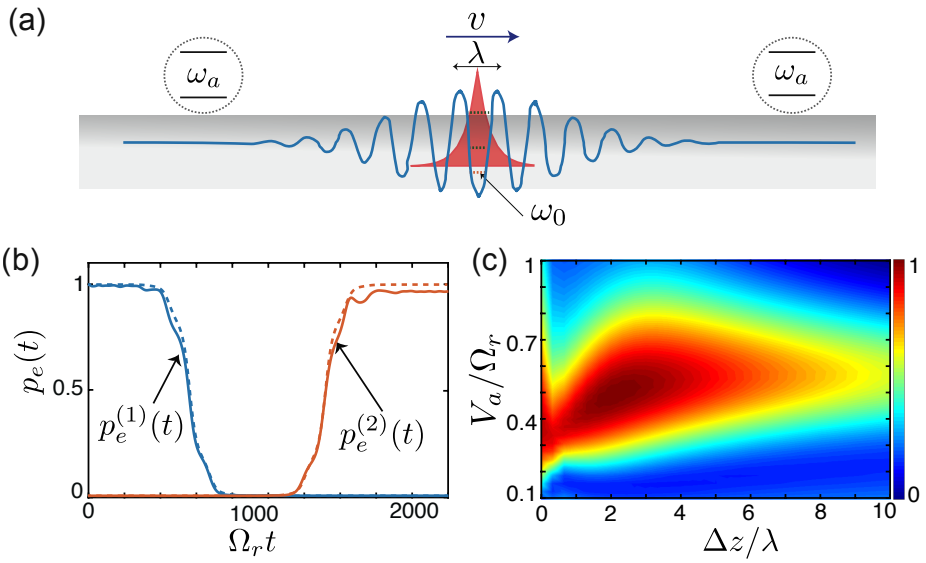

Figure 6.6: (a) Sketch of the set up where the interaction among the atoms is mediated by the photonic bound state of a propagating potential well. (b) Excitation transfer between two atoms as function of time as predicted for the full model (continuous line) and the effective moving cavity model (dashed lines). The two qubits are located at a distance $|z_2 - z_1|/\lambda = 6$ with frequencies tuned to $\delta/\Omega_r = -0.096$. The potential has parameters $V_a/E_r = 0.5$, $\Delta z/\lambda = 2$ and $\Omega/\Omega_r = 0.05$. The bare coupling strength is fixed to $g/(\sqrt{\lambda}\Omega_r) = 0.007$. (c) Population of the second atom, $p_e^{(2)}(T_f)$, as function of the acoustic wave width Δz and depth V_a. The plot is obtained by using the effective cavity model and the rest of the parameters are the same used in (b).

support of this in Fig. 6.6(c) we plot the second atom population at the end of the protocol, $p_e^{(2)}(T_f)$, as function of the acoustic wave width, Δz and strength V_a. This plot demonstrates a lot of flexibility for finetuning the emitter-photon interaction, assuming that ω_a, g and the speed of sound are fixed.

6.4 Chiral quantum optics in 2D

For the implementation of larger quantum networks it would be preferable to arrange the emitters in 2D lattices instead of along 1D arrays to achieve a better connectivity and scalability. However, photons emitted into 2D waveguides quickly spread into all directions and for two emitters separated by only several wavelengths, the ability to deterministically exchange photons becomes vanishingly small. In this section we show that the mechanism of acoustic emission control can be used to overcome this problem and to achieve fully directional emitter-emitter interactions even in a 2D scenario.

6.4.1 Band structure and directional emission

In the following we generalize our previous model to the case of a 2D photonic structure, where the photons are strongly confined along the z-axis, but propagate freely in the $x-y$ plane [see Fig. 6.7(a)]. The field Hamiltonian in this case reads

$$H_f(t) = \int d^2\mathbf{r}\, \psi^\dagger(\mathbf{r}) \left(\hbar\omega_e - \frac{\hbar^2}{2m^*}\nabla^2_{\mathbf{r}} + V(\mathbf{r},t) \right) \psi(\mathbf{r}), \tag{6.42}$$

where $\mathbf{r} = (x, y)$, and $V(\mathbf{r}, t)$ is the potential for the photons generated by acoustic waves inside the 2D waveguide structure. For the following discussion, we will focus explicitly on a combination of two plane waves propagating in orthogonal directions,

$$V(\mathbf{r},t) = V_x \cos\left(k_{a,x}x - \Omega_x t\right) + V_y \cos\left(k_{a,y}y - \Omega_y t\right), \tag{6.43}$$

with speed of sound and wavelength given respectively by $v_x = \Omega_x/k_{a,x}$ $\lambda_x = 2\pi/k_{a,x}$ and $v_y = \Omega_y/k_{a,y}$ $\lambda_y = 2\pi/k_{a,y}$.

To evaluate the emission characteristic of a single emitter under the influence of this modulation, we focus again on the weak-coupling regime and extend the Bloch-Floquet theory developed in Sec. 6.2.1 to two dimensions. From this analysis we obtain the quasi-energy bands $\tilde{\omega}_n(\mathbf{k})$, within the first BZ defined by $k_{a,x}$ and $k_{a,y}$. Spontaneous emission occurs for all wavevectors, where the resonance condition

$$\omega_a = \tilde{\omega}_n(\mathbf{k}) + \Omega_x\ell + \Omega_y\ell', \tag{6.44}$$

is satisfied, which defines a set of isoenergetic lines within the first BZ. The differential emission rate $d\Gamma_{n,\ell,\ell'}(\mathbf{k})$ into a specific direction depends again on the local group velocity $\tilde{\mathbf{v}}_g(\mathbf{k}) = \nabla_{\mathbf{k}}\tilde{\omega}_n(\mathbf{k})$ and the amplitude of the corresponding expansion coefficients $u^{(\ell,\ell')}_{n\mathbf{k}}$. This calculation can be carried out numerically for arbitrary parameters, but in the remaining discussion we will focus on the regime, where the acoustic potential is already sufficiently strong such that the bands are well separated. In this case the emission is dominated by resonances in the lowest quasi-energy band ($n = 1$) and with $\ell = \ell' = 0$. Under this assumption the total emission rate is

$$\Gamma \simeq \int_{\text{res}} d\Gamma_{1,0,0}(\mathbf{k}) = \frac{g^2}{2\pi}\int_{\text{res}} d\mathbf{k} \frac{|u^{(0,0)}_{1\mathbf{k}}|^2}{|\tilde{\mathbf{v}}_g(\mathbf{k})|}, \tag{6.45}$$

where the integration runs over the line of k-vectors satisfying the resonance condition (6.44) for $n = 1, \ell = \ell' = 0$.

In Fig. 6.7 we plot the lowest quasi-energy band together with the vector field profile of the quasi-group velocity for three different configurations. For a static potential, $v_x = v_y = 0$, and sufficiently strong amplitude $V_x = V_y$, the system reduces to regular 2D tight-binding lattice with a dispersion relation of the form $\omega(\mathbf{k}) \simeq -2J\cos(k_x) - 2J\cos(k_y)$. As shown in Fig. 6.7(b), in this case the emission is fully isotropic for ω_a near the bottom of the band, while in the middle of the band the group velocities along the resonance line point mainly into four directions. It has previously been shown [198, 199] that in the ideal tight-binding limit, this

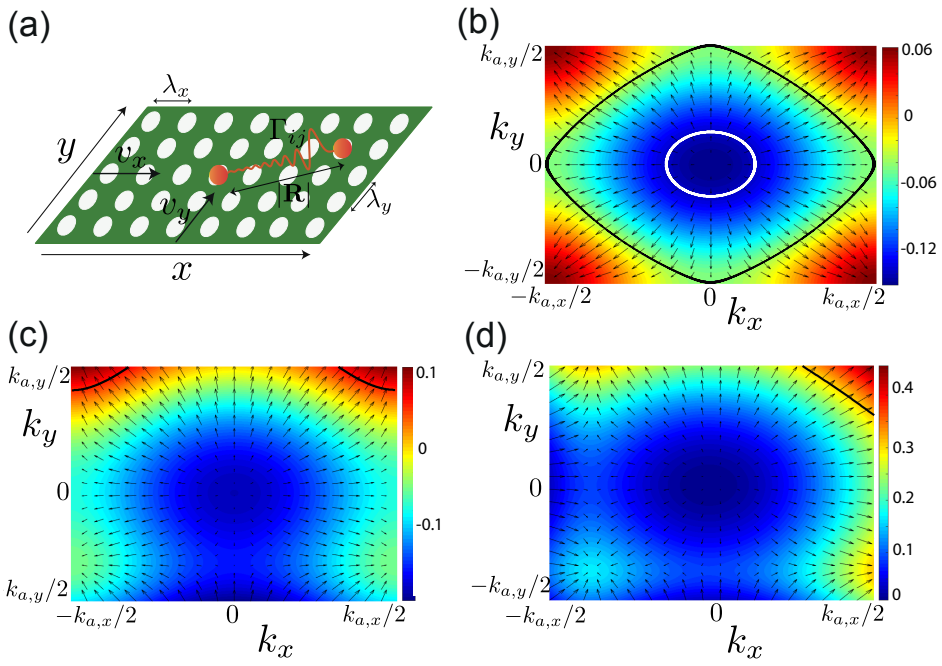

Figure 6.7: (a) Sketch of the setup where a 2D photonic crystal slab is dynamically modulated by two orthogonal acoustic waves propagating with velocity v_x and v_y. (b)-(d) Two dimensional dispersion relation $\tilde{\omega}_1(\mathbf{k})/\Omega_r$ plotted for the case of $\mathbf{\Omega} = 0$ (b), $\mathbf{\Omega}/\Omega_r = (0, 0.2)$ (c) and $\mathbf{\Omega}/\Omega_r = (0.2, 0.2)$ (d). In all plots a potential strength of $\mathbf{V}/E_r = (0.4, 0.4)$ is assumed. The black and white curves in the plot represent the isoenergetic path corresponding to a specific atomic frequency ω_a. In particular, $\delta/\Omega_r = -0.14$(b)(white line), $\delta/\Omega_r = -0.045$(b)(black line), $\delta/\Omega_r = 0.1$(c)(black line) and $\delta/\Omega_r = 0.1$(d)(black line). The black arrows represent the vectorial field associated to the photonic quasi-group velocity $\tilde{\mathbf{v}}_g(\mathbf{k})$.

results in a highly peaked emission of photons along the four diagonals. In realistic bandstructures as assumed here, the regions of low group velocities near the corners of the isoenergetic lines can change this picture and result instead in a dominant emission along the x and y directions (see discussion below). In any case, since for a static potential the reflection symmetry is not broken, the emission can be highly peaked, but will always occur into at least four different directions. In the presence of the acoustic potential, the bandstructure and therefore the emission becomes asymmetric. This is illustrated in Fig. 6.7(c) for a single wave in y direction, $V_x = 0$ and $V_y \neq 0$, and in Fig. 6.7(d) for the case of two acoustic waves of equal strength and speed. As in the 1D case, the acoustic wave tilts the quasi energy bands and for frequencies ω_a near the upper band edge resonant emission can occur in one direction, but not along the opposite. For the case where the two acoustic waves have the same speed [Fig. 6.7(d)] this can lead to a configuration, where all the group velocities along the resonance line point in the same direction. This seems to suggest that in this limit we could get a focussed unidirectional emission in 2D.

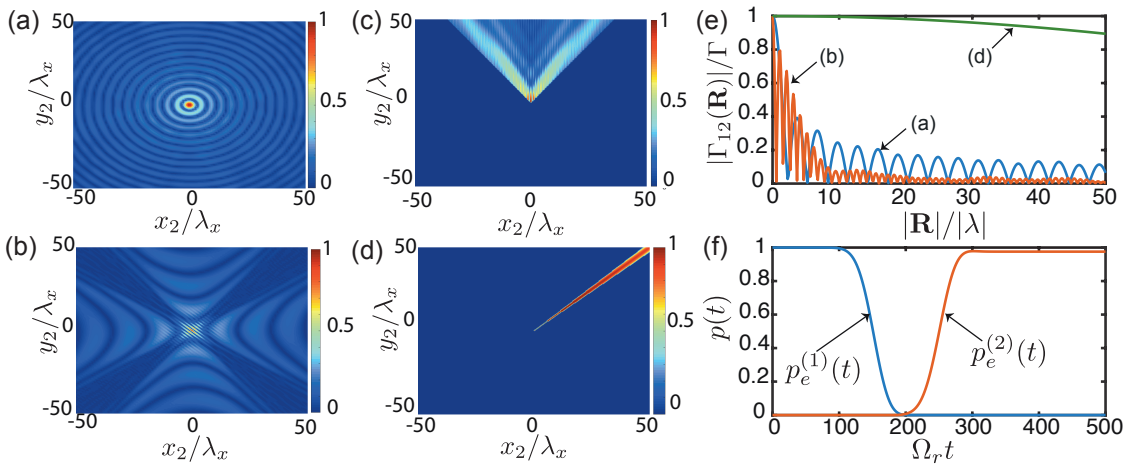

Figure 6.8: (a)-(d) 2D plot of $|\Gamma_{12}(\mathbf{R})|/\Gamma$ as function of the position of the second atom $\mathbf{r}_2 = (x_2, y_2)$ assumed that the first is located in the center of the structure $\mathbf{r}_1 = 0$. The case considered are the same indicated by the isoenergetic path in Fig. 6.7(b)-(d). (e) Plot of $|\Gamma_{12}(\mathbf{R})|/\Gamma$ for the same cases as before as function of the atom-atom distance assuming that the second atom is located along the diagonal $\mathbf{r}_2 = (r, r)$. (f) State transfer protocol involving the same pulse for the coupling strength given in [201]. Here we assumed the second atom to be located at position $\mathbf{r}_2 = (6, 6)$ and we fix $V/E_r = 2.5$, $\mathbf{\Omega}/\Omega_r = (0.3, 0.3)$, $g/\sqrt{|\lambda|}\Omega_r = 0.085$ and $\delta/\Omega_r = -2.93$.

In the following we are going to show that this is indeed the case.

6.4.2 Chiral dipole-dipole interactions

While the explicit evaluation of $d\Gamma(\mathbf{k})$ for the scenario described above would already show a peaked emission into a single direction, it is less useful as a quantitative measure for assessing the implementation of quantum state transfer protocols between two emitters located at positions $\mathbf{r}_1$ and $\mathbf{r}_2$ and separated by $\mathbf{R} = \mathbf{r}_2 - \mathbf{r}_1$. In this case also the spreading of photon wavepacket or interference effects must be taken into account. It is thus useful to consider the correlated decay rate

$$\Gamma_{12}(\mathbf{R}) = \frac{g^2}{2\pi} \int_{\text{res}} d\mathbf{k} \frac{|u_{1\mathbf{k}}^{(0,0)}|^2 e^{i\mathbf{k}\cdot\mathbf{R}}}{|\tilde{\mathbf{v}}_g(\mathbf{k})|} \tag{6.46}$$

that quantifies the ability to emit and reabsorb photons over a given distance. In Fig. 6.8 the normalized absolute value of $\Gamma_{12}(\mathbf{R})$ is plotted as function of the second atom position $\mathbf{r}_2$ assuming that the first atom is located at the center of the structure $\mathbf{r}_1 = 0$. In particular we consider the various scenarios discussed in Fig. 6.7.

Fig. 6.8(a)-(b) show the two cases where the potential is static. The first plot clearly shows an isotropic emission, that decays with the distance approximately as a Bessel function $\Gamma_{12}(\mathbf{R}) \sim J_0(|\mathbf{k}_0\mathbf{R}|)$ [see the blue line of Fig. 6.8(e)]. Here the frequency of the Bessel function is given by the resonant wave-vector k_0. Note that

this is true within the Markovian description, so it is not valid close to divergencies in the density of state (for instance at $k_0 \sim 0$). In particular, close to the band edges the dipole-dipole interaction becomes short range [see also the discussion done in Sec. 3.2.2]. In the second plot we consider the isoenergetic path shown by the white line in Fig. 6.7(b). As we discussed in the previous section, even if the emission is anisotropic it still occurs in all directions just with different rates and involving different group velocities.

The novelty of considering the propagating perturbation is evident in Fig. 6.8(c)-(d). In the first figure the acoustic wave is propagating only along the y direction and the atomic frequency is chosen to intersect the dispersion relation along the isoenergetic path shown in Fig. 6.7(c). In this case the atomic emission becomes directional and creates the analogous of a Cherenkov cone (even if here the dispersion is not linear in contrast with the usual Cherenkov physics).

An even more interesting case arises when the two acoustic waves are propagating with the same speed. In this case Fig. 6.8(d) clearly confirms the intuitive picture obtained from the bandstructures and the group velocity profile in Fig. 6.7(d), namely the ability to obtain a highly focused emission of photons along a single line. To emphasize this point we plot in Fig. 6.8(e) $|\Gamma_{12}(\mathbf{R})|$ as a function of the atom-atom distance assuming that the second atom is placed along the diagonal of the crystal, $\mathbf{r}_2 = (r, r)$. We can see that, while in the static case the correlated decay decreases quickly with the distance [blue and red lines], in the scenario described by Fig. 6.8(d) the two emitters can efficiently interact along this diagonal even when being many wavelengths apart, i.e. $|\mathbf{R}| \sim 30\lambda$ [see green line]. Of course, by changing the direction of the two acoustic waves, an emission into any of the four diagonals can be selected, which provides a full connectivity of 2D arrays.

This result suggests that by using our scheme we could achieve an almost "chiral 1D" interaction in a 2D structure. To confirm this result we implemented a typical excitation transfer protocol, largely used in chiral waveguide QED [200, 201], that involves a time pulse on the coupling strength to achieve a perfect absorption of the emitted photon. The essential ingredient for this protocol is the full unidirectionality of the waveguide. The result is shown in Fig. 6.8(f), where we were able to achieve an almost perfect state transfer for an atomic distance of $|\mathbf{R}| \simeq 10\lambda$.

6.5 Implementation

In chapters 2 and 3 we presented different nanophotonic waveguides and photonic crystal structures where embedded quantum dots as well as trapped atoms can be efficiently coupled to the waveguide modes. For the schemes described in this chapter, photonic crystal waveguides made out of diamond [122, 137, 117] are of particular interest. Diamond has excellent optical properties and the sound velocity $v \approx 10^4$ is considerably higher than in other materials. As we briefly discussed in chapter 3 there are already several well-studies emitters, like the nitrogen-vacancy (NV) or the silicon-vacancy (SiV) centers, which are ideally suited for quantum information processing applications.

Bulk or surface acoustic waves can be launched into such a photonic waveguide using electrical interdigital transducers (IDT) that allow to have control on the shape and on the strength of the acoustic pulse [189, 188, 194]. This waves can induce a refractive index modulation of the order of $\delta n/n_0 \simeq 10^{-4}$ [192, 193]. For an optical band at a frequency of about $\omega_c/(2\pi) \approx 350$ THz, this results in a potential depth of $V_a/\hbar = \omega_c \frac{\delta n}{n_0} \approx 2\pi \times 35$ GHz. On the other hand, for continuous waveguide with cut-off or in conventional photonic crystals, typical effective masses of the photons are on the order of $m^* \approx 5 \times 10^{-36}$ kg. In order to show how this implementation can match the requirements to achieve the acoustic emission control that we proposed, let us consider separately the localized and the extended acoustic wave cases.

- For the conveyor belt model presented in section 6.3.2, it is necessary that the system respects the following hierarchy of energy scales

$$\Gamma_{\rm ng} \ll \Gamma \sim \Omega \ll |\delta_{n\neq 0,k}|, \tag{6.47}$$

  where we remind that $\delta_{n,k}$ is the detuning of the atomic frequency from all the photonic modes besides the lowest bound state.

  To show that (6.47) can be fulfilled we consider an acoustic wavelength of $\lambda \approx 30\mu m$. In this case we find $\Omega/2\pi \approx 500$MHz and $\Omega_r/2\pi \approx 70$GHz, which leads to the ratios $V_a/E_r \approx 0.5$ and $\Omega/\Omega_r \approx 0.01$. Note that the potential strength is the same as that one used for the simulations in Fig. 6.6. Such a potential can induce a photonic bound state with the a detuning from the band edge of about $|\delta| \approx 5$GHz. This is much bigger than Ω. On the other hand decay rates into the waveguide on the order of few hundred MHz can be easily achieved in nowdays implementations. The main limitation is then given by dissipation of the system into the environment. For atoms and many solid-state emitters, this rate is in the range of $1 - 10$ MHz. Thus it should be possible to implement the conveyor belt model by sending acoustic modulation on top of waveguides with band edges.

- The situation is different for the extended acoustic wave case presented in Sec. 6.2. Indeed we have shown that acoustic modulations becomes relevant when V_a and the phonon frequency Ω become comparable to the recoil energy E_r and recoil frequency Ω_r, respectively. For an acoustic wave with $\Omega/(2\pi) \approx 1$ GHz, and $\lambda \approx 15\,\mu$m, we then obtain $\Omega_r/2\pi \approx 300$ GHz. These numbers give the ratios $V_a/E_r \approx 0.1$ and $\Omega/\Omega_r \simeq 0.003$. The main problem in this configuration is that the acoustic wave is not fast enough to induce a substantial band deformation. In the following we will show that it is possible to achieve the regime where acoustic waves and photon co-propagate by considering a narrow bandwidth waveguide setup.

6.5.1 Slow-light waveguides implementation: a super-lattice model

In order to explore the effects discussed for the extended acoustic wave it is necessary to further reduce the effective photon mass. In general, this can be achieve

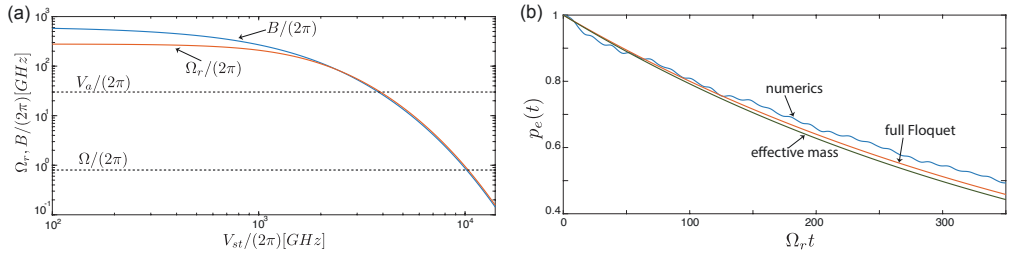

Figure 6.9: (a) Logarithmic plot of the recoil energy Ω_r and of the static bandwidth B as a function of the the static potential V_{st}. The dashed lines represent the value of the acoustic wave frequency Ω and potential V_a generated by a refractive index modulation of $\delta n/n \simeq 10^{-4}$. Here we fixed the optical frequency to $\omega_e/(2\pi) = 350$ THz and the acoustic wavelenght to $\lambda = 3a = 15\mu m$. (b) Comparison of the excited state population evaluated with different approaches: numerical simulation (blue line), full Floquet theory (red line) and the effective mass approximation(blue line).

by imposing an additional static potential, $V_{\rm st}(z)$, with a periodicity a. If this potential is sufficiently strong, it will generate a band with dispersion relation $\omega(k) \simeq (B/2)\cos(ka)$, and with an enhanced effective mass near the origin of $m^* = 2\hbar/(Ba^2)$. For a periodicity a which is larger than the optical wavelength, the bandwidth B can be substantially reduced, as shown in Fig. 6.9(a) for a simply case of $V_{\rm st}(z) = V_{\rm st}\cos(k_{\rm st}z)$ with $k_{\rm st} = 2\pi/a$. In essence, the whole array is divided into coupled cavities, in which case the propagation is considerable slower than in regular photonic crystal waveguide. As shown in Fig. 6.9(a) by creating such a "mini-band" of width $B/(2\pi) \approx 10$ GHz, we already obtain $m^* \approx 10^{-34}$kg and $\Omega_r/(2\pi) \approx 10$ GHz, which leads to a ratio of $\Omega/\Omega_r \approx 0.1$, consistent with our requirements. Note that in the presence of the static modulation, the full optical potential entering in Hamiltonian $H_f(t)$ is given by

$$V(z,t) = V_{\rm st}\cos(k_{\rm st}z) + V_a\cos(k_a z - \Omega t), \tag{6.48}$$

which in general makes the analysis of the emission processes considerably more involved than in the case of a continuous waveguide as we will show in the following.

Let us assume a super-lattice configuration where the acoustic wavelength is a multiple $M > 1$ of the static potential lattice constant, i.e. $\lambda = Ma$. In the static limit $V(z,t) = V(z)$ the acoustic potential breaks each band of the original band structure generated by $V_{\rm st}(z)$ into M sub-bands. Each of these sub-bands can be described in the first Brillouin zone by a quasi-momentum $k \in (-\pi/\lambda, \pi/\lambda]$ and labelled by the index n as shown in Fig. 6.10(a). In the case where the acoustic wave is propagating the description becomes more involved. To solve equation (6.6) we use the following modified decomposition:

$$u_{nk}(z,t) = \sum_{\ell\ell'} u_{nk}^{(\ell,\ell')} e^{i(k+k_a\ell)z} e^{-i(\tilde{\omega}_n(k)+\Omega\ell')t}, \tag{6.49}$$

where, compared to the $V_{\rm st} = 0$ case, we introduce two separate indices ℓ, ℓ' for space

and time. Inserting this ansatz into Eq. (6.6) we obtain the Floquet Hamiltonian

$$H_F = \begin{bmatrix} \ddots & & & & & \iddots \\ & H_{\rm st}+\mathbb{I}2\Omega & H_a^+ & 0 & 0 & \\ & H_a^- & H_{\rm st}+\mathbb{I}\Omega & H_a^+ & 0 & \\ & 0 & H_a^- & H_{\rm st} & H_a^+ & \\ & 0 & 0 & H_a^- & H_{\rm st}-\mathbb{I}\Omega & \\ & 0 & 0 & 0 & H_a^- & H_{\rm st}-\mathbb{I}2\Omega \\ \iddots & & & & & \ddots \end{bmatrix} \tag{6.50}$$

where

$$H_{{\rm st},\ell\ell'} = \begin{cases} \Omega_r(\ell+\frac{k}{k_a})^2, & \ell=\bar{\ell}' \\ \frac{V_{\rm st}}{2\hbar}, & |\ell-\ell'|=M \\ 0, & \text{otherwise} \end{cases} \tag{6.51}$$

and

$$H^{\pm}_{a,ll'} = \begin{cases} \frac{V_a}{2\hbar}, & \ell-\ell'=\pm 1 \\ 0, & \text{otherwise.} \end{cases} \tag{6.52}$$

Note that now the time dependence is embedded in a bigger time independent Hilbert space. Similarly to the single potential case by diagonalizing (6.50) we get the quasi-energies $\tilde{\omega}_n(k)$ and the coefficients $u_{nk}^{(\ell,\ell')}$. Note that the ansatz (6.49) still satisfies the commutation rules (A.3). The proof is similar to the one detailed in (6.12) with the only difference that the following relation for the coefficients should be used $\sum_n u_{nk}^{(\ell,r)} u_{nk}^{(\ell,r')} = \delta_{\ell\ell'}\delta_{rr'}$.

Proceeding as before, we can solve the dynamics described by Hamiltonian (6.10) working under the assumption $g/\sqrt{\lambda} \ll \Omega$. Again in the limit $g/\sqrt{\lambda} \ll B_n$, where B_n is the width of the n-th band, we can perform a Markov approximation and obtain the following expression for the total atomic decay rate:

$$\Gamma = \sum_\alpha \frac{\left(\sum_{rr'} g^*_{\alpha r} g_{\alpha r'}\right)}{|\tilde{v}_{g\alpha}|} \tag{6.53}$$

where $g_{\alpha r} = g u_{n_\alpha k_\alpha}^{(\ell_\alpha, r)}$ and the index α labels the solutions of $\omega_{eg} = \Omega l_\alpha + \tilde{\omega}_{n_\alpha}(k_\alpha)$ with $l_\alpha = \pm 1, \pm 2, ...$ Equation (6.53) shows that more contributions and resonances have to be taken into account compare to the single potential case. From the expression for the atomic decay (6.53) a directionality plot, similar to that one of Fig. 6.2, can still be obtained. As shown in Fig 6.10(b)-(c) a directional emission both in the forward and backward direction can be still achieved. Here we plot the emitted photonic wavefunction, computed with a full simulation of the model. From Fig. 6.10(a) we observe that, compare to the single potential case, the chiral emission is weakly affected by the additional decay channels arising from the modulation induced by $V_{\rm st}$. A simplified description of this super-lattice configuration can be obtain for the lower band in the limit where the recoil energy of the static potential, $\Omega_r^{\rm st} = \hbar k_{\rm st}^2/(2m^*)$, is large compared to the recoil energy associated with the acoustic

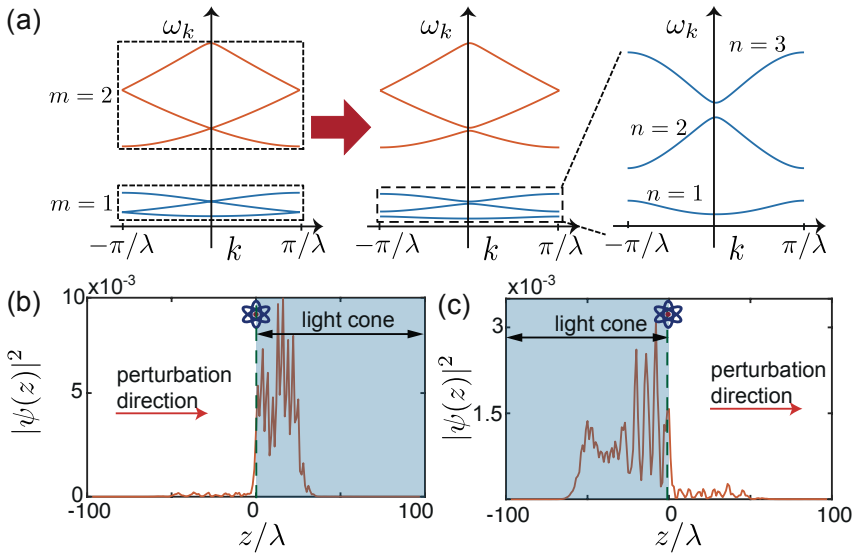

Figure 6.10: (a) Sketch of the band structure corresponding to a super-lattice with period $M = 3$. In the absence of the acoustic perturbation the band structure is determined only by the static potential $V_{\rm st}$ and the bands are labelled by the index m. For a finite acoustic potential each band breaks into M sub-bands. Here we use the index n to label all the bands in this configuration. (b)-(c) Snapshot of the emitted photon wavepacket for $V_{\rm st}/E_r = 2.5$ and $V_a/E_r = 0.25$. In (b) $\Omega/\Omega_r = 0.3$ and $\delta/\Omega_r = -0.25$. In (c) $\Omega/\Omega_r = 0.45$ and $\delta/\Omega_r = 0.3$.

wave Ω_r. This is always true in the limit of $M \gg 1$ where we recover the continuous waveguide limit. In this regime the effect of the static potential $V_{\rm st}$ consists in just a renormalization of the effective photon mass that is give by $m^* = 2\hbar/(Ba^2)$. This is illustrated in Fig. 6.9(b) , where the exact decay process of a single emitter in the presence of $V_{\rm tot}$ is compared to the theory of Sec.6.2 with a reduced effective mass and to the full Floquet theory here developed. We observe that this effective mass approximation is already pretty good for $M = 3$ as long as the lower band is considered.

Chapter 7

Exciting a bound state in the continuum through multi-photon scattering plus delayed quantum feedback

In section 2.3.3 we introduced the bound states in the continuum (BIC) as a class of states that completes, together with the scattering states, the waveguide energy spectrum. These are bound stationary states that arise *within* a continuum of unbound states unlike the bound states that occur in band gaps that we extensively discussed in chapters 3 and 4. In section 2.3.3 we concentrated on the case where the BIC consist by two emitters dressed with a single photon that is strictly confined between them [19, 27, 28]. An analogous scenario arises when one of the two atoms is replaced by a mirror [66, 68].

A typical question is how to form and prepare such states in order to enable potential applications such as light trapping and quantum information processing. A natural way to populate these states is through spontaneous emission of the emitter(s) as discussed in section 2.3.3. This approach for exciting the BIC is most effective in the Markovian regime where the characteristic photonic time delay (e.g. the photon round-trip time between a qubit and a mirror or between two qubits) is very short. This is because the atomic component of the BIC progressively shrinks for growing time delay in favor of a larger photonic component [68, 19, 29]. This makes such decay-based schemes ineffective for long enough mirror-emitter and/or inter-emitter distances. This is a major limitation when entanglement creation is the main goal [19].

A possible approach to generate these states in the regime of significant time delay consists of preparing an initial state that overlaps with the photonic component of the BIC. In practice this calls for techniques based on photon scattering. As discussed in section 2.3.3 a single photon scattered off the emitter(s) cannot excite the BIC since it lives in a subspace orthogonal to the scattering states. When it

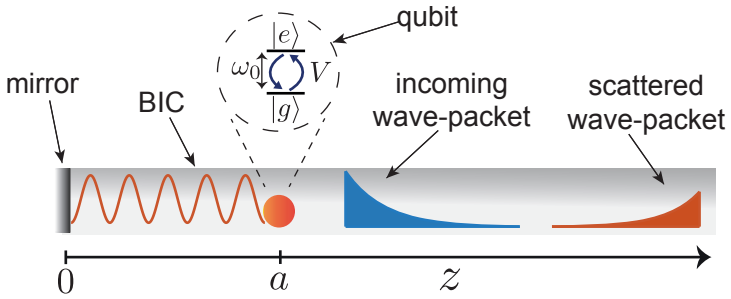

Figure 7.1: Single atom coupled to a semi-infinite waveguide. The atom is placed at a distance a from a perfect mirror located at the end of the waveguide, $z = 0$. When a BIC exists it can be excited by an incoming two-photon wavepacket.

comes to multi-photon scattering, however, because of the intrinsic nonlinearity of qubits, this argument does not hold any more.

The idea is similar to the one presented by Longo *et al.* [58, 59]. In these papers it was shown that the bound states outside of the photonic continuum of an array of resonators coupled to a qubit can be excited through multi-photon scattering. This effect relies on the structure of the energy spectrum of dressed states in the two-excitation sector of the Hilbert space, which we discussed in chapter 4.

In this chapter we show that a BIC in a waveguide-QED setup can be indeed excited via multi-photon scattering even if its energy does not lie in a photonic gap. This effect crucially relies on the time delay of the photon and occurs in the non-Markovian regime. We consider both paradigmatic setups of a qubit coupled to a semi-infinite waveguide and a pair of distant qubits coupled to an infinite waveguide. In either case, generating the BIC results in single-photon trapping in the form of a perfectly sinusoidal wavefunction and stationary excitation of the emitters.

In this work I contributed as a leading author and performed most of the analytic and numerical calculations in collaboration with Y. L. Fang under the supervision of F. Ciccarello and H. U. Baranger. A publication containing these results has been posted on arxiv [69] and has been submitted to a peer-review journal.

7.1 Model

In this work we consider two different configurations where a BIC can exist. The first setting consists of an atom placed inside a semi-infinite waveguide and in the second case we consider two emitters coupled to an infinite waveguide. While the model and the properties of the second scenario were discussed in section 2.3.3 the first was not discussed in this thesis so far so we will introduce it here.

Let us consider the setup shown in Fig. 7.1 where a two-level atom is coupled to the 1D field of a semi-infinite waveguide with a linear dispersion relation $\omega_k = v_g|k|$ (where v_g is the photon group velocity and k the wavevector along the z-axis). The emitter's ground and excited states are separated in energy by $\omega_a = v_g k_0$, where k_0 is

the resonant wavevector. The end of the waveguide lies at $z = 0$ [see Fig. 7.1] and is represented by an effective perfect mirror, while the atom is placed at a distance a from the mirror. The Hamiltonian under the rotating wave approximation is similar to the one given in Eq. (2.25) and reads

$$H = \omega_a \sigma_+\sigma_- - iv_g\int_0^\infty \mathrm{d}z\Big[a_R^\dagger(z)\frac{d}{dz}a_R(z) - a_L^\dagger(z)\frac{d}{dz}a_L(z)\Big] + g\int_0^\infty \mathrm{d}z\left[\big(a_L^\dagger(z)+a_R^\dagger(z)\big)\sigma_- + \mathrm{H.c.}\right]\delta(z-a)\,, \tag{7.1}$$

where we remind that $a_{R/L}(z)$ are the bosonic field operators annihilating a right-going (left-going) photon at position z.

In the single-excitation subspace ($N_e = 1$), the spectrum of (7.1) consists of an infinite continuum of odd-parity unbound dressed states $\{|\phi_k\rangle\}$, each with energy $\omega_k = v_g|k|$ [6, 7, 9, 11, 22, 19]. These states can be interpreted as scattering eigenstates in which a left-incoming resonant photon is eventually reflected by the mirror with 100% probability. Similarly to the two-atom case, when the condition $k_0 a = m\pi$ with $m = 1, 2, ...$ is matched, a further stationary state $|\phi_b\rangle$ exists, which is a BIC. This state has the same energy $\omega_b = \omega_a$ as the atom and reads [68]

$$|\phi_b\rangle = b\left(\sigma_+ + \sqrt{\tfrac{2\Gamma}{v}}\int_0^a \mathrm{d}z\,\sin(k_0 z)a^\dagger(z)\right)|g\rangle|0\rangle, \tag{7.2}$$

where $a^\dagger(z)$ is the operator that creates a photon at the position z and $\Gamma = 2g^2/v_g$ is the usual atom decay rate (in the absence of mirror). Note that in this state the photonic component is bigger compare to the two-atom BIC given in (2.41). This is because here we replaced one of the two atoms by a mirror, which fully reflects any photon impinging on it. The BIC is fully specified (up to an irrelevant global phase factor) by the emitter excited-state population given by

$$|b|^2 = \frac{1}{1+\frac{\Gamma}{2}\tau}\,, \tag{7.3}$$

where again $\tau = 2a/v_g$ is the delay time. The BIC is formed strictly inside the space between the mirror and the atom $0 \le z \le a$, where the photonic wave-function is a purely sinusoidal. When the BIC exists, i.e., $k_0 a = m\pi$, the atom does not fully decay. Indeed, the initial state $|e, 0\rangle$ overlaps with the BIC by the amount $\langle e, 0|\phi_b\rangle = b$, hence $|b|^2$ represents also the probability of generating the BIC via spontaneous emission. Based on Eq. (7.3) this probability monotonically decreases with the rescaled delay time $\Gamma\tau$, showing that this generation scheme is most effective when $\Gamma\tau$ is small.

7.2 BIC generation through multi-photon scattering

7.2.1 Excitation trapping scheme

The bound state (7.2) cannot be populated via single-photon scattering since such a process involves only the unbound states $\{|\phi_k\rangle\}$ (orthogonal to $|\phi_b\rangle$). An impinging

photon, after a transient during which it can momentarily enter the atom-mirror region and excite the atom, will be eventually fully released and reflected back. We thus send, instead, a two-photon wave-packet to the atom initially unexcited. In this way, as we will show in the following, it is possible to excite the BIC with a not negligible probability.

Let us consider the generic state of the system at time t in the two-excitation sector ($N_e = 2$):

$$|\Psi(t)\rangle = \left(\sum_{\eta} \int_0^{\infty} \mathrm{d}z\, \psi_\eta(z,t) a_\eta^\dagger(z)\sigma_+ + \sum_{\eta,\eta'} \tfrac{1}{\sqrt{2}} \iint_0^{\infty} \mathrm{d}z\mathrm{d}y\, \chi_{\eta,\eta'}(z,y,t) a_\eta^\dagger(z) a_{\eta'}^\dagger(y)\right)|g\rangle|0\rangle, \tag{7.4}$$

where the indices η, η' take the values $\eta, \eta' = R, L$. Here $\chi_{\eta,\eta'}(z,y,t)$ is the wave-function of the two-photon component, while $\psi_\eta(z,t)$ is the probability amplitude that the emitter is excited and a right/left propagating photon is found at position z. Let us assume to send a localized two-photon wavepacket propagating from the right towards the end of the waveguide as sketched in Fig. 7.1. If the atom is initially in the ground state the initial joint state reads

$$|\Psi(0)\rangle = \tfrac{A}{\sqrt{2}} \iint_0^{\infty} \mathrm{d}z\mathrm{d}y \left[\phi_L^1(z)\phi_L^2(y) + 1 \leftrightarrow 2\right] a_L^\dagger(z) a_L^\dagger(y)|g\rangle|0\rangle, \tag{7.5}$$

where A is the normalization factor and $\phi_L^i(z)$ the wave-function of a single left-propagating photon. We first consider for simplicity a two-photon exponential wavepacket [sketched in Fig. 7.1] such that $\phi_L^1(z) = \phi_L^2(z) = e^{-\alpha|z-a|-ik_0(z-a)}\theta(z-a)$, where α is the wavevector width in k-space (hence $\Delta\omega = v_g\alpha$ is the bandwidth) and k_0 the carrier wavevector resonant with the emitter. Note that in the way it is defined, the front of the wavepacket reaches the emitter at $t = 0$.

For the following discussion it is useful to define the quantities

$$P_e(t) = \sum_{\eta} \int_0^{\infty} \mathrm{d}z\, |\psi_\eta(z,t)|^2, \tag{7.6}$$

$$P_{\mathrm{ph}}(t) = \sum_{\eta,\eta'} \int_0^{a} \mathrm{d}z \int_a^{\infty} \mathrm{d}y\, |\chi_{\eta,\eta'}(z,y,t)|^2, \tag{7.7}$$

which represent respectively, the population of the emitter and the probability that one of the two photons lies in the region $[0,a]$ while the other in the interval (a,∞).

We numerically solve the dynamics described by the model (7.1) for a scenario where the BIC (7.2) exists. The results are shown in Fig. 7.2. As the wavepacket impinges on the qubit [see Fig. 7.2(a)] its population P_e exhibits a rise followed by a drop (indicating photon absorption and re-emission, respectively) eventually converging to a small finite steady value, which shows that part of the excitation absorbed from the wave-packet is trapped.

The behavior of the field in the same process is illustrated in Figs. 7.2(b) and 7.2(c). They show, respectively, the spatial profile of the two-photon probability density function $|\chi(z,y,t_f)|^2 = \sum_{\eta,\eta'} |\chi_{\eta,\eta'}(z,y,t_f)|^2$ [see Eq. (7.4)] and the total photon density $n(z) = \langle\Psi(t_f)|\hat{a}^\dagger(z)a(z)|\Psi(t_f)\rangle$ at a time t_f long enough such that the

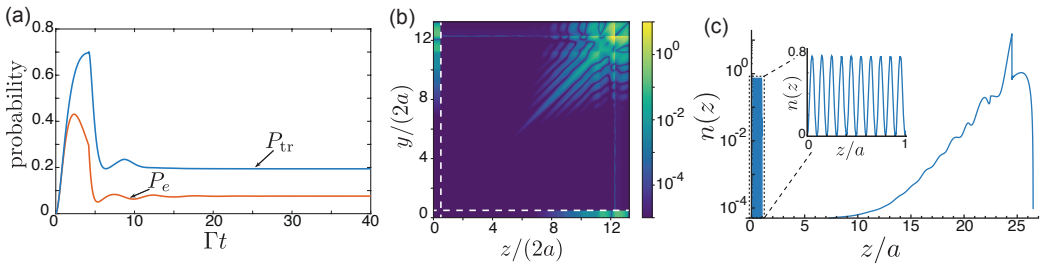

Figure 7.2: BIC generation via two-photon scattering. (a) Evolution of the qubit population P_e and trapping probability $P_{\rm tr}$. (b) Two-photon probability density function $|\chi(z,y)|^2$ at the end of scattering ($t = t_f$). The white dashed lines z=a and y=a mark the position of the atom. (c) Spatial profile of the total photon density $n(z)$ at the end of the scattering. The inset highlights the sinusoidal wavefunction in the range $0 \le z \le a$. Panels (b) and (c) are plotted in a logarithmic scale for t_f=80/Γ. In (a)-(c), we considered a two-photon exponential wavepacket (see main text) and set $k_0 a = 10\pi$, $\Gamma\tau = 3$ and $\alpha = \Gamma/2v$.

scattering process is over. From both plots we can see that the wavepacket is not entirely reflected back. Indeed a significant fraction remains trapped between the mirror and emitter, forming a perfectly sinusoidal stationary wave with wave-vector k_0 [see Fig. 7.2(c)]. Note that this stationary wave has a single-photon nature. Indeed, Fig. 7.2(b) shows that either both photons are scattered by the emitter (top right corner) or one is scattered and the other remains trapped in the atom-mirror region (top left and bottom right corners). The probability that both photons are trapped is instead zero (bottom left corner).

Looking at these outcomes and considering the form of the BIC given in Eq. (7.2), we can conjecture that after the scattering process the joint state has the form

$$|\Psi(t)\rangle = \int_a^\infty \mathrm{d}z\, \xi(x,t) a_R^\dagger(z)|\phi_b\rangle \; + \iint_a^\infty \mathrm{d}z\mathrm{d}y\, \beta(z,y,t)\, a_R^\dagger(z) a_R^\dagger(y)|g,0\rangle. \qquad (7.8)$$

Here the first term describes the BIC excited and a single photon leaving the atom-mirror region, while the second term corresponds to two outgoing photons. Note that equation (7.8) is valid only in the long-time limit, $t \gg \tau$, when the scattering process is over.

If we are actually interested in evaluating the probability to excite a BIC a more relevant quantity that can be computed numerically is given by $P_{\rm tr} = P_e + P_{\rm ph}$ [see Eq. (7.2.1) and (7.6)]. This quantity represents the probability that either a photon is trapped between the mirror and the atom or that the emitter is excited. It can be easily shown that if Eq. (7.8) holds then the asymptotic value of $P_{\rm tr}$ satisfies

$$P_{\rm tr}(\infty) = \int_a^\infty \mathrm{d}z\, |\xi(z,\infty)|^2 = P_{\rm BIC} = \left(1 + \tfrac{\Gamma}{2}\tau\right) P_e(\infty), \qquad (7.9)$$

where $P_{\rm BIC}$ represents the probability of generating the BIC (7.2). The time dependence of $P_{\rm tr}$ is shown in Fig. 7.2(a). It reaches a finite steady value that is larger

than $P_e(\infty)$ by exactly the factor $(1+\Gamma\tau/2)$, in full agreement with the last identity in Eq. (7.9), confirming the conjecture in Eq. (7.8) and thus the generation of the BIC. Note that the identity $P_{\rm tr}(\infty)=(1+\Gamma\tau/2)P_e(\infty)$ was checked in all of the numerical results presented in this work.

7.2.2 Discussion

Dependence on time delay

A crucial point of our BIC generation scheme is that a significant delay time is essential in order to get a non-negligible trapping. For instance, the parameter set in figure Fig. 7.2 correspond to $\Gamma\tau = \pi$. To highlight this dependence further, we report in Fig. 7.3(a) the steady values of P_e, $P_{\rm ph}$ and $P_{\rm tr}$, as functions of $\Gamma\tau$ for the two-photon scattering process. Here, for each value of $\Gamma\tau$, we used the optimal wave packet width, $\alpha_{\rm opt}$, that maximizes the BIC trapping. Its dependence on $\Gamma\tau$ is shown in Fig. 7.3(b). In general we observe three different regimes for the trapping process that are discussed in the following.

- In the Markovian regime, $\Gamma\tau \ll 1$, we observe from Fig. 7.3(a) that both the photon trapping and the atom's stationary excitation are negligible. This is in sharp contrast to spontaneous emission schemes for which this is instead the optimal regime. An intuitive explanation of this behaviour is the following. During the scattering one of the two photons excites the atom while the other is transmitted and, after being reflected by the mirror, escapes the atom-mirror region before that the absorbed photon is re-emitted by the atom.

- When the retardation time starts to be more significant, the trapping probability reaches a maximum at a delay of the order of $\Gamma\tau \sim 1$. In this regime the first absorbed photon gets re-emitted by the atom on the same time scale on which the transmitted photon comes back, allowing the relaxation into the BIC.

- For large delay times, $\Gamma\tau \gg 1$, P_e becomes negligible while $P_{\rm ph}$ and $P_{\rm tr}$ seems to saturate only to weakly decrease with $\Gamma\tau$ (note that extend this simulation for larger time delays is numerically challenging). Remarkably in this regime the BIC becomes almost completely photonic. This means that with our scheme we can capture an almost pure single photon (not dressed by atomic excitation), which is not achievable in spontaneous emission, where the state is always dressed [see Eqs. (7.2)].

Detuned wave-packets

From Fig. 7.3(a)-(b) we can see that, in the regime where the trapping probability is not negligible, $\Gamma\tau \gtrsim 1$, the optimal width is on the order of $\alpha \sim \Gamma/(4v_g)$. This agrees with the general expectation [see e.g. Refs. [202, 203, 204]] that the photon absorption during the scattering transient is maximum when the wave-packet width

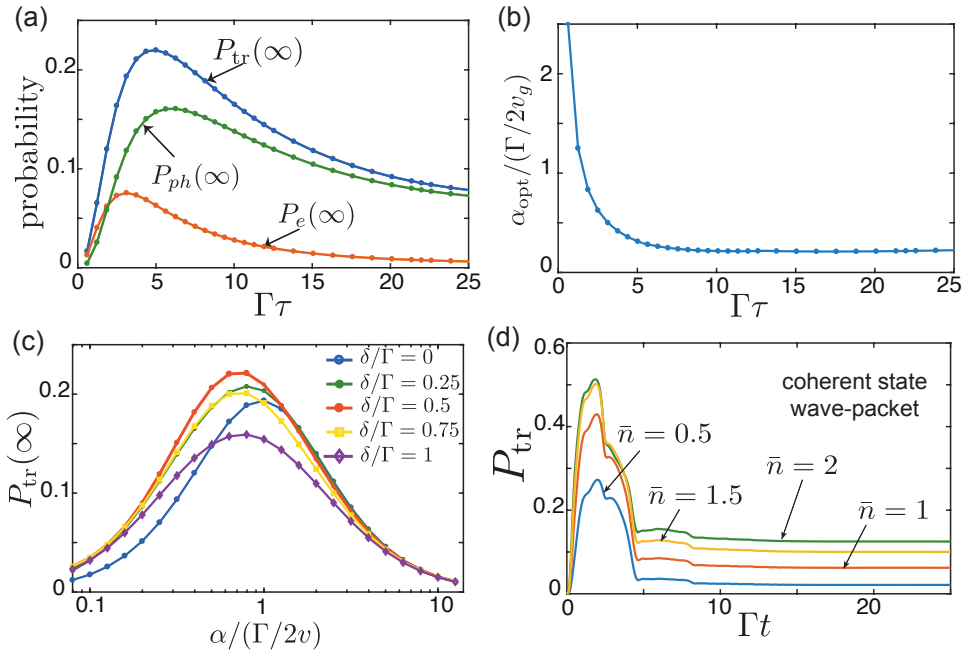

Figure 7.3: (a) Asymptotic values of P_e, $P_{\rm ph}$ and $P_{\rm tr}$ as function of the rescaled time delay $\Gamma\tau$. At each point of $\Gamma\tau$ we set the wave-packet width to the value that maximizes $P_{\rm tr}$, $\alpha = \alpha_{\rm opt}$, using the results given in (b). (b) Optimal wave-packet width, $\alpha_{\rm opt}$, as a function of $\Gamma\tau$. (c) $P_{\rm tr}(\infty) = P_{\rm BIC}$ as a function of the width of the wavepacket for different values of the detuning δ. Here we considered a wavepacket featuring one photon with carrier wavevector $k_1 = k_0 + \delta/v_g$ and the other with $k_2 = k_0 - \delta/v_g$. We set $k_0 a = 10\pi$, $\Gamma\tau = 3$. (d) $P_{\rm tr}$ versus time for a coherent-state wavepacket with different average photon number, $\bar{n}$. Here we considered the same shape for the wave packets and parameters as in 7.2 (a). For computational purposes, only contributions up to three-photon Fock states were considered.

is of the order of the atomic decay rate. On the other hand this value is also connected to the fact that the photon capture occurs through a nonlinear scattering process. Indeed, in [205] it was pointed out that, when two photons scatter from a TLA, the nonlinear scattering flux is peaked at two side frequencies detuned by $\Gamma/2$ from the atomic resonance. Thus, the requirement to observe the capture on resonance is that the wave-packet width should be able to properly resolve these side peaks. This argument becomes more evident in Fig. 7.3(c) where we plot the trapping probability as a function of the wave-packet width for one of the input photons blue-detuned from the atomic frequency while the other red-detuned by the same amount δ. We indeed observe that the capture probability can be further maximized by tuning the input photons on resonance with the side peaks, $\delta = \Gamma/2$. This also requires to consider a slightly smaller wave-packet width to properly resolve the nonlinear scattering peaks.

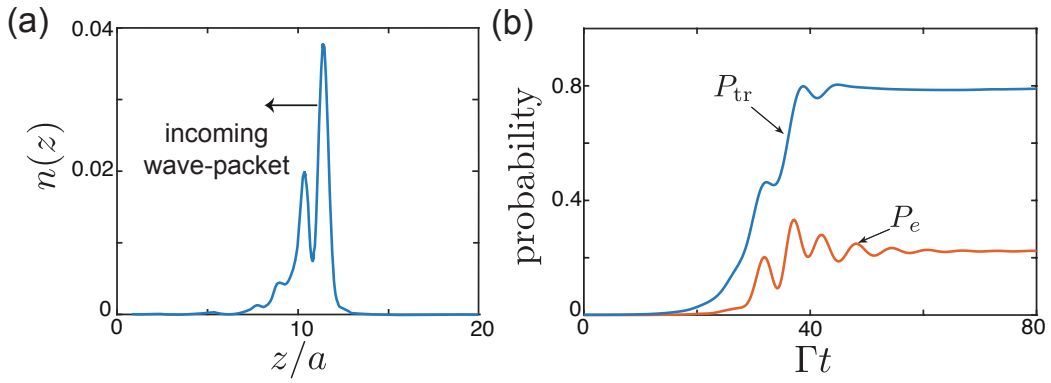

Figure 7.4: BIC generation scheme for the one-qubit setup using a shaped two-photon wave-packet. (a) Photon density profile of the incoming wave-packet. (b) $P_{\rm tr}$ and P_e versus time. For this plot we fixed the distance to $k_0 a = 20\pi$ and the time delay to $\Gamma\tau = 5$ to maximize the photon trapping probability [see Fig. 7.3(a)].

Coherent-state wave-packet

It is natural to ask whether the BIC excitation through photon scattering is a peculiarity of the two-excitation subspace or if it can persists when more than photons are involved. To answer this question we extended our numerical simulation to the third excitation subspace and we found that the BIC can still be generated with a considerable probability. In particular, in an experiment, it would be easier to send a weak coherent photon pulse instead of a two photon wave-packet. We thus considered the same setup, parameters, and wavepacket shape $\phi(z)$ as in Fig. 7.2(a), but assumed as an initial state the following coherent-state pulse [11]

$$|\beta\rangle = e^{-|\beta|^2} \sum_{m=0}^{\infty} (\beta^m/m!) \left(\int \mathrm{d}z\, \phi(z) a^\dagger(z) \right)^m |g,0\rangle, \tag{7.10}$$

where $\bar{n} = |\beta|^2$ is the average photon number. In Fig. 7.3(d) we show the trapping probabilities as a function of time for different values of the average photon number. In this simulation we truncated to the third excitation subspace so the results are valid only for low-power coherent pulses. We note that for $\bar{n} = 2$, $P_{\rm tr}(\infty)$ is comparable to the one obtained with the two-photon pulse. This suggest that the BIC can be generated also using weak coherent states.

Increasing the BIC generation probability

The exponential pulse considered for Figs. 7.2-7.5, is commonly used in the literature [203, 204] and we choose it for illustrative purposes and computational efficiencies. On the other end the trapping probability, $P_{\rm tr}(\infty)$, could be strongly enhanced by engineering different wavepacket shapes.

In order to find a more suitable wave-packet shape we consider the time reversal scenario of our problem, where a BIC is initially excited and a single photon packet

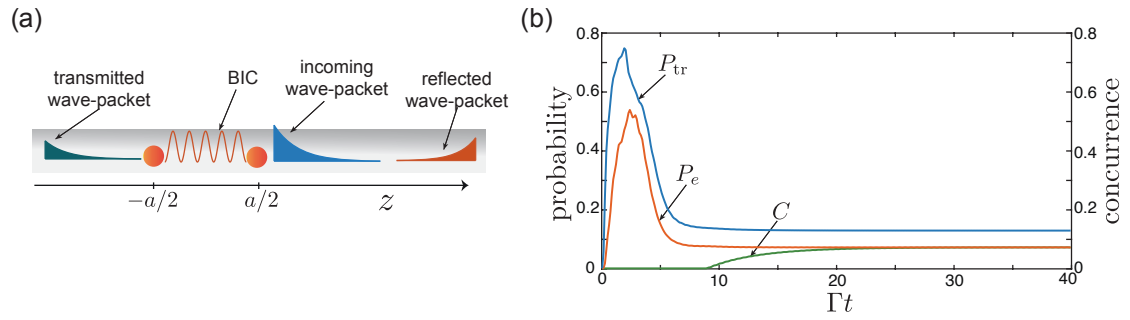

Figure 7.5: (a) Two-atoms coupled to an infinite waveguide. A two-photon wave-packet is sent through the emitters and excites the BIC, yielding stationary entanglement between the atoms. (b) Total atomic population, P_e, trapping probability $P_{\rm tr}$ and atom-atom concurrence C versus time in a two-photon scattering process. The shape of the incident wave packet and parameters are the same as in Fig. 7.2.

is sent through the emitter. If ideally we could determine the single photon packet that completely releases the BIC the two outgoing photons at the end of the process would constitute the perfect wave-packet input for our BIC generation scheme.

Following this intuition we use a single photon gaussian wavepacket of the form

$$\phi^L(z) = \frac{1}{\sqrt[4]{\pi\Delta z^2}} e^{-\frac{(z-a)^2}{2\Delta z^2} - ik_0(z-a)}, \tag{7.11}$$

where Δz is the packet width. In particular, we fix the packet width to $\Delta z = 2v_g/\Gamma$, which minimizes $P_{\rm tr}(\infty)$ in the reverse problem.

In this case the shape of the final two photon outgoing packet, even if it does not correspond to the optimal input, turns out to be a much better ansatz for our original problem. In Figure 7.4 we show that the replacement of the exponential two-photon wave-packet with the output of the reverse problem [given in Fig. 7.4(a)] yields a trapping probability of $P_{\rm tr}(\infty) \simeq 80\%$, a value about four times larger than that one previously obtained. Note that here we set the parameters such that $\Gamma\tau = 5$, roughly corresponding to the maximum of $P_{\rm tr}(\infty)$ in Fig. 7.3(b). This result shows that, in principle, with a properly shaped wave packets it should be possible to excite the BIC through non-linear scattering with probability close to one.

7.3 Two-atom BIC

In this last section we consider a case analogous to that one treated so far: two atoms in an infinite waveguide located at positions $z_1 = -a/2$ and $z_2 = a/2$ and separated by a distance a, as shown in Fig. 7.5(a). As we discussed in section 2.3.3, also in this configuration there exists a BIC in the single excitation subspace that presents a photon localized in the inter-atomic region. The explicit form of the BIC for this setup was given in Eq. (2.41). Note that in this case the relation between the

trapping probability and the atomic amplitude is given by $P_{\rm tr}(\infty)$=$(1+\Gamma\tau/4)P_e(\infty)$. The atomic component of the BIC state it consists of a symmetric/antisymmetric (depending on whether m is odd or even), maximally entangled state that can be harvested by tracing out the field. Thus it is interesting to see if it is possible to generate entanglement between the two atoms by using our scattering-based scheme.

With this goal in mind let us define the generic state of the system at a time t,

$$\begin{aligned}|\Psi(t)\rangle = \Bigg(f(t)\sigma_+^1\sigma_+^2 + \sum_\eta \int_{-\infty}^{\infty} \mathrm{d}z\, \psi_\eta^1(z,t) a_\eta^\dagger(z)\sigma_+^1 + \sum_\eta \int_{-\infty}^{\infty} \mathrm{d}z\, \psi_\eta^2(z,t) a_\eta^\dagger(z)\sigma_+^2 \\ + \sum_{\eta,\eta'} \tfrac{1}{\sqrt{2}} \iint_{-\infty}^{\infty} \mathrm{d}z_1 \mathrm{d}z_2\, \chi_{\eta,\eta'}(z,y,t) a_\eta^\dagger(z) a_{\eta'}^\dagger(y)) \Bigg) |g\rangle|0\rangle,\end{aligned} \tag{7.12}$$

where the apex i in $\psi_\eta^i(z,t)$ refers to the first or the second atom. The total qubit population and the photon trapping population are defined in manner similar to the atom-mirror case:

$$P_e(t)=|f(t)|^2 + \sum_\eta \int_{-\infty}^{\infty} \mathrm{d}z\, |\psi_\eta^1(z,t)|^2 + \sum_\eta \int_{-\infty}^{\infty} \mathrm{d}z\, |\psi_\eta^2(z,t)|^2, \tag{7.13}$$

$$P_{\rm ph}(t)=\sum_{\eta,\eta'} \int_{-a}^{a} \mathrm{d}z \int_{-\infty}^{-a} \mathrm{d}y\, |\chi_{\eta,\eta'}(z,y,t)|^2 + \sum_{\eta,\eta'} \int_{-a}^{a} \mathrm{d}z \int_{a}^{\infty} \mathrm{d}y\, |\chi_{\eta,\eta'}(z,y,t)|^2. \tag{7.14}$$

The excitation trapping probability is then again given by $P_{\rm tr} = P_e + P_{\rm ph}$. To evaluate the amount of entanglement generated with our scheme we use the concurrence introduced in section 2.2.1. For our setup it is explicitly given by

$$C(t) = \max\left(0, 2|\mathrm{C_{12}(t)}| - \sqrt{|\mathrm{f(t)}|^2 \mathrm{P_{ph}}}\right). \tag{7.15}$$

where

$$C_{12}(t)=\sum_\eta \int_{-\infty}^{\infty} \mathrm{d}z\, (\psi_\eta^1(z,t))^* \psi_\eta^2(z,t), \tag{7.16}$$

is the atomic coherence.

For the following example we considered the same exponential wavepacket as in Fig. 7.2 and we simulate the scattering process with the two atoms. In Fig. 7.5(b) we plot the resulting evolution of the total atomic population, P_e, the trapping probability, $P_{\rm tr}$, and the concurrence. Similar to the atom-mirror case there is a finite probability to excite the BIC. In this case the reduced steady state of the two atoms is indeed entangled as shown from the finite steady value of the concurrence.

.

Chapter 8

Harvesting multi-qubit entanglement from ultrastrong interactions in circuit QED

Throughout this thesis so far we have focused on physical situations where the atom-light interaction can be correctly described within the rotating wave approximation. For many years it has been experimentally challenging to reach regimes where this approximation breaks down. The situation has recently changed, in particular, in the field of circuit QED [70, 71], where a single superconducting two-level system can be coupled to a microwave resonator mode [206, 207, 208, 209, 210, 211, 212]. In this context interaction strengths comparable to the photon energy have been demonstrated in a number of experiments [213, 214, 215, 216, 217]. This regime, that goes beyond the usual strong coupling of cavity QED, it is often referred as *ultrastrong* coupling regime [72, 73].

A crucial difference of this regime compared to usual cavity QED can already be found in the ground state, which is not anymore just a trivial vacuum state with no excitations. In the ultrastrong coupling regime the physics of the ground state can indeed change drastically and various effects like spontaneous vacuum polarization [218, 219, 220], light-matter decoupling [221, 74] and different degrees of entanglement [74, 222, 223, 224, 225] have been discussed.

Among several effects here we want to focus in particular on a recent result, where it has been shown that, in the USC regime, a system consisting of multiple superconducting qubits coupled to a single mode of a microwave resonator can exhibit, in the ground and in the low-energy states, a high degree of multiqubit entanglement [74]. However, this entanglement it is not easy to access since any operation on the state would necessarily introduce a strong perturbation to the system.

In this project we propose an entanglement-harvesting protocol [227, 228, 229, 230, 231, 232, 233], which can extract the entanglement from the USC states and convert it into equivalent entangled states of decoupled qubits. The protocol requires a time-dependent tuning of some of the system parameters and combines

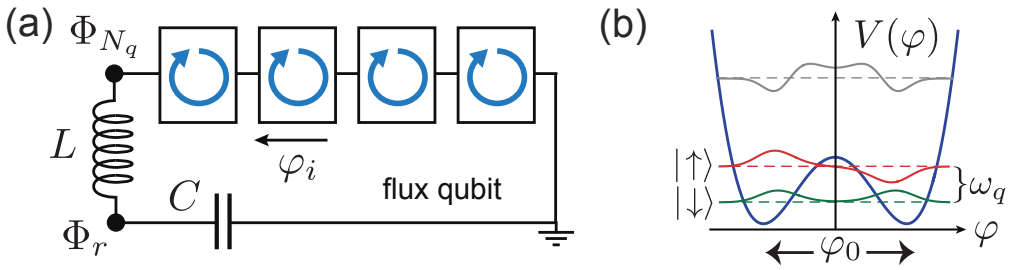

Figure 8.1: (a) Sketch of the circuit QED setup: multiple flux qubits are inductively coupled to an LC microwave resonator. Here $\Phi_{N_q} = \Phi_0 \sum_{i=1}^{N_q} \varphi_i$. (b) Each flux qubit is represented by the two lowest states $|\downarrow\rangle$ and $|\uparrow\rangle$ of an effective double-well potential for the phase variable φ.

both adiabatic and nonadiabatic variations. As we will show, the protocol turns out to be particularly robust with respect to temperature, disorder and lack of tunability because the entangled state is protected by the strong atom-field interaction.

In this work I contributed as a second author and I supported F. Armata (first author) to develop the protocol. In particular, I also performed part of the analytic and numerical calculations. The circuit implementation of this protocol was entirely developed by T. Jaako and is not reported here (see [75]). The work was done under the supervision of P. Rabl and M. S. Kim and the results were published on Physical Review Letters 119 (18), 183602 (2017).

8.1 Introduction to the model

8.1.1 Hamiltonian

For the following discussion we consider a circuit QED system consisting of a single mode LC resonator with capacitance C and inductance L, which is coupled collectively to an even number of $N_q = 2, 4, 6, \ldots$ of flux qubits [see Fig. 8.1(a)]. The whole circuit is described by the Hamiltonian (see [75, 74] for the derivation of the Hamiltonian from a Lagrangian formalism [234])

$$\mathcal{H} = \frac{Q_r^2}{2C} + \frac{(\Phi_r - \Phi_0 \sum_{i=1}^{N_q} \varphi_i)^2}{2L} + \sum_{i=1}^{N_q} H_q^{(i)}, \tag{8.1}$$

where Q_r and Φ_r are charge and flux generalized operators for the resonator obeying $[\Phi_r, Q_r] = i\hbar$, and $\Phi_0 = \hbar/(2e)$ is the reduced flux quantum. In Eq. (8.1) H_q^i denotes the free qubits Hamiltonian while φ_i is the difference of the superconducting phase associated with each flux qubit. The second term of Hamiltonian (8.1) is explicitly given by

$$\frac{(\Phi_r - \Phi_0 \sum_{i=1}^{N_q} \varphi_i)^2}{2L} = \frac{\Phi_r^2}{2L} - \sum_{i=1}^{N_q} \frac{\varphi_i \Phi_r}{L} + \sum_{i,j=1}^{N_q} \frac{\varphi_i \varphi_j}{2L}, \tag{8.2}$$

where the first term combined with $\frac{Q_r^2}{2C}$ provides the resonator energy, the second term the collective qubit-photon coupling and the last term a collective qubit-qubit interaction. This qubit-qubit interaction is usually neglected for cavity QED systems with weak or moderately strong couplings. However, this term is crucial in the USC regime and it is responsible for the nontrivial ground-state correlations that are at the basis of this project, as we will discuss in the following. Note that here, apart from the coupling of each individual qubit to the resonator, we did not included any direct coupling among the qubits (for an extended model that includes direct dipole-dipole interactions see [222]).

At cryogenic temperatures, at which the superconducting circuits operate, the elementary excitations of the system are quantized. Therefore, we can express the conjugate resonator variables in terms of annihilation and creation operators a and $a^\dagger$, writing $\Phi_r = \sqrt{\hbar/(2C\omega_r)}(a + a^\dagger)$ and $Q_r = i\sqrt{\hbar C\omega_r/2}(a^\dagger - a)$, where $\omega_r = \sqrt{1/LC}$ is the resonator frequency. The energy spectrum of the flux qubit can be instead approximately described by a double well potential, as depicted in Fig. 8.1(b). Here we assume that the qubit dynamics can be restricted to the two lowest tunneling states $|\downarrow\rangle$ and $|\uparrow\rangle$ of this potential. This approximation allows us to write $\varphi_i = \varphi_0^i \sigma_x^i$ where $\varphi_0^i = 2\langle\downarrow_i |\varphi_i| \uparrow_i\rangle$ and σ_x^i is the usual Pauli operator. Under these approximations, we can rewrite Hamiltonian (8.1) in the following quantized form

$$\mathcal{H} = \hbar\omega_r a^\dagger a + \hbar \sum_{i=1}^{N_q} \frac{g_i}{2}(a^\dagger + a)\sigma_x^i + \hbar \sum_{i=1}^{N_q} \frac{\omega_q^i}{2}\sigma_z^i + \hbar \sum_{i,j=1}^{N_q} \frac{g_i g_j}{4\omega_r}\sigma_x^i \sigma_x^j, \tag{8.3}$$

where ω_q^i are the qubit-level splittings. Here the collective qubit-resonator interaction is mediated by the couplings $g_i = \Phi_0\sqrt{|\varphi_0^i|^2\omega_r/(2\hbar L)}$.

For this work we are primarily interested in a symmetric configuration, i.e., $g_i = g$ and $\omega_q^i = \omega_q$. In this case the Hamiltonian (8.3) can be expressed in terms of collective angular momentum operators $S_n = \sum_i \sigma_n^i/2$ and reduces to the extended Dicke Hamiltonian [74, 222]

$$\mathcal{H} = \hbar\omega_r a^\dagger a + \hbar g(a^\dagger + a)S_x + \hbar\omega_q S_z + \hbar\frac{g^2}{\omega_r}S_x^2. \tag{8.4}$$

The ultrastrong coupling regime, where the RWA approximation ceases to be valid, is reached when $g > \omega_r, \omega_q$. This condition can be achieved not only with the flux-qubits implementation that we are considering [218, 226, 235, 236, 210, 209], but also with several charge qubit designs [74, 222]. Our flux qubits choice relies on the fact that, in the protocol that we are going to present, it is necessary to tune the coupling strength, $g(t)$ and the qubit frequency, $\omega_q(t)$. This can be done by controlling the matrix element φ_0^i and the height of the tunnel barrier via local magnetic fluxes [226, 231]. A specific four-junction qubit design [236, 237], which combines strong interactions with a high degree of tunability, is detailed in the Supplemental Material of [75].

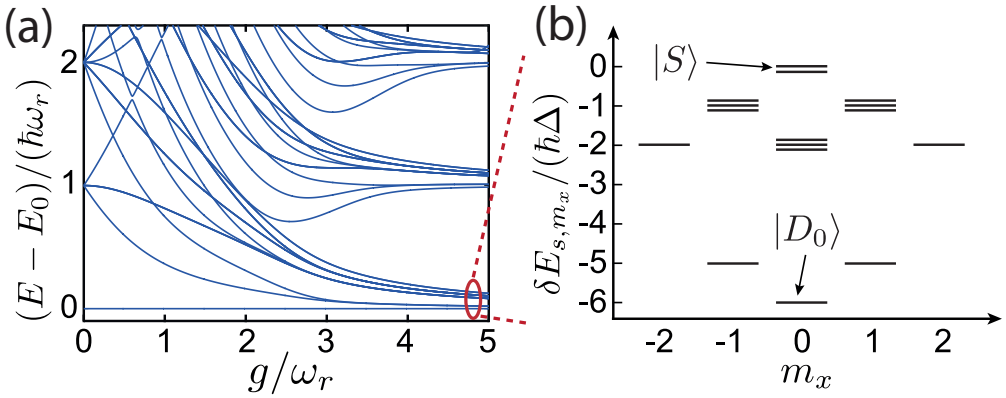

Figure 8.2: (a) Energy spectrum (with respect to the ground-state energy E_0) of the extended Dicke model (8.4) as a function of the coupling strength g for $N = 4$ and $\omega_q = \omega_r$. (b) Ordering of the lowest energy states in the USC regime as determined by Eq. (8.7) for the case $N_q = 4$. The multiple lines indicate the two- and threefold degeneracy of states with total angular momentum $s = 0$ and $s = 1$, respectively.

8.1.2 Spectrum

Let us discuss the spectral properties of Hamiltonian (8.4). In the usual cavity QED scenario the coupling is much smaller than the qubits and resonator frequencies, $g \ll \omega_r, \omega_q$. In this regime we can make a rotating wave approximation and obtain the standard Tavis-Cummings model (see Sec. 1.3.2), where the ground state is trivially given by having both the resonator and the qubits unexcited, $|G\rangle = |n = 0\rangle \otimes |\downarrow\rangle^{\otimes N_q}$. In the specific case where the qubits are also off resonance with the resonator, $|\omega_q - \omega_r| \gg g$, the states of the qubits can be individually prepared, manipulated, and measured by additional control fields. This is of fundamental relevance if the final goal is to implement quantum information processing.

In the ultrastrong coupling limit, where the coupling strength becomes comparable to the qubit and resonator frequencies, $g \geq \omega_r, \omega_q$, the coupling terms $\sim S_x$ and $\sim S_x^2$ becomes important and the level structure changes completely. This is illustrated in Fig. 8.2(a) where the energy levels are plotted as a function of g/ω_r. In particular, for couplings $g/\omega_r \gtrsim 3$ the spectrum separates into manifolds of 2^{N_q} nearly degenerate states. In this regime the eigenstates of Hamiltonian (8.4) can be obtained by applying a displacement operator to the photon number states $|n\rangle$ [74]:

$$|\Psi_{s,m_x,n}\rangle \simeq e^{-\frac{g}{\omega_r}(a^\dagger - a)S_x}|n\rangle \otimes |s, m_x\rangle. \tag{8.5}$$

Here $|s, m_x\rangle$ s are collective spin states and s is the total spin with $m_x = -s, \ldots, s$ being the spin projection quantum number; i.e., $S_x|s, m_x\rangle = m_x|s, m_x\rangle$. The corresponding eigenenergies of these states are given by:

$$E_{s,m_x,n} \simeq \hbar\omega_r n + \delta E^{(n)}_{s,m_x}. \tag{8.6}$$

In particular, within the lowest manifold, the remaining level splittings are given by

$$\delta E^{(0)}_{s,m_x} = \hbar\Delta\left[m_x^2 - s(s+1)\right], \qquad \Delta = \frac{\omega_q^2\omega_r}{2g^2}, \tag{8.7}$$

and the resulting ordering of the states is shown in Fig. 8.2(b) for $N_q = 4$ qubits.

For an even numbers of qubits, N_q, there are some states of the spectrum in the USC regime that present a high degree of qubit-qubit entanglement. In particular, in this work we are interested in states where the angular momentum has vanishing projection along x, $m_x = 0$, and $s = N_q/2$ or $s = 0$. The first case corresponds to the ground state of the USC regime that is of the form $|\tilde{G}\rangle \simeq n = |0\rangle \otimes |D_0\rangle$, where $|D_0\rangle = |s = N_q/2, m_x = 0\rangle$ [indicated in Fig. 8.2(b)] denotes a fully symmetric Dicke state. For instance, in the paradigmatic cases of $N_q = 2, 4$ the qubits states are respectively given by (in the rotated x basis)

$$|s = 1, m_x = 0\rangle = \frac{1}{\sqrt{2}}(|\uparrow\downarrow\rangle_x + |\downarrow\uparrow\rangle_x), \tag{8.8}$$

$$|s = 2, m_x = 0\rangle = \frac{1}{\sqrt{6}}(|\downarrow\downarrow\uparrow\uparrow\rangle_x + |\uparrow\uparrow\downarrow\downarrow\rangle_x + |\downarrow\uparrow\uparrow\downarrow\rangle_x + |\uparrow\downarrow\downarrow\uparrow\rangle_x + |\downarrow\uparrow\downarrow\uparrow\rangle_x + |\uparrow\downarrow\uparrow\downarrow\rangle_x). \tag{8.9}$$

The second case is represented by the energetically highest manifold (always within the lowest excitation manifold) $|\tilde{E}\rangle = |n = 0\rangle \otimes |S\rangle$, where $|S\rangle$ indicates states with total angular momentum $s = 0$ and $S_z|S\rangle = S_x|S\rangle = 0$ [see Fig. 8.2(b)]. For $N_q = 2$ and $N_q = 4$ qubits they are given by

$$|s = 0, m_x = 0\rangle = \frac{1}{\sqrt{2}}(|\uparrow\downarrow\rangle_x - |\downarrow\uparrow\rangle_x), \tag{8.10}$$

and

$$|s = 0, m_x = 0\rangle = \begin{cases} |S\rangle = \frac{1}{\sqrt{3}}(|\uparrow\uparrow\downarrow\downarrow\rangle_x + |\downarrow\downarrow\uparrow\uparrow\rangle_x) - \frac{1}{\sqrt{12}}(|\uparrow\downarrow\uparrow\downarrow\rangle_x + |\uparrow\downarrow\downarrow\uparrow\rangle_x + |\downarrow\uparrow\uparrow\downarrow\rangle + |\downarrow\uparrow\downarrow\uparrow\rangle_x), \\ |S'\rangle = \frac{1}{2}(|\uparrow\downarrow\uparrow\downarrow\rangle_x - |\uparrow\downarrow\downarrow\uparrow\rangle_x - |\downarrow\uparrow\uparrow\downarrow\rangle_x + |\downarrow\uparrow\downarrow\uparrow\rangle_x). \end{cases} \tag{8.11}$$

The interest in these states not only relies on the high degree of entanglement, but also on the fact that they can be decoupled from the cavity field. This is almost the case for the $s = N_q/2$ states, when the coupling is sufficiently strong, $g/\omega_r \gtrsim 3$ [74], while it occurs in all parameter regimes for the $s = 0$ states that are exact dark states of Hamiltonian (8.4). Although theoretically fascinating, these maximally entangled states can not be externally addressed since any attempt to locally manipulate or measure the individual qubits would necessarily introduce a severe perturbation to the entire strongly coupled system. In the following we will present two suitable protocols (one for $s = N_q/2$ one for $s = 0$) to convert these states into equivalent states energetically isolated from the resonator, where they become available as an entanglement resource for further use.

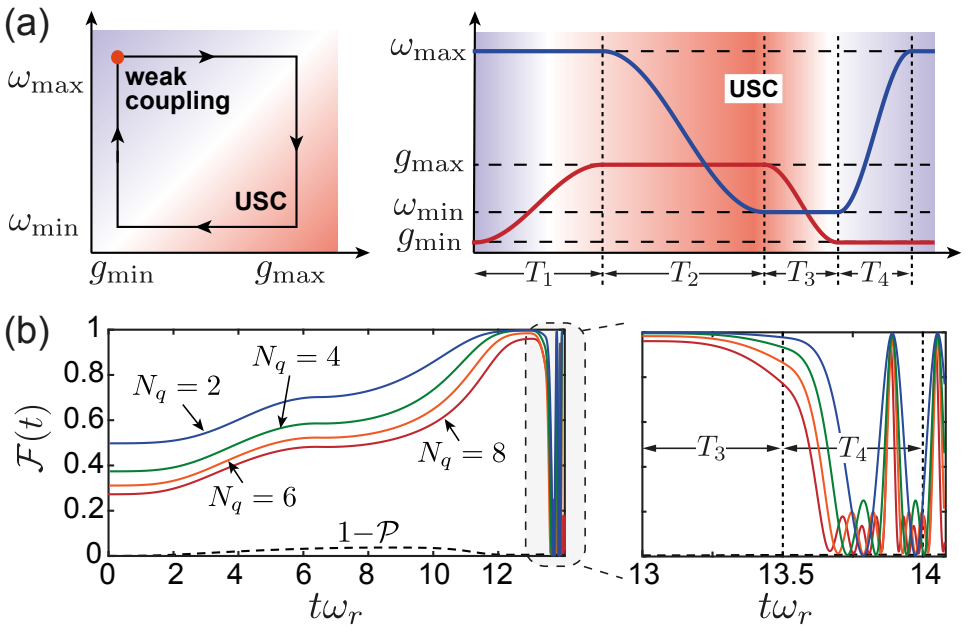

Figure 8.3: (a) Sketch of the protocol and general pulse sequence for the qubit parameters $\omega_q(t)$ and $g(t)$ considered for the implementation of the entanglement harvesting protocol. (b) The fidelity $\mathcal{F}(t)$ is plotted as a function of time and for different qubit numbers. The dashed line indicates the quantity $1-\mathcal{P}(t)$, where $\mathcal{P}(t) = \mathrm{Tr}\{\rho_q^2(t)\}$ is the purity of the reduced qubit state $\rho_q(t) = \mathrm{Tr}_r\{\rho(t)\}$ for the case $N_q = 4$. For all values of N_q the same parameters $\omega_{\max}/\omega_r = 20$, $\omega_{\min}/\omega_r = 0.5$, $g_{\max}/\omega_r = 4.5$, $g_{\min}/\omega_r = 0.1$ and times intervals $T_1 = T_2 = 6.5\omega_r^{-1}$ and $T_3 = T_4 = 0.5\omega_r^{-1}$ have been assumed.

8.2 Protocol for the states with $s = N_q/2$

8.2.1 Entanglement harvesting

In order to be able to address the entanglement states presented in the previous section we here consider the possibility of tuning over time the qubit frequency $\omega_q(t)$ and the coupling strength $g(t)$ of Hamiltonian (8.4).

The main idea of the protocol that we are going to propose is sketched in 8.3(a) where we consider a general pulse sequence of $\omega_q(t)$ and $g(t)$. The protocol starts by initializing the system in the ground state $|G\rangle$ of the weakly coupled system, where the qubits are far detuned from the cavity, $\omega_q = \omega_{\max} \gg \omega_r$, and the coupling is set to a minimal value, $g = g_{\min} < \omega_r$. In the first two steps, T_1 and T_2, the system is adiabatically tuned into the USC regime by applying two pulses that bring the coupling and the qubit frequency to a maximal and a low value, $g_{\max} > \omega_r$ and $\omega_{\min} \lesssim \omega_r$, respectively. This process prepares the system in the USC ground state $|\tilde{G}\rangle$. In the successive steps, T_3 and T_4 we close the loop of Fig. 8.3(a) and we separate again the qubits and the resonator mode. The main difference here is that now we apply nonadiabatic pulses to the parameters in the reverse order. Ideally,

during this part of the protocol the system simply remains in state $|\tilde{G}\rangle$ and becomes the desired excited state of the weakly coupled system at the final time $T_{\rm f} = \sum_{n=1}^{4} T_n$.

In order to correctly implement this sequence we need to respect two conditions on the speed of the pulse. First, we require that the adiabatic preparation stage must be slow compared to the time scales set by $\omega_{\rm max}^{-1}$ and $g_{\rm max}^{-1}$. This is actually not a a problem. Indeed the time scale relative to $\omega_{\rm max}^{-1}$ and $g_{\rm max}^{-1}$ is really fast (compared for example to typical system decoherence time) and thus this part of the protocol can still be implemented very rapidly. For the nonadiabatic decoupling processes instead we need to be fast compared to the time scales ω_r^{-1}, $\omega_{\rm min}^{-1}$, and $g_{\rm min}^{-1}$. This condition can also be fulfilled. Indeed these time scales are slow enough to make the required switching times experimentally accessible and consistent with the two-level approximation assumed in our theoretical model. To prove the efficiency of our protocol we numerically solve the full time-dependent dynamics, given by the Hamiltonian (8.4), with the time dependent parameters $\bar{\omega}_q(t)$ and $g(t)$. After that the protocol is completed, in order to verify that we successfully prepared the desired states, we evaluate the fidelity $\mathcal{F}(t) = {\rm Tr}\{\rho({\rm t})|{\rm D}_0\rangle\langle{\rm D}_0|\}$, where $\rho(t)$ is the density operator of the full system. In Fig. 8.3(b) we plot the $\mathcal{F}(t)$ for a specific set of pulse parameters listed in the figure caption. We see that the entanglement extraction fidelity (EEF) $\mathcal{F}_{\rm E} = \max\{\mathcal{F}(t)|t \geq T_{\rm f}\}$, i.e., the maximal fidelity after the decoupling step, reaches near perfect values of $\mathcal{F}_{\rm E} \simeq 0.95 - 0.99$ for different numbers of qubits, without any further fine-tuning of the control pulses. Note that the fidelity oscillations at the end of the sequence are simply due to the fact that $|D_0\rangle$ is not an eigenstate of the bare qubit Hamiltonian, $H_q = \omega_q S_z$. However, this evolution does not affect the purity or the degree of entanglement of the final qubit state and can be undone by local qubit rotations.

8.2.2 Robustness of the protocol

Lack of tunability

In principle our protocol would work perfectly if, in the nonadiabatic step, we could completely and instantaneously switch off the coupling. This would leave the qubits in the final desired state state, $|D_0\rangle$, disentangled from the resonator mode. Obviously, in a realistic implementation, the switching off time, T_4, has a finite duration and the coupling, $g_{\rm min}$, cannot be turned off completely. In general possible limitations to the protocol might come from a lack of complete tunability of both $g(t)$ and $\omega_q(t)$.

To discuss these points let us take a look at Fig. 8.4(a), which shows the evolution of the lowest eigenenergies during different stages of the protocol for the case $N = 2$ and a finite value of $g_{\rm min}$. In this case the non-vanishing coupling $g_{\rm min}$ induces several avoided crossings during the final ramp-up step, which prevents a fully nonadiabatic decoupling and limits the fidelity for a finite time T_4. In Fig. 8.4(b) we plot the extraction fidelity, EEF, for the same parameters as in Fig. 8.4(a), but for varying $g_{\rm min}$ and T_4. This plot indeed shows the expected trade-off between the minimal coupling and the residual switching time, but also that the protocol is rather robust

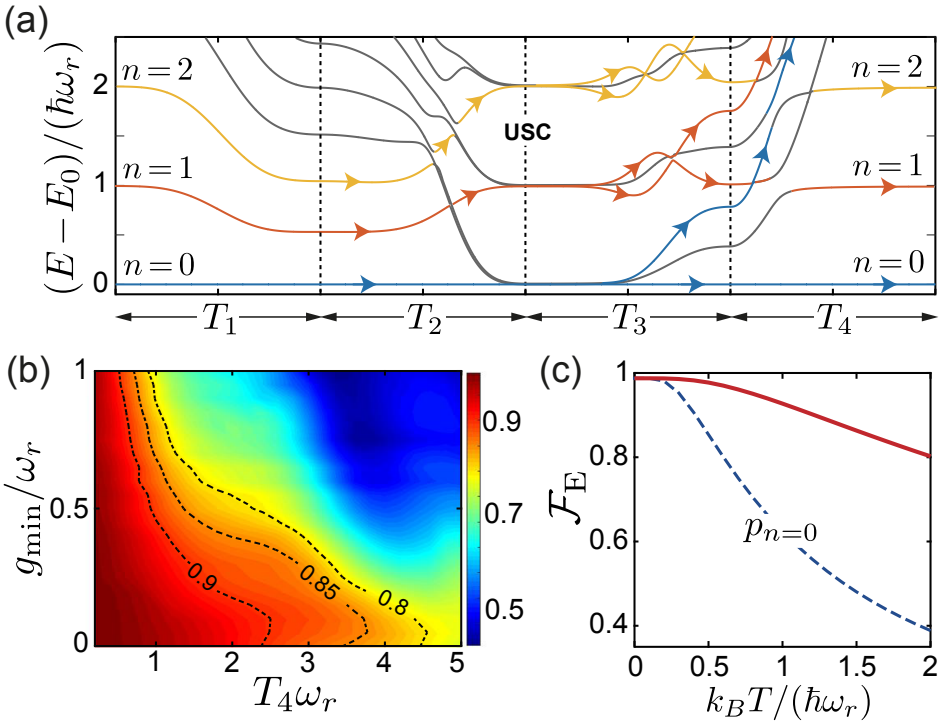

Figure 8.4: (a) Lowest eigenvalues during different stages of the protocol for the case $N = 2$. Here $g_{\min}/\omega_r = 0.2$, $\omega_{\min}/\omega_r = 0.4$, and in the final step of the protocol $\omega_{\max}/\omega_r = 5$. For clarity only the $s = 1$ states are shown and all time intervals have been stretched to equal lengths. For different initial photon number states $|n\rangle$, the colored segments and arrows indicate the ideal evolution of the systems, which maximizes the probability to end up in the qubit state $|D_0\rangle = (|\uparrow\uparrow\rangle - |\downarrow\downarrow\rangle)/\sqrt{2}$. Nonadiabatic crossings occur during the fast decoupling steps (T_3 and T_4), but also for small avoided crossings in the excited state manifolds during the preparation step (T_2). (b) Plot of the EEF for varying $T_4(= T_3)$ and $g_{\min}$ and for $N = 4$. (c) EEF (solid line) for a resonator mode, which is initially in a thermal state at temperature T, for $N = 4$. The dashed line indicates the corresponding population of the ground state manifold. All the other pulse parameters in panels (a), (b) and (c) are the same as in Fig. 8.2(b).

and fidelities of $\mathcal{F}_E \sim 0.9$ are still accessible over a wide parameter range. Similar conclusions can be obtained when a partial dependence between the pulses for $g(t)$ and $\omega_q(t)$ or nonuniform couplings $g_i(t)$ and frequencies $\omega_q^i(t)$ due to fabrication uncertainties are taken into account. This point is also analyzed in the following where we will take in account the effect of disorder in the system. In general we can conclude that no precise fine-tuning of the system parameters is required to implement this protocol.

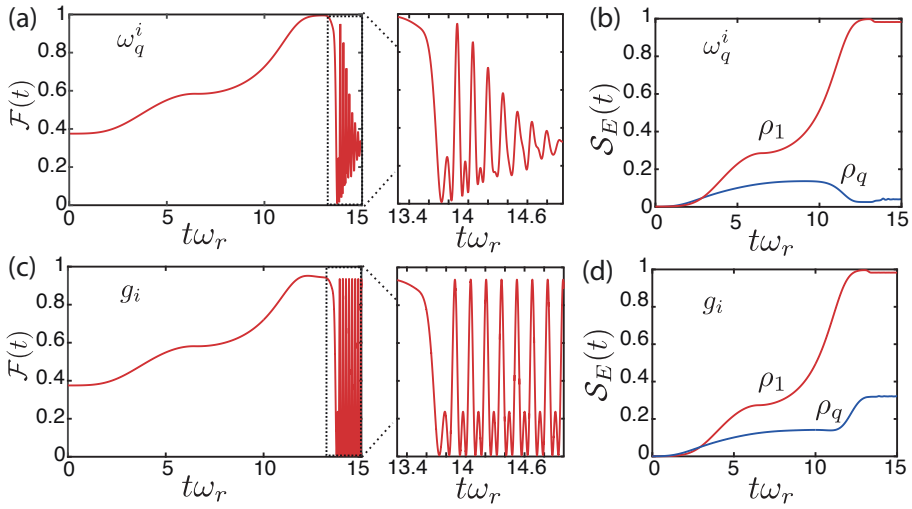

Figure 8.5: (a)-(d) Fidelity and entanglement entropy as function of time in the presence of disorder obtained by averaging over 10 simulation runs for $N = 4$. In particular we show the entanglement entropy $S_E(t) = -\mathrm{Tr}\{\rho(\mathrm{t})\log_2(\rho(\mathrm{t}))\}$ for the reduced density matrix of the qubit subsystem ($\rho_q(t)$) (blue line) and of a single qubit ($\rho_1(t) = \mathrm{Tr}_{\mathrm{N-1}}\{\rho_{\mathrm{q}}(\mathrm{t})\}$) (red line). In (a)-(b) we have considered qubit frequency disorder, while in (c)-(d) a disorder in the individual coupling strengths. All the parameters for the protocol are the same as in Fig 8.3.

Extracting entanglement from a thermal state

In our protocol we have assumed a rather low value for the resonator frequency, ω_r, in order to enhance both g/ω_r as well as the nonadiabatic switching times. Considering that typical resonator frequencies are on the order of few GHz (see the discussion on the experimental implementation), this implies that even at temperatures of $T = 20$ mK the equilibrium populations of higher resonator states with $n \geq 1$ cannot be neglected.

To better investigate this point, in Fig. 8.4(c) we plot the EEF as a function of the temperature T, assuming an initial resonator state $\rho_{\mathrm{th}} = \sum_n p_n|n\rangle\langle n|$, where $p_n = \bar{n}^n/(1+\bar{n})^{n+1}$ is the thermal distribution for a mean excitation number $\bar{n} = 1/(e^{\hbar\omega_r/k_BT} - 1)$. The plot shows also the corresponding ground state population as function of the temperature. We see that the EEF is higher than the population in the ground state, meaning that also the higher photon number states contribute significantly to the final entangled state. The origin of this surprising effect can be understood from the eigenvalue plot in Fig. 8.4(a). For example, by starting from a single excitation eigenstate in the weak-coupling regime, e.g. $|n = 1\rangle \otimes |\downarrow\rangle^{\otimes N}$, we see that is efficiently mapped on the corresponding USC state $|n = 1\rangle \otimes |s = N/2, m_x = 0\rangle$, passing only through a weak, higher-order avoided crossing. Therefore, the intermediate, and as a result also the final, qubit state is one with the resonator being in state $|1\rangle$. For higher photon numbers the avoided crossings become more relevant and the population can get lost into unwanted states. Nevertheless the protocol

still approximately implements the mapping $|n\rangle \otimes |\downarrow\rangle^{\otimes N} \to |n\rangle \otimes |s = N/2, m_x = 0\rangle$, independent of the resonator state $|n\rangle$. This feature makes it rather insensitive to thermal occupations that involves the lower excitation states and avoids additional active cooling methods for initializing the system in state $|G\rangle$.

Disorder

As we previously mentioned our entanglement-harvesting protocol is also robust with respect to fabrication disorder and control imprecisions on the relevant parameter. To see this point we re-do the numerical simulations shown in Fig. 8.3(b) assuming that, in each run of the protocol, the individual qubit frequencies evolve as $\omega_q^i(t) = \omega_q(t)(1 + \epsilon_i)$, where $\omega_q(t)$ follows the ideal pulse given in Fig. 8.3(a) and the ϵ_i are randomly chosen from the interval $[-0.1, 0.1]$. In Fig. 8.5(a) we plot the fidelity averaged over the different runs. We see that the main part of the protocol is essentially unaffected by frequency disorder, since the system is initially in the ground state and in the USC regime the system is dominated by the interaction terms. Frequency disorder only becomes important in the final decoupled state, where it dephases the symmetric state $|D_0\rangle$. Note, however, that for a fixed frequency distribution, this dephasing can be undone, since as shown in Fig. 8.5(b), it leads to almost no degradation of the degree of entanglement of the qubit state. In Fig. 8.5(c) and (d) the same plots are shown for the case of coupling disorder $g_i(t) = g(t)(1 + \epsilon_i)$. Although, this type of disorder has a stronger influence on the evolution of the state, the plot shows that our protocol does not require strictly identical couplings and variation of around 10% still lead to EEF $\mathcal{F}_{\mathrm{E}} \gtrsim 0.9$ and almost no degradation of the qubit-qubit entanglement. In this case the main quantity affected is the entanglement entropy of the qubit subsystem, which does not approach the value of zero, thus showing that qubits and resonator are not perfectly decoupled. However, we note that this measure of entanglement is very sensitive in our case, since the qubit state we achieve at the end of the protocol coincides with our target state with fidelity above 90%.

Experimental considerations

Let us make here some simple estimates for a possible experimental implementation of the protocol. Let us consider, for example, qubits with a frequency of $\omega_{\max}/(2\pi) \approx$ 10 GHz coupled to a lumped-element resonator of frequency $\omega_r/(2\pi) = 500$ MHz. The required maximal coupling strength of $g_{\max} \simeq 4.5\omega_r \approx 2\pi \times 2.25$ GHz is then consistent with experimentally demonstrated values [209, 210]. For these parameters, the nonadiabatic switching times assumed in Fig. 8.3(b) correspond to $T_{3,4} \simeq 0.16$ ns. These switching times are within reach of state-of-the-art waveform generators and a modulation of flux qubits on such time scales has already been demonstrated [238]. At the same time the duration of the whole protocol, $T_{\mathrm{f}} = 15/\omega_r \approx 5$ ns, is still much faster than typical flux qubit coherence times of 1-100 μs [239] or the lifetime of a photon, $T_{\mathrm{ph}} = Q/\omega_r$, in a microwave resonator of quality factor $Q = 10^4 - 10^6$.

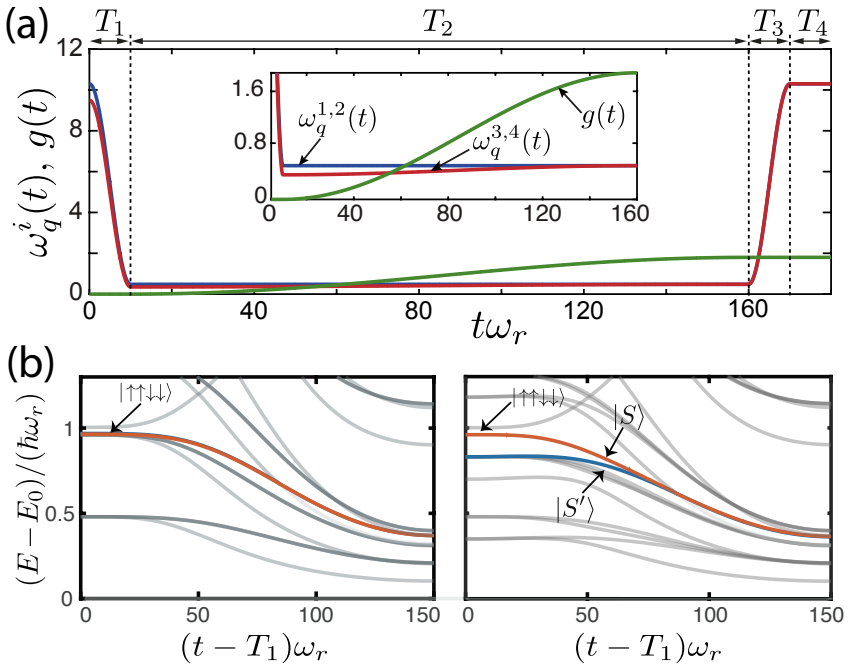

Figure 8.6: (a) Pulse sequence for harvesting the 4-qubit entangled state $|S\rangle$ with total angular momentum $s = 0$. As shown in the inset, during the first part of the protocol a finite difference between the qubit frequencies $\omega_q^{1,2}$ and $\omega_q^{3,4}$ is used to break the symmetry and couple different angular momentum states. (b) Evolution of the eigenvalues during the second step of the protocol for extracting the state $|S\rangle$. The colored lines indicate the states, which are adiabatically converted into the two $s = 0$ states, $|S\rangle$ and $|S'\rangle$. In the first plot all qubit frequencies are the same, $\omega_q^i = 0.48\omega_r$, while in the second plot the values $\omega_q^{1,2} = 0.48\omega_r$ and $\omega_q^{3,4} = 0.35\omega_r$ have been assumed. In both plots the couplings $g_i = g$ are increased symmetrically during the period T_2, i.e., the plotted time span from the value $g_{\min} = 0$ to the value $g_{\max} = 1.8\omega_r$. Note that for these modest coupling values, the state $|S\rangle$ is not yet the energetically highest state in the $n = 0$ manifold [see Fig. 8.2].

Another experimental concern could come from the influence of the higher resonator modes. For the kind of resonator that we are considering the next higher mode is estimated to be at $\omega_e/2\pi \sim 10$ GHz. In Ref. [74] it is shown that for such a high ratio $\omega_e/\omega_r > 20$, the effect of a higher circuit mode has no relevant influence on the resulting USC physics. By using an optimized design to increase this frequency or simply changing the maximal qubit frequency to, e.g., 8 GHz would avoid a resonant coupling to this mode without affecting the protocol.

In conclusion, although many experimental techniques for implementing and operating circuit QED systems in the USC regime are still under development, these estimates clearly demonstrate the feasibility of realizing high-fidelity control operations in such devices. For a detailed discussion on a specific implementation that we proposed we refer to the supplementary material of our paper [75].

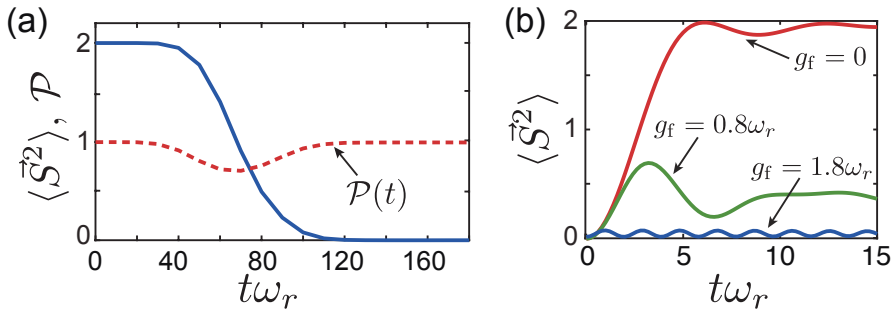

Figure 8.7: (a) The expectation value of the total spin, $\langle \vec{S}^2(t) \rangle$, (solid line) and the purity of the reduced qubit state, $\mathcal{P}(t)$, (dashed line) are plotted for the pulse sequence shown in (a) and for an initial state $|\Psi_0\rangle = |0\rangle \otimes |\uparrow\uparrow\downarrow\downarrow\rangle$. (b) Evolution of the extracted state $|0\rangle \otimes |S\rangle$ (characterized by the expectation value of the total spin) after the protocol for different final values of the couplings g_f. Here we have assumed random distributions of the qubit frequencies (see main text).

8.3 Harvesting singlet states

In this section we consider the singlet states $|s = 0, m_x = 0\rangle$ introduced in section 8.1.2 and shown in Fig. 8.2(b). As we discussed, these states are dark states of Hamiltonian (8.4) and remain decoupled from the cavity field in all parameter regimes. This means that these states are not connected to any of the bare qubit states in a simple adiabatic way. Nevertheless, these states can still be prepared by using an adapted protocol as described in Fig. 8.6(a).

Similar to the ground-state protocol, we start from the decoupled regime where $g \simeq 0$ and $\omega_q^i \gg \omega_r$, but we initialize the system in the excited qubit state $|\Psi_0\rangle = |0\rangle \otimes |\uparrow\uparrow\downarrow\downarrow\rangle$ ($|\Psi_0\rangle = |0\rangle \otimes |\uparrow\downarrow\rangle$ for $N = 2$), where half of the qubits are in the excited state and half in the ground state. Note that for $N = 4$ and a fully symmetric system, the $s = 0$ manifold is two-fold degenerate and spanned, e.g., by the basis states given in Eq. (8.11). To prepare a well-defined state, we break the symmetry by creating an offset between the qubit frequencies, for example, by setting $\omega_q^{1,2} \neq \omega_q^{3,4}$. Once the state $|\Psi_0\rangle$ is prepared, all the qubit frequencies are lowered below the resonator frequency such that $\omega_q^i < \omega_r/2$. This is done in time step T_1 while keeping $g \simeq 0$. As shown in Fig. 8.6(b), after this initial step all the relevant qubit states are below the first excited photon state. This configuration avoids undesired level crossings with higher photon number states during the next step of the protocol and only the $n = 0$ manifold must be considered.

During the second step $\omega_q^i \leq \omega_r/2$, but we still keep a finite frequency difference between the qubits to separate the state $|\uparrow\uparrow\downarrow\downarrow\rangle$ from other states with two qubits excited. This difference between the degenerate and non-degenerate qubit frequencies can be visualized in Fig. 8.6(b). As the coupling g is slowly increased while the difference in the qubit frequencies is tuned to zero, the state $|\uparrow\uparrow\downarrow\downarrow\rangle$ is adiabatically transformed into the $s = 0$ state $|S\rangle$. During this process the state $|S\rangle$ become almost

completely degenerate with the other $s = 0$ state $|S'\rangle$ [see Fig. 8.6(b)]. However, also the non-adiabatic coupling between these two states is almost negligible, such that the preparation process is still adiabatic on the timescale of the protocol.

In the last step of the protocol, the qubit frequencies are ramped up to the initial values as shown in Fig. 8.6(a). At this point maintaining a frequency offset is not crucial anymore. Note that in this last protocol step there are not restrictions on the operational time T_3 because the system is now in the dark state $|S\rangle$ and completely decoupled from the resonator mode.

As before we numerically simulate the dynamics given by (8.4) implementing the protocol that we just described. In Fig. 8.7(a) we plotted the expectation value of the total spin, $\langle \vec{S}^2(t) \rangle$, and the purity of the reduced qubit state, $\mathcal{P}(t)$ as function of time. We see that indeed we are able to bring the system into a pure state, which lives in the subspace $s = 0$.

Compared to the ground-state protocol, this protocol for harvesting the state $|S\rangle$ requires a fine tuning of the parameters and is less robust against imperfections. On the other hand it owns another important feature. By retaining a finite coupling $g_\mathrm{f} = g(t = T_\mathrm{f}) \sim \omega_r$ at the end of the protocol, the extracted dark state $|S\rangle$ is energetically separated from all other states with $s \neq 0$ and it is thereby protected against small frequency fluctuations. This effect is illustrated in Fig. 8.7(b), which shows the evolution of the extracted state $|S\rangle$ in the presence of small random shifts of the individual qubit frequencies. In particular, we assume random distributions of the qubit frequencies, $\omega_q^i = \omega_q(1 + \epsilon_i)$, where $\omega_q/\omega_r = 10$ and the ϵ_i are chosen randomly from the interval $[-0.05, 0.05]$. For $g_\mathrm{f} = 0$ this leads to dephasing of the qubits and a rapid transition out of the $s = 0$ subspace. This dephasing can be substantially suppressed by keeping the coupling at finite values. From Fig. 8.7(b) we see that this effect is already relevant for moderate values of the coupling, e.g. $g/\omega_r \gtrsim 1.8$. This example shows that USC effects can be used not only to generate complex multiqubit entangled states, but also to protect them.

Summary and outlook

In this doctoral thesis we have presented and discussed a new paradigm for atom-light interactions that occurs when one or multiple quantum emitters are coupled to the field confined in a one dimensional slow-light waveguide. In such a waveguide the photonic band can be strongly decreased compared to usual broadband or photonic crystal waveguides. This feature gives rise to a plethora of new interesting effects that were extensively analyzed in this thesis and that we are going to summarize here.

First, we have described in detail the atom-photon bound states that represent, in a slow-light waveguide QED setup, the main elementary excitations of the system. To proceed with our analysis we have introduced a basic tight binding model, made out of an array of coupled resonators. This model intuitively explains the physics of the system and encodes various effects, which have been previously described in the limiting cases of broadband waveguides and cavity QED. Based on this system, we have identified the necessary requirements that are needed to observe atom-photon bound states under realistic experimental conditions. These requirements have turned out to be correct, indeed few months after our publication, a single atom-photon bound state has been observed in an array of microwave resonators coupled to a superconducting qubit [139].

In the same project we have also discussed the essential properties of multi-atom dressed-state excitations. In this case, due to the localized nature of the bound states, the interaction between the emitters becomes short range. This interaction does not involve only the atomic excitation, but the full dressed state and can lead to a partial melting of the bound-state energies into the continuum, when specific coupling conditions are met. Also these predictions were recently observed in a superconducting circuit implementation [140].

An important part of our work was the extension of the atom-photon bound states to the multi-photon case. In particular, we have demonstrated the existence of these states for an arbitrary number of excitations and we have discussed the quantum nonlinear optical features of these states. We are currently in contact with experimental groups to find a strategy to observe these multi-photon states that require stronger coupling strength and more sophisticated fabrication and detection techniques.

The combination of multi-photon and multi-atom effects represents a starting point to further explore complex many-body effects in waveguide QED systems.

Recently, a first step in this direction was done by T. Shi et al. in [161], where the bound states of an ensemble of atoms coupled to a slow-light waveguide were discussed up to three excitations. The interesting point of this regime is the possibility to go beyond the effective Hamiltonian description, restricted to the atomic excitations, by keeping the full polaritonic nature of the states. This opens a new scenario where it could be possible to combine quantum non-linear optics with few and many-body physics, maybe achieving a regime where dipole-dipole interactions and phase transitions could depend on the number of excitations. Along this direction it would be interesting, for future research, to develop suitable analytical and numerical techniques to treat this otherwise complex problem.

In the second project that we have presented in this thesis, we have studied atom-photon interactions in the regime, where the atomic velocities are comparable to the maximal speed of light of a narrow-bandwidth waveguide. Under such conditions the atomic motion drastically changes photon emission and transfer processes and induces not only directionalities, but also non-perturbative effects. Indeed, the combination of Doppler shift and finite band-width leads to a tilting of the photonic spectrum and gives rise to in-the-band divergencies of the photonic density of states. In this project we have also proposed a possible implementation consisting of Rydberg atoms flying above a coupled array of microwave resonators, which can be experimentally explored with present-day technology.

Besides the fundamental interest in observing and probing these velocity-induced modifications of the atom-light interaction, having moving qubits is not the ideal scenario if the final goal is to implement quantum information processing. For this purpose and in light of the previous results, we have considered a scenario where multiple emitters are coupled to a slow-light waveguide that is dynamically modulated by a propagating acoustic wave. Similar to the moving atom case, we have demonstrated that in this system it is possible to achieve a directional emission caused by the deformation of the photonic band induced by the acoustic wave. Remarkably, this emission can be controlled by properly shaping the acoustic wave packet and can be exploited to implement efficient excitation transfer and entanglement generation schemes among several static emitters.

A promising application of this idea occurs when acousto-modulated 2D photonic lattices are considered. In this case, we have found that the band deformation produced by the acoustic wave can lead to an innovative scenario where an effectively one dimensional chiral interaction among the emitters is achievable in two dimensions. This is possible because photons get emitted into a single, highly focused direction with a slow radial decay. Such a feature allows to implement excitation transfer and quantum information protocols between the emitters in a way that would not be obtainable otherwise. These results open new interesting prospects for building complex quantum network, where quantum information, after having been processed on the atoms, can be coherently transferred to the photons and distributed around via phononic conveyor belts.

Regarding future research perspective, besides the engineering of specific schemes for quantum information processing, it would be interesting to investigate others lat-

tice geometries. Indeed, different band structures combined with a shaping of the acoustic wave modulation could affect the atom-light interactions in a totally different way. In general, extending the problem to several excitations and emitters could give rise to new interesting scenarios for simulation many-body physics, due to the possibility of having a time-dependent control of the interactions. Finally, it would be very interesting to analyze the physics of such acousto-optical waveguides in the regime, where also the phonons are treated fully quantum mechanically. The combination of phononic, photonic and atomic degrees of freedom it is still not investigated, due to the intrinsic complexity of the problem, and developing analytical and numerical methods able to provide some intuitions on this regime could give rise to many interesting effects.

In conclusion, in this thesis we have shown how slow-light waveguides represent a novel experimentally achievable platform where atom-light interaction can be strongly modified. The intrinsic non-linearity of these interactions combined with the possibility of achieving control over them, gives rise to many new opportunities for quantum simulations and quantum information processing applications.

Acknowledgments

My Ph.D. in Vienna has been an extremely positive experience in terms of scientific achievements, professional growth and personal life. I have been very lucky to be part of the CoQuS (Complex Quantum Systems) Ph.D. program, which allowed me to get in touch and meet many wonderful and interesting people who made these years great.

First, I want to thank my supervisor, Peter Rabl. Starting a Ph.D. is always a wild card both for the student and the professor. For me, luckily, Peter turned out to be simply the perfect supervisor. Scientifically, I felt honored to learn from his wide knowledge of physics, his insights and intuitions as much as I appreciated his being humble, practical, and unassuming. Besides being a great scientist, I have really appreciated him as a person. He was always available for every question or need and he made a lot of efforts to support me in any situation. For this, I can only be grateful to him.

My thanks also go to all the current and past members of my research group for the many interesting scientific and non-scientific discussions we had. My thanks especially are for: Yuri Minoguchi, Tuomas Jaako, Julian Huber and Daniele De Bernardis who never made my routine boring. A special mention goes to Thomas J. Milburn who passed away two years ago. He was a friend and a great person, and I miss him a lot. I want also to thank Arno Rauschenbeutel's group. In particular, Jurgen Volz and Philipp Schneeweiss for the stimulating discussion we had.

In general, I want to thank all the CoQuS people who have created an amazing environment during these four exciting years of doctoral research and life. Thanks to the CoQuS, I also had the opportunity to spend two months at Harvard University. This has been an extremely formative and stimulating experience and I want to thank some of the people who supported me during my visit: Martin J. A. Schuetz, Hannes Pichler, Efi Shahmoon, Hossein Sadeghpour and the group of Misha D. Lukin. During my stay in U.S.A I had also the chance to visit the group of Harold U. Baranger at the Duke University. From that visit, we started a fruitful collaboration involving also his former PhD Yao-Lung L. Fang.

This last collaboration was made possible thanks to Francesco Ciccarello, a researcher from my previous university in Palermo, with whom I have extensively and successfully collaborated during my Ph.D. In remembering Palermo and the early stage of my scientific career, I take the opportunity to thank my mentors: Roberto Passante, Lucia Rizzuto and Massimo Palma. A special mention goes to my good

friend Federico Armata. We started to study physics together since the first days of our bachelor. I am really happy that we had the chance to achieve a publication together during our respective PhD.

In conclusion, after having thanked all the people who had contributed to my past and present research achievements, I want also to thank Darrick Chang (who has already been my collaborator in the past) who offered me the possibility to continue my scientific growth by joining his group at ICFO.

Appendix A

Appendix

A.1 Master equation

In this Appendix we outline the derivation of the master equation (3.41) in the weak coupling limit $g/J \to 0$. Starting from Hamiltonian (3.38) we change into an interaction picture with respect to $H_0 = \sum_i \omega_a |e\rangle_i\langle e| + H_c$ and we obtain the atom-field interaction Hamiltonian

$$H_{\rm int}(t) = g \sum_{i=1}^{N_a} \left(\sigma_+^i E(x_i,t) e^{i\omega_a t} + \sigma_-^i E^\dagger(x_i,t) e^{-i\omega_a t} \right), \tag{A.1}$$

where

$$E(x,t) = \frac{1}{\sqrt{N}} \sum_k e^{-i\omega_k t} e^{ikx} a_k, \tag{A.2}$$

is the field operator at site x and $k = 2\pi m/N$ with $m = -N/2, -N/2+1, ..., N/2-1$. The field operators obey the commutation relations

$$[E(x,t), E^\dagger(x',t')] = \Phi(x-x', t-t'), \tag{A.3}$$

where

$$\begin{aligned} \Phi(z,\tau) =& \frac{1}{N} \sum_k e^{-ikz} e^{-i\omega_k \tau} \\ =& \frac{e^{-i\omega_c \tau}}{N} \sum_{n=0}^{N-1} e^{-i2\pi zn/N} e^{i2J\cos(2\pi n/N)\tau} \\ =& \frac{e^{-i\omega_c \tau}}{N} \sum_{n=0}^{N-1} e^{i2\pi zn/N} \sum_{m=-\infty}^{\infty} i^m J_m(2J\tau) e^{i2\pi nm/N} \\ =& e^{-i\omega_c \tau} i^{|z|} J_{|z|}(2J\tau). \end{aligned} \tag{A.4}$$

Up to second order in g and by performing the usual Born-Markov approximation [78], we end up with a time-local master equation governing the time evolution of the atom's reduced density operator

$$\dot\rho(t) = -\int_0^\infty d\tau \, {\rm Tr}_c\{[H_{\rm int}(t), [H_{\rm int}(t-\tau), \rho_c \otimes \rho(t)]]\}, \tag{A.5}$$

where in the absence of any driving fields $\rho_c = |0\rangle\langle 0|$ is the vacuum state of the waveguide modes. The master equation can be expressed in the form

$$\dot{\rho} = \sum_{ij} A_{ij} \left(\sigma_-^j \rho \sigma_+^i - \sigma_+^i \sigma_-^j \rho \right) + A_{ij}^* \left(\sigma_-^i \rho \sigma_+^j - \rho \sigma_+^j \sigma_-^i \right), \tag{A.6}$$

where

$$\begin{aligned} A_{ij} =& g^2 \int_0^\infty d\tau \, \langle E(x_i, t) E^\dagger(x_j, t-\tau) \rangle e^{i\omega_a \tau} \\ =& g^2 \int_0^\infty d\tau \, \Phi(x_i - x_j, \tau) e^{i\omega_a \tau} e^{-\gamma_c \tau/2} \\ =& g^2 i^{|x_i - x_j|} \int_0^\infty d\tau \, J_{|x_i - x_j|}(2J\tau) e^{-\left(\frac{\gamma_c}{2} - i\delta\right)\tau} \end{aligned} \tag{A.7}$$

and the cavity decay rate γ_c appears through the replacement $\omega_c \to \omega_c - i\gamma_c/2$. The final integral can now be evaluated with the help of

$$\int_0^\infty d\tau \, J_m(a\tau) e^{-b\tau} = \frac{1}{\sqrt{a^2 + b^2}} \left(\frac{a}{b + \sqrt{a^2 + b^2}} \right)^m, \tag{A.8}$$

and we obtain

$$A_{ij} = \frac{g^2 e^{iK|x_i - x_j]}}{\sqrt{4J^2 - \left(\delta + i\frac{\gamma_c}{2}\right)^2}}, \tag{A.9}$$

where K is given in Eq. (3.44). Finally, since $A_{ij} = A_{ji}$ we can regroup the individual terms into the form given in Eq. (3.41), where we identify . $\Gamma_{ij} = 2\mathrm{Re}\{A_{ij}\}$ and $U_{ij} = 2\mathrm{Im}\{A_{ij}\}$.

The derivation of the master equations relies on the validity of the Born-Markov approximation, which requires that the kernel in Eq. (A.7) either decays faster or oscillates faster than the system evolution time set by the coupling $\sim g$. For a single atom this condition is satisfied as long as $g \ll |\tilde{v}_g(\delta)|$ and by assuming in addition that $\gamma_a \ll |\tilde{v}_g(\delta)|$, we can also add to Γ_{ii} the bare atomic decay, without influencing the coupling to the waveguide.

For multiple atoms the Bessel function $J_{|x_i - x_j|}(2J\tau)$ reaches its maximum at a finite time

$$\tau \approx \frac{|x_i - x_j|}{2J}, \tag{A.10}$$

which reflects the minimal time it takes a photon to propagate between the atoms. More generally, for the validity of a time-local master equation for N_a-atoms with spacing Δx we must ensure that the maximal retardation time $\tau_R \sim (N_a - 1)\Delta x/|\tilde{v}_g(\delta)|$ is short compared to the system evolution determined by the single-atom spontaneous-emission time Γ^{-1} with $\Gamma = 2g^2/|\tilde{v}_g(\delta)|$. This yields

$$g \ll \frac{|\tilde{v}_g(\delta)|}{\sqrt{(N_a - 1)\Delta x}} \tag{A.11}$$

as a slightly more stringent condition for large systems. See also Ref. [19, 14].

A.2 Multi-atom bound-states

Here we address a number of properties of the multi-atom bound-state levels in the case $N_a = 2$ and $N_a \gg 1$ with the goal of proving the salient features of the energy spectra in Fig. 4.9 and 4.11 discussed in the main text.

A.2.1 $N_a = 2$

Below the continuum, i.e., for $E < -2J$, both $\Sigma_e(E)$ and $\Sigma_o(E)$ monotonically decrease with E [see Eq. (4.50)]. Thereby, if the value taken by the linear function $y = E - \delta$ at $E = -2J$ lies above $\Sigma_s(-2J)$ then a single bound state (for fixed s) of energy $E_{-,s} < -2J$ certainly occurs. This condition thus explicitly reads $-2J - \delta > \Sigma_s(-2J)$. This is always fulfilled for $s = e$ given that $\Sigma_e(-2J) = -\infty$. Instead, for s=o, by calculating $\Sigma_o(-2J) = -g^2|x_1 - x_2|/(2J)$ [see Eq. (4.50) for $E \to (-2J)^+$], the above condition results in

$$g > \frac{2J\sqrt{1+\frac{\delta}{2J}}}{\sqrt{|x_1 - x_2|}} = \frac{g_m}{\sqrt{|x_1 - x_2|}}, \tag{A.12}$$

where g_m is the same as in Eq. (4.65). Hence, as discussed in Sec. 4.3.2, both $E_{-,e}$ and $E_{-,o}$ solutions exist for any interatomic distance when $g > g_m$.

If instead $g < g_m$, at the critical distance $|x_1 - x_2| = (g_m/g)^2$ the solution $E_{-,o}$ merges with the continuum, i.e., $E_{-,o} = -2J$, and it no longer exists for $|x_1 - x_2| < x_m$ (see Fig. 4.9). Moreover, note that in the light of the geometrical criterion given above if $E_{-,o}$ exists then $E_{-,o} > E_{-,e}$ since $\Sigma_o(E) > \Sigma_e(E)$ [see Eq. (4.50)]. Eq. (A.12) holds for $\delta > -2J$. For $\delta \leq -2J$, $E_{-,o}$ always exists since $-2J - \delta$ is positive while $\Sigma_o(2J)$ is negative anyway.

As for bound states *above the continuum*, a similar reasoning can be carried out. Recalling that $\Sigma_s(-E) = -\Sigma_s(E)$, we have $\Sigma_o(2J) = g^2|x_1 - x_2|/(2J)$ and $\Sigma_e(2J) = +\infty$ with both functions $\Sigma_s(E)$ mononically decreasing with E for $E > 2J$. The condition for the existence of a bound state will now read $2J - \delta < \Sigma_s(2J)$. Again, it is always fulfilled when $s = e$ since $\Sigma_e(2J)$ diverges to $+\infty$. Instead, for $s = o$ the threshold condition for $\delta < 2J$ reads

$$g > \frac{2J\sqrt{1-\frac{\delta}{2J}}}{\sqrt{|x_1 - x_2|}}, \tag{A.13}$$

which is analogous to Eq. (A.12) but the replacement $\delta \to -\delta$ in the expression of g_m. For $\delta > 2J$ both levels $E_{+,s}$ exist. Moreover, since now $\Sigma_o(E) < \Sigma_e(E)$ we have $E_{+,o} < E_{+,e}$.

To summarize, outside the continuum, a pair of bound states of even symmetry and energies $E_{\pm,e}$ always exist, one above and one below the photonic band. At most two further odd-symmetry bound states of energies $E_{\pm,o}$ may be present as well, depending on the values of g, $|x_1 - x_2|$ and δ. Note that, for $|\delta| < 2J$, the critical

coupling strengths appearing in Eqs. (A.12) and (A.13) are different, which entails that three cases are possible: $E_{+,o}$ exists while $E_{-,o}$ does not (or vicecersa), $E_{\pm,o}$ both exist, $E_{\pm,o}$ both do not exist. Combining together Eqs. (A.12) and (A.13), the conditions for these three cases to occur, for $|\delta| \leq 2J$, read

$$g > \frac{2J\sqrt{1+\frac{|\delta|}{2J}}}{\sqrt{|x_1-x_2|}} \;\Leftrightarrow\; \text{both } E_{+,o} \text{ and } E_{-,o} \text{ exist}\,, \tag{A.14}$$

$$\frac{2J\sqrt{1-\frac{|\delta|}{2J}}}{\sqrt{|x_1-x_2|}} < g < \frac{2J\sqrt{1+\frac{|\delta|}{2J}}}{\sqrt{|x_1-x_2|}} \;\Leftrightarrow\; \text{only } E_{\mathrm{sgn}\,(\delta),\mathrm{o}} \text{ exists}, \tag{A.15}$$

$$g < \frac{2J\sqrt{1-\frac{|\delta|}{2J}}}{\sqrt{|x_1-x_2|}} \;\Leftrightarrow\; \text{neither } E_{+,o} \text{ nor } E_{-,o} \text{ exist}\,. \tag{A.16}$$

A.2.2 $N_a \gg 1$

The analysis for $N_a \gg 1$ proceeds similarly to the $N_a = 2$ case. The explicit self-energy functions $\Sigma_{s=e,o}(E)$ are obtained from Eqs. (4.47), (4.66) and (4.10). Like in the 2-atom case, $\Sigma_e(E) > \Sigma_o(E)$ [$\Sigma_e(E) < \Sigma_o(E)$] for $E > 2J$ ($E < -2J$) with $\Sigma_e(E)$ diverging to $+\infty$ and $-\infty$ for $E \to (2J)^+$ and $E \to (-2J)^-$, respectively. Instead, $\Sigma_o(\pm 2J) = \pm g^2 \Delta x/(4J)$.

Accordingly, the same geometrical criterion as in the previous subsection entails that the conditions for the existence of $E_{+,o}$ and $E_{-,o}$ are the same as in Eqs. (A.12) and (A.13), respectively, apart from the factor $\sqrt{2}$ on either right-hand side. The same factor thereby appears in Eqs. (A.14)-(A.16), which are now interpreted as the conditions for establishing whether none [Eq. (A.14)], only one [Eq. (A.15)] or both [Eq. (A.16)] of the metabands merge with the photonic band.

Bibliography

[1] W.H. Louisell *Quantum Statistical Properties of Radiation*, John Wiley and Sons (1990)

[2] C. Cohen-Tannoudji, J. Dupont-Roc, G. Grynberg, *Photons and Atoms: Introduction to Quantum Electrodynamics*, Wiley-VCH (1997).

[3] S. Haroche and J. M. Raimond, *Exploring the Quantum* (Oxford University Press, Oxford, 2006).

[4] A. Reiserer and G. Rempe, *Cavity-based quantum networks with single atoms and optical photons*, Rev. Mod. Phys. **87**, 1379 (2015).

[5] H. J. Kimble, *The quantum internet*, Nature **453**, 19 (2008).

[6] J. T. Shen and S. Fan, *Coherent Single Photon Transport in a One- Dimensional Waveguide Coupled with Superconducting Quantum Bits*, Phys. Rev. Lett. **95**, 213001 (2005).

[7] J. T. Shen and S. Fan, *Strongly correlated multiparticle transport in one dimension through a quantum impurity*, Phys. Rev. A **76**, 062709 (2006).

[8] D. E. Chang, A. S. Sorensen, E. A. Demler, and M. D. Lukin, *Quantum Optics with Surface Plasmons*, Nature Phys. **3**, 807 (2007).

[9] J. T. Shen and S. Fan, *Theory of single-photon transport in a single-mode waveguide*, Phys. Rev. A **79**, 023837 (2009).

[10] D. Witthaut and A. S. Sørensen, *Photon scattering by a three-level emitter in a one- dimensional waveguide*, New J. Phys. **12** 043052 (2010).

[11] H. Zheng, D. J. Gauthier, and H. U. Baranger, *Waveguide QED: Many-body bound-state effects in coherent and Fock-state scattering from a two-level system*, Phys. Rev. A **82**, 063816 (2010).

[12] M. Pletyukhov, and V. Gritsev, *Scattering of massless particles in one-dimensional chiral channel*, New J. Phys. **14**, 095028 (2012).

[13] M. Ringel, M. Pletyukhov, and V. Gritsev, *Topologically protected strongly-correlated states of photons*, New J. Phys. **16**, 113030 (2014).

[14] T. Shi, D. E. Chang, and J. Ignacio Cirac, *Multiphoton-scattering theory and generalized master equations*, Phys. Rev. A **92**, 053834 (2015).

[15] D. E. Chang, L. Jiang, A. V. Gorshkov, and H. J. Kimble, *Cavity QED with atomic mirrors*, New J. Phys. **14**, 063003 (2012).

[16] D. E. Chang, J. I. Cirac, and H. J. Kimble, *Self-Organization of Atoms along a Nanophotonic Waveguide*, Phys. Rev. Lett. **110**, 113606 (2013).

[17] T. Grießer and H. Ritsch, *Light-Induced Crystallization of Cold Atoms in a 1D Optical Trap*, Phys. Rev. Lett. **111**, 055702 (2013).

[18] A. González-Tudela, D. Martin-Cano, E. Moreno, L. Martin-Moreno, C. Tejedor, and F.J. Garcia-Vidal, *Entanglement of two qubits mediated by one-dimensional plasmonic waveguides*, Phys. Rev. Lett. **106**, 020501 (2011).

[19] C. Gonzales-Ballestero, F. J. Garcia-Vidal, and E. Moreno, *Non-Markovian effects in waveguide-mediated entanglement*, New J. Phys. **15**, 073015 (2013).

[20] A. González-Tudela and D. Porras, *Mesoscopic Entanglement Induced by Spontaneous Emission in Solid-State Quantum Optics*, Phys. Rev. Lett. **110**, 080502 (2013).

[21] K. Stannigel, P. Rabl and P. Zoller, *Driven-dissipative preparation of entangled states in cascaded quantum-optical networks*, New J. Phys. **14**, 063014 (2012).

[22] H. Zheng, and H. U. Baranger, *Persistent Quantum Beats and Long-Distance Entanglement from Waveguide-Mediated Interactions*, Phys. Rev. Lett. **110**, 113601 (2013).

[23] C. Gonzalez-Ballestero, A. Gonzalez-Tudela, F. J. Garcia-Vidal, and E. Moreno, *Chiral route to spontaneous entanglement generation*, Phys. Rev. B **92**, 155304 (2015).

[24] C. Gonzalez-Ballestero, E. Moreno, F. J. Garcia-Vidal, A. Gonzalez-Tudela, *Non-reciprocal few-photon devices based on chiral waveguide-emitter couplings*, Phys. Rev. A **94**, 063817 (2016).

[25] T. Ramos, H. Pichler, A. J. Daley and P. Zoller, *Quantum Spin Dimers from Chiral Dissipation in Cold-Atom Chains*, Phys. Rev. Lett. **113**, 237203 (2014).

[26] H. Pichler, T. Ramos, A. J. Daley and P. Zoller, *Quantum optics of chiral spin networks*, Phys. Rev. A **91**, 042116 (2015).

[27] P. Facchi, M. S. Kim, S. Pascazio, F. V. Pepe, D. Pomarico, and T. Tufarelli, *Bound states and entanglement generation in waveguide quantum electrodynamics*, Phys. Rev. A **94**, 043839 (2016).

[28] P. Facchi, S. Pascazio, F. V. Pepe, and K. Yuasa, *Long-lived entanglement of two multilevel atoms in a waveguide*, J. Phys. Comm. **2**, 035006 (2018).

[29] E. S. Redchenko and V. I. Yudson, *Decay of metastable excited states of two qubits in a waveguide*, Phys. Rev. A **90**, 063829 (2014).

[30] D. Dzsotjan, A. S. Sørensen, and M. Fleischhauer, *Quantum emitters coupled to surface plasmons of a nanowire: A Green' s function approach*, Phys. Rev. B **82**, 075427 (2010).

[31] H. Zheng, D. J. Gauthier, and H. U. Baranger, *Waveguide-QED-Based Photonic Quantum Computation*, Phys. Rev. Lett. **111**, 090502 (2013).

[32] F. Ciccarello, D. E. Browne, L. C. Kwek, H. Schomerus, M. Zarcone, and S. Bose, *Quasideterministic realization of a universal quantum gate in a single scattering process*, Phys. Rev. A **85**, 050305(R) (2012).

[33] E. Yablonovitch, *Inhibited Spontaneous Emission in Solid-State Physics and Electronics*, Phys. Rev. Lett. **58**, 2059 (1987).

[34] P. Bykov, *Spontaneous emission from a medium with a band spectrum*, Sov. J. Quant. Electron. **4**, 7 (1975).

[35] J. D. Thompson, T. G. Tiecke, N. P. de Leon, J. Feist, A. V. Akimov, M. Gullans, A. S. Zibrov, V. Vuletić, and M. D. Lukin, *Coupling a single trapped atom to a nanoscale optical cavity*, Science **340**, 1202 (2013).

[36] T. G. Tiecke, J. D. Thompson, N. P. de Leon, L. R. Liu, V. Vuletić and M. D. Lukin, *Nanophotonic quantum phase switch with a single atom*, Nature **508**, pages 241 (2014).

[37] C.-L. Hung, S. M. Meenehan, D. E. Chang, O. Painter, H. J. Kimble, *Trapped atoms in one-dimensional photonic crystals*, New J. Phys. **15**, 083026 (2013).

[38] A. Goban, et al., *Atom-light interactions in photonic crystals*, Nat. Commun. **5**, 3808 (2014).

[39] J. D. Hood, A. Goban, A. Asenjo-Garcia, M. Lu, S.P. Yu, D. E. Chang, and H. J. Kimble, *Atom-atom interactions around the band edge of a photonic crystal waveguide*, PNAS **113**, 38 (2016).

[40] P. Lodahl, S. Mahmoodian, and S. Stobbe, *Interfacing single photons and single quantum dots with photonic nanostructures*, Rev. Mod. Phys. **87**, 347 (2015).

[41] S. John and J. Wang, *Quantum electrodynamics near a photonic band gap: Photon bound states and dressed atoms*, Phys. Rev. Lett. **64**, 2418 (1990).

[42] S. John and J. Wang, *Quantum optics of localized light in photonic band gap*, Phys. Rev. B **43**, 12772 (1991).

[43] S. John and T. Quang, *Spontaneous emission near the edge of a photonic band gap*, Phys. Rev. A **50**, 1764 (1994).

[44] G. Kurizki, *Two-atom resonant radiative coupling in photonic band structures*, Phys. Rev. A **42**, 2915 (1990).

[45] A. G. Kofman, G. Kurizki, and B. Sherman, *Spontaneous and induced atomic decay in photonic band structures*, J. Mod. Opt. **41**, 353 (1994).

[46] P Lambropoulos, G. M. Nikolopoulos, T. R. Nielsen, and S. Bay, *Fundamental quantum optics in structured reservoirs*, Rep. Prog. Phys. **63**, 455 (2000).

[47] S. Bay, P. Lambropoulos, and K. Mölmer, *Atom-atom interaction in strongly modified reservoirs*, Phys. Rev. A **55**, 1485 (1997).

[48] E. Shahmoon, and G. Kurizki, *Nonradiative interaction and entanglement between distant atoms*, Phys. Rev. A **87**, 033831 (2013).

[49] J. S. Douglas, H. Habibian, C. L. Hung, A. V. Gorshkov, H. J. Kimble, and D. E. Chang, *Quantum many-body models with cold atoms coupled to photonic crystals*, Nature Photon. **9**, 326 (2015).

[50] J. S. Douglas, T. Caneva, and D. E. Chang, *Photon Molecules in Atomic Gases Trapped Near Photonic Crystal Waveguides*, Phys. Rev. X **6**, 031017 (2016).

[51] M. T. Manzoni, L. Mathey and D. E. Chang, *Designing exotic many-body states of atomic spin and motion in photonic crystals*, Nat. Commun. **8**,14696 (2017).

[52] G. Calajó, F. Ciccarello, D. Chang and P. Rabl, *Atom-field dressed states in slow-light waveguide QED*, Phys. Rev. A **93**, 033833 (2016).

[53] M. J. Hartmann, F. G. S. L. Brandão and M. B. Plenio, *Strongly Interacting Polaritons in Coupled Arrays of Cavities*, Nature Phys. **2**, 849 (2006).

[54] A. D. Greentree, C. Tahan, J. H. Cole, and C. L. Hollenberg, *Quantum phase transitions of light*, Nature Phys. **2**, 856 (2006).

[55] D. G. Angelakis, M. F. Santos, and S. Bose, *Photon-blockade-induced Mott transitions and XYspin models in coupled cavity arrays*, Phys. Rev. A **76**, 031805(R) (2007).

[56] L. Zhou, Z. R. Gong, Y. X. Liu, C. P. Sun, and F. Nori, *Controllable Scattering of a Single Photon inside a One-Dimensional Resonator Waveguide*, Phys. Rev. Lett. **101**, 100501 (2008).

[57] T. Shi and C. P. Sun, *Lehmann-Symanzik-Zimmermann reduction approach to multiphoton scattering in coupled-resonator arrays*, Phys. Rev. B **79**, 205111 (2009).

[58] P. Longo, P. Schmitteckert, and K. Busch, *Few-Photon Transport in Low-Dimensional Systems: Interaction-Induced Radiation Trapping*, Phys. Rev. Lett. **104**, 023602 (2010).

[59] P. Longo, P. Schmitteckert, and K. Busch, *Few-Photon Transport in Low-Dimensional Systems*, Phys. Rev. A **83**, 063828 (2011).

[60] F. Lombardo, F. Ciccarello, and G. M. Palma, *Photon localization versus population trapping in a coupled-cavity array*, Phys. Rev. A **89**, 053826 (2014).

[61] T. Shi, Y-H. Wu, A. Gonzalez-Tudela and J. I. Cirac, *Bound States in Boson Impurity Models*, Phys. Rev. X **6**, 021027 (2016).

[62] E. Sánchez-Burillo, D.Zueco, L. Martín-Moreno, J. J. García-Ripoll, *Dynamical signatures of bound states in waveguide QED*, Phys. Rev. A **96**, 023831 (2017).

[63] G. Calajó and P. Rabl, *Strong coupling between moving atoms and slow-ligth Cherenkov photons*, Phys. Rev. A **95**, 043824 (2017).

[64] C. W. Hsu, B. Zhen, A. D. Stone, J. D. Joannopoulos, and M. Soljačić, *Bound states in the continuum*, Nature Reviews Materials **1**, 16048 (2016).

[65] J.Von Neumann, E. Wigner, *Uber merkwÃ¼rdige diskrete Eigenwerte. Uber das Verhalten von Eigenwerten bei adiabatischen Prozessen*, Phys. **30**, 465 (1929).

[66] S. Longhi, *Bound states in the continuum in a single-level Fano-Anderson model*, Eur. Phys. J. B, **57**, 45-51 (2007).

[67] S. Tanaka, S. Garmon, G. Ordonez, and T. Petrosky, *Electron trapping in a one-dimensional semiconductor quantum wire with multiple impurities*, Phys. Rev. B **76**, 153308 (2007).

[68] T. Tufarelli, M.S. Kim, and F. Ciccarello, *Non-Markovianity of a quantum emitter in front of a mirror*, Phys. Rev. A **90**, 012113 (2014).

[69] G. Calajó, Y.-L. L. Fang, H. U. Baranger, and F. Ciccarello, *Exciting a Bound State in the Continuum through Multi-Photon Scattering plus Delayed Quantum Feedback*, arXiv:1811.02582 (2018).

[70] A. Wallraff, D. I. Schuster, A. Blais, L. Frunzio, R. S. Huang, J. Majer, S. Kumar, S. M. Girvin, and R. J. Schoelkopf, *Strong coupling of a single photon to a superconducting qubit using circuit quantum electrodynamics*, Nature (London) **431**, 162 (2004).

[71] A. Blais, R.-S. Huang, A. Wallraff, S. M. Girvin and R. J. Schoelkopf, *Cavity quantum electrodynamics for superconducting electrical circuits: An architecture for quantum computation*, Phys. Rev. A **69**, 062320 (2004).

[72] C. Ciuti, G. Bastard, and I. Carusotto, *Quantum vacuum properties of the intersubband cavity polariton field*, Phys. Rev. B **72**, 115303 (2005).

[73] J. Casanova, G. Romero, I. Lizuain, J. J. García-Ripoll, and E. Solano, *Deep Strong Coupling Regime of the Jaynes-Cummings Model*, Phys. Rev. Lett. **105**, 263603 (2010).

[74] T. Jaako, Z.-L. Xiang, J.J. Garcia-Ripoll, and P. Rabl, *Ultrastrong coupling phenomena beyond the Dicke model*, Phys. Rev. A **94**, 033850 (2016).

[75] F. Armata, G. Calajó, T. Jaako, M.S. Kim, and P. Rabl *Harvesting Multiqubit Entanglement from Ultrastrong Interactions in Circuit Quantum Electrodynamics*, Phys. Rev. Lett. 119 **18**, 183602 (2017).

[76] R. H. Dicke, *Coherence in Spontaneous Radiation Processes*, Phys. Rev. **93**, 99 (1954).

[77] M. Gross and S. Haroche, *Superradiance: An Essay on the Theory of Collective Spontaneous Emission*, Phys. Rep. **93**, 301, (1982).

[78] H. P. Breuer and F. Petruccione, *The Theory of Open Quantum Systems* (Oxford, Oxford University Press, 2002).

[79] D.F. Walls, G. J. Milburn, *Quantum Optics* (Springer, 1994).

[80] C. Gardiner, P. Zoller, *Quantum noise: a handbook of Markovian and non-Markovian quantum stochastic methods with applications to quantum optics* (Springer Science and Business Media, 2004).

[81] W. E. Lamb, R. C. Retherford, *Fine Structure of the Hydrogen Atom by a Microwave Method*, Phys. Rev. **72**, 241 (1947).

[82] A. Asenjo-Garcia, M. Moreno-Cardoner, A. Albrecht, H. J. Kimble, and D. E. Chang, *Exponential Improvement in Photon Storage Fidelities Using Subradiance and "Selective Radiance" in Atomic Arrays*, Phys. Rev. X **7**, 031024 (2017).

[83] H. Zoubi and H. Ritsch, *Lifetime and Emission Character- istics of Collective Electronic Excitations in Two- Dimensional Optical Lattices*, Phys. Rev. A **83**, 063831 (2011).

[84] D. Plankensteiner, L. Ostermann, H. Ritsch, and C. Genes, *Selective Protected State Preparation of Coupled Dissipative Quantum Emitters*, Sci. Rep. **5**, 16231 (2015).

[85] G. Facchinetti, S. D. Jenkins, and J.Ruostekoski, *Storing Light with Subradiant Correlations in Arrays of Atoms*, Phys. Rev. Lett. **117**, 243601 (2016).

[86] V. D. Vaidya, Y. Guo, R. M. Kroeze, K. E. Ballantine, A. J. Kollár, J.N. Keeling, B. L. Lev, *Tunable-range, photon-mediated atomic interactions in multimode cavity QED*, Phys. Rev. X **8**, 021030 (2018).

[87] N. M. Sundaresan, Y. Liu, D. Sadri, L. J. Szocs, D. L. Underwood, M. Malekakhlagh, H. E. Tureci, and A. Houck, *Beyond Strong Coupling in a Multimode Cavity*, Phys. Rev. X **5**, 021035 (2015).

[88] D. E. Chang, V.Vuletic, and M. D. Lukin, *Quantum nonlinear optics - photon by photon*, Nat. Photon. **8**, 685 (2014).

[89] K. M. Birnbaum, A. Boca, R. Miller, A. D. Boozer, T. E. Northup, and H. J. Kimble, *Photon blockade in an optical cavity with one trapped atom*, Nature **436**, 87 (2005).

[90] A. Kubanek, A. Ourjoumtsev, I. Schuster, M. Koch, P. W. H. Pinkse, K. Murr, and G. Rempe, *Two-Photon Gateway in One-Atom Cavity Quantum Electrodynamics*, Phys. Rev. Lett. **101**, 203602 (2008).

[91] E. M. Purcell, H. C. Torrey, and R. V. Pound, *Resonance Absorption by Nuclear Magnetic Moments in a Solid*, Phys. Rev. A **69**, 37 (1946).

[92] M. Tavis and F. W. Cummings, *Exact Solution for an N-Molecule-Radiation-Field Hamiltonian*, Phys. Rev. **170**, 379 (1968).

[93] M. G. Raizen, R. J. Thompson, R. J. Brecha, H. J. Kimble and H. J. Carmichael, *Normal-mode splitting and linewidth averaging for two-state atoms in an optical cavity*, Phys. Rev. Lett. **63**, 240 (1989).

[94] Y. Zhu, D. J. Gauthier, S. E. Morin, Q. Wu, H. J. Carmichael, and T. W. Mossberg *Vacuum Rabi splitting as a feature of linear-dispersion theory: Analysis and experimental observations*, Phys. Rev. Lett. **64**, 2499 (1990).

[95] F. Bernardot, P. Nussenzveig, M. Brune, J. M. Raimond and S. Haroche, *Normal-mode splitting and linewidth averaging for two-state atoms in an optical cavity*, Europhys. Lett. **17**, 33 (1992).

[96] J. M. Fink, R. Bianchetti, M. Baur, M. Goppl, L. Steffen, S. Filipp, P. J. Leek, A. Blais, and A. Wallraff *Dressed Collective Qubit States and the Tavis-Cummings Model in Circuit QED*, Phys. Rev. Lett. **103**, 083601 (2009).

[97] G. Agarwal, S. Gupta, and R. Puri, *Fundamentals of Cavity Quantum Electrodynamics*, (World Scientific Publishing Company Incorporated, 1995).

[98] Y. Kaluzny, P. Goy, M. Gross, J-M Raimond and S. Haroshe, *Observation of Self-Induced Rabi Oscillations in Two-Level Atoms Excited Inside a Resonant Cavity: The Ringing Regime of Superradiance*, Phys. Rev. Lett. **51**, 1175 (1983).

[99] S. Haroche, *Rydberg atoms and radiation in a resonant cavity: a simple system to test basic quantum optics effects*, New Trends in Atomic Physics, Grynberg and Stora editors, North Holland (1984).

[100] D. Meschede, H. Walther, and G. Müller, *One-Atom Maser*, Phys. Rev. Lett. **54**, 551 (1985).

[101] G. Rempe, H. Walther, and N. Klein, *Observation of quantum collapse and revival in a one-atom maser*, Phys. Rev. Lett. **58**, 353 (1987).

[102] R. J. Thompson, G. Rempe, and H. J. Kimble *Observation of quantum collapse and revival in a one-atom maser*, Phys. Rev. Lett. **68**, 1132 (1992).

[103] S. T. Dawkins, R. Mitsch, D. Reitz, E. Vetsch, A. Rauschenbeutel, *Dispersive Optical Interface Based on Nanofiber-Trapped Atoms*, Phys. Rev. Lett. **107**, 243601 (2011).

[104] D. Reitz, C. Sayrin, R. Mitsch, P. Schneeweiss, and A. Rauschenbeutel, *Coherence Properties of Nanofiber-Trapped Cesium Atoms*, Phys. Rev. Lett. **110**, 243603 (2013).

[105] R. Yalla, M. Sadgrove, K. P. Nayak and K. Hakuta, *Cavity Quantum Electrodynamics on a Nanofiber Using a Composite Photonic Crystal Cavity*, Phys. Rev. Lett. **113**, 143601 (2014).

[106] J. Volz, M. Scheucher, C. Junge, and A. Rauschenbeutel, *Nonlinear π phase shift for single fibre-guided photons interacting with a single resonator-enhanced atom*, Nat. Photon. **8**, 965 (2014).

[107] P. Solano, P. Barberis-Blostein, F. K. Fatemi, L. A. Orozco, S. L. Rolston, *Super-radiance reveals infinite-range dipole interactions through a nanofiber*, Nat. Commun. **8**, 1857 (2017).

[108] P. Solano, J. A.Grover, J. E.Hoffman, S. Ravets, F. K.Fatemi, L. A.Orozco, S. L.Rolston,*Optical Nanofibers: a new platform for quantum optics*, Advances in Atomic, Molecular, and Optical Physics **66**, 439 (2017).

[109] M. Arcari, et al., *Near-Unity Coupling Efficiency of a Quantum Emitter to a Photonic Crystal Waveguide*, Phys. Rev. Lett. **113**, 093603 (2014).

[110] A. Javadi et. al, *Single-photon non-linear optics with a quantum dot in a waveguide* Nat. Commun. **6**, 8655 (2015).

[111] O. Astafiev, A. M. Zagoskin, A. A. Abdumalikov, Jr., Yu. A. Pashkin, T. Yamamoto, K. Inomata, Y. Nakamura, and J. S. Tsai, *Resonance fluorescence of a single artificial atom*, Science **327**, 840 (2010).

[112] I.-C. Hoi, C. M. Wilson, G. Johansson, T. Palomaki, B. Peropadre, and P. Delsing, *Demonstration of a Single-Photon Router in the Microwave Regime*, Phys. Rev. Lett. **107**, 073601 (2011).

[113] A. F. van Loo, A. Fedorov, K. Lalumiére, B. C. Sanders, A. Blais, and A. Wallraff, *Photon-Mediated Interactions Between Distant Artificial Atoms*, Science **342**, 1494 (2013).

[114] J. A. Mlynek, A. Abdumalikov, C. Eichler, and A. Wallraff, *Observation of Dicke superradiance for two artificial atoms in a cavity with high decay rate*, Nat. Commun. **5**, 5186 (2014).

[115] A. R. Hamann, et. al, *Nonreciprocity realized with quantum nonlinearity*, arxiv 1806.00182 (2018).

[116] M. A. Lemonde, S. Meesala, A. Sipahigil, M.J.A. Schuetz, M.D. Lukin, M. Loncar, and P. Rabl, *Phonon Networks with Silicon-Vacancy Centers in Diamond Waveguides*, Phys. Rev. Lett. **120**, 213603 (2018).

[117] M. J. Burek, N. P. de Leon, B. J. Shields, B. J. M. Hausmann, Y. Chu, Q. Quan, A. S. Zibrov, H. Park, M. D. Lukin, and M. Loncar, *Free-Standing Mechanical and Photonic Nanostructures in Single-Crystal Diamond*, Nano Lett. **12**, 6084 (2012).

[118] S. Ali Momenzadeh, et al. *An integrated diamond nanophotonics platform for quantum-optical networks*, Nano Lett. **15** 165 (2014).

[119] B. Khanaliloo, H. Jayakumar, A. C. Hryciw, D. P. Lake, H. Kaviani, and P. E. Barclay, *Single-Crystal Diamond Nanobeam Waveguide Optomechanics*, Phys. Rev. X **5**, 041051 (2015).

[120] B. Khanaliloo, H. Jayakumar, A. C. Hryciw, D. P. Lake, H. Kaviani, and P. E. Barclay, *Single-Crystal Diamond Nanobeam Waveguide Optomechanics*, Phys. Rev. X **5**, 041051 (2015).

[121] S. Meesala, Y.-I. Sohn, H. A. Atikian, S. Kim, M. J. Bu- rek, J. T. Choy, and M. Loncar, *Enhanced Strain Coupling of Nitrogen-Vacancy Spins to Nanoscale Diamond Cantilevers*, Phys. Rev. Appl. **5**, 034010 (2016).

[122] A. Sipahigil, et al. *An integrated diamond nanophotonics platform for quantum-optical networks*, Science **354**, 847 (2016).

[123] M. J. Burek, et al. *Fiber-Coupled Diamond Quantum Nanophotonic Interface*, Phys. Rev. App. **8**, 024026 (2017).

[124] J. Petersen, J. Volz, and A. Rauschenbeutel, *Chiral nanophotonic waveguide interface based on spin-orbit interaction of light*, Science **346**, 67 (2014).

[125] R. Mitsch, C. Sayrin, B. Albrecht, P. Schneeweiss, and A. Rauschenbeutel, *Quantum state-controlled directional spontaneous emission of photons into a nanophotonic waveguide*, Nat. Commun. **5**, 5713 (2014).

[126] I. Söllner, et al., *Deterministic photon-emitter coupling in chiral photonic circuits*, Nature Nanotech. **10**, 775 (2015).

[127] P. Lodahl, S. Mahmoodian, S. Stobbe, P. Schneeweiss, J. Volz, A. Rauschenbeutel, H. Pichler, P. Zoller, *Chiral Quantum Optics*, Nature **541**, 473 (2017).

[128] W. K. Wootters, *Entanglement of Formation of an Arbitrary State of Two Qubits*, Phys. Rev. Lett. **80**, 2245 (1998).

[129] H. Carmichael, *Quantum trajectory theory for cascaded open systems*, Phys. Rev. Lett. **70**, 2273 (1993).

[130] K. Stannigel, P. Rabl, A. S. Sörensen, M. D. Lukin, and P. Zoller, *Optomechanical transducers for quantum-information processing*, Phys. Rev. A **84**, 042341 (2011).

[131] T. Ramos, B. Vermersch, P. Hauke, H. Pichler, and P. Zoller *Non-Markovian dynamics in chiral quantum networks with spins and photons*, Phys. Rev. A **93**, 062104 (2016).

[132] J. Lu, L. Zhou, H.C. Fu, and L. M. Kuang, *Quantum decoherence in a hybrid atom-optical system of a one-dimensional coupled-resonator waveguide and an atom*, Phys. Rev. A **81**, 062111 (2010).

[133] Y. Suematsu, and K. Furuya, *Theoretical spontaneous emission factor of iniection lasers*, IEICE of Japan **60**, 467 (1977).

[134] T. F. Krauss, *Slow light in photonic crystal waveguides*, J. Phys. D Appl. Phys. **40**, 2666 (2007).

[135] J. D. Joannopoulos, S. G. Johnson, J. N. Winn, R. D. Meade, *Molding the Flow of Light*, (Princeton University Press), (1995).

[136] K. Schneider and P. Seidler, *Strong optomechanical coupling in a slotted photonic crystal nanobeam cavity with an ultrahigh quality factor-to-mode volume ratio*, Optics Express **13**, 13850 (2016).

[137] M. K. Bhaskar, D.D. Sukachev, A. Sipahigl, R. E. Evans, M. J. Burek,C. T. Nguyen, L. J. Rogers, P. Siyushev, M. H. Metsch, H. Park, F. Jelezko, M. Loncar, and M. D. Lukin, *Quantum Nonlinear Optics with a Germanium-Vacancy Color Center in a Nanoscale Diamond Waveguide*, Phys. Rev. Lett. **118**, 223603 (2017).

[138] R. El-Ganainy and S. John, *Resonant dipole-dipole interaction in confined and strong-coupling dielectric geometries*, New J. Phys. **15**, 083033 (2013).

[139] Y. Liu and A. Houck, *Quantum electrodynamics near a photonic bandgap*, Nature Phys. **13**, 48 (2017).

[140] N. M. Sundaresan, R. Lundgren, G. Zhu, A. V. Gorshkov, and A. Houck, *Interacting Qubit-Photon Bound States with Superconducting Circuits*, arxiv 1801.10167 (2018).

[141] A. Yariv, Y. Xu, R. K. Lee, and A. Scherer *Coupled-resonator optical waveguide: a proposal and analysis*, Optics Letters **24**, 11 (1999).

[142] S. Olivier, C. Smith, M. Rattier, H. Benisty, C. Weisbuch, T. Krauss, R. Houdré, and U. Oesterlé, *Miniband transmission in a photonic crystal coupled-resonator optical waveguide*, Optics Letters **26**, 13 (2001).

[143] Y. Louyer, D. Meschede and A. Rauschenbeutel, *Tunable whispering-gallery mode resonators for cavity quantum electrodynamics*, Phys. Rev. A **72**, 031801(R) (2005).

[144] M. Pöllinger, *Bottle microresonators for applications in quantum optics and all-optical signal processing,* Dissertation Thesis (2010).

[145] M. Pöllinger, D. O'Shea, F. Warken and A. Rauschenbeutel, *Ultrahigh-Q Tunable Whispering-Gallery-Mode Microresonator*, Phys. Rev. Lett. **103**, 053901 (2009).

[146] M. Sumetsky and J. M. Fini, *Surface nanoscale axial photonics*, Opt. Express **19**, 26470 (2011).

[147] M. Sumetsky and Y. Dulashko, *SNAP: Fabrication of long coupled microresonator chains with sub-angstrom precision*, Opt. Express **20**, 27896 (2012).

[148] D. Underwood, W. E. Shanks, J. Koch, and A. Houck, *Low disorder microwave cavity lattices for quantum simulation with photons*, Phys. Rev. A **86**, 023837 (2012).

[149] A. Tomadin and R. Fazio, *Many-body phenomena in QED-cavity arrays*, J. Opt. Soc. Am. B **27**, A130 (2010).

[150] C. Noh and D. G. Angelakis, *Quantum simulations and many-body physics with light*, Rep. Prog. Phys **80**, 1 (2016).

[151] T. Shi and C. P. Sun, *Two-Photon Scattering in One Dimension by Localized Two-Level System*, arXiv:0907.2776v1 (2010).

[152] D. Roy, *Correlated few-photon transport in one-dimensional waveguides: Linear and nonlinear dispersions*, Phys. Rev. A **83**, 043823 (2011).

[153] G. Díaz-Camacho, D. Porras, and J. J. García-Ripoll, *Photon-mediated qubit interactions in one-dimensional discrete and continuous models*, Phys. Rev. A **91**, 063828 (2015).

[154] M. P. Schneider, T. Sproll, C. Stawiarski, P. Schmitteckert, and K. Busch, *Green's-function formalism for waveguide QED applications*, Phys. Rev. A **93**, 013828 (2016).

[155] S. E. Kocabas, *Effects of Modal Dispersion on Few Photon - Qubit Scattering in One-Dimensional Waveguides*, Phys. Rev. A **93**, 033829 (2016).

[156] J. Lu, L. Zhou, H. C. Fu, and L.-M. Kuang, *Quantum decoherence in a hybrid atom-optical system of a one-dimensional coupled-resonator waveguide and an atom*, Phys. Rev. A **81**, 062111 (2010).

[157] J. G. Pedersen, S. Xiao, and N. A. Mortensen, *Limits of slow light in photonic crystals*, Phys. Rev. B **78**, 153101 (2008).

[158] E. N. Economou, *Green Functions in Quantum Physics* (Springer-Verlag, Berlin, 1979).

[159] J. C. Hernández-Herrejón, F. M. Izrailev, and L. Tessieri , Journal of Physics A: Mathematical and Theoretical **43**, 425004 (2010).

[160] S. Lorenzo, F. Lombardo F. Ciccarello, and G. M. Palma, *Quantum non-Markovianity induced by Anderson localization*, Sci. Rep. **7**, 42729 (2017).

[161] T. Shi, A. Gonzalez-Tudela and J. I. Cirac, *Effective many-body Hamiltonians of qubit-photon bound states*, arXiv:1806.02527 (2018).

[162] T. Sproll, C. Martens, M. P. Schneider, F. Intravaia, K. Busch, *Non-perturbative and non-Markovian Förster-interaction in waveguiding systems*, arXiv:1804.01703 (2018).

[163] P. A. Cherenkov, *Visible Radiation Produced by Electrons Moving in a Medium with Velocities Exceeding that of Light*, Dokl. Akad. Nauk **2**, 451 (1934) [Phys. Rev. **52**, 378 (1937)].

[164] J. D. Jackson, *Classical electrodynamics* (John Wiley & Sons, 1962).

[165] Z. Huang and K. J. Kim, *Review of x-ray free-electron laser theory*, Phys. Rev. ST Accel. Beams **10**, 034801 (2007).

[166] S. Stenholm, *The semiclassical theory of laser cooling*, Rev. Mod. Phys. **58**, 699 (1986).

[167] H. J. Metcalf and P. van der Straten, *Laser Cooling and Trapping* (Springer, 1999).

[168] K. M. Birnbaum, A. Boca, R. Miller, A. D. Boozer, T. E. Northup, and H. J. Kimble, *Photon blockade in an optical cavity with one trapped atom*, Nature (London) **436**, 87 (2005).

[169] B. Hacker, S. Welte, G. Rempe, and S. Ritter, *A photon-photon quantum gate based on a single atom in an optical resonator*, Nature (London) **536**, 193 (2016).

[170] C. Luo, M. Ibanescu, S. G. Johnson, J. D. Joannopoulos, *Cerenkov Radiation in Photonic Crystals*, Science **299**, 5605 (2003).

[171] C. Luo, M. Ibanescu, E. J. Reed, S. G. Johnson, J. D. Joannopoulos, *Doppler Radiation Emitted by an Oscillating Dipole Moving inside a Photonic Band-Gap Crystal*, Phys. Rev. Lett. **96**, 043903 (2006).

[172] D. Petrosyan and M. Fleischhauer, *Quantum Information Processing with Single Photons and Atomic Ensembles in Microwave Coplanar Waveguide Resonators*, Phys. Rev. Lett. **100**, 170501 (2008).

[173] S. D. Hogan, J. A. Agner, F. Merkt, T. Thiele, S. Filipp, and A. Wallraff, *Driving Rydberg-Rydberg Transitions from a Coplanar Microwave Waveguide*, Phys. Rev. Lett. **108**, 063004 (2012).

[174] C. Hermann-Avigliano, R. Celistrino Teixeira, T. L. Nguyen, T. Cantat-Moltrecht, G. Nogues, I. Dotsenko, S. Gleyzes, J. M. Raimond, S. Haroche, and M. Brune, *Long coherence times for Rydberg qubits on a superconducting atom chip*, Phys. Rev. A **90**, 040502(R) (2014).

[175] M. A. Beck, J. A. Isaacs, D. Booth, J. D. Pritchard, M. Saffman, R. McDermott, *Optimized Coplanar Waveguide Resonators for a Superconductor-Atom Interface*, Appl. Phys. Lett. **109**, 092602 (2016).

[176] S. Longhi, *Bound states of moving potential wells in discrete wave mechanics*, Europhys Lett. **120**, 12 (2018).

[177] D. Schrader, S. Kuhr, W. Alt, M. Müller, V. Gomer, and D. Meschede, *An optical conveyor belt for single neutral atoms*, Appl. Phys. B **73**, 819 (2001).

[178] P. Schneeweiss, S. T. Dawkins, R. Mitsch, D. Reitz, E. Vetsch, and A. Rauschenbeutel, *A nanofiber-based optical conveyor belt for cold atoms*, Appl. Phys. B **110**, 279 (2013).

[179] A. Yariv, *Optical electronics* (Saunders College Publishing, Philadelphia), 1991

[180] G. E. Ponchak, E. M. Tentzeris, and L. P. B. Katehi, *Characterization of Finite Ground Coplanar Waveguide With Narrow Ground Planes*, Int. J. Microcircuits Electronic Packaging **20**, 2 (1997).

[181] M. Gillick, I. D. Robertson, and J. S. Joshi, *Direct analytical solution for the electric field distribution at the conductor surfaces of coplanar waveguides*, IEEE Trans. Microw. Theory Tech. **41**, 1 (1993).

[182] L. Frunzio, A. Wallraff, D. Schuster, J. Majer, and R. Schoelkopf, *Fabrication and Characterization of Superconducting Circuit QED Devices for Quantum Computation*, IEEE Trans. Appl. Supercond. **15**, 860 (2005).

[183] P. Lancuba and S. D. Hogan, *Electrostatic trapping and in situ detection of Rydberg atoms above chip-based transmission lines*, J. Phys. B: At. Mol. Opt. Phys. **49**, 074006 (2016).

[184] M. F. Yanik and S. Fan, *Dynamic Photonic Structures: Stopping, Storage, and Time Reversal of Light*, Studies In App. Math. **115**, 233 (2005).

[185] S. Longhi, *Stopping and time reversal of light in dynamic photonic structures via Bloch oscillations*, Phys. Rev. E **75**, 026606 (2007).

[186] Z. Yu and S. Fan, *Complete optical isolation created by indirect interband photonic transitions*, Nat. Phot. **3**, 91 (2009).

[187] M. Minkov and S. Fan, *Localization and time-reversal of light through dynamic modulation*, Phys. Rev. B **97**, 060301(R) (2018).

[188] F. J. R. Schülein, E. Zallo, P. Atkinson, O. G. Schmidt, R. Trotta, A. Rastelli, A. Wixforth, and H. J. Krenner, *Directional and Dynamic Modulation of the Optical Emission of an Individual GaAs Nanowire Using Surface Acoustic Waves*, Nano Lett. **11**, 1512 (2011).

[189] J. B. Kinzel, D. Rudolph, M. Bichler, G. Abstreiter, J. J. Finley, G. Koblmüller, A. Wixforth,and H. J. Krenner, *Fourier synthesis of radiofrequency nanomechanical pulses with different shapes*, Nat. Nanotech. **10**, 512 (2015).

[190] D. B. Sohn, S.Kim, and G. Bahl, *Time-reversal symmetry breaking with acoustic pumping of nanophotonic circuits*, Nat. Phot. **12**, 91 (2018).

[191] G. Calajó, L. Rizzuto, and R. Passante, *Control of spontaneous emission of a single quantum emitter through a time-modulated photonic-band-gap environment*, Phys. Rev. A **96**, 023802 (2017).

[192] M. M De Lima Jr and P. V. Santos, *Modulation of photonic structures by surface acoustic waves*, Rep. Prog. Phys. **68**, 1639 (2005).

[193] D. A. Fuhrmann, S. M. Thon, H. Kim, D. Bouwmeester, P. M. Petroff, A. Wixforth and H. J. Krenner, *Dynamic modulation of photonic crystal nanocavities using gigahertz acoustic phonons*, Nat. Photon. **5**, 605 (2011).

[194] J. Pustiowski, K. Müller, M. Bichler, G. Koblmüller, J. J. Finley, A. Wixforth, and H. J. Krenner,*Independent dynamic acousto-mechanical and electrostatic control of individual quantum dots in a LiNbO3-GaAs hybrid*, App. Phys. Lett. **106**, 013107 (2015).

[195] M. O. Scully, S. Y. Zhu, and A. Gavrielides, *Degenerate Quantum-Beat Laser: Lasing without Inversion and Inversion without Lasing*, Phys. Rev. Lett. **62**, 24 (1989).

[196] D. Browne, and M. Plenio, *Robust generation of entanglement between two cavities mediated by short interactions with an atom*, Phys. Rev. A **67**, 012325 (2003).

[197] A. Messina, *A single atom-based generation of Bell states of two cavities*, Eur. Phys. J. D **18**, 379 (2002).

[198] A. González-Tudela , J.I. Cirac, *Markovian and non-Markovian dynamics of quantum emitters coupled to two-dimensional structured reservoirs*, Phys. Rev. Lett., **119** 143602 (2017).

[199] A. González-Tudela and J.I. Cirac, *Quantum Emitters in Two-Dimensional Structured Reservoirs in the Nonperturbative Regime*, Phys. Rev. A, **96** 043811 (2017).

[200] J. I. Cirac, P. Zoller, H. J. Kimble, and H. Mabuchi, *Quantum State Transfer and Entanglement Distribution among Distant Nodes in a Quantum Network*, Phys. Rev. Lett. **78**, 3221 (1997).

[201] K. Stannigel, P. Rabl, A. S. Sørensen, M. D. Lukin, and P. Zoller, *Optomechanical transducers for quantum-information processing*, Phys. Rev. A **84**, 44 (2011).

[202] B. Q. Baragiola, R. L. Cook, A. M. Branczyk, and J. Combes, *N-photon wave packets interacting with an arbitrary quantum system*, Phys. Rev. A **86**, 013811 (2012).

[203] Y.-L. L. Fang, F. Ciccarello, and H. U. Baranger, *Non-Markovian dynamics of a qubit due to single-photon scattering in a waveguide*, New J. Phys. **20**, 043035 (2018).

[204] E. Rephaeli and S. Fan, *Stimulated Emission from a Single Excited Atom in a Waveguide*, Phys. Rev. Lett. **108**, 143602 (2012).

[205] Y.-L. L. Fang and H. U. Baranger, *Multiple emitters in a waveguide: Non-reciprocity and correlated photons at perfect elastic transmission*, Phys. Rev. A **96**, 013842 (2017).

[206] T. Niemczyk, *et al.*, *Circuit quantum electrodynamics in the ultrastrong-coupling regime*, Nat. Phys. **6**, 772 (2010).

[207] P. Forn-Díaz, J. Lisenfeld, D. Marcos, J. J. García-Ripoll, E. Solano, C. J. P. M. Harmans, and J. E. Mooij, *Observation of the Bloch-Siegert Shift in a Qubit-Oscillator System in the Ultrastrong Coupling Regime*, Phys. Rev. Lett. **105**, 237001 (2010).

[208] A. Baust, E. Hoffmann, M. Haeberlein, M. J. Schwarz, P. Eder, J. Goetz, F. Wulschner, E. Xie, L. Zhong, F. Quijandría, D. Zueco, J.-J. García-Ripoll, L. García-Álvarez, G. Romero, E. Solano, K. G. Fedorov, E. P. Menzel, F. Deppe, A. Marx, and R. Gross, *Ultrastrong coupling in two-resonator circuit QED*, Phys. Rev. B **93**, 214501 (2016).

[209] P. Forn-Díaz, J. J. García-Ripoll, B. Peropadre, M. A. Yurtalan, J.-L. Orgiazzi, R. Belyansky, C. M. Wilson, and A. Lupascu, *Ultrastrong coupling of a single artificial atom to an electromagnetic continuum*, Nat. Phys. **13**, 39 (2017).

[210] F. Yoshihara, T. Fuse, S. Ashhab, K. Kakuyanagi, S. Saito, and K. Semba, *Superconducting qubit-oscillator circuit beyond the ultrastrong-coupling regime*, Nat. Phys. **13**, 44 (2017).

[211] Z. Chen, Y. Wang, T. Li, L. Tian, Y. Qiu, K. Inomata, F. Yoshihara, S. Han, F. Nori, J. S. Tsai, and J. Q. You, *Multi-photon sideband transitions in an ultrastrongly coupled circuit quantum electrodynamics system*, Phys. Rev. A **96**, 012325 (2017).

[212] S. J. Bosman, M. F. Gely, V. Singh, A. Bruno, D. Bothner, and G. A. Steele, *Multi-mode ultra-strong coupling in circuit quantum electrodynamics*, arXiv:1704.06208 (2017).

[213] Y. Todorov, A. M. Andrews, R. Colombelli, S. De Liberato, C. Ciuti, P. Klang, G. Strasser, and C. Sirtori, *Ultrastrong Light-Matter Coupling Regime with Polariton Dots*, Phys. Rev. Lett. **105**, 196402 (2010).

[214] T. Schwartz, J. A. Hutchison, C. Genet, and T. W. Ebbesen, *Reversible Switching of Ultrastrong Light-Molecule Coupling*, Phys. Rev. Lett. **106**, 196405 (2011).

[215] M. Geiser, F. Castellano, G. Scalari, M. Beck, L. Nevou, and J. Faist, *Ultrastrong Coupling Regime and Plasmon Polaritons in Parabolic Semiconductor Quantum Wells*, Phys. Rev. Lett. **108**, 106402 (2012).

[216] G. Scalari, C. Maissen, S. Cibella, R. Leoni, C. Reichl, W. Wegscheider, M. Beck, and J. Faist, *THz ultrastrong light-matter coupling*, Il Nuovo Saggiatore **31**, 4 (2015).

[217] Q. Zhang, M. Lou, X. Li, J. L. Reno, W. Pan, J. D. Watson, M. J. Manfra, and J. Kono, *Collective non-perturbative coupling of 2D electrons with high-quality-factor terahertz cavity photons*, Nat. Phys. **12**, 1005 (2016).

[218] P. Nataf and C. Ciuti, *Vacuum Degeneracy of a Circuit QED System in the Ultrastrong Coupling Regime*, Phys. Rev. Lett. **104**, 023601 (2010).

[219] P. Nataf and C. Ciuti, *No-go theorem for superradiant quantum phase transitions in cavity QED and counter-example in circuit QED*, Nat. Commun. **1**, 72 (2010).

[220] M. Bamba, K. Inomata, and Y. Nakamura, *Superradiant Phase Transition in a Superconducting Circuit in Thermal Equilibrium*, Phys. Rev. Lett. **117**, 173601 (2016).

[221] S. De Liberato, *Light-Matter Decoupling in the Deep Strong Coupling Regime: The Breakdown of the Purcell Effect*, Phys. Rev. Lett. **112**, 016401 (2014).

[222] D. De Bernardis, T. Jaako, and P. Rabl, *Cavity quantum electrodynamics in the non-perturbative regime*, Phys. Rev. A **97**, 043820 (2018).

[223] G. Levine and V. N. Muthukumar, *Entanglement of a qubit with a single oscillator mode*, Phys. Rev. B **69**, 113203 (2004).

[224] A. P. Hines, C. M. Dawson, R. H. McKenzie, and G. J. Milburn, *Entanglement and bifurcations in Jahn-Teller models*, Phys. Rev. A **70**, 022303 (2004).

[225] S. Ashhab and F. Nori, *Qubit-oscillator systems in the ultrastrong-coupling regime and their potential for preparing nonclassical states*, Phys. Rev. A **81**, 042311 (2010).

[226] G. Romero, D. Ballester, Y. M. Wang, V. Scarani, and E. Solano, *Ultrafast Quantum Gates in Circuit QED*, Phys. Rev. Lett. **108**, 120501 (2012).

[227] B. Reznik, A. Retzker, and J. Silman, *Violating Bell's inequalities in vacuum*, Phys. Rev. A **71**, 042104 (2005).

[228] M. Han, S. J. Olson, and J. P. Dowling, *Generating entangled photons from the vacuum by accelerated measurements: Quantum-information theory and the Unruh-Davies effect*, Phys. Rev. A **78**, 022302 (2008).

[229] A. Auer and G. Burkard, *Entangled photons from the polariton vacuum in a switchable optical cavity*, Phys. Rev. B **85**, 235140 (2012).

[230] S. J. Olson and T. C. Ralph, *Extraction of timelike entanglement from the quantum vacuum*, Phys. Rev. A **85**, 012306 (2012).

[231] C. Sabin, B. Peropadre, M. del Rey, and E. Martin-Martinez, *Extracting Past-Future Vacuum Correlations Using Circuit QED*, Phys. Rev. Lett. **109**, 033602 (2012).

[232] G. Salton, R. B. Mann, and N. C. Menicucci, *Acceleration-assisted entanglement harvesting and rangefinding*, New J. Phys. **17**, 035001 (2015).

[233] L. Dai, W. Kuo and M. C. Chung, *Extracting entangled qubits from Majorana fermions in quantum dot chains through the measurement of parity*, Sci. Rep. **5**, 11188 (2015).

[234] U. Vool and M. Devoret, *Introduction to Quantum Electromagnetic Circuits*, Int. J. Circ. Theor. Appl. **45**, 897 (2017).

[235] J. Bourassa, J. M. Gambetta, A. A. Abdumalikov, O. Astafiev, Y. Nakamura, and A. Blais, *Ultrastrong coupling regime of cavity QED with phase-biased flux qubits*, Phys. Rev. A **80**, 032109 (2009).

[236] B. Peropadre, D. Zueco, D. Porras, and J. J. García-Ripoll, *Nonequilibrium and Nonperturbative Dynamics of Ultrastrong Coupling in Open Lines*, Phys. Rev. Lett. **111**, 243602 (2013).

[237] Y. Qiu, W. Xiong, X.-L. He, T.-F. Li, and J. Q. You, *Four-junction superconducting circuit*, Sci. Rep. **6**, 28622 (2016).

[238] C. M. Wilson, G. Johansson, A. Pourkabirian, J. R. Johansson, T. Duty, F. Nori, and P. Delsing, *Observation of the dynamical Casimir effect in a superconducting circuit*, Nature (London) **479**, 376 (2011).

[239] F. Yan, S. Gustavsson, A. Kamal, J. Birenbaum, A.P. Sears, D. Hover, D. Rosenberg, G. Samach, T. J. Gudmundsen, J. L. Yoder, T. P. Orlando, J. Clarke, A. J. Kerman, and W. D. Oliver, *The flux qubit revisited to enhance coherence and reproducibility*, Nat. Commun. **7**, 12964 (2016).

Curriculum Vitae

M.Sc. Giuseppe Calajò

TU Wien - Atominstitut
Wiedner Hauptstrasse 8-10
1040 Wien, Austria

giuseppecalajo@gmail.com
Phone(austrian): +43 681 81430089
Phone(italian): +39 320 1895699

Education

Sep. 2014- **TU Wien**
PhD in Physics part of the doctoral program CoQuS
Field: Theoretical Quantum Optics (Supervisor: Assoc. Prof. P. Rabl)
Title of PhD thesis (under submission):
"Atom-field interaction in slow-light waveguide QED"

2011-2013 **University of Palermo**
Master of Science in Physics
Title of Master Thesis:
"Spontaneous emission of an atom in dynamical photonic crystal "
Mark: 110/110 cum laude

2008-2011 **University of Palermo**
Bachelor degree in Physical Sciences
Title of Bachelor Thesis: "The Unruh Effect "
Mark: 110/110 cum laude

2008 **Liceo classico G. Meli, Palermo**
Classical high school diploma

Work experience

Sep. 2014- **Atominstitut, TU Wien**
PhD student in Theoretical Quantum Optics

List of Publications

1. *Harvesting multi-qubit entanglement from ultrastrong interactions in circuit QED*
   F. Armata, G. Calajo, T. Jaako, M.S. Kim, and P. Rabl
   Phys. Rev. Lett. **119**, 183602 (2017)

2. *Control of spontaneous emission of a single quantum emitter through a time-modulated photonic-band- gap environment*
   G. Calajo, L. Rizzuto, and R. Passante
   Phys. Rev. A **96**, 023802 (2017)

3. *Strong coupling between moving atoms and slow-light Cherenkov photons*
   G. Calajo and P. Rabl,
   Phys. Rev. A **95**, 043824 (2017)

4. *Atom-field dressed states in slow-light waveguide QED*
G. Calajo, F. Ciccarello, D. Chang, and P. Rabl,
Phys. Rev. A **93**, 033833 (2016)

Languages and Skills

Italian (native), English (fluent)
Matlab, Mathematica, C++, LaTeX, Adobe Illustrator